Wideband Low-Profile Antenna Arrays: Fundamental Limits and Practical Implementations

Dissertation

Presented in Partial Fulfillment of the Requirements for the Degree Doctor of Philosophy in the Graduate School of The Ohio State University

By

Jonathan Doane, B.S., M.S.

Graduate Program in Electrical and Computer Engineering

The Ohio State University

2013

Dissertation Committee:

Dr. John Volakis, Co-Advisor

Dr. Kubilay Sertel, Co-Advisor

Dr. Chris Baker

Abstract

Advanced wireless communication and sensing systems have created a growing need for high performance, compact antennas. Low-profile wideband phased arrays are of particular interest, and have recently been shown to be capable of extremely large bandwidths. However, the size, weight, and cost of phased arrays still makes them impractical for many applications. The development of thinner, lightweight, and inexpensive wideband arrays is critical to improving the capabilities of small platforms such as small unmanned aerial vehicles.

Like all antennas, phased arrays are limited by a fundamental compromise between size and performance. Although the theoretical limitations of electrically small antennas have been well known for over 60 years, similarly general limits have not yet been developed for periodic antenna arrays. In the first part of this thesis, we derive a new fundamental bandwidth limit for any periodic array that is backed by a conducting ground plane and constructed from passive and reciprocal materials. This limit is related to several critical design factors, including the array's thickness, polarization, scan angle, materials used, as well as the overall complexity of the array design. We also consider the common case when all radiating currents are confined to a thin planar sheet placed above the ground plane. We show here that such planar phased arrays have a fundamental impedance bandwidth limit of 8.3:1 (with VSWR$\leq$2:1), in

the absence of material loading. This bandwidth may be further improved by adding dielectric superstrate or magnetic substrate material layers.

Knowledge of such fundamental bandwidth limits is extremely useful in the design of practical wideband arrays, which is the focus of the second part of this thesis. A key challenge with many wideband arrays is developing a feed circuit that supports extremely wide bandwidths without significantly adding to the size, weight, and cost of the design. Here, we demonstrate a novel approach that overcomes this problem by exploiting the natural reactance of the feed circuit as a simple impedance matching network for the array. The result is a simultaneous reduction in size and weight and improvement in bandwidth compared to other feeding techniques. We refer to our design as the *Tightly Coupled Dipole Array with Integrated Balun* (TCDA-IB), and it achieves 7.35:1 bandwidth while maintaining a low VSWR of $\leq$ 2.65:1 while scanning to $\pm 45°$ in all planes. A prototype 8×8 array was constructed and demonstrated excellent performance relative to simulation. We also demonstrate that by adding reconfigurable components to the TCDA-IB, its maximum scan angle may by increased to as much as $\pm 70°$ while maintaining a 5:1 impedance bandwidth.

Our fundamental bandwidth limits reveal for the first time the extent of the realizable design space for wideband low-profile arrays, and suggest there are significant opportunities for further improvement. Several practical techniques are also presented for increasing bandwidth and scanning performance while reducing the total size, weight and cost of the array. In summary, the ongoing development of high-performance wideband low-profile arrays will likely remain an important and fertile area of research for the foreseeable future.

To Andi

Acknowledgments

I am incredibly lucky to have had the opportunity to study with and learn from two great advisors, Prof. Kubilay Sertel and Prof. John Volakis. I will always be thankful to Prof. Volakis for inviting me to the ElectroScience Lab, and for his unwavering support and encouragement. His energy and enthusiasm is contagious and I consider it a privilege to have been his student. I wish to also thank Prof. Sertel for his generous mentorship and friendship over the last three years. I have learned a tremendous amount from him, and his personal and professional example has meant a great deal to me.

I would also like to thank Prof. Chris Baker, Prof. Atilla Eryilmaz, Prof. Jin-Fa Lee, and Prof. Prabhakar Pathak for their guidance and support.

Although there is not enough room to acknowledge them all, I have had the tremendous privilege of working alongside a number of other excellent students and staff at the ElectroScience Laboratory, whose friendship I have greatly appreciated. I would like to especially thank Yiannis Tzanidis and Will Moulder, whose related work on wideband arrays has inspired and guided much of my own research.

Most of all, I would like to thank my beautiful wife Andi, whose love, support and patience made this possible.

Vita

May 15, 1978 ....Born - Grand Rapids, MI.

1999 ......................................B.S. Electrical Engineering, Michigan
Technological University.

2001 ......................................M.S. Electrical Engineering, Michigan
Technological University.

2001-2003 ....Electrical Engineer, Rockwell Collins,
Inc.

2003-2007 ....Campus Minister, InterVarsity Christian Fellowship.

2007-2010 ....Senior Electrical Engineer, Rockwell
Collins, Inc.

2010-present ....Graduate Research Associate, Ohio
State University.

Publications

J. Doane, K. Sertel, J. Volakis, "Matching Bandwidth Limits for Arbitrarily Polarized PEC-Backed Arrays". IEEE *Trans. Antennas Propag.*, in preparation.

J. Doane, K. Sertel, J. Volakis, "A Wideband, Wide Scanning Tightly Coupled Dipole Array with Integrated Balun". IEEE *Trans. Antennas Propag.*, in review.

J. Doane, K. Sertel, J. Volakis, "Matching Bandwidth Limits for Arrays Backed by a Conducting Ground Plane". IEEE *Trans. Antennas Propag.*, to appear, May 2013.

J. Doane, K. Sertel, J. Volakis, "Bandwidth Limits for Lossless Planar Arrays over a Ground Plane". *Electronics Letters*, Vol 48, No. 10, May 2012.

H. Xin, J. West, J. Mather, J. Doane, J. Higgins, H. Kazemi, M. Rosker, "A Two-Dimensional Millimeter Wave Phase Scanned Lens Utilizing Analog Electromagnetic Crystal (EMXT) Waveguide Phase Shifters". IEEE *Trans. Antennas Propag.*, Vol 53, No. 1, Jan 2005.

Fields of Study

Major Field: Electrical and Computer Engineering

    Studies in:

        Electromagnetics
        Mathematics
        Signal Processing

Table of Contents

List of Tables

List of Figures

xvii

xx

xxiii

Chapter 1: Introduction to Wideband Low-Profile Phased Arrays

The demand for more bandwidth is skyrocketing at an exponential rate. The average speed of a high-end personal internet connection increases by more than 50% every year [1], and with the advent of smart phones and mobile broadband, traffic on cellular networks is growing at an even faster rate [2], see Fig. 1.1.

This trend is unlikely to slow down, nor is it limited to mass market commercial technologies. Today's military systems must collect and process a tremendous amount of data from various sensors distributed among personnel, equipment, satellites, manned and unmanned vehicles, and then redistribute this information to a myriad of end users. This level of interconnectivity provides the modern warfighter with unprecedented informational superiority and situational awareness.

However, developing the next generation of robust wireless networks, radios, and sensors that can keep pace with this voracious appetite for more information is not an easy task. Platforms such as small unmanned aerial vehicles (UAV) or compact hand-held devices have limited available size, weight, and power, yet they still must be equipped with high performance RF sensors and provide high bandwidth connectivity. Moreover, the distribution of these capabilities across a large number of users and platforms requires low-cost implementations. There is therefore significant interest in

(a) Personal Internet Connection Speed

(b) Annual Growth of Cellular Data Traffic
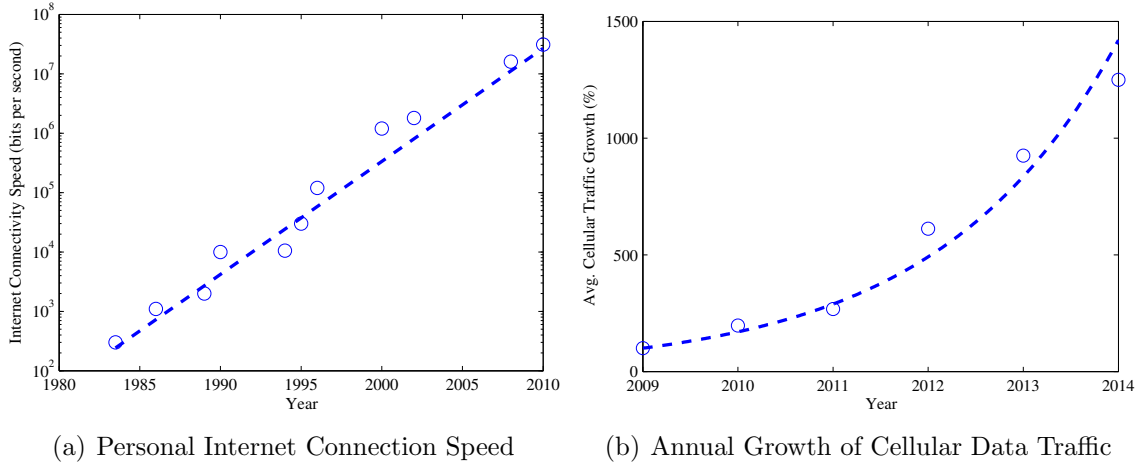
Figure 1.1: Exponential growth in bandwidth usage. (a) Speed of a high-end personal internet connection, showing 55% annual growth [1]. (b) Average cellular traffic showing 70% annual growth in recent years [2].

developing new wideband antenna technology that can provide greater performance in a compact and cost effective form.

Of particular interest are low-profile phased arrays that can operate over wide bandwidths (3:1 or more) with a wide scanning field of view ($\geq \pm 45°$). Phased arrays are ideal for many applications because their high gain directional beams enable long range point-to-point communication and high-resolution sensing. Unlike reflectors, phased arrays can be mounted conformally on the skin of a vehicle, and can produce multiple electronically steered beams.

Another emerging application for wideband arrays is for multi-functional RF systems. Installing multiple antennas on a platform is often undesirable for aerodynamic, structural, and budgetary reasons. Therefore, rather than using a separate antenna for each system, a single wideband array may support a collection of individual systems and radios [3]. Fig. 1.2 depicts common waveforms and frequency bands used in

2

Radio	# of Waveforms	Radio	# of Waveforms
ARC-190	1	JTRS GMR	6
ARC-210	3	JTRS HMS	6
PRC-117F	5	JTRS Goal	32
Blackberry	5	**ART Goal**	**> 100**

HMS = Handheld, Manpack, Small Form Factor
GMR = Ground Mobile Radio
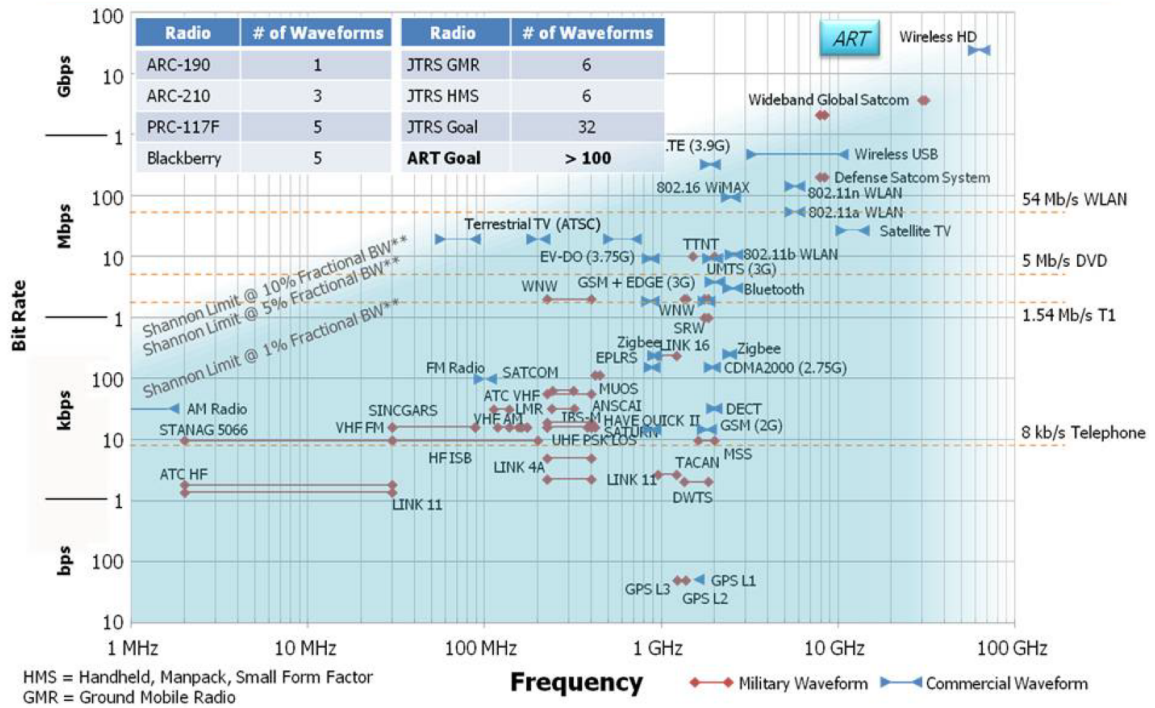
Figure 1.2: Modern military and commercial platforms use many radios spanning many decades of bandwidth. Without wideband multi-functional antennas, each radio would require a separate antenna. Figure courtesy of Dr. Dev Palmer and Dr. Sanjay Raman, DARPA/MTO.

commercial and military environments. A UAV or telecommunications base station may contain radios that span several decades of bandwidth, stretching the capabilities of current wideband arrays. Reconfigurable systems such as software defined radios and adaptive radars may also require wideband arrays in order to support their various operational modes, waveforms, and bands.

Despite their usefulness, the size, weight, and cost of wideband phased arrays still makes them impractical for some applications and platforms. While the capabilities of the underlying electronics continue to grow exponentially each year, there is unfortunately not a similar exponential trend in antenna capabilities. Rather, the laws

3

of physics impose fundamental limits on the size and performance of electromagnetic systems – Moore's law does not apply to Maxwell's equations. Nevertheless, there remains opportunity for improvement, and recent years have seen several advancements in state-of-the-art wideband low-profile phased arrays.

The goal of this thesis is two-fold. First and foremost, we seek to determine the fundamental limits of performance for low-profile phased arrays, and to establish which design factors are most critical to reaching this limit. Secondly, we seek to determine how our understanding of these limitations may be applied to develop practical wideband arrays that achieve superior bandwidth and electrical performance, while reducing the total size, weight, and cost of the system.

1.1 Wideband Arrays above a Conducting Ground Plane

Antenna miniaturization is a challenging problem, famously illustrated by the Wheeler-Chu limits [4], [5], which define the maximum possible gain and bandwidth for any electrically small antenna. Although high gain arrays are not electrically small and thus the Wheeler-Chu limits do not provide a useful bound, they do face a similar miniaturization problem. Just as reducing the electrical size of a small antenna has a dramatic effect on its gain and bandwidth, placing an antenna array in close proximity to a conducting ground plane will also significantly deteriorate its performance.

The reason for this phenomenon can be understood by considering the current distribution of a low profile array placed above a ground plane, as shown in Fig. 1.3. For an array radiating in the z direction, the radiating currents must lie in the x-y plane. The virtual currents below the ground plane are the mirror image of the
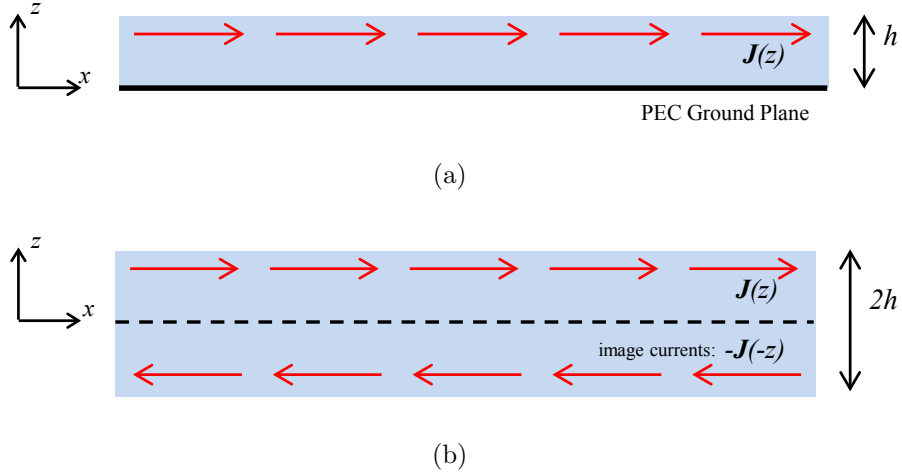
Figure 1.3: (a) A low-profile array of height h above a conducting ground plane. For an array radiating at broadside, radiating currents are horizontal (b) Representation of the array using image theory. If h is electrically small, the image currents will cancel and prevent efficient broadside radiation.

primary currents, running in the opposite direction. If the array is sufficiently thick, these image currents may not necessarily degrade the performance of the array. In fact, if the primary currents are $\lambda/4$ above the ground plane, the image currents add constructively and the array will radiate efficiently. However, if the array is electrically thin ($h \ll \lambda/4$), the primary and image currents will add destructively, regardless of how sophisticated the array design may be. The array will therefore have large currents, however it will radiate very little power. This ratio of stored (reactive) power to radiated (real) power is denoted by the *quality factor* or Q of the system. Since, as is well known, the impedance bandwidth of a simple resonant circuit is fundamentally limited by its Q [6], low-profile PEC-backed arrays also have a fundamental bandwidth limit which depends on their electrical thickness.
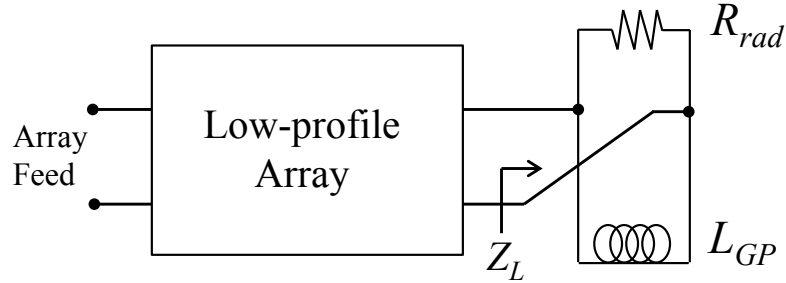
Figure 1.4: Equivalent circuit for a low-profile array backed by a conducting ground plane. The radiation resistance R_{rad} and the ground plane inductance L_{GP} form a reactive load Z_L to be matched by the array. The Fano bandwidth limit of the load Z_L establishes a fundamental bandwidth limit for the array.

A useful way to quantify the Q of a low-profile array is to represent the ground plane as a reactive load to the array. When the array is electrically thin, the ground plane can be modeled by an inductance L_{GP} in parallel to the radiation resistance R_{rad}, as depicted in Fig. 1.4. Viewed in this manner, the array itself can be treated simply as a black-box impedance matching network to a fixed load impedance. With such a model, circuit theory may be used to obtain fundamental constraints on the performance of any low-profile array. Perhaps even more importantly, network synthesis techniques may be applied to inspire new array designs with performance that approaches these theoretical limits. This paradigm of treating array analysis and design as an impedance matching problem is quite useful, and forms the basis of our overall approach to wideband low-profile arrays.

1.2 Survey of Wideband Array Technologies

A number of wideband array technologies have been developed which address the challenges described above using a variety of different techniques. In this section, we

provide a brief introduction to several of the most popular types of wideband arrays, their operational principles, and their relative strengths and weaknesses.

1.2.1 Tapered Slot and Traveling Wave Arrays
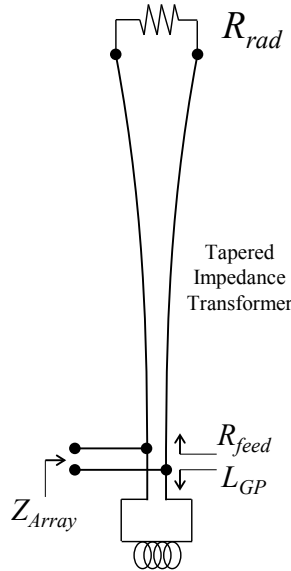
Figure 1.5: A tapered transmission line can be used to reduce the effective radiation resistance at the feedpoint, mitigating the ground plane inductance over a wide bandwidth.

As depicted in Fig. 1.4, the bandwidth limitations of PEC-backed arrays result from the inductance of the ground plane in parallel with the radiation resistance. This can be mitigated by either increasing the effective inductance or reducing the effective radiation resistance, so that the reactance seen at the feed point is minimized. In practice, a tapered transmission line can be placed between the feed point and the top of the array to reduce the effective radiation resistance, as shown in Fig 1.5. With

$R_{feed} \ll L_{GP}$, the input impedance Z_{Array} becomes mostly real, and the array can operate effectively over a wide band, with the high end cutoff being limited by the onset of grating lobes.

Vivaldi Arrays
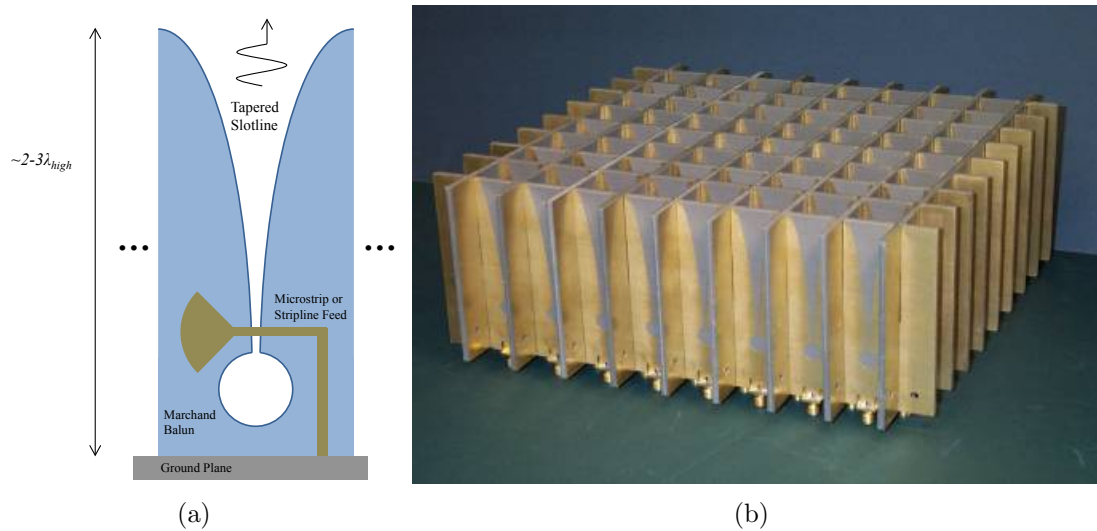
Figure 1.6: Vivaldi Array. (a) Sketch of Vivaldi element with balun and feedline. (b) Photo of Vivaldi Array, from [7], ©2008 IEEE.

The most basic implementation of this concept is the so-called *Vivaldi* array[1], which uses an exponentially tapered slot line fed by a Marchand balun, as shown in Fig. 1.6. Vivaldi arrays have been in use for almost 40 years [9, 10], and are still perhaps the most well known type of wideband phased array. They are capable of 10:1 bandwidth or more, and can scan to $> 45°$ from broadside [11, 12].

[1]The name Vivaldi is apparently due to "a resemblance to the shape of a cello or violin, instruments used by Antonio Vivaldi." [8]

As the effective bandwidth of the impedance transformation provided by the tapered slot line is determined by its length, wideband Vivaldi arrays must be fairly thick, commonly 2-3λ at the highest frequency. Therefore, a major drawback of Vivaldi arrays is that they are not very low-profile. In addition to their height, Vivaldi arrays also suffer from high cross-polarization when scanning. This is because there are strong vertical currents running down the length of the slotline, perpendicular to the plane of the array. When array radiates at broadside, these currents are normal to the direction of propagation and therefore do not radiate. However as the array is scanned, these currents begin to produce significant cross-polarization. This can even result in "polarization reversal" where the cross-polarized radiation level exceeds the co-polarization level. For wideband Vivaldi arrays, this may occur with as small a scan angle as 30° [12].

Vivaldi arrays have been used for many wideband applications, from fire-control radars to radio astronomy. However, the significant electrical thickness and poor polarization purity limits their usefulness for certain applications. Overcoming such limitations of Vivaldi arrays has motivated much of the recent focus on alternate low-profile wideband array technologies.

Balanced Antipodal Vivaldi Arrays

The Balanced Antipodal Vivaldi Array (BAVA) represents an improvement to the standard Vivaldi design that mitigates some of the above drawbacks [14]. Rather than using only a simple flared slot, the radiating BAVA element is shaped like a pair of "bunny ears" which provide a smooth transition between a stripline feed and the radiating elements, as seen in Fig. 1.7. The BAVA therefore does not require a separate balun section, which reduces its total height. Moreover, the additional degrees
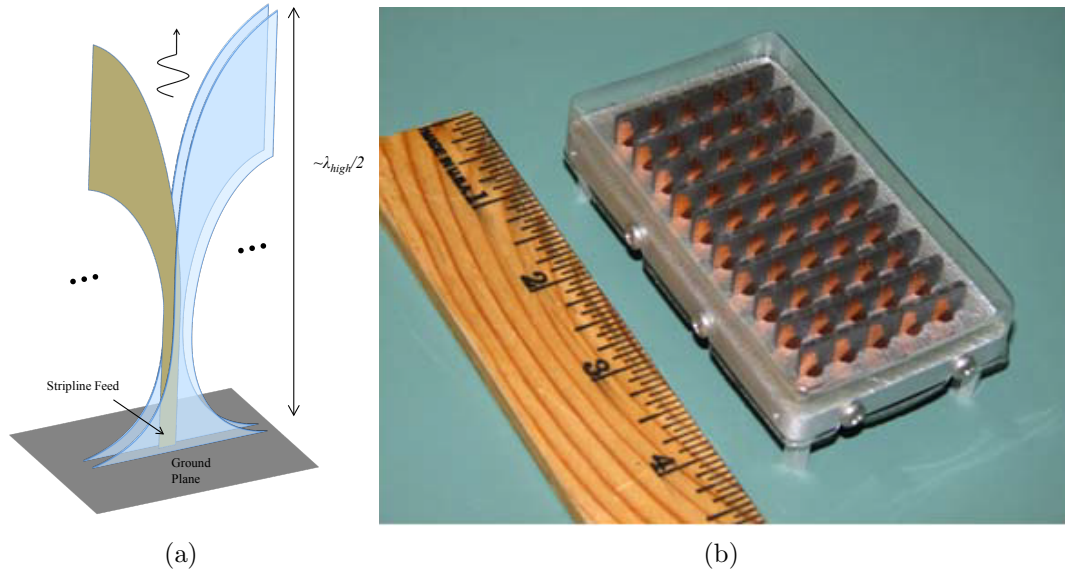
Figure 1.7: Balanced Antipodal Vivaldi Array (BAVA). (a) Sketch of BAVA element. (b) Photo of BAVA Array, from [13], ©2010 IEEE.

of freedom afforded by the shape of the radiating element allow further reduction in thickness, so that that the BAVA is typically only $\sim \lambda/2$ tall at the highest frequency.

However, this reduction in thickness results in a corresponding reduction of impedance bandwidth compared to the standard Vivaldi. A BAVA operating over a 5:1 bandwidth was shown in [15]. More recently, a BAVA with 10:1 bandwidth has been demonstrated, albeit with a fairly high impedance mismatch of VSWR≤4 when scanning to 45° [16].

1.2.2 Tightly Coupled and Connected Arrays

While tapered slot arrays such as the Vivaldi and BAVA primarily make use of the vertical dimension to achieve wideband performance, tightly coupled arrays and connected arrays make use of the horizontal dimension, through mutual coupling. The

idea that mutual coupling in arrays can be beneficial may seem counterintuitive, as it is often perceived as a detrimental effect. However, it is easy to see that a low-profile array without significant mutual coupling can never achieve wideband performance.
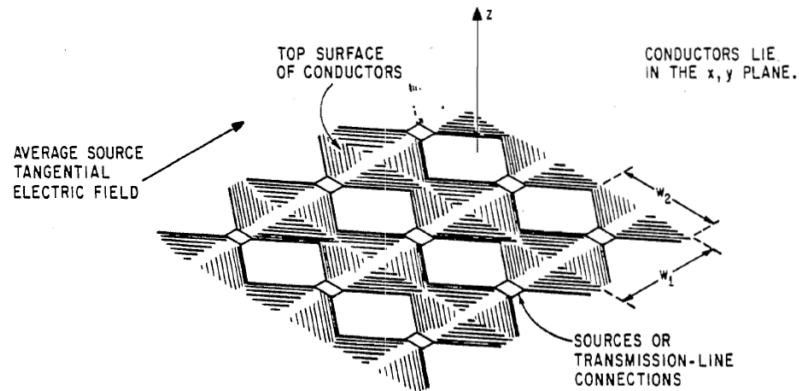
(a) Baum's "Planar Distributed Source"

(b) Munk's "Current Sheet Array"

Figure 1.8: Tightly Coupled and Connected Arrays. (a) Baum's "Planar Distributed Source", formed from connected radiating elements, from [17]. Used with permission. (b) The "Current Sheet Array", formed from dipole elements with interdigitated capacitors between neighboring elements, from [18], ©2008, John Wiley and Sons.

11

The high frequency response of any periodic array is limited by the onset of grating lobes. For scanning arrays, the element spacing cannot be greater than $\sim \lambda/2$ at the top of the band. If mutual coupling is negligible, the low end performance of an array is limited by the small electrical size of the individual elements. With both the high- and low-frequency performance constrained, the bandwidth is fundamentally limited. However, this limitation can be overcome by introducing mutual coupling. If each element interacts significantly with its neighboring elements, its effective electrical size will be increased. In this case, the individual elements no longer operate as isolated antennas, and the bandwidth is not limited by the dimensions of the unit cell. Arrays with strong mutual coupling can support currents at wavelengths that are much larger than the dimensions of a single element. Although the onset of grating lobes still fundamentally limits high-frequency performance, the low end performance can be significantly improved in this manner, allowing tightly coupled arrays to operate over extremely large fractional bandwidths.

The idea of using interconnected array elements to improve the low-end performance was suggested as early as 1970, by Baum [17], see Fig. 1.8a. This idea was more recently re-introduced by Munk [19], who was inspired in part by his extensive work with Frequency Selective Surfaces (FSS) [20], and in part by Wheeler's use of a infinite sheet of continuous current as a convenient way to model phased arrays [21, 22]. Munk recognized that if there were a way to physically implement Wheeler's ideal current sheet, such an array would have excellent bandwidth and scanning performance. His implementation consisted of small dipoles that are capacitively coupled at their tips. He referred to this design as the *Current Sheet Array* [18, 19, 23], pictured in Fig. 1.8b. Others have since referred to such arrays as *Tightly*

Coupled Arrays [24, 25]. When the radiating elements are directly connected rather than capacitively coupled, they are instead referred to as *Connected Arrays* [26, 27].

Circuit Models for Tightly Coupled Arrays above a Ground Plane

(a)

(b)
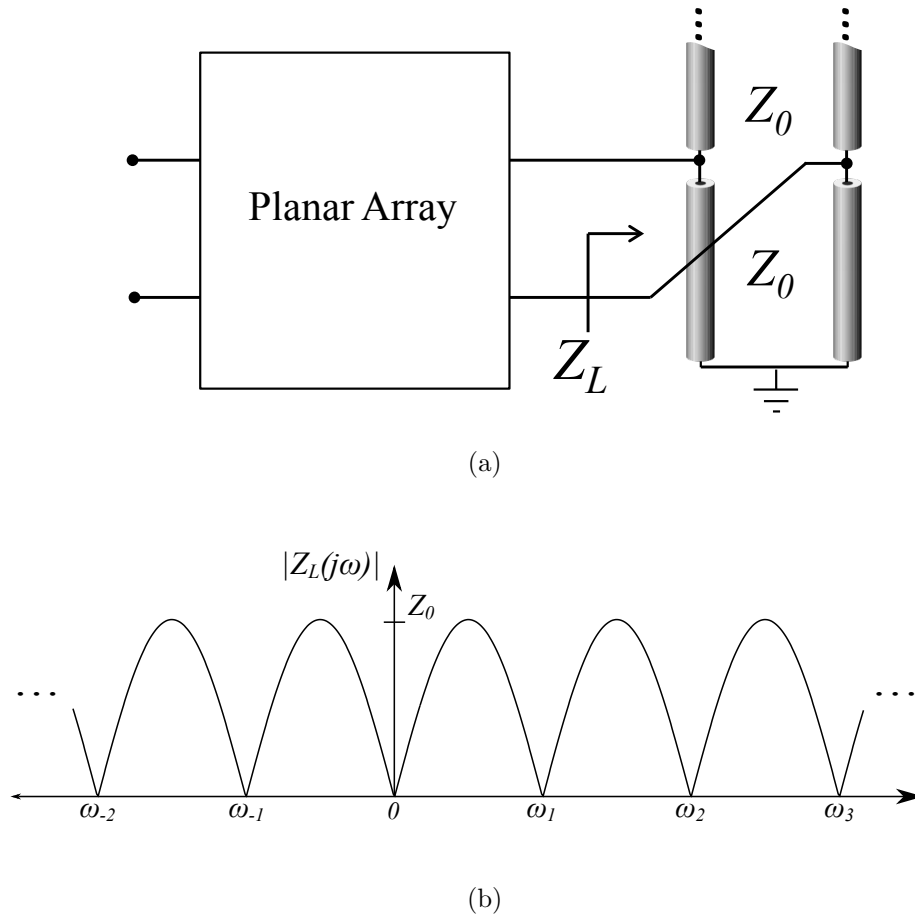
Figure 1.9: The radiation load for any planar array is represented by a pair of transmission lines with the impedance of free space. (a) If the array is placed above a ground plane, the lower transmission line is short circuited at the location of the ground. (b) The magnitude of the impedance Z_L, showing short circuits at the periodic frequencies ω_n.
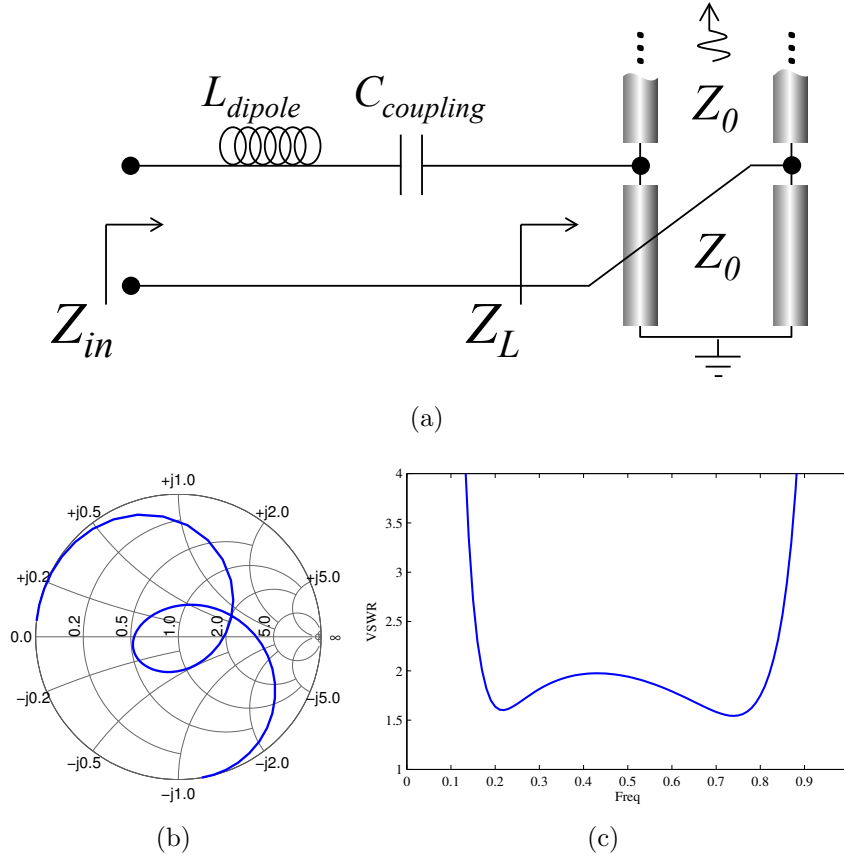
Figure 1.10: (a) Approximate equivalent circuit for a current sheet array implemented with tightly coupled dipoles. (b) Smith Chart showing impedance of Z_{in}. (c) VSWR of optimized array, demonstrating 4.5:1 bandwidth with VSWR$\leq$2.

An infinitely large connected array in free space has no fundamental low-end cutoff, and is theoretically capable of unlimited fractional bandwidth [28]. This is exemplified by the well-known principle that any self-complimentary structure will be frequency-independent [29]. However, in practice, the array must usually be installed above a conducting ground plane. At low frequencies, the ground plane will short-circuit the array and prevent efficient radiation, as depicted in Fig. 1.3. Additionally, since all of the radiating currents are contained in a single plane, the image currents will

also interfere destructively when the height of the array reaches $\lambda/2$, and then again periodically at every half-wavelength interval. For tightly coupled arrays (and all planar arrays without grating lobes), the ground plane can be modeled as a short circuited transmission line in parallel with the radiation resistance, as shown in Fig. 1.9a. The resulting load impedance is plotted in Fig. 1.9b, with the periodic short circuits clearly shown. This can be interpreted as a slightly more specific form of the circuit shown in Fig. 1.4, since a short-circuited transmission line stub can be modeled as an inductance at low frequencies [30].

Compensation for these ground plane effects is the reason why Munk did not directly connect the dipoles in his current sheet array, but inserted a series capacitance between neighboring elements. This capacitance, along with the self-inductance of the dipoles compensates for the shunt reactance of the transmission line stub, as seen in Fig. 1.10. This series $L - C$ circuit may be thought of as a simple impedance matching network for the the load Z_L. In this way, Munk was able to obtain nearly 5:1 bandwidth with a *Tightly Coupled Dipole Array* (TCDA), matched to VSWR≤2 at broadside [19]. In contrast, connected dipole arrays without inter-element capacitive loading are capable of only ∼40% (1.5:1) bandwidth when placed above a ground plane [27].

Alternate Implementations of Tightly Coupled Arrays

In addition to dipoles, other types of radiating elements can also be used to create an effective current sheet. The *Long Slot Array* uses continuous slots [31,34] as shown in Fig. 1.11a. This can be viewed simply as the dual of the connected dipole array. Spirals have also been used as elements of wideband arrays [35]. The *Interwoven Spiral Array* (ISPA), shown in Fig. 1.11b, uses tightly coupled spiral elements to achieve

15
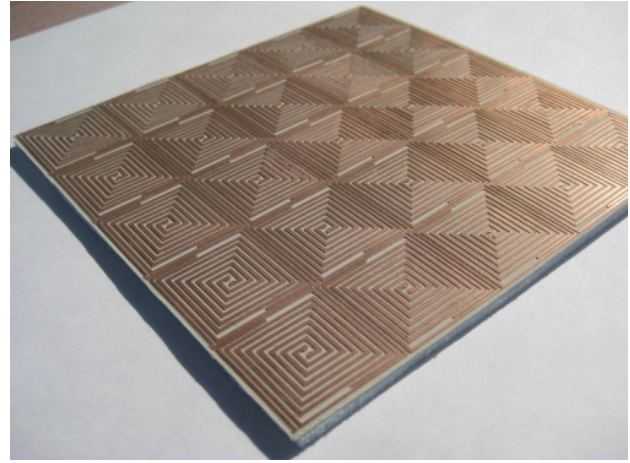
(a) Long Slot Array

(b) Interwoven Spiral Array (ISPA)
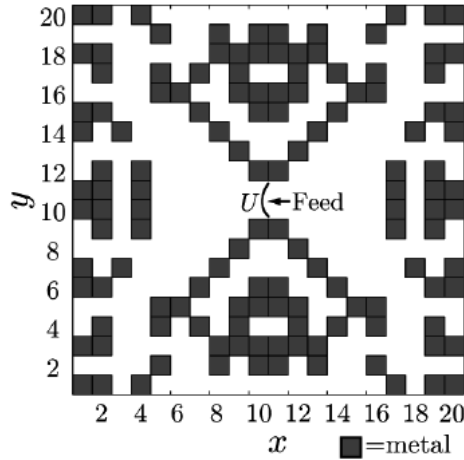
(c) Fragmented Aperture Array

Figure 1.11: The current sheet array concept can be implemented in various forms. (a) Long Slot Array (LSA), achieving 10:1 bandwidth using a ferrite loaded substrate, from [31], ©2008 IEEE. (b) Interwoven Spiral Array (ISPA), achieving 10:1 bandwidth without material loading [32]. Figure courtesy of Ioannis Tzanidis. (c) Fragmented Aperture Array unit cell, showing pixelated surface optimized by genetic algorithm, from [33], ©2005 IEEE.

an incredibly large 10:1 bandwidth with VSWR$\leq$2 without the use of any material loading [32]. However, the ISPA also suffers from high cross-polarization at the edges of the band, and experiences resonances when scanning away from broadside.

The so-called *Fragmented Aperture Array* does not use traditional antenna elements such as dipoles, slots, or spirals, but rather uses a computer algorithm to design the shape of the radiating element [33,36]. The element is defined on a pixelated grid as seen in Fig. 1.11c, and an optimization routine determines which "pixels" should be metalized and which should be left open. Such arrays have been shown to yield 8:1 bandwidth with ≤3dB mismatch loss, when placed above a ground plane [36].

1.2.3 Use of Materials in Wideband Arrays

The use of bulk materials can also significantly affect the behavior and performance of wideband arrays. One option is to load the volume between the radiating currents and ground plane with a dielectric *substrate*, as shown in Fig. 1.12a. One might initially assume that this would improve the performance of the array, since it increases the effective electrical thickness of the array. While this may be effective at a single frequency, it is actually counterproductive when operating the array over a large bandwidth. A dielectric substrate will lower the impedance of the transmission line stub in the circuit of Fig. 1.10, which increases the reactance of the load Z_L and reduces the bandwidth of the array.

Magnetic substrate materials on the other hand, have the opposite effect. They *increase* the impedance of the substrate transmission line, which reduces the net reactance of Z_L. As a result, ferrites and other magnetic materials provide a very effective manner of compensating for ground plane effects and significantly improving bandwidth [31, 37–39]. However, magnetic materials are in practice often heavy and lossy, and thus may not be practical for many applications. The engineering of

17

ε_0

Radiating Currents

$\mu_{sub}, \varepsilon_{sub}$

h_{sub}

Ground Plane

(a) Planar Array with Substrate Material Loading

ε_0

ε_{sup}

h_{sup}

Radiating Currents

ε_0

h_{sub}

Ground Plane
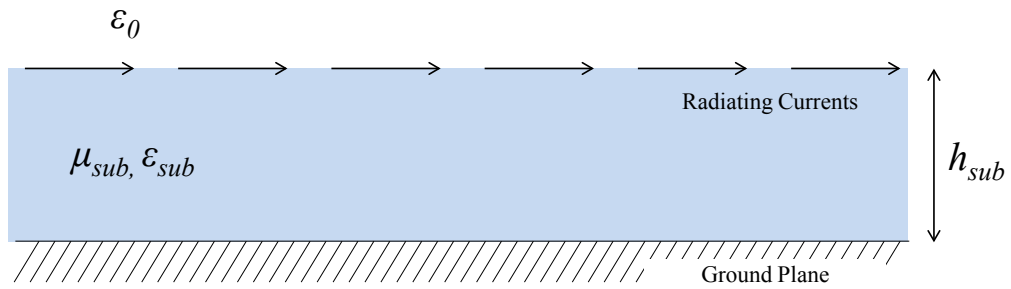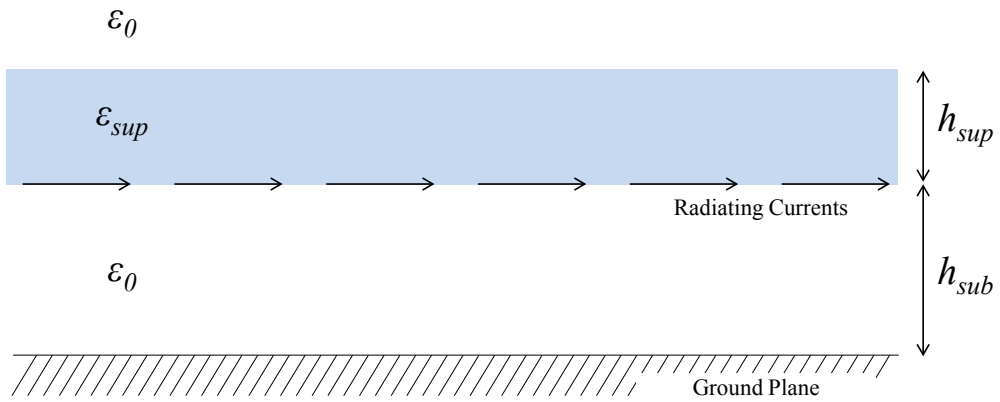
(b) Planar Array with Superstrate Material Loading

Figure 1.12: Material loading in planar arrays. (a) Magnetic substrates generally improve bandwidth, whereas dielectric substrates reduce bandwidth. (b) Dielectric superstrates can improve bandwidth as well as scanning performance.

improved magnetic materials therefore continues to be an area of significant interest [40–44].

In addition to substrate loading, materials may also be placed above the radiating currents. Such materials are then referred to as *superstrates*, see Fig. 1.12b. If a dielectric superstrate is approximately $\lambda/4$ thick, it will act as a quarter-wave imped-ance transformer, analogous to the tapered transmission line shown in Fig. 1.5. The effective radiation resistance is thus lowered, making the input impedance more real and improving the bandwidth [19]. A superstrate can also be seen as asymmetrically loading the top side of the array so that more power is radiated up and away from the ground plane. Furthermore, dielectric superstrates can improve the stability of the impedance over scan, increasing the scan volume of the array [45]. For this reason, dielectric superstrates are occasionally referred to as *Wide Angle Impedance Matching* (WAIM) layers. Superstrates have been used for planar arrays such as tightly coupled dipoles or slots [23], as well as for traveling wave arrays such as Vivaldis [11].

Lossy materials may also be used to improve wideband performance. Without lossy materials, it is impossible to operate a planar array across the $\lambda/2$ short-circuit resonant frequency caused by the ground plane (*c.f.* Fig. 1.9b). However, if the reflections from the ground plane are partially absorbed, this limitation is removed and the total impedance bandwidth can be significantly increased. In this way, arrays with bandwidths above 30:1 have been achieved [46]. The intentional introduction of loss into the array of course results in some reduction of radiation efficiency. How-ever, these losses can be mitigated by combining a dielectric superstrate with a lossy substrate. In this way, the *Superstrate Enhanced Substrate Loaded Array* (SESLA) achieves greater than 70% efficiency over a 21:1 bandwidth [25].

1.3 Performance of Low-Profile Wideband Arrays

All of the above array technologies have their own particular strengths and weak-nesses, and are suitable for various applications. In order to directly compare various array designs, we must be cautious to ensure a fair "apples to apples" comparison. This is because not all arrays are optimized to the same set of performance specifica-tions, such as VSWR and maximum scan angle, and some normalization is needed to account for these differences. We therefore introduce a new array performance metric P_A, defined as,

$$P_A = \frac{B \log 1/|\Gamma_{max}|}{\cos \theta_{max}}, \quad \text{(lossless arrays)}, \tag{1.1}$$

where B is the bandwidth defined as $B = (\omega_{max} - \omega_{min})/\sqrt{\omega_{max}\omega_{min}}$ and θ_{max} is the angle from broadside that defines a conical scan volume for the array. Γ_{max} is then the worst-case reflection coefficient seen at the array feed port (or at the unit cell, for periodic array simulations), over the entire scan-volume defined by θ_{max} and the frequency band $\omega_{low} - \omega_{high}$. We also note that here and elsewhere in this thesis, log refers to the natural logarithm.

This metric is of course only relevant if the array has negligible losses. If the array is lossy, then an equivalent metric is given by,

$$P_A = \frac{B |\log(1 - \eta_{min})|}{2 \cos \theta_{max}}, \quad \text{(lossy arrays)}, \tag{1.2}$$

where η_{min} is the total efficiency of the array, including losses from both absorption and impedance mismatch, and $\eta_{min} \leq 1 - |\Gamma_{max}|^2$.

The metric P_A may seem like a rather arbitrary combination of bandwidth, scan angle, and matching efficiency. However, we will show in Chapter 3 that this quantity arises naturally from the analysis of the fundamental limits of such arrays. The design

of any low-profile wideband array involves engineering trade-offs between bandwidth, efficiency, and scan angle. For example, it is trivial to improve B and/or θ_{max} at the expense of Γ_{max}. However, for an array of a given thickness, if such trade-offs are performed optimally, the quantity P_A will generally be conserved. This therefore provides a convenient single metric that represents the overall performance of wideband, low-profile, scanning phased arrays, and permits a direct comparison between various designs.
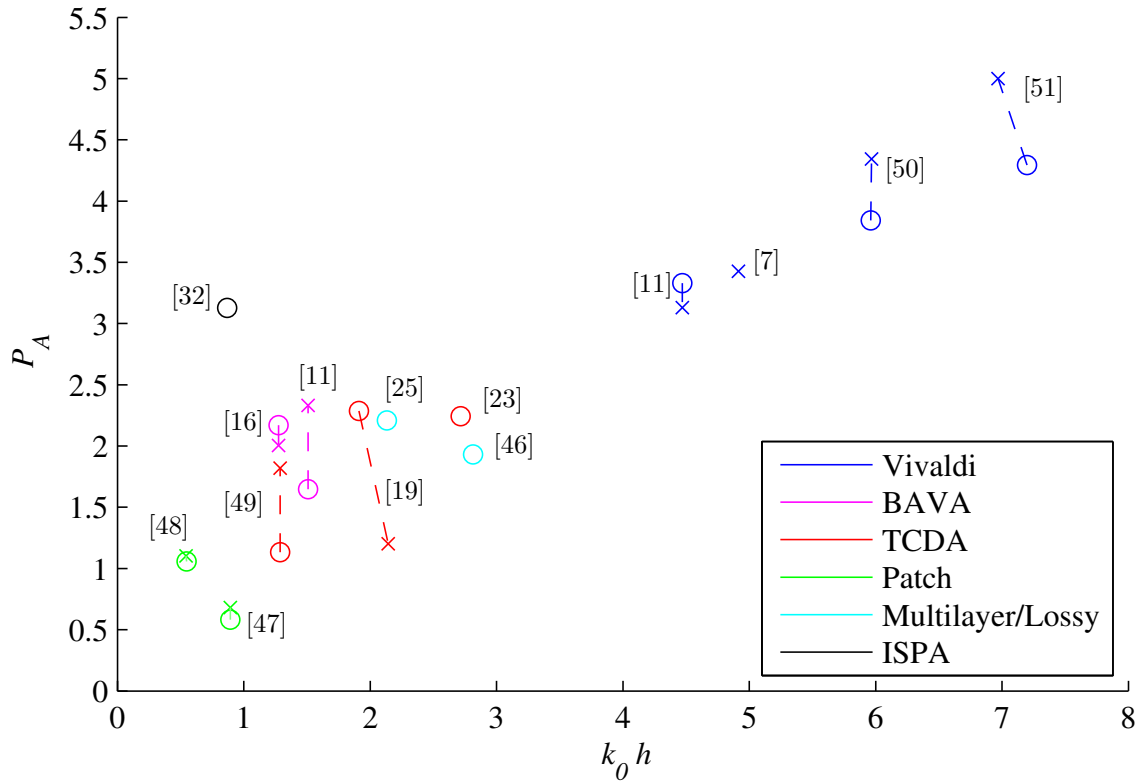
Figure 1.13: Survey of wideband PEC-backed arrays vs. electrical thickness. Broadside performance is denoted by '∘' and scanning performance by '×', with points representing the same design connected by a dotted line. Arrays are color-coded based on the type of radiating element.

In Fig. 1.13, P_A is plotted for a number of wideband arrays versus their electrical thickness $k_0 h$, measured from the top of the ground plane to the top of the array at the center frequency $\omega_0 = \sqrt{\omega_{low}\omega_{high}}$. Here, several observations may be made. As expected, we observe a general correlation between performance and thickness. The thick Vivaldi arrays have the largest P_A, and the thinner patch arrays have the smallest P_A. The cluster of arrays with $k_0 h \approx \pi/2$ corresponds to single layer planar arrays operating near the optimal $\lambda/4$ height. The primary outlier to the performance vs. height trend is the ISPA array [32], which is quite thin but maintains a very high P_A. This behavior is discussed in depth in Chapter 3, and here we remark only that the polarization bandwidth of the ISPA is not as large as its impedance bandwidth.

This survey provides the essential context for our research, and raises two significant questions. The first question is, given this general empirical relationship between array thickness and performance, can we quantitatively establish an absolute performance limit for any low-profile PEC-backed array? Secondly, what engineering choices or design approaches might be taken in order to effectively optimize the performance of practical wideband low-profile arrays, relative to these fundamental limits? Addressing these two questions is the goal of this thesis.

1.4   New Contributions and Organization of this Thesis

This thesis is organized in two parts, corresponding to the above two questions. In the first part, we derive new fundamental performance limits for low-profile PEC-backed arrays, similar to the Wheeler-Chu limits for electrically small antennas. Chapter 2 reviews the basic mathematics of *dispersion relations*, which provide the

theoretical foundation for our study of bandwidth limits for arrays. Chapter 3 develops an impedance matching model for arbitrary PEC-backed arrays and applies a dispersion relation based on Fano's limit [6]. In this way, we obtain a fundamental performance limit for any PEC-backed array constructed from passive, LTI, and reciprocal materials. Although others have developed similar theoretical limits for certain types of arrays, our limit is the first that applies to such a broad class of arrays, regardless of the radiating element design.

Chapter 4 extends these results to provide a specific bandwidth limit for arrays formed by a single planar radiating surface, including those with substrate and/or superstrate material loading. These planar array limits apply to many popular types of wideband arrays such as dipole arrays, slot arrays, fragmented aperture arrays, patch arrays, etc.

The second part of this thesis addresses practical considerations in the design of wideband low-profile arrays, in light of the fundamental limits. In contrast to the field of electrically small antennas, which have essentially reached the theoretical limits of performance [52], our results suggest that there remain significant opportunities for further improvement of wideband arrays before their theoretical limits are reached. The field of wideband low-profile arrays therefore remains an important and fertile area of research for the foreseeable future.

One particular design problem encountered with many types of wideband arrays is the implementation of a wideband feed, which often requires additional external circuitry. In Chapter 5, we propose a method for integrating a compact balun within a wideband dipole array. Through the use of an approximate circuit model, we apply impedance matching theory to optimize the balun and array design. The result is

a simultaneous reduction in size, weight and cost of the array with an increase in bandwidth compared to other feeding techniques. This design, which we refer to as the *Tightly Coupled Dipole Array with Integrated Balun* (TCDA-IB), is detailed in Chapter 6 and yields a bandwidth of 7.35:1 with VSWR ≤ 2.65 while scanning to $\pm 45°$ in all planes. To our knowledge, the TCDA-IB is the first low-profile array with a bandwidth of greater than 7:1 and VSWR $< 3:1$ over the entire scan volume, that does not use ferrite loading, lossy matching, or require external feed circuitry. A prototype array was built and tested, and compares very will with simulation.

Chapter 7 focuses on further improvement of the wide-angle scanning performance of the TCDA-IB, and proposes a technique for using reconfigurable components to increase the maximum scan angle to $60 - 70°$, with minimal reduction in bandwidth and efficiency. Subsequently, Chapter 8 summarizes our overall conclusions and offers several opportunities for further research into these topics.

Part I: Fundamental Limits of Wideband Low-Profile Antenna Arrays

Chapter 2: Causality, Dispersion Relations, and Theoretical Limits of Physical Systems

In this chapter, we will explore from first principles the concept of dispersion relations and their important consequences for physical systems. The theory is based on causality, the basic fact that an event cannot precede its own cause in time. This fact has obvious implications when looking at signals in the time domain, i.e. a signal which arrives at the input to some system at time t_0 cannot influence the output of the system prior to t_0. However there are several other less obvious corollaries that arise when causal signals are analyzed in the frequency domain. Specifically, the real and imaginary parts (or magnitude and phase) of the Fourier Transform of any causal signal cannot be defined independently, but actually contain the same information. This relatively simple idea has a number of important consequences which may be used to derive fundamental constraints on the frequency response of many types of physical systems, such as materials [53, 54], scattering of acoustic [55, 56], electromagnetic [57–59], and quantum-mechanical [57, 60] waves, and electrically small antennas [4, 5, 61, 62].

This chapter does not itself represent new research, but rather is intended to provide an introduction to these fundamental physical limits that arise from the enforcement of causality. Our intent is to illustrate these concepts in a simple and

26

straightforward manner so that in later chapters, the reader may easily follow their application to the specific problem of developing bandwidth limits for antenna arrays. As such, we will attempt to preserve mathematical rigor where possible, but our priority will be to present the fundamental concepts in a clear, intuitive, and accessible manner. For a more complete and rigorous treatment, many excellent resources are available [57, 63–65].

Much of the central concepts are rooted in the mathematical theory of complex analysis. For those with some familiarity with the tools of complex analysis, the mathematics are not overly challenging, but are indeed rather simple and elegant. Complex analysis provides a powerful and beautiful system which often yields greater insight and intuition than is possible when working only in the real domain. However, when working in the complex plane, the underlying physical significance of the mathematics is not always obvious or intuitive. Therefore, we will first begin with a simple demonstration that may be easily understood while remaining in the real domain.

2.1 Response of an "Ideal" Filter

Suppose we wish to design an ideal band-stop filter, as shown in Fig. 2.1, such that a narrow frequency band $\omega_1 < |\omega| < \omega_2$ is completely blocked, while the magnitude and phase of all other frequencies pass through unaltered. Could such a filter be physically constructed?

Let us treat this filter as a black-box system and make no assumptions on its internal construction. How would this system respond to an hypothetical input signal $f_{in}(t)$, such as shown in Fig. 2.2a?. Note that the input signal begins at $t = 0$, such that $f_{in}(t) = 0$ for all $t < 0$. The frequency domain of the signal is shown in Fig.

27

(a) "Ideal" filter

(b) Frequency response of "ideal" filter
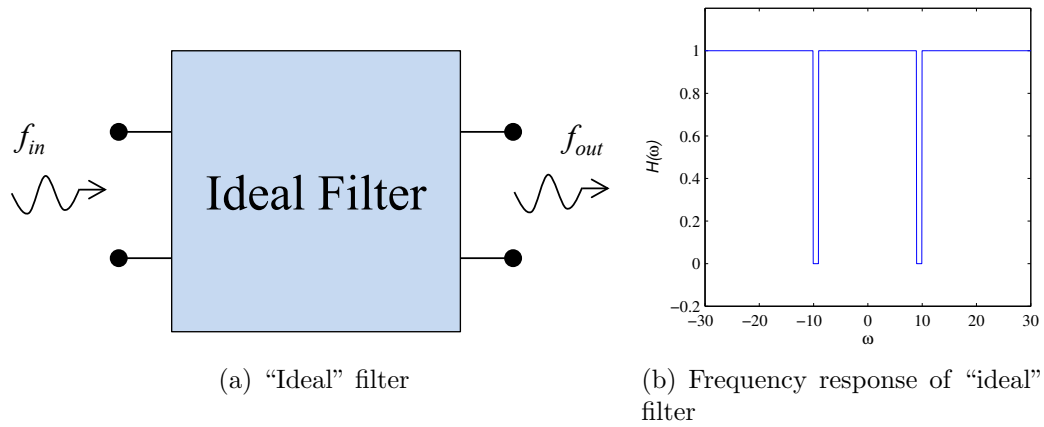
Figure 2.1: Proposed "ideal" filter which perfectly attenuates all frequencies in a narrow band $\omega_1 < |\omega| < \omega_2$, and transparently passes all other frequencies with no attenuation or phase shift. (a) Filter block representation (b) Frequency response.

(a) Example input: Time domain

(b) Example input: Frequency domain
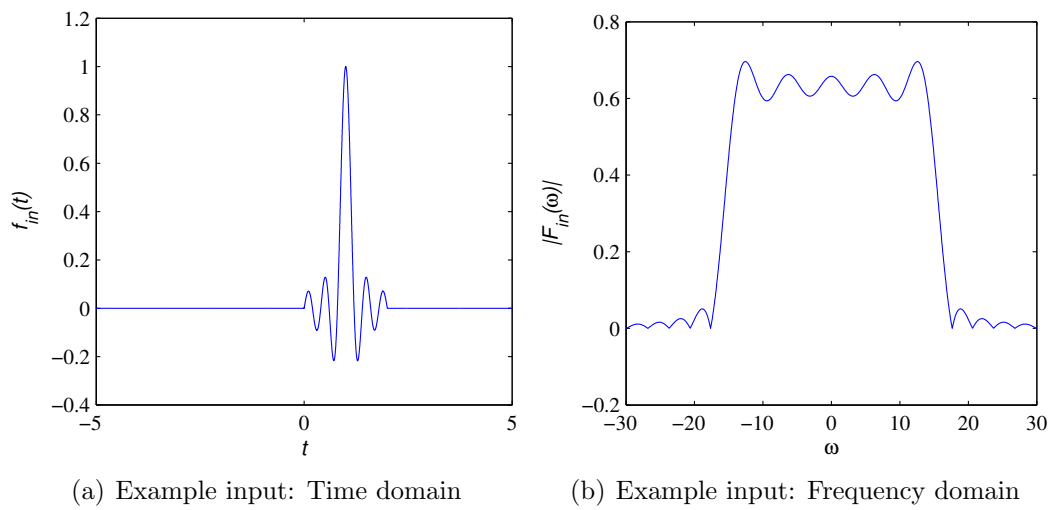
Figure 2.2: Example input signal (a) time domain signal $f_{in}(t)$ (b) magnitude of frequency domain signal $|F_{in}(\omega)|$.

(a) Output of example signal: Time domain

(b) Output of example signal: Frequency domain
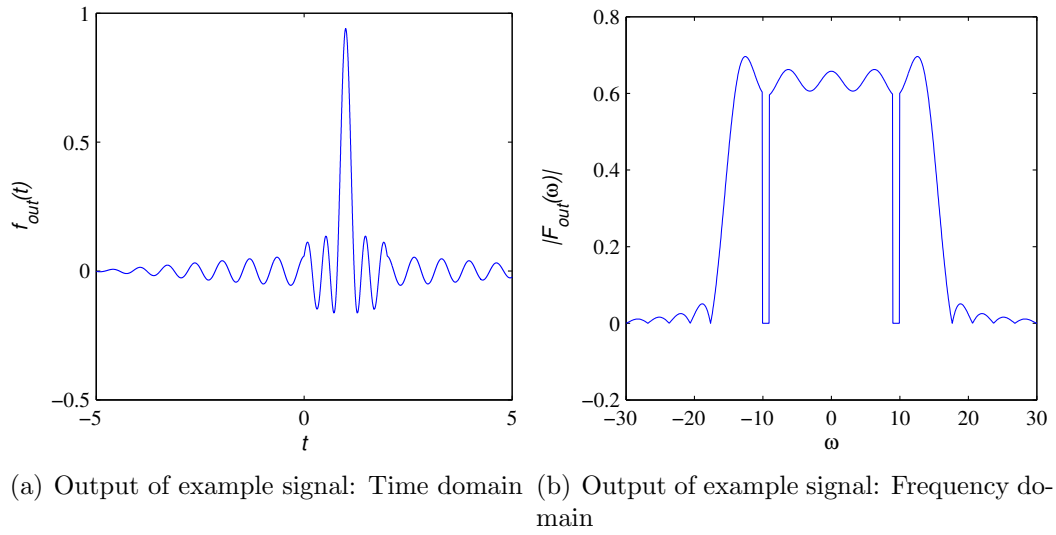
Figure 2.3: Signal after passing through "ideal" filter (a) time domain signal $f_{out}(t)$ (b) magnitude of frequency domain signal $|F_{out}(\omega)|$.
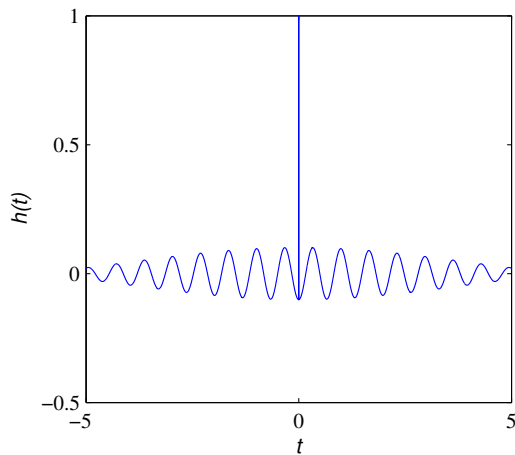
Figure 2.4: Non-causal impulse response of "ideal" filter, $h(t) = \mathcal{F}^{-1}[H(\omega)]$.

2.2b. If this signal is applied to the ideal filter of Fig. 2.1, all frequency components $\omega_1 < |\omega| < \omega_2$ will be completely attenuated, and the remaining frequencies will be unaffected. Thus the output signal in the frequency domain can be easily computed by simply zeroing the frequencies of the input signal within the stop-band, as shown in Fig. 2.3. The time-domain output signal $f_{out}(t)$ is then determined from the inverse Fourier Transform of the frequency domain signal. Note that $f_{out}(t) \neq 0$ for $t < 0$. Therefore, in order to realize the prescribed frequency response, the filter must begin to generate the signal f_{out} prior to the arrival of f_{in}. This not only requires that the filter be non-passive, but more problematically, this violates causality because the filter has no "knowledge" of f_{in} prior to $t = 0$, and therefore could not possibly begin to produce the appropriate filtered output. Such non-causal filters may be approximated if the signal is recorded and post-processed, for example on a computer. However, physically constructing such a filter to operate in real time is clearly not possible.

The condition of causality therefore imposes a significant restriction which prevents the assignment of an arbitrary complex frequency response to any physical system. For linear, time-invariant (LTI) systems, with which we are primarily concerned, a necessary and sufficient condition for causality is that the impulse response of the system must itself be causal (identically equal to zero for all $t < 0$). The impulse response of the proposed ideal filter is shown in Fig. 2.4, and is clearly non-causal. Because the impulse response of a LTI system is completely determined by its frequency-domain transfer function, it is clear that time-domain causality must also

have consequences in the frequency domain, and that the frequency response of any physically realizable system must be carefully constructed so as to preserve causality.[2]

The difficulty with the proposed "ideal" filter is that both the magnitude and the phase response have been determined a priori, without regard to causality. However, if the output phase could be adjusted as needed, the desired magnitude response could perhaps in theory be preserved. This would require each transmitted frequency to be phase shifted by a certain amount, so that the sum over all frequencies perfectly cancels for all $t < 0$. Although it may not be obvious how such a phase response should be constructed, it is clear that this phase function must depend on the attenuation function. Therefore, causality in the time domain imposes a fundamental relationship between the magnitude and phase of the corresponding signal in the frequency domain.

The result is that a causal LTI system with an arbitrary magnitude response will generally be *dispersive*, since variations in magnitude will create varying phase shifts at different frequencies in order to preserve causality. The exact relationship between the magnitude and phase functions (or equivalently the real and imaginary parts) of the complex frequency response are thus referred to as *dispersion relations*. A method for deriving these dispersion relations is presented in the following section.

2.2   Titchmarsh's Theorem and Dispersion Relations

In order to determine the dispersion relations for a given signal, it is most convenient to extend the domain of interest to the full complex plane, via the Laplace

---

[2]This is stating things somewhat backwards – the frequency response of any physical system will of course satisfy causality automatically. However, when developing a theoretical model or considering fundamental limits, causality may need to be intentionally enforced to ensure that the model represents physical reality.
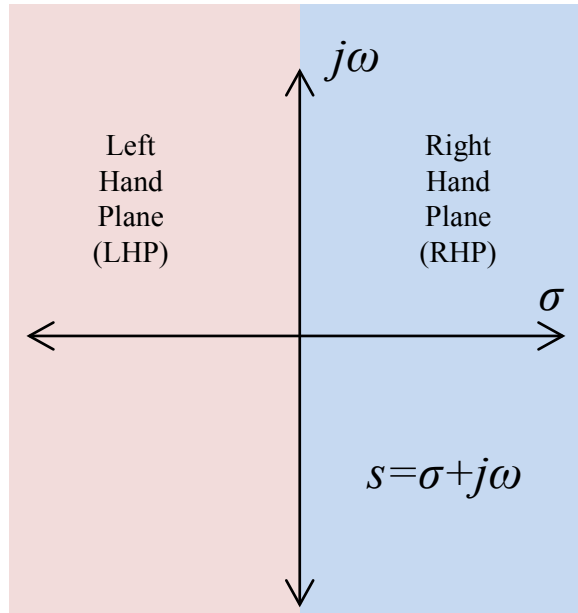
Figure 2.5: Complex s-plane, with $s = \sigma + j\omega$. We denote the *Right Hand Plane* (RHP) as $\sigma > 0$ and the *Left Hand Plane* (LHP) as $\sigma < 0$.

Transform. Our complex frequency variable is defined as $s = \sigma + j\omega$, with the complex s-plane shown in Fig. 2.5. The time-domain function $f(t)$ is mapped to a complex frequency-domain function $F(s)$ by the (bilateral) Laplace Transform, defined as

$$F(s) = \mathcal{L}[f(t)] = \int_{-\infty}^{\infty} e^{-st} f(t) dt. \tag{2.1}$$

Note that the behavior of $F(s)$ on the $j\omega$-axis corresponds to the Fourier Transform of $f(t)$.

Consider the Laplace Transform of a causal signal $f_c(t)$. Because $f_c(t) = 0$ for all $t < 0$, the Laplace integral of a causal signal can be restricted to only positive time,

$$F_c(s) = \int_0^{\infty} e^{-st} f_c(t) dt. \tag{2.2}$$

32

Note that the integral in (2.2) is not guaranteed to converge for all s. However, if $f_c(t)$ is square integrable, then by Parseval's Theorem, the Laplace Transform on the $j\omega$-axis (i.e. the Fourier Transform) must also be square integrable, and thus (2.2) must converge almost everywhere on the $j\omega$-axis. Moreover, if the integral converges for $\sigma = 0$, then it must also converge for all $\sigma > 0$. This is guaranteed by the causality of $f_c(t)$, since the additional factor of $e^{-\sigma t}$ in the integrand will only improve the convergence when both t and σ are positive. Therefore, all square-integrable, causal functions $f_c(t)$ have a Laplace Transform $F_c(s)$ which is guaranteed to be analytic (no poles, branch-cuts, or other singularities) in the open right hand s-plane (RHP).[3]

2.2.1 Contour Integrals in the Complex Plane
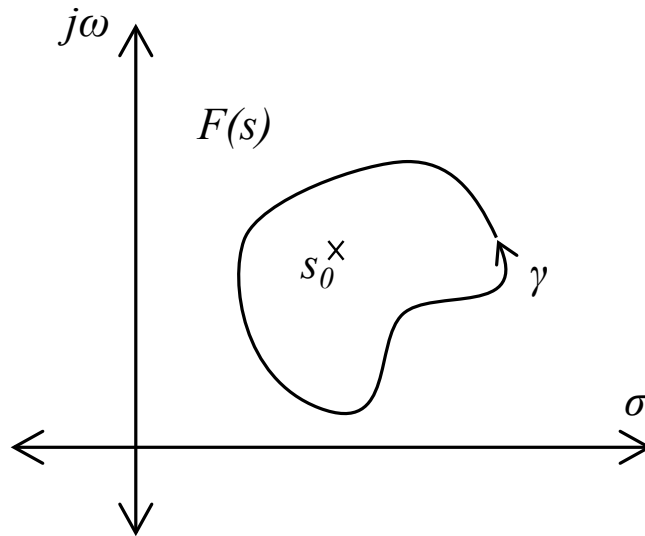
Figure 2.6: Contour for evaluating $F(s_0)$ by Cauchy's integral formula in a region where $F(s)$ is analytic

[3]Although $F_c(s)$ may not be point-wise analytic on the $j\omega$-axis, the Paley-Wiener theorem guarantees that there exists an analytic continuation of $F_c(s)$ into the open right hand s-plane, provided that $f_c(t)$ is both causal and square integrable. A more rigorous proof may be found in [57].

The analytic property of $F_c(s)$ is incredibly significant, as it allows us to take advantage of the rich properties of analytic functions. In particular, Cauchy Integral Formula states that for any function $F(s)$ that is analytic in a given region, the value of the function at an interior point s_0 can be found by an integral over a closed path γ which encloses s_0 within a single counterclockwise loop, as shown in Fig. 2.6.

$$F(s_0) = \frac{1}{2\pi j} \oint_\gamma \frac{F(s)}{s - s_0} ds. \qquad (2.3)$$
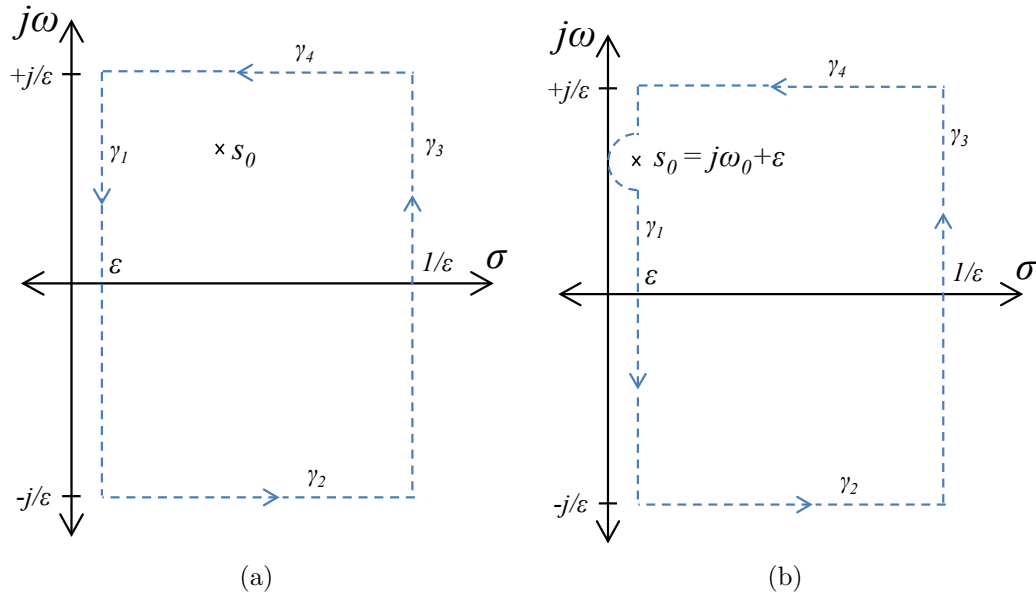
Figure 2.7: Contour for evaluating $F_c(s_0)$ from Cauchy integral formula. (a) s_0 in open RHP plane (b) s_0 on $j\omega$-axis

Consider the path shown in Fig. 2.7a. Because the entire path is in the analytic open RHP, we may apply (2.3) to obtain an expression for the function at any point in the open RHP in terms of an integral over the path.

34

Taking the limit as $\epsilon \to 0^+$, we can see that the integral over the path γ_3 must vanish, since (2.2) becomes exponentially small as $\sigma \to +\infty$. Also, if $F_c(j\omega)$ is square integrable, then it must have finite support and vanish as $\omega \to \pm\infty$. Therefore the integrals over the paths γ_2 and γ_4 also vanish. The only contribution to the integral therefore must come from the path γ_1. Taking the limit $\epsilon \to 0^+$, and using ξ as the variable of integration, $F_c(s_0)$ can be written explicitly as

$$F_c(s_0) = \frac{1}{2\pi} \int_{-\infty}^{+\infty} \frac{F_c(j\xi)}{s_0 - j\xi} d\xi, \quad \mathrm{Re}\, s_0 > 0. \tag{2.4}$$

Equation (2.4) is remarkable, in that it allows us to compute the exact value of $F_c(s_0)$ anywhere in the open RHP, simply from knowledge of its behavior on the $j\omega$-axis. Of course, (2.4) is valid only for s_0 in the open RHP. If s_0 is instead in the open LHP, the integrand will be completely analytic in the open right hand ξ-plane, and the integral over the closed path equals zero. Equivalently, if s_0 remains in the open RHP, but in (2.4) we replace s_0 with $-s_0$, the integral must also vanish,

$$\frac{1}{2\pi} \int_{-\infty}^{+\infty} \frac{F_c(j\xi)}{s_0 + j\xi} d\xi = 0, \quad \mathrm{Re}\, s_0 > 0. \tag{2.5}$$

Adding (2.4) and (2.5), we obtain

$$F_c(s_0) = \frac{s_0}{\pi} \int_{-\infty}^{+\infty} \frac{F_c(j\xi)}{s_0^2 + \xi^2} d\xi, \quad \mathrm{Re}\, s_0 > 0. \tag{2.6}$$

Note that because $1/(s_0^2 + \xi^2)$ is even in ξ, only the even part of $F_c(j\xi)$ will contribute to the result. Because the time-domain signal $f_c(t)$ is real-valued, $\mathrm{Re}\, F_c(j\xi)$ is purely even, and $\mathrm{Im}\, F_c(j\xi)$ is purely odd. We can therefore write (2.6) as

$$F_c(s_0) = \frac{2s_0}{\pi} \int_{0}^{+\infty} \frac{\mathrm{Re}\, F_c(j\xi)}{s_0^2 + \xi^2} d\xi, \quad \mathrm{Re}\, s_0 > 0. \tag{2.7}$$

Therefore, the value of $F_c(s_0)$ can be determined anywhere in the RHP based only on knowledge of the real part of the function on the positive $j\omega$-axis, an even stronger

35

result than (2.4). We will see below that this relationship between the local response (i.e. the value of $F_c(s_0)$ at a single point) and the global response (i.e. the integral of $F_c(j\omega)$ over real positive frequencies) is central in the development of fundamental limits for physical, causal systems.

2.2.2 Contour Integrals on the Boundary of Analyticity

Suppose now that we wish to compute $F_c(s_0)$ at some point not in the open RHP, but at a point on the $j\omega$-axis itself. In this case, we must be cautious since the point of interest is no longer in an open region of analyticity, but is on the boundary. However, we may include a semicircular distortion to the path as shown in Fig. 2.7b, and then evaluate a point just to the right of the $j\omega$-axis. As before, the integral over the paths γ_2, γ_3, and γ_4 vanish, and the integral over γ_1 with the semicircular distortion is written as,

$$
\begin{aligned}
F_c(j\omega_0) = \lim_{\epsilon \to 0^+} & \int_{j(\omega_0+\epsilon)+\epsilon}^{j/\epsilon+\epsilon} \frac{F_c(s)}{2\pi j(s - j\omega_0 - \epsilon)} ds + \\
& \int_{-j/\epsilon+\epsilon}^{j(\omega_0-\epsilon)+\epsilon} \frac{F_c(s)}{2\pi j(s - j\omega_0 - \epsilon)} ds + \\
& \int_{\pi/2}^{3\pi/2} \frac{F_c(j\omega_0 + \epsilon(1 + e^{j\phi}))}{2\pi} d\phi.
\end{aligned}
\tag{2.8}
$$

In the limit as $\epsilon \to 0^+$, the first two integrals can be interpreted as a principal value integral over the entire $j\omega$-axis, minus the singularity at $\omega = \omega_0$, and the third integral over the semicircular contour evaluates to $F_c(j\omega_0)/2$. Thus, after a minor notation change of $\omega_0 \to \omega$ and $\omega \to \xi$, (2.8) simplifies to

$$
F_c(j\omega) = \frac{1}{\pi j} \int_{-\infty}^{\infty} \frac{F_c(j\xi)}{\omega - \xi} d\xi.
\tag{2.9}
$$

Taking the real and imaginary parts of (2.9), we find

$$
\operatorname{Re} F_c(j\omega) = \frac{1}{\pi} \int_{-\infty}^{\infty} \frac{\operatorname{Im} F_c(j\xi)}{\omega - \xi} d\xi,
\tag{2.10}
$$

36

$$\operatorname{Im} F_c(j\omega) = -\frac{1}{\pi} \int_{-\infty}^{\infty} \frac{\operatorname{Re} F_c(j\xi)}{\omega - \xi} d\xi. \tag{2.11}$$

These equations are the dispersion relations mentioned above which define the relationship between the real and imaginary parts of $F_c(j\omega)$ such that $f_c(t)$ represents a causal signal. In fact, (2.10) implies (2.11), and vice versa, and either one is sufficient to satisfy (2.9). The relationship defined by (2.10)-(2.11) is known as the *Hilbert Transform*, and functions such as $\operatorname{Re} F_c(j\omega)$ and $\operatorname{Im} F_c(j\omega)$ which are Hilbert transforms of each other are known as *conjugate harmonic functions*.

2.2.3 Titchmarsh's Theorem

The above results are summarized by *Titchmarsh's Theorem* which states [57],

Theorem. *For any square integrable function $F(j\omega)$, the following statements are equivalent:*

- *The inverse Fourier Transform $f(t)$ of $F(j\omega)$ vanishes for $t < 0$, i.e. $f(t)$ is causal.*

- *$F(j\omega)$ is, for almost all $j\omega$, the limit as $\sigma \to 0^+$ of an analytic function $F(j\omega + \sigma)$ which is analytic in the open RHP, and square integrable over any line in the open RHP parallel to the $j\omega$-axis.*

- $\operatorname{Re} F(j\omega)$ *and* $\operatorname{Im} F(j\omega)$ *are Hilbert Transforms each other.*

In the preceding section, we demonstrated how this theorem is a direct result of the behavior of causal functions in the complex frequency plane. Although this is an incredibly elegant and powerful way to analyze the problem, it may not provide a tremendous amount of intuitive insight as to exactly how these relations arise. We

therefore present an alternate (although somewhat less rigorous) demonstration of Titchmarsh's Theorem from [66]. The dispersion relations are a direct result of the fact that even real functions in the time-domain have purely real frequency-domain responses, and odd real functions in the time-domain have purely imaginary frequency-domain responses. Thus the real and imaginary parts of a frequency-domain signal correspond to the even and odd parts of the real-valued time-domain signal, respectively. Moreover, a causal signal cannot have even and odd time-domain parts that are independent, but these actually contain the same information. This therefore fixes the relationship between the real and imaginary parts of the signal in the frequency domain.

Consider a causal signal $f_c(t)$, decomposed into its even and odd parts, $f_e(t)$ and $f_o(t)$ such as shown in Fig 2.8. The three functions are defined as

$$f_e(t) = f_e(-t) = [f_c(t) + f_c(-t)]/2, \tag{2.12}$$

$$f_o(t) = -f_o(-t) = [f_c(t) - f_c(-t)]/2, \tag{2.13}$$

$$f_c(t) = f_e(t) + f_o(t). \tag{2.14}$$

Because $f_c(t) = f_e(t) + f_o(t) = 0$ for $t < 0$, it is obvious that the even and odd parts must have equal magnitude and opposite sign for $t < 0$. It follows that $f_e(t) = f_o(t)$ for $t > 0$. Therefore, the odd part is equal to the even part times the signum function,

$$f_o(t) = sgn(t)f_e(t), \tag{2.15}$$

where $sgn(t) = +1$ for $t > 0$, $sgn(t) = -1$ for $t < 0$, and $sgn(0) = 0$.

Because the Fourier Transform of an even real function is purely real, and the Fourier Transform of an odd real function is purely imaginary, we can easily decompose the Fourier Transform of $f_c(t)$ into its real part Re $F_c(\omega)$ given by the the Fourier

38

(a) Causal signal $f_c(t)$

(b) Even part of $f_c(t)$
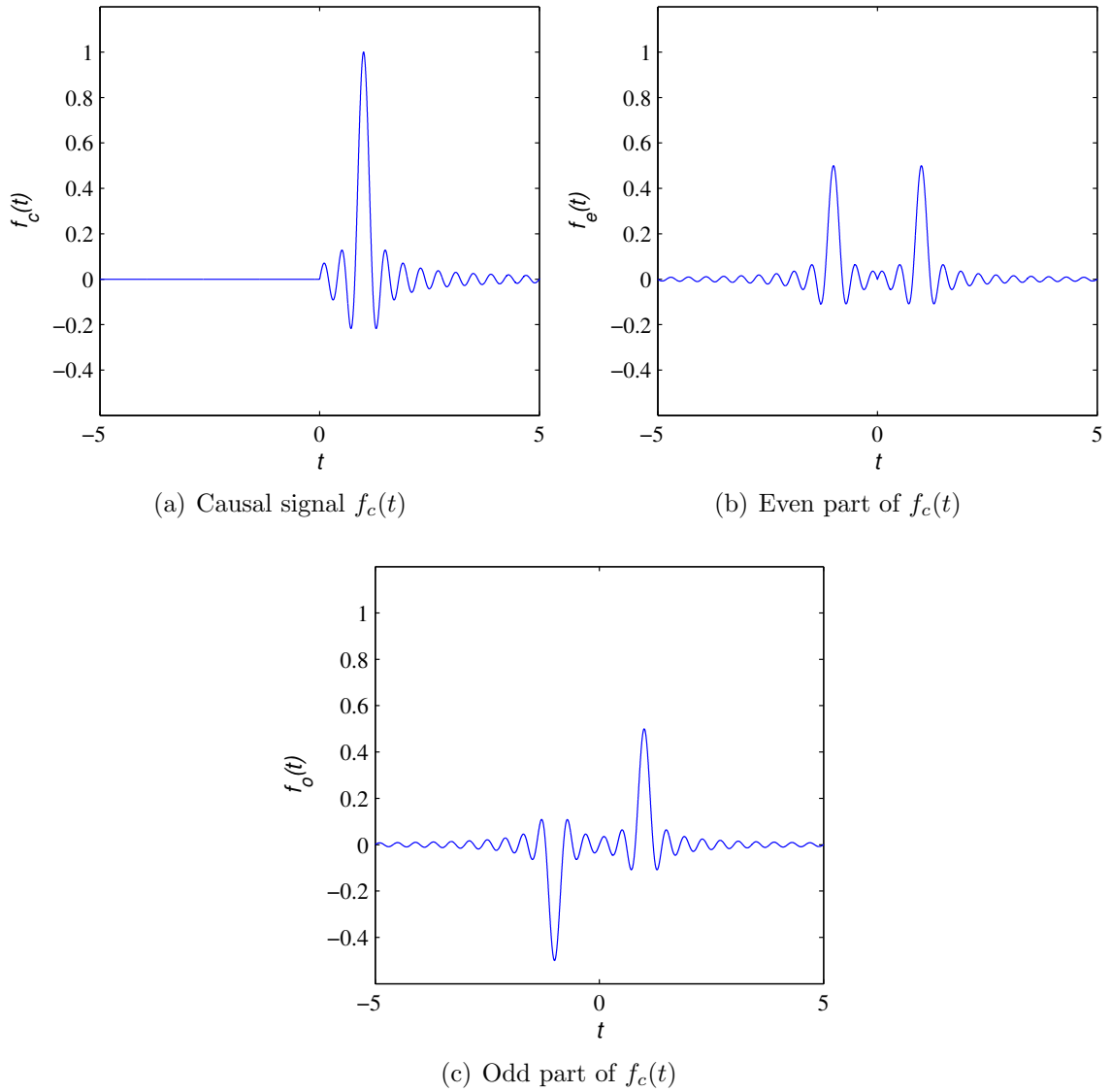
(c) Odd part of $f_c(t)$

Figure 2.8: (a) Example causal signal $f_c(t)$ (b) Even part of signal, $f_e(t) = [f_c(t) + f_c(-t)]/2$ (c) Odd part of signal, $f_o(t) = [f_c(t) - f_c(-t)]/2$. Note that $f_o(t) = sgn(t)f_e(t)$.

Transform of $f_e(t)$, and its imaginary part $\operatorname{Im} F_c(\omega)$, given by the Fourier Transform of $f_o(t)$,

$$\operatorname{Re} F_c(\omega) = \mathcal{F}[f_e(t)](\omega), \tag{2.16}$$

$$j \operatorname{Im} F_c(\omega) = \mathcal{F}[f_o(t)](\omega) = \mathcal{F}[sgn(t)f_e(t)](\omega). \tag{2.17}$$

Since the Fourier Transform of the product of two functions is given by the convolution of the transforms of the individual functions, we can rewrite (2.17) as

$$j \operatorname{Im} F_c(\omega) = \frac{1}{2\pi} \left(\mathcal{F}[sgn(t)](\omega) * \mathcal{F}[f_e(t)](\omega) \right). \tag{2.18}$$

Although $sgn(t)$ technically does not have a proper Fourier Transform, we may make use of its Laplace Transform, $2/s$, which is valid everywhere on the $j\omega$-axis except at the origin. In this way, we can write (2.18) as

$$j \operatorname{Im} F_c(\omega) = \frac{1}{2\pi} \left(\frac{2}{j\omega} * \operatorname{Re} F_c(\omega) \right), \tag{2.19}$$

$$\operatorname{Im} F_c(\omega) = -\frac{1}{\pi} \int_{-\infty}^{\infty} \frac{\operatorname{Re} F_c(\xi)}{\omega - \xi} d\xi, \tag{2.20}$$

which is equivalent to the result found above in (2.11), when the integral is interpreted as a principal value by removing the singular point at the origin.

2.2.4 Magnitude-Phase Relations for Causal Signals

In addition to a relationship between the real and imaginary parts of a signal, dispersion relations can also be formulated between the magnitude and phase of a signal. Consider the natural logarithm of the frequency-domain signal $F(j\omega)$,

$$\log F(j\omega) = \log |F(j\omega)| + j \arg F(j\omega). \tag{2.21}$$

If the signal is causal, $F(j\omega)$ can be analytically continued into the open RHP as $F(s)$. If $F(s)$ also happens to have no zeros in the open RHP, then the function

$\log F(s)$ will also be analytic everywhere in the open RHP. Such functions with no open RHP zeros are called *minimum phase*.

If $F(s)$ is not minimum phase, there exists a unique decomposition into a minimum phase function $F_m(s)$, times an *all-pass function* $\eta(s)$, as shown in Fig. 2.9. An all-pass function has zeros and poles that are located symmetrically across the $j\omega$-axis, and therefore has unity magnitude on the $j\omega$-axis. Therefore, $F(j\omega)$ and $F_m(j\omega)$ have the same magnitude. The minimum phase function $F_m(s)$ is identical to $F(s)$, except that all open RHP zeros are moved symmetrically across the $j\omega$-axis to the LHP. The all pass function $\eta(s)$ contains all of the open RHP zeros of $F(s)$, and for each zero, a matching pole is placed in the LHP symmetrically across the $j\omega$-axis. Because all poles and zeros must occur in conjugate pairs, we may construct $\eta(s)$ as

$$\eta(s) = \pm \prod_k \frac{s - s_k}{s + s_k}, \tag{2.22}$$

where $F(s_k) = 0$ and $\operatorname{Re} s_k = \sigma_k > 0$. The minimum phase decomposition of $F(s)$ is then given by

$$F(s) = \eta(s) F_m(s). \tag{2.23}$$

Because $F_m(s)$ is analytic and has no zeros in the open RHP, $\log F_m(s)$ is likewise analytic in the open RHP. However, several additional conditions are required in order for a given function to represent the frequency-domain magnitude of a causal signal. These conditions are stated precisely by the Paley-Wiener Theorem [64],

Theorem. *A function $a(\omega)$ which is the amplitude of the Fourier Transform of a causal square-integrable time-domain function must meet all of the following criteria:*

- $a(\omega) > 0,$ *(almost everywhere)*
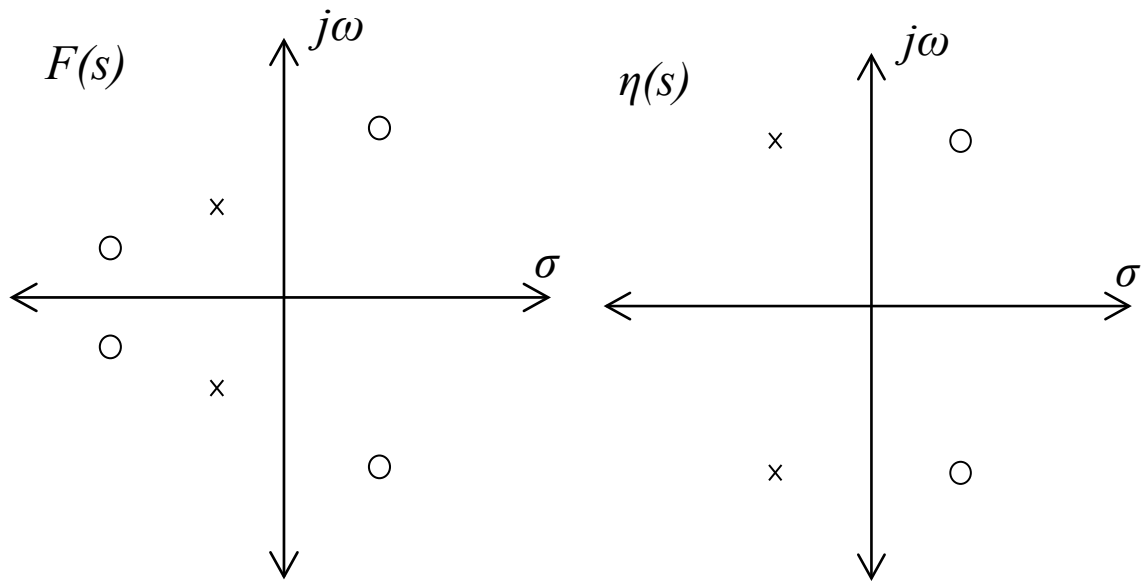
(a) Pole-zero plot of example signal $F(s)$

(b) Pole-zero plot of all-pass $\eta(s)$
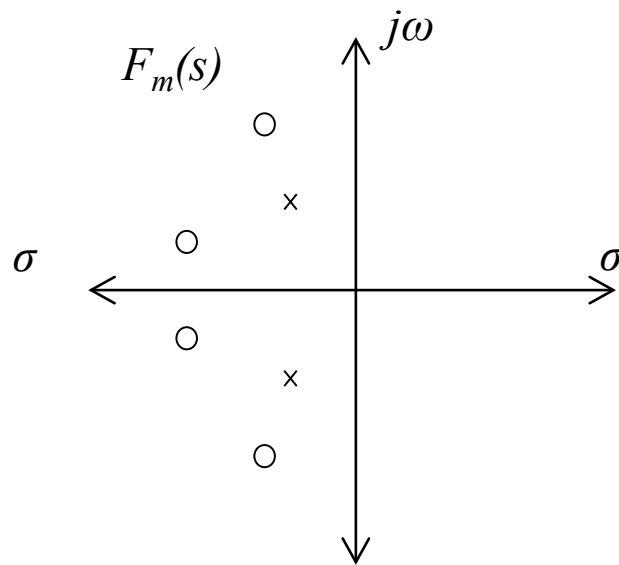
(c) Pole-zero plot of minimum phase function $F_m(s)$

Figure 2.9: (a) Pole-zero plot of an example signal $F(s)$ in the complex s-plane. Zero locations are represented as '○', and poles are represented as '×'. (b) All pass function $\eta(s)$ built from the open RHP zeros of $F(s)$, with $|\eta(j\omega)| = 1$. (c) Minimum phase function $F_m(s)$, such that $F(s) = \eta(s)F_m(s)$ and $|F_m(j\omega)| = |F(j\omega)|$.

- $a(\omega)$ *itself is square-integrable*[4]

- $\displaystyle \int_{-\infty}^{+\infty} \frac{|\log a(\omega)|}{1+\omega^2} d\omega < +\infty$

If the Paley-Wiener conditions are satisfied by the amplitude function $|F_m(j\omega)|$, and if $F_m(s)$ is minimum phase, then we can apply (2.11) to function $\log F_m(s)$, yielding a relationship between its magnitude and phase response,

$$\arg F_m(j\omega) = -\frac{1}{\pi} \int_{-\infty}^{\infty} \frac{\log |F_m(j\xi)|}{\omega - \xi} d\xi. \tag{2.24}$$

Therefore, the phase of a causal signal is uniquely determined by its magnitude, provided it is minimum phase (no open RHP zeros), and the magnitude function satisfies the Paley-Wiener Theorem. For a general function $F(s)$ that is not minimum phase, we may represent the phase function by its minimum phase component plus the phase of its all-pass component as defined by (2.23).

$$\arg F(j\omega) = \arg \eta(j\omega) - \frac{1}{\pi} \int_{-\infty}^{\infty} \frac{\log |F(j\xi)|}{\omega - \xi} d\xi. \tag{2.25}$$

Another useful form of the magnitude-phase relations can be found by applying (2.7) to obtain

$$\log F(s) = \log \eta(s) + \frac{2s}{\pi} \int_{0}^{\infty} \frac{\log |F(j\xi)|}{s^2 + \xi^2} d\xi, \quad \operatorname{Re} s > 0. \tag{2.26}$$

The above results finally allow us to revisit the ideal filter proposed at the beginning of the chapter. Can we determine an appropriate phase response given the

---

[4]Technically, a high-pass transfer function $H(\omega)$ is excluded by the Paley-Wiener Theorem, since its magnitude is not square-integrable. However, if $H(\omega)$ converges to a constant H_∞ as $\omega \to \pm\infty$, that constant may be subtracted and Paley-Wiener applied to the function $H(\omega) - H_\infty$ [67].

(a) Filter's desired amplitude response

(b) Corresponding minimum phase response to ensure causality

(c) Resulting causal impulse response
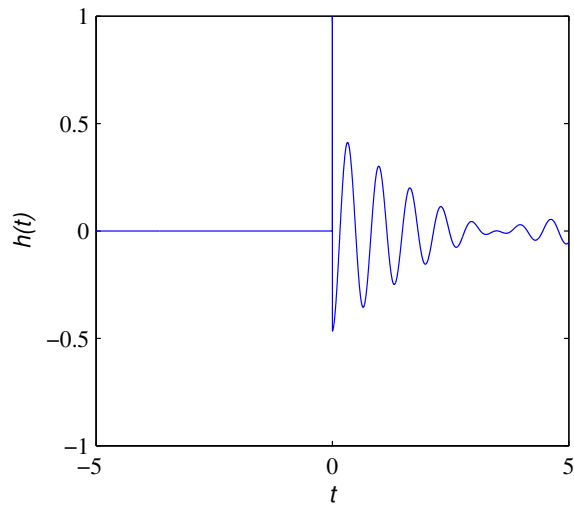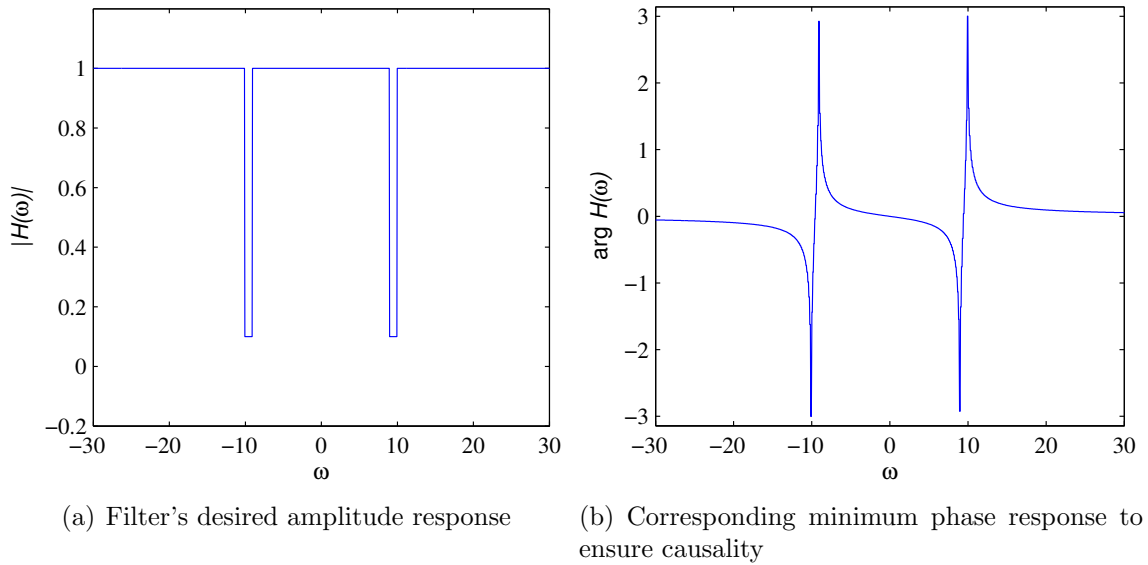
Figure 2.10: (a) Magnitude and (b) corresponding (minimum) phase response of a physically realizable filter. This filter differs from that of Fig. 2.1 in that the stop-band gain is increased from zero to 0.1, and the phase is now computed using (2.24). (c) The impulse response of the filter, which can be seen to now be causal.

desired ideal amplitude response shown in Fig. 2.1? Interestingly, this is still not possible, because the magnitude function does not satisfy Paley-Weiner.[5]

In order to construct a physically realizable band-stop filter, we must avoid setting the magnitude identically equal to zero, other than at a countable number of isolated frequency points. We will therefore set the stop-band gain to 0.1, rather than identically zero, and compute the phase function from (2.24) or (2.26). The resulting magnitude and phase responses, as well as the resulting causal impulse response, are shown in Fig. 2.10.

2.3 Kramers-Kronig Relations

We will now introduce several applications of dispersion relations for characterizing physical systems. The first (and perhaps most well-known) use of dispersion relations was discovered by Kramers [54] and Kronig [53], and pertains to the propagation of light through a material. Consider an electromagnetic plane wave propagating in the $+x$ direction through some homogeneous material with index of refraction $n(\omega)$. In general, the index of refraction is a complex number, written as

$$n(\omega) = n'(\omega) + jn''(\omega), \tag{2.27}$$

where $n'(\omega)$ is a real function which determines the phase velocity of the wave in the material, and $n''(\omega)$ is a real function which determines the absorbtion of the wave by the material. The frequency-domain electric field at position x is given by

$$E(x, \omega) = E(0, \omega)G(x, \omega), \tag{2.28}$$

[5]However, the rectangular magnitude function in Fig. 2.1 could be interpreted as a Butterworth or Chebychev band-stop response in the limit as the order tended to infinity, which then does satisfy Paley-Wiener.[64]

where $G(x,\omega) = e^{-j\omega x n(\omega)/c}$ is the propagator function, c is the speed of light in a vacuum, and $E(0,\omega)$ is the frequency-domain electric field at the origin. The time-domain electric field at position x is then given by

$$E(x,t) = \int_{-\infty}^{\infty} E(0,t')g(x,t-t')dt', \qquad (2.29)$$

where $g(x,t)$ is the inverse Fourier Transform of the propagator. Because the wave cannot travel faster than the speed of light, the field at point x, $E(x,t)$, can only be influenced by the field at the origin, $E(0,t')$, for $t' < t - x/c$. Therefore, the function $g(x,t)$ must be zero for all $t < x/c$. This condition is referred to as *relativistic causality*. The frequency domain propagator $G(x,\omega)$ can thus be written as

$$e^{-j\omega x n(\omega)/c} = \int_{x/c}^{\infty} g(x,t)e^{-j\omega t}dt. \qquad (2.30)$$

Multiplying both sides by $e^{j\omega x/c}$, and applying a shift in integration coordinates, we obtain

$$e^{-j\omega x[n(\omega)-1]/c} = \int_{0}^{\infty} g(x,t'+x/c)e^{-j\omega t'}dt', \qquad (2.31)$$

and $g(x,t'+x/c) = 0$ for all $t' < 0$. Therefore, the function $e^{-j\omega x[n(\omega)-1]/c}$ represents the Fourier Transform of a causal time-domain signal. Provided that the material is not completely lossless, (2.31) will tend to zero as $\omega \to \pm\infty$, and thus will be square integrable. By Titchmarsh's Theorem, $e^{-sx[n(s)-1]/c}$ must therefore be analytic in the open RHP.

We can also prove that $n(s)$ itself must also be analytic in the open RHP. The logarithm of an analytic function is analytic provided the function has no zeros. We can write $e^{-sx[n(s)-1]/c}$ as $e^{sx/c}(e^{-sn(s)})^{x/c}$, and recognize that in the finite s-plane, this equals zero only if $e^{-sn(s)} = 0$. However, this would imply that $(e^{-sn(s)})^{x/c}$ contains a

branch cut for some choice of x/c, which is not permitted. Therefore, $n(s)$ must also be analytic in the open RHP.

Furthermore, it can be shown through physical arguments [57] that $n(\omega) \to 1$ as $\omega \to \pm\infty$. Thus, the quantity $n(\omega) - 1$ is square integrable and the dispersion relations from Titchmarsh Theorem may be applied to find a relationship between $n'(\omega)$ and $n''(\omega)$,

$$n'(\omega) = 1 + \frac{1}{\pi} \int_{-\infty}^{\infty} \frac{n''(\xi)}{\omega - \xi} d\xi, \tag{2.32}$$

$$n''(\omega) = -\frac{1}{\pi} \int_{-\infty}^{\infty} \frac{n'(\xi) - 1}{\omega - \xi} d\xi. \tag{2.33}$$

We may alternatively define $n''(\omega)$ in terms of the material's absorption coefficient (or extinction coefficient) $\beta(\omega)$,

$$n''(\omega) = \frac{c\beta(\omega)}{2\omega}. \tag{2.34}$$

Using the fact $n''(\omega)$ must be odd and $\beta(\omega)$ even, we may write (2.32) as

$$n'(\omega) = 1 + \frac{c}{\pi} \int_{0}^{\infty} \frac{\beta(\xi)}{\xi^2 - \omega^2} d\xi. \tag{2.35}$$

The consequence of (2.32)-(2.35) is that the phase velocity and absorption of a wave in any material are not independent, but depend critically on one another. Importantly, these relations can be shown to apply not only to strictly homogeneous materials, but also to engineered materials, e.g. metamaterials. In fact, certain properties of metamaterials (e.g. negative index of refraction, high impedance surfaces, etc.) can often be shown to be fundamentally narrow-band and/or lossy by use of dispersion relations such as (2.35). The derivation of such physical limits for materials and metamaterials is an ongoing research area of significant interest [68–75].

2.4 Bode-Fano Matching Bandwidth Limits

In addition to characterizing the frequency response of materials based on causality, dispersion relations can also be used to develop physical limits for circuits and networks. In 1945, Bode [76] used dispersion relations to demonstrate a fundamental bandwidth limit for matching networks connected to a capacitive load. This work was further generalized by Fano [6] in 1950 to develop fundamental matching bandwidth limits for loads of arbitrary impedance. Fano also demonstrated how to compute a bandwidth limit when the complexity (order) of the matching network is limited. Fano's work was further extended by Youla [77] and Carlin [78], who simplified Fano's method by using the technique of complex normalization. Because Fano's setup of the problem is simpler and somewhat more accessible, whereas Youla and Carlin's mathematical formulation is easier to use, we will present a synthesis of their methods below.
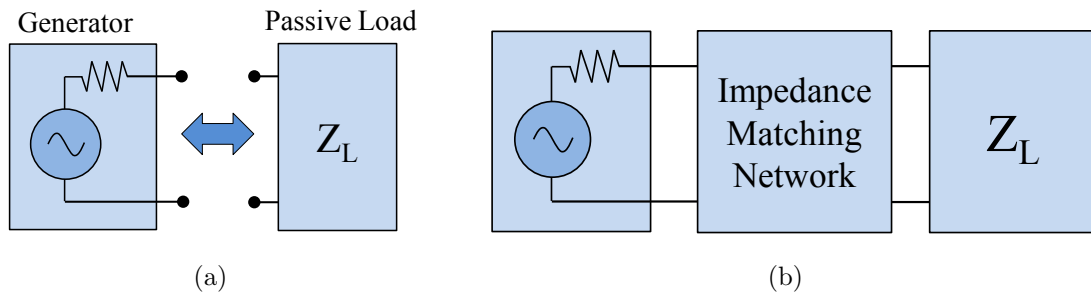
Figure 2.11: (a) Generator and load to be connected with minimal mismatch. (b) Insertion of a reactive matching network designed to minimize the impedance mismatch between the generator and load over a band of interest.

The impedance matching problem is illustrated in Fig. 2.11 and can be stated as follows. Given some frequency-dependent and passive load $Z_L(\omega)$, we wish to connect a generator with real impedance such that the impedance mismatch is minimized over some band of interest. Without loss of generality, we may normalize the system so that the generator has an impedance of 1Ω. If the generator is directly connected to the load, it is unlikely that the resulting impedance mismatch will be acceptable if Z_L differs significantly from unity. Therefore, an additional *impedance matching network* (or *equalizer network*) may be inserted between the generator and load, which can be designed to reduce the mismatch over some frequency band of interest. We assume that the impedance matching network is passive, reciprocal, LTI, and lossless[6].

A remarkable result proved by Darlington [79] is that any physically realizable load impedance can be represented as a lossless two-port reactive network terminated in a unit resistance. This synthesis is based on characterizing the *transmission zeros* of the load, which are the frequencies at which no power can be dissipated in the load. An example is an inductive load such as a parallel $R - L$ network, which has a simple transmission zero at $\omega = 0$. The transmission zeros of an arbitrary load $Z_L(s)$ are located at the poles of $Z_L(s)$ on the $j\omega$-axis, as well as at the closed RHP zeros of the even part of the impedance, $r(s) = (Z_L(s) + Z_L(-s))/2$ [64].

The overall system can thus be thought of as a cascaded two-port network formed by two sub-networks, the matching network and the reactive portion of the load, as shown in Fig. 2.12. Both sub-networks may be described by their scattering properties, normalized to 1Ω. We define the reflection from the right and left hand

---

[6]The assumption of losslessness is not restrictive, since losses in the matching network cannot improve power transfer [64]. Lossy matching can easily be considered by defining the bandwidth in terms of total matching efficiency.
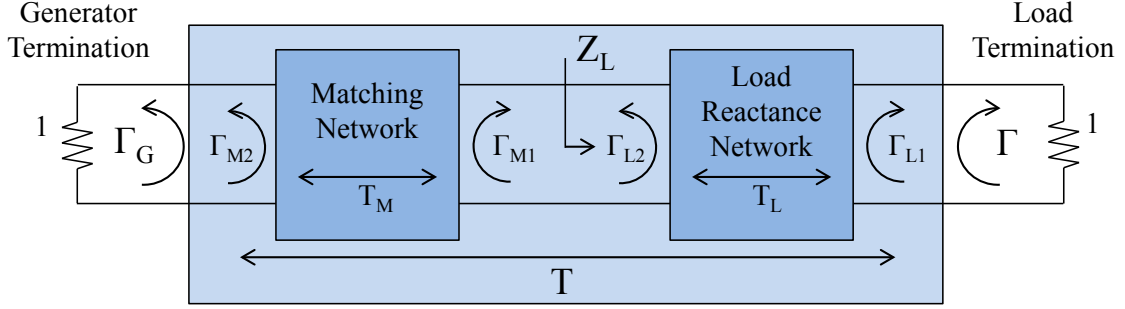
Figure 2.12: Impedance matching problem shown as a cascaded two-port network. The load impedance Z_L is decomposed into a lossless reactive two-port network terminated by a unit resistance.

sides of the impedance matching network as Γ_{M1} and Γ_{M2}, respectively, and the transmission coefficient through the matching network as T_M. Likewise, we define the reflection from the right and left hand sides of the load reactance network as Γ_{L1} and Γ_{L2}, respectively, and its transmission coefficient as T_L. The scattering parameters for the overall cascaded network can then be computed as

$$\Gamma = \Gamma_{L1} + \Gamma_{M1} \frac{T_L^2}{1 - \Gamma_{L2}\Gamma_{M1}} \tag{2.36}$$

$$T = \frac{T_L T_M}{1 - \Gamma_{L2}\Gamma_{M1}} \tag{2.37}$$

where Γ is defined as the reflection looking into the cascaded network from the load side, and T is the transmission coefficient through the cascaded network. Although we may be primarily interested in the magnitude of the reflection seen by the generator, Γ_G, we note that because the total network is lossless and reciprocal, $|\Gamma_G| = |\Gamma|$ on the $j\omega$-axis. From (2.36)-(2.37), it can be seen that for any transmission zero of the load in the open RHP, denoted s_0, we have $\Gamma(s_0) = \Gamma_{L1}(s_0)$. Moreover, if the transmission zero has multiplicity n, the first $n-1$ derivatives of $\Gamma(s_0)$ and $\Gamma_{L1}(s_0)$

must also be equal[7]. Therefore, the transmission zeros of the load represent critical points at which the behavior of the overall network is completely determined by the load alone and is independent of the matching network design.

This fact allows us to make use of dispersion relations, which relate information about the overall frequency response of a function to its behavior at a single frequency point. Because we wish to determine constraints on the magnitude of the reflection coefficient $\Gamma(s)$, we will apply the magnitude-phase dispersion relations. Therefore, we will work with the functions $\log 1/\Gamma(s)$ and $\log 1/\Gamma_{L1}(s)$, with the inverse of the reflection coefficient being used so that the logarithm will be positive. Expanding these functions as Taylor series around a point s_0 we obtain,

$$\log 1/\Gamma(s) = B_0^{s_0} + B_1^{s_0}(s - s_0) + B_2^{s_0}(s - s_0)^2 + ..., \quad s \to s_0 \tag{2.38}$$

$$\log 1/\Gamma_{L1}(s) = A_0^{s_0} + A_1^{s_0}(s - s_0) + A_2^{s_0}(s - s_0)^2 + ..., \quad s \to s_0 \tag{2.39}$$

It can be shown [64] that if the load has a transmission zero of multiplicity n at frequency s_0 in the closed RHP (counting double zeros on the $j\omega$-axis only once), the following relations apply:

If Re $s_0 > 0$,

$$B_i^{s_0} = A_i^{s_0}, \quad i = 0, 1, 2, ..., n - 1. \tag{2.40}$$

If Re $s_0 = 0$ and $Z_L(s_0) \neq \infty$,

$$B_i^{s_0} = A_i^{s_0}, \quad i = 0, 1, 2, ..., 2n - 2, \tag{2.41}$$

$$\frac{B_{2n-1}^{s_0} - A_{2n-1}^{s_0}}{r_{2n}^{s_0}} \geq 0. \tag{2.42}$$

---

[7]If the transmission zero lies on the $j\omega$-axis, it will necessarily be a double-zero and the first $2n - 1$ derivatives will be equal. Furthermore, since the denominator $1 - \Gamma_{L2}\Gamma_{M1}$ may also contain a zero on the $j\omega$-axis, the $(2n - 1)^{th}$ derivative may be an inequality rather than an equality.

If $\operatorname{Re} s_0 = 0$ and $Z_L(s_0) = \infty$,

$$B_i^{s_0} = A_i^{s_0}, \quad i = 0, 1, 2, ..., 2n - 2, \tag{2.43}$$

$$\frac{B_{2n-1}^{s_0} - A_{2n-1}^{s_0}}{r_{2n-2}^{s_0}} \leq \frac{1}{c_{-1}}, \tag{2.44}$$

where $r_i^{s_0}$ is the ith coefficient of the power series of $r(s) = (Z_L(s) + Z_L(-s))/2$ taken around the point s_0, and c_{-1} is the residue of $Z_L(s)$ at s_0.

At this point, we introduce the dispersion relations. If Z_L is a passive load ($\operatorname{Re} Z_L(s) \geq 0$ in the open RHP), then $\Gamma(\omega)$ will satisfy the Paley-Wiener criteria and we may apply (2.26) to obtain

$$\log 1/\Gamma(s) = \log 1/\eta(s) + \int_0^\infty \Psi(s, \xi) \log 1/|\Gamma(j\xi)| d\xi, \quad \operatorname{Re} s > 0. \tag{2.45}$$

where $\Psi(s, \xi)$ is defined as

$$\Psi(s, \xi) = \frac{2s}{\pi(s^2 + \xi^2)} \tag{2.46}$$

We may also represent the $\Psi(s, \xi)$ and $\log 1/\eta(s)$ functions as a Taylor series around s_0,

$$\log 1/\eta(s) = \eta_0^{s_0} + \eta_1^{s_0}(s - s_0) + \eta_2^{s_0}(s - s_0)^2 + ..., \quad s \to s_0 \tag{2.47}$$

$$\Psi(s, \xi) = \Psi_0^{s_0}(\xi) + \Psi_1^{s_0}(\xi)(s - s_0) + \Psi_2^{s_0}(\xi)(s - s_0)^2 + ..., \quad s \to s_0 \tag{2.48}$$

Thus, by matching like coefficients of s, we can represent (2.45) as a set of integral equations

$$B_i^{s_0} = \eta_i^{s_0} + \int_0^\infty \Psi_i^{s_0}(\xi) \log 1/|\Gamma(j\xi)| d\xi, \quad i = 0, 1, 2, ... \tag{2.49}$$

The relations (2.40)-(2.44) allow us to determine $B_i^{s_0}$ from $A_i^{s_0}$, which can be directly calculated from the Darlington equivalent of the load impedance via (2.39). The set of equations (2.49) then establishes the fundamental constraints that must be satisfied by any physically realizable matching network.

52

If the load to be matched has a large number of transmission zeros, the constraints (2.40)-(2.44) and (2.49) involve multiple simultaneous integral equations that may become rather unwieldy and difficult to express as a simple bandwidth limit. However, for simpler load impedances, the constraints are fairly easy to apply, as we shall demonstrate next.

2.4.1 Bandwidth Limit for a Simple Load
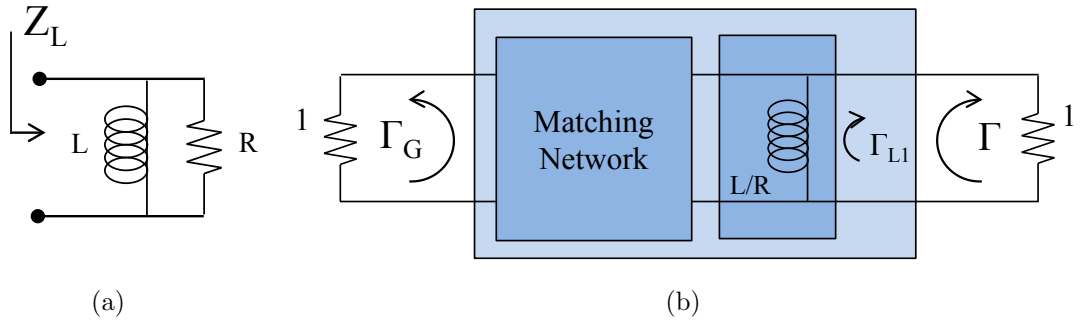
Figure 2.13: (a) Load to be matched consisting of parallel $R - L$ network (b) Renormalized load in Darlington form, with matching network.

Consider a simple load shown in Fig. 2.13a consisting of a simple resistor R in parallel with an inductor L. We wish to determine the fundamental bandwidth limit when the load is matched with a lossless reciprocal network as shown in Fig. 2.13b. Here, the load is renormalized and represented by its Darlington equivalent form, as in Fig. 2.12. Note that the load only has a single transmission zero at $s_0 = 0$. We can therefore compute the series expansion of $\Psi(\xi, s)$ and $\log 1/\eta(s)$ as

$$\Psi(s, \xi) = \frac{2}{\pi \xi^2} s + ..., \quad s \to 0 \tag{2.50}$$

$$\log 1/\eta(s) = \eta_0^0 + \sum_k \frac{2}{\sigma_k} s + ..., \quad s \to 0 \tag{2.51}$$

where η_0^0 equals either 0 or $j\pi$, depending on the sign of $\eta(0)$, and σ_k is the real part of the kth zero of $\eta(s)$. Since $\Psi_0^0 = 0$, the $i = 0$ equation in (2.49) simply reduces to $\eta_0^0 = B_0^0$. For $i = 1$, we obtain

$$B_1^0 = \sum_k \frac{2}{\sigma_k} + \frac{2}{\pi} \int_0^\infty \frac{\log 1/|\Gamma(j\xi)|}{\xi^2} d\xi. \tag{2.52}$$

The term B_1^0 is related to A_1^0 by (2.42). A_1^0 is computed from the load reflection coefficient $\Gamma_{L1}(s)$,

$$\Gamma_{L1}(s) = \frac{Ls - R}{Ls + R}. \tag{2.53}$$

The series expansion of $\log 1/\Gamma_{L1}(s)$ is then

$$\log 1/\Gamma_{L1}(s) = -j\pi + \frac{2L}{R} s + ..., \quad s \to 0. \tag{2.54}$$

We find $r_2^0 = -(L/R)^2$, and thus (2.42) yields

$$B_1^0 \le \frac{2L}{R}. \tag{2.55}$$

Plugging this into (2.52), we obtain

$$\frac{2L}{R} \ge \sum_k \frac{2}{\sigma_k} + \frac{2}{\pi} \int_0^\infty \frac{\log 1/|\Gamma(j\xi)|}{\xi^2} d\xi. \tag{2.56}$$

Since all zeros of $\eta(s)$ lie in the RHP, each σ_k must be positive and their inclusion will reduce the bandwidth. In general, the maximum bandwidth is usually given by the minimum phase solution (i.e. $\eta(s) = \pm 1$), however the inclusion of an all-pass is occasionally necessary in order to satisfy (2.40)-(2.44) when the load contains multiple transmission zeros.

The magnitude of the reflection coefficient $\Gamma_G(j\omega)$ seen by the generator when matching to a parallel $R - L$ load is therefore fundamentally limited by

$$\int_0^\infty \frac{\log 1/|\Gamma_G(j\omega)|}{\omega^2} d\omega \leq \frac{\pi L}{R}, \tag{2.57}$$

since $|\Gamma_G(j\omega)| = |\Gamma(j\omega)|$.

The inequality (2.57) provides a general expression for the maximum impedance bandwidth that may be provided by any passive, linear matching network, configured as in Fig. 2.13. However, even simpler expressions may be developed for certain canonical frequency responses.
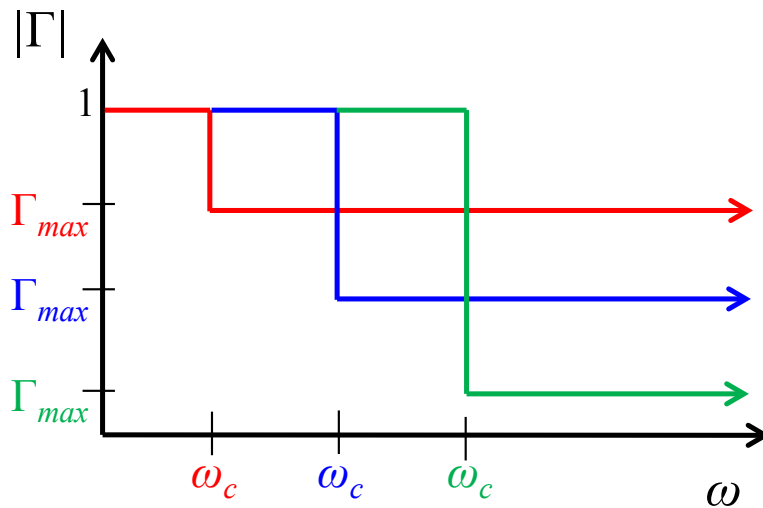
Figure 2.14: Ideal high-pass response to $R - L$ load. As the cutoff frequency is reduced, the matching tolerance must be relaxed.

Suppose we wish to implement a high-pass match to the $R - L$ load, as shown in Fig. 2.14. What is the lowest cutoff frequency ω_c that could be obtained for a given mismatch tolerance of Γ_{max}. Examining (2.57), we see that the optimal configuration

producing the smallest ω_c is a rectangular response, with $|\Gamma(j\omega)| = \Gamma_{max}$ for $\omega > \omega_c$, and $|\Gamma(j\omega)| = 1$ for $\omega < \omega_c$. The limit can then be written as

$$\int_{\omega_c}^{\infty} \frac{\log 1/\Gamma_{max}}{\omega^2} d\omega \leq \frac{\pi L}{R}, \qquad (2.58)$$

which yields a lower bound for the cutoff frequency of

$$\omega_c \geq \frac{R}{\pi L} \log \frac{1}{\Gamma_{max}}. \qquad (2.59)$$

The limit obtained from the ideal rectangular response is referred to as the *Bode limit*, since Bode [76] was the first to derive impedance bandwidth limits using this method. For a low-pass match to a parallel $R - C$ network, a similar limit can be obtained,

$$\omega_c \leq \frac{1}{\pi RC} \log \frac{1}{\Gamma_{max}}. \qquad (2.60)$$

2.4.2   The Q-Bandwidth Limit

The above limits for $R - L$ and $R - C$ loads may be further generalized using standard low-pass to band-pass (or high-pass to band-pass) transformations, yielding a bandwidth limit for any first-order circuit,

$$QB_{\infty} \leq \frac{\pi}{\log 1/\Gamma_{max}}, \qquad (2.61)$$

where $B_{\infty} = (\omega_{high} - \omega_{low})/\omega_0$ and $\omega_0 = \sqrt{\omega_{high}\omega_{low}}$. Q is a measure of the ratio between real and reactive power in the load, and is defined for parallel resonant circuits as

$$Q_{parr} = \omega_0 RC = \frac{R}{\omega_0 L}, \qquad (2.62)$$

and for series resonant circuits as

$$Q_{series} = \frac{\omega_0 L}{R} = \frac{1}{\omega_0 RC}. \qquad (2.63)$$

56

The limit expressed in (2.61) is of course the famous Q-Bandwidth limit, and is an incredibly convenient form for expressing the fundamental bandwidth limit for any simple resonant load. However, because it is derived for circuits with only a single transmission zero on the $j\omega$-axis, it is not applicable to wideband matching of more complex, multi-resonant loads. For multi-resonant loads with multiple transmission zeros, the bandwidth limit must be evaluated from (2.40)-(2.44) and (2.49).

2.4.3   Finite-Order Matching Limits

In addition to deriving the limits for loads of arbitrary impedances, Fano [6] extended Bode's result to account for the physical matching networks of finite order. By "order" we refer to the order of the rational polynomial representation of the frequency response, or equivalently the number of ladder sections required to implement the matching network. The ideal rectangular response of the Bode limit would require a matching network of infinite order, and therefore cannot be realized in practice.

Rather than using an ideal rectangular function, a more realistic response is given by the Chebyshev polynomials. For a given order, these polynomials provide the optimal approximation to the rectangular function[8]. Therefore, for an optimal finite-order response, the $B_i^{s_0}$ terms in (2.40)-(2.44) are determined by the series expansion of the Chebyshev response, rather than by (2.49). The solution of this problem, even for a single transmission zero, involves solving several transcendental equations [6]. However, an approximation is given in [80], which is valid to within a few percent,

$$QB_n \leq \left(b_n \sinh\left(\frac{1}{a_n} \log \frac{1}{\Gamma_{max}} \right) + \frac{1-b_n}{a_n} \log \frac{1}{\Gamma_{max}} \right)^{-1}, \qquad (2.64)$$

---

[8]Actually, the elliptic functions are optimal, but are more difficult to work with and the difference is usually negligible [6].

where n is the total order of the matching network and load. The coefficients a_n and b_n are given in Table 2.1, along with QB_n computed for VSWR=2:1 ($\Gamma_{max} = 1/3$). For a simple matching network (small n), the bandwidth will be reduced, since the in-band ripple must be larger and the slope at the edges of the band is reduced, see Fig. 2.15. However, as the order n is increased, the Chebyshev response begins to look more like the ideal rectangular response, and the bandwidth approaches the Bode limit (2.61).
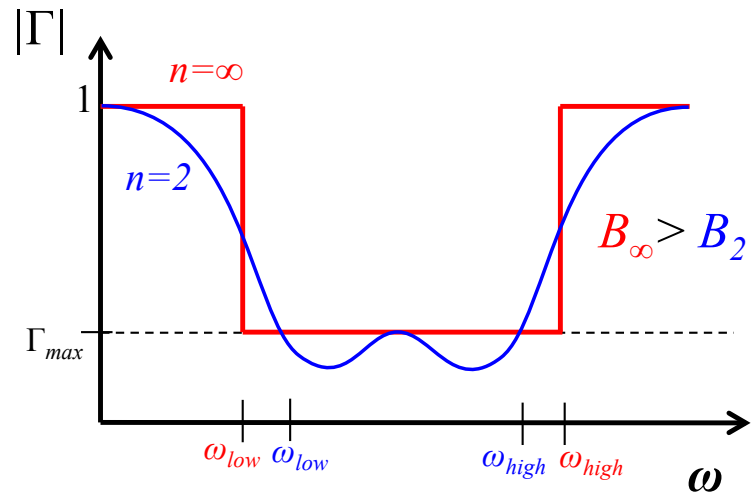
Figure 2.15: Infinite-order vs. finite order band-pass frequency response. For the same load impedance, bandwidth increases with higher-order matching.

Table 2.1: Coefficients of (2.64) for finite-order matching, from [80], and QB_n for VSWR=2:1

n	a_n	b_n	QB_n (VSWR=2:1)
1	1	1	0.750
2	2	1	1.733
3	2.413	0.678	2.146
4	2.628	0.474	2.358
5	2.755	0.347	2.481
6	2.838	0.264	2.564
7	2.896	0.209	2.625
8	2.937	0.160	2.660
∞	π	0	2.857

2.5 Complex Normalization and Youla's Method

One limitation of Fano's method is that the load must be expressed in Darlington form, which is often inconvenient for complex loads. Youla [77] extended Fano's method through the use of complex normalization. In order to properly define scattering parameters for a network, a reference impedance must be defined. This reference impedance is often chosen to be 50 Ω, but may of course be any impedance. However, the well known equation for the reflection Γ from a load Z_L,

$$\Gamma = \frac{Z_L - Z_0}{Z_L + Z_0}, \tag{2.65}$$

is valid only when the reference impedance Z_0 is real. Nevertheless, the definition of scattering parameters may be extended to complex reference impedances by the theory of *complex normalization* [81].

As is well known, the reflection is zero when the load and reference impedances are complex conjugates, i.e. when $Z_L(j\omega) = \overline{Z_0(j\omega)}$. The concept of conjugation may be extended to the entire complex plane by taking the *paraconjugate* of $Z_0(s)$, defined as $Z_0(-s)$, and typically denoted Z_{0*}. We may naturally wish to extend (2.65) to complex reference impedances as

$$\Gamma \stackrel{?}{=} \frac{Z_L - Z_{0*}}{Z_L + Z_0}. \tag{2.66}$$

However, we note that because the poles of Z_0 are in the LHP, Γ will have poles in the RHP, which violates causality. We must therefore modify our definition to account for this.
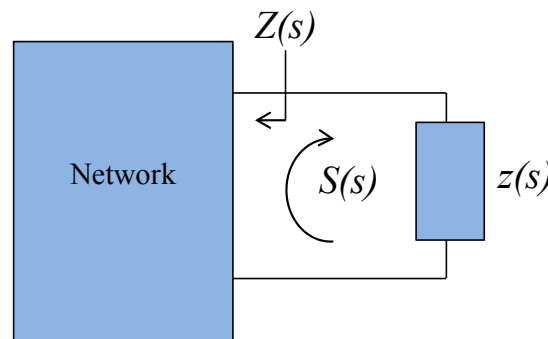
Figure 2.16: Reflection coefficient $S(s)$ for a port in a network normalized to a complex load $z(s)$. The impedance looking into the network is defined as $Z(s)$.

To do so, we first define several parameters relating to the network and load. Referring to Fig. 2.16, we define a network terminated in a load impedance $z(s)$ which

is constructed from passive, lumped components. The function $z(s)$ will therefore be rational and positive-real in the RHP. The *para-hermitian* (even) part of $z(s)$ is defined as

$$r(s) = \frac{z(s) + z_*(s)}{2}.$$ (2.67)

Note that $r(s)$ is the same as defined above in Section 2.4. Since $z(s)$ is rational, we may express it as the ratio of two polynomials, $z(s) = n(s)/d(s)$. We then define $b(s)$ as an all-pass function based on the poles of $z(s)$,

$$b(s) = d_*(s)/d(s)$$ (2.68)

Given the above definitions, the network's reflection coefficient $S(s)$, normalized to the load $z(s)$, can be written as [64]

$$S(s) = b(s)\frac{Z(s) - z_*(s)}{Z(s) + z(s)}$$ (2.69)

where $Z(s)$ is the impedance looking into the network, with all other ports terminated in their proper impedances. The reflection coefficient $S(s)$ will go to zero when the network is conjugate matched to the load impedance. The all-pass function $b(s)$ is necessary to remove the poles of z_* so that $S(s)$ will be analytic in the RHP, preserving causality. In fact, the construction of the complex normalized reflection is equivalent to Darlington synthesis, and $S(s)$ is exactly equal to $\Gamma(s)$, as defined in Fig. 2.12 [82]. We can therefore use complex normalization to easily evaluate the Fano limit. This is the basis of Youla's matching theory [77]. The use of complex normalization has other advantages, such as being valid not only for passive networks, but also active impedances as well.

From the above parameters, we may also provide a formal definition of the transmission zeros of the reference impedance $z(s)$. The transmission zeros are the closed

RHP zeros of the function $F(s)$ [64],

$$F(s) = \frac{4r(s)b(s)}{(z(s)+1)^2} \tag{2.70}$$

Note that all transmission zeros on the $j\omega$-axis will appear with multiplicity $2n$, but this is considered an nth order transmission zero when computing the matching constraints from (2.40)-(2.44).

From (2.69), Youla obtained

$$b(s) - S(s) = \frac{2r(s)b(s)}{Z(s)+z(s)}, \tag{2.71}$$

and determined that at every transmission zero, $S(s) = b(s)$. Writing (2.71) as

$$\log 1/b(s) - \log 1/S(s) = \log\left(1 - \frac{2r(s)}{Z(s)+z(s)}\right), \tag{2.72}$$

we may define the following Taylor series around the transmission zero s_0,

$$\log 1/S(s) = B_0^{s_0} + B_1^{s_0}(s - s_0) + B_2^{s_0}(s - s_0)^2 + ..., \quad s \to s_0 \tag{2.73}$$

$$\log 1/b(s) = A_0^{s_0} + A_1^{s_0}(s - s_0) + A_2^{s_0}(s - s_0)^2 + ..., \quad s \to s_0 \tag{2.74}$$

The coefficients of (2.73) and (2.74) are precisely the same coefficients as defined above in (2.38) and (2.39), and are governed by the same relations (2.40)-(2.44)[9]. However, in Youla's formulation, the Darlington equivalent form of $z(s)$ does not need to be constructed.

Youla's formulation of complex normalization as it relates to impedance matching has also been applied to the problem of *double matching* [83], i.e. when both the generator and load have complex impedances, and to *multi-port matching* [84, 85],

---

[9]In fact the relations (2.40)-(2.44) are in the form as developed by Youla. Fano expressed his general matching constraints in integral form [6]. Nevertheless, the Fano and Youla constraints are mathematically equivalent.

when there are multiple loads to be simultaneously matched by a passive network with three or more ports. As we will see in the following chapter, the multi-port matching problem is applicable to the question of bandwidth limits for arrays when the array is allowed to radiate with multiple modes.

Chapter 3: Bandwidth Limits for Arrays Backed by a Conducting Ground Plane

We turn now to the particular problem of determining the fundamental bandwidth limitations of PEC-backed antenna arrays. One of the most significant problems in developing practical wideband arrays is overcoming the reactance of a nearby conducting ground plane, which is required for low-profile installation on most platforms. As described in Chapter 1, various different strategies have been applied to mitigate these ground plane effects. However, in addition to the development of new practical designs and techniques, it is also important to develop a better understanding of the theoretical limitations of PEC-backed arrays.

By quantifying the fundamental limits, we will gain a better understanding of what is possible. An improved knowledge of the physically realizable design space allows us to establish realistic goals that aggressively advance the state-of-the-art, without wasting time and energy on the physically impossible. Such limits also may provide insight into which parameters are critical to performance, and guide practical engineering decisions, e.g. will magnetic materials be required to meet the given design specifications, or, how will the bandwidth be affected if the scan volume is

increased? Finally, fundamental limits provide a valuable metric with which to evaluate designs against an objective standard. It is useful to know whether a design is nearly optimal, or if significant further improvements may be possible.

Such limits for electrically small antennas have been well known for over 60 years [4, 5], and these limits have enabled and guided the development of optimal small antennas [52]. However, these limits are not useful for characterizing highly directive arrays. Nevertheless, various performance limits for certain types of arrays above a ground plane have been developed through theoretical and empirical means. In [46], an empirical rule of thumb was proposed for the minimum height of wideband arrays. An approximate bandwidth limit was developed in [86] for self-complimentary arrays with multilayer dielectric superstrates. A minimum Q was also determined for arrays comprised of cylindrical electric [87] and equivalent magnetic [88] currents. However, all of the above results apply only to specific types of arrays, and do not provide a general limit for arbitrary PEC-backed arrays.

In this chapter, we will develop a general bandwidth limit that is valid for any electrically large periodic array that is backed by a perfect electrically conducting (PEC) ground plane and constructed from passive, reciprocal, and LTI materials. The low frequency asymptotic behavior of an arbitrary PEC-backed array is first determined through homogenization, yielding a PEC-backed slab model. This is then used to obtain a constraint on the matching efficiency through Fano's method. Doing so, a simple expression is found for the maximum bandwidth of any array above a PEC ground plane. The limit is irrespective of the array's internal geometry (e.g. planar, multi-layer, or volumetric), and allows for dielectric and/or magnetic material loading. We will also explore the effect that polarization and scanning have

65

on the array's bandwidth. Finally, the finite-order Fano limits are used to determine a relationship between the array's bandwidth and its overall complexity.

3.1   Scattering from PEC-Backed Arrays

Consider a general array as depicted in Fig. 3.1. We assume that the array is periodic, backed by a PEC ground plane, and constructed from passive, linear, time-invariant (LTI), and reciprocal materials. However, no other restrictions are placed on the array design and our analysis is applicable to a large class of arrays. To understand the radiating properties of the array, it is convenient to first examine its scattering properties.

The array is illuminated by an incident plane wave traveling in the $\hat{\boldsymbol{k}}$ direction, which may be decomposed into TE and TM components, i.e. the electric (TE) or magnetic (TM) field is transverse with respect to $\hat{\boldsymbol{z}}$. As depicted in Fig. 3.1, the electric field of the TE wave is aligned with the unit vector $\hat{\boldsymbol{p}}_{\boldsymbol{TE}}$, where $\hat{\boldsymbol{p}}_{\boldsymbol{TE}} \cdot \hat{\boldsymbol{z}} = 0$, and the electric field of the TM wave is aligned with the unit vector $\hat{\boldsymbol{p}}_{\boldsymbol{TM}}$, where $(\hat{\boldsymbol{k}} \times \hat{\boldsymbol{p}}_{\boldsymbol{TM}}) \cdot \hat{\boldsymbol{z}} = 0$.

Without loss of generality, homogenization may be used to model the array's low frequency scattering properties as a PEC-backed slab with static material properties ϵ_r and μ_r [89]. These represent the response of the array to static electric and magnetic fields which are co-polarized with the corresponding TE or TM plane wave. We note that the effective static permittivity ϵ_r depends not only on the dielectric materials within the array but also on conducting inclusions, and in general may be arbitrarily large. However, μ_r is determined solely by the relative static permeability of any magnetic materials contained within the array, averaged over volume. As such, μ_r
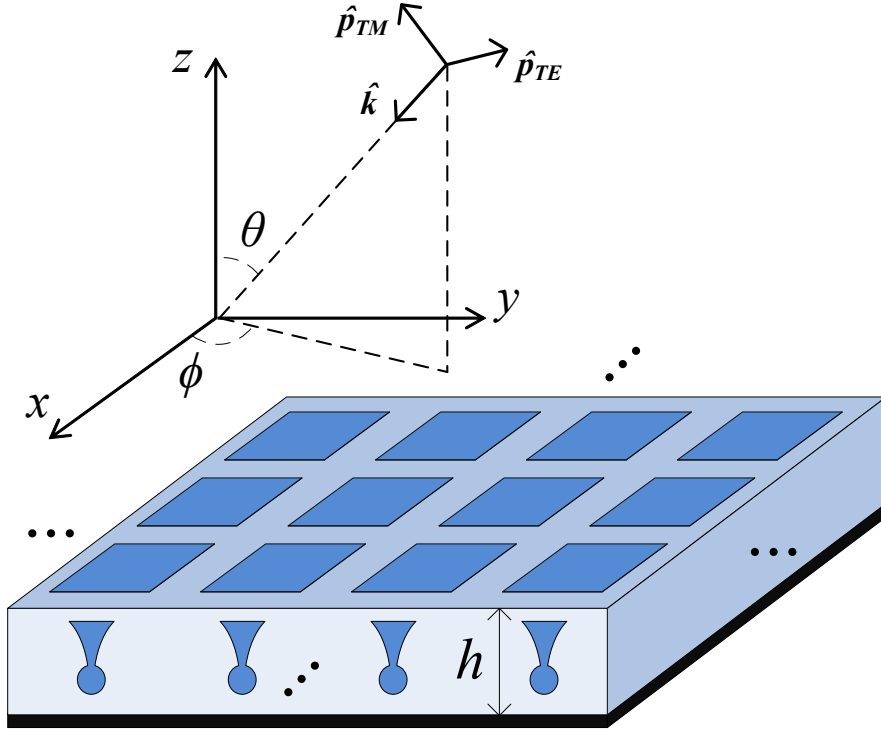
Figure 3.1: Illustration of a periodic array with arbitrary geometry above a PEC ground plane. Polarization vectors $\hat{\boldsymbol{p}}_{TE}$ and $\hat{\boldsymbol{p}}_{TM}$ are depicted for an incident plane wave traveling in the $\hat{\boldsymbol{k}}$ direction.

is unity for all arrays that do not contain magnetic materials [90]. Using the low frequency expansion of the plane wave reflection coefficient for a homogeneous PEC-backed slab given in [69], we have

$$\Gamma_{TE}(s) = -1 + \left(\frac{2h}{c} \mu_r \cos \theta \right) s + \mathcal{O}(s^2), \text{ as } s \to 0, \tag{3.1}$$

$$\Gamma_{TM}(s) = -1 + \left(\frac{2h}{c} \frac{\mu_r - \epsilon_r^{-1} \sin^2 \theta}{\cos \theta} \right) s + \mathcal{O}(s^2), \text{ as } s \to 0. \tag{3.2}$$

for TE or TM polarization. Here, θ is the angle of incidence from normal, h is the maximum height of the array from the PEC-ground plane, c is the speed of light in a vacuum, and $s = \sigma + j\omega$ is the complex frequency variable.

3.2 Network Model for PEC-Backed Arrays

To relate the behavior of Γ_{TE} and Γ_{TM} to standard array parameters such as radiation efficiency and impedance bandwidth, we proceed to represent the array using a simple three-port network, shown in Fig. 3.2. For a passive periodic array illuminated by a plane wave, as shown in Fig. 3.1, the TE and TM components of the plane wave can be identified as the fundamental TE and TM Floquet modes. These two modes are represented in Fig. 3.2 by ports 2 and 3, which are terminated with the corresponding Floquet mode impedances Z_{TE} and Z_{TM}, respectively. The associated voltage reflection coefficients are denoted as Γ_{TE} and Γ_{TM}, and are governed by (3.1) and (3.2), respectively.

Some or all of the power absorbed by the array from the incident plane wave may be delivered to an array feed port, represented by port 1 in Fig. 3.2. This port is terminated by the impedance of a generator or transmission line and has an associated voltage reflection coefficient Γ_A. Although a receiving array has been described, the equivalent transmitting case follows from reciprocity.

For a periodic array, the only other radiating modes are grating lobes which occur only if the array does not have sufficiently small inter-element spacing. If grating lobes are present, they can be represented as losses within the network. If the array is free from grating lobes and does not contain any ohmic losses, then the three-port network is also lossless.
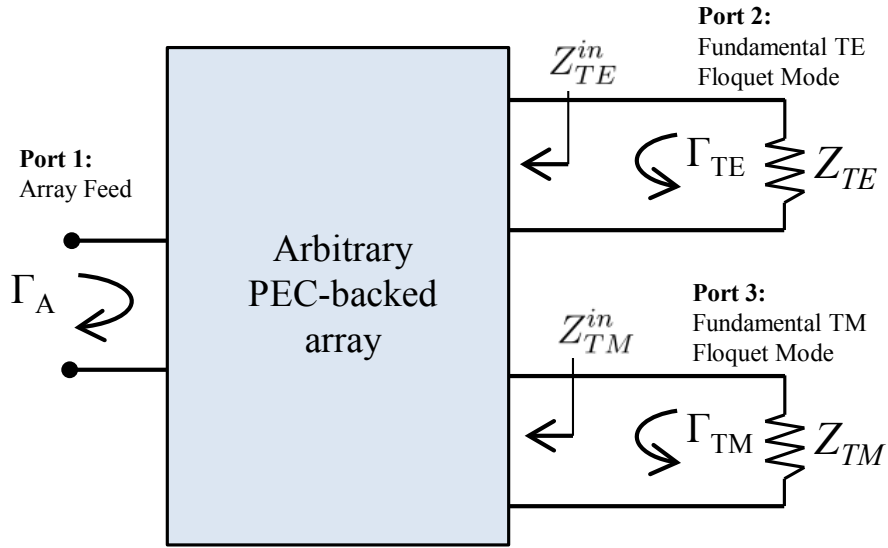
Figure 3.2: Equivalent three-port model for an arbitrary periodic array, as in Fig. 3.1. This network describes the coupling between the array feed port and the fundamental TE and TM Floquet modes. The contribution of all higher-order Floquet modes is included within the network itself. If the array does not contain ohmic losses and no grating lobes are excited, the network is lossless.

We emphasize that although the higher-order evanescent Floquet modes are not explicitly represented in Fig. 3.2, this does not mean that they are disregarded or that the model is only approximate. Rather, the contribution of all higher-order evanescent modes is implicitly included within the reactance of the arbitrary three-port network. In this sense, the design of an optimal matching network corresponds to the optimal configuration of higher-order Floquet modes that maximizes the overall bandwidth and performance of the array.

3.2.1 Synthesis of the Ground Plane Reactance as an Inductive Load

To analyze the above equivalent circuit using impedance matching theory, it is convenient to have an arbitrary matching network terminated in frequency-dependent loads [84]. However, the network as shown in Fig. 3.2 is not arbitrary, but is limited by the constraints (3.1)-(3.2). Nevertheless, we may represent these constraints explicitly as complex load impedances using Darlington synthesis [91]. From (3.1)-(3.2), we express the input admittance of the two Floquet ports as

$$Y_{TE}^{in}(s) = \frac{1}{Z_{TE}} \frac{c}{h\mu_r \cos\theta} \frac{1}{s} + \mathcal{O}(s^0), \text{ as } s \to 0, \tag{3.3}$$

$$Y_{TM}^{in}(s) = \frac{1}{Z_{TM}} \frac{c\cos\theta}{h(\mu_r - \epsilon_r^{-1}\sin^2\theta)} \frac{1}{s} + \mathcal{O}(s^0), \text{ as } s \to 0. \tag{3.4}$$

This indicates that the Darlington synthesis of the input impedances $Z_{TE}^{in} = 1/Y_{TE}^{in}$ and $Z_{TM}^{in} = 1/Y_{TM}^{in}$ each must begin with a shunt inductance, which we define as L_{TE} and L_{TM}, respectively. Normalizing to unit resistances, and using the fact that ϵ_r is unbounded, these inductances are found to be

$$L_{TE} \le \frac{h\mu_r \cos\theta}{c}, \tag{3.5}$$

$$L_{TM} \le \frac{h\mu_r}{c\cos\theta}. \tag{3.6}$$

We can therefore represent the system as a completely arbitrary three-port network terminated in reactive loads, as shown in Fig. 3.3. The load which terminates the ith port is defined as z_i, viz.

$$z_1(s) = 1,$$
$$z_2(s) = \frac{sL_{TE}}{1 + sL_{TE}}, \tag{3.7}$$
$$z_3(s) = \frac{sL_{TM}}{1 + sL_{TM}}.$$
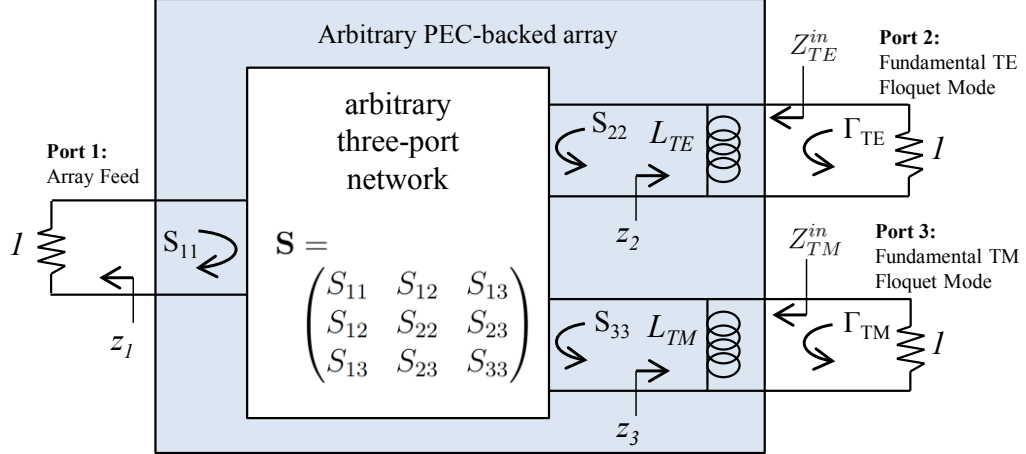
Figure 3.3: Equivalent model for an arbitrary periodic array. The matching constraints given by (3.1)-(3.2) have been interpreted as inductive loads for the TE and TM ports. The resulting three port network defined by the matrix $\mathbf{S}(s)$ is normalized to the complex loads at each terminal, and is otherwise arbitrary.

We define the associated scattering matrix for the arbitrary network as $\mathbf{S}$, and normalize each port to the corresponding load impedance z_i using complex normalization [81]. Because complex normalization and Darlington synthesis are mathematically equivalent [82], S_{22} is equivalent to Γ_{TE}, and S_{33} is equivalent to Γ_{TM}. The system in Fig. 3.3 is therefore equivalent to that of Fig. 3.2, with the constraints (3.1)-(3.2) explicitly represented by the complex load impedances z_2 and z_3. In this form, the system now represents a well-defined three-port impedance matching problem, with an arbitrary matching network and frequency-dependant loads.

3.3 Bandwidth Limits: TE or TM Excitation

For arrays whose polarization is principally TE or TM, analysis of the above system becomes straightforward, because only one of the radiating modes must be

considered and the system becomes a simple two-port network as shown in Fig. 3.4. This is the case for linearly polarized arrays scanned in the principle planes, for example. Although explicit consideration of the intercardinal scan planes requires that TE-TM coupling also be accounted for, the impedance bandwidth in the principal planes is generally indicative of the bandwidth of the array over the entire scan volume. The single-mode analysis also applies to arrays of arbitrary polarization at broadside (since the TE and TM modes are degenerate at $\theta = 0$), provided that the polarization is constant over frequency. The matching bandwidth limits under TE or TM excitation are therefore of significant interest and pertain to a wide range of practical array design problems.
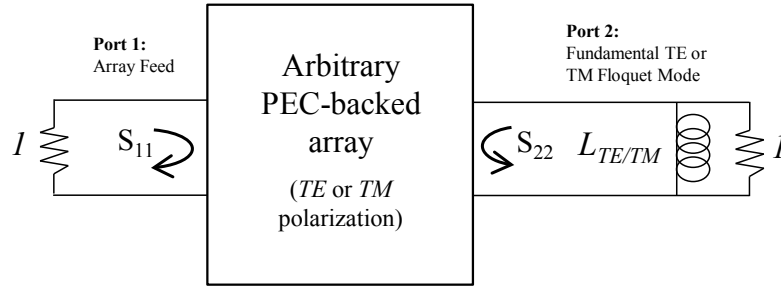
Figure 3.4: Equivalent two-port model for an arbitrary PEC-backed array, in which either the TE mode or the TM mode is principally excited. Any excitation of the other mode is considered cross-polarization, and can be represented as a loss within the two-port network.

Referring to Fig. 3.4, the reflection coefficient of the excited Floquet mode is S_{22}, normalized to the $R - L$ load impedance, using (3.5)-(3.6) to define the inductance. From (2.57) the bandwidth limit for an inductance L in parallel with a unit resistance

is given by

$$\int_0^\infty \omega^{-2} \log 1/|1/S_{22}(j\omega)| d\omega \leq \pi L. \tag{3.8}$$

Plugging in (3.5)-(3.6), we then have

$$\int_0^\infty \omega^{-2} \log |1/S_{22}(j\omega)| d\omega \leq \frac{\pi \mu_r h \cos^p \theta}{c}. \tag{3.9}$$

where p represents the choice of polarization, with $p = +1$ for TE and $p = -1$ for TM. If the array contains neither ohmic losses nor grating lobes, then $|S_{11}| = |S_{22}|$, and (3.9) directly yields a bound for the impedance mismatch at the array feed.

The inequality (3.9) establishes a fundamental limit for the performance of any physically realizable linearly-polarized array above a ground plane, constructed from passive, reciprocal, and LTI materials. Notably, it is a simple expression involving the total height, scan angle, and average magnetic permeability of the array. A corresponding result for PEC-backed absorbers was given in [68] for normal incidence. In fact, (3.9) can be considered a generalization of [68] to oblique incidence. The similarity of arrays to absorbers is not surprising, because a receiving array may be viewed as a special case of an absorbing structure.

We can define the operational band of the array over the continuous frequency range ω_{low} to ω_{high} with a maximum impedance mismatch tolerance of Γ_{max}. To determine the maximum possible bandwidth $B = (\omega_{high} - \omega_{low})/\omega_0$, we may make the ideal assumption that the impedance mismatch is constant within the band ($|S_{11}| = |S_{22}| = \Gamma_{max}$), and totally mismatched elsewhere ($|S_{11}| = |S_{22}| = 1$). Under this condition, (3.9) can be evaluated as

$$B_\infty \leq \frac{\pi \mu_r k_0 h \cos^p \theta}{\log 1/|\Gamma_{max}|}. \tag{3.10}$$

Here, k_0 is the free space wavenumber at the center frequency $\omega_0 = \sqrt{\omega_{high}\omega_{low}}$. The subscript "$\infty$" indicates that this ideal response is only theoretically obtainable by an infinitely complex array that behaves as an infinite-order impedance matching network.

Array bandwidth can alternatively be defined by the ratio $BR = \omega_{high}/\omega_{low}$, a bandwidth definition often used when $(\omega_{high} - \omega_{low})/\omega_0 > 1$, viz.

$$BR_\infty \leq \left(1 - \frac{\pi \mu_r k_{low} h \cos^p \theta}{\log 1/|\Gamma_{max}|}\right)^{-1}, \tag{3.11}$$

where k_{low} is the free space wavenumber at ω_{low}. Of course, (3.11) is valid only when the right hand side is positive, otherwise the bandwidth ratio is unbounded.

In the more realistic case when the array contains ohmic losses (or has grating lobes within the band of interest), then not all of the power accepted at port 1 is delivered to port 2. Therefore, in Fig. 3.4, $|S_{11}| \neq |S_{22}|$ and (3.9) is not applicable at the array feed. However, we may still find a bandwidth limit by introducing the array efficiency factor η, equal to the power transmission coefficient between port 1 and port 2. This efficiency metric accounts not only for ohmic losses, but also for losses in the realized gain due to impedance mismatch or grating lobes. For arrays with such losses, we define the operational band of the array as a continuous frequency range over which the efficiency is above some minimum efficiency η_{min}. Applying the relation $\eta \leq 1 - |S_{22}|^2$ to (3.10), we obtain the following bandwidth limit based on the minimum efficiency of the array,

$$B_\infty \leq \frac{2\pi \mu_r k_0 h \cos^p \theta}{|\log(1 - \eta_{min})|}. \tag{3.12}$$
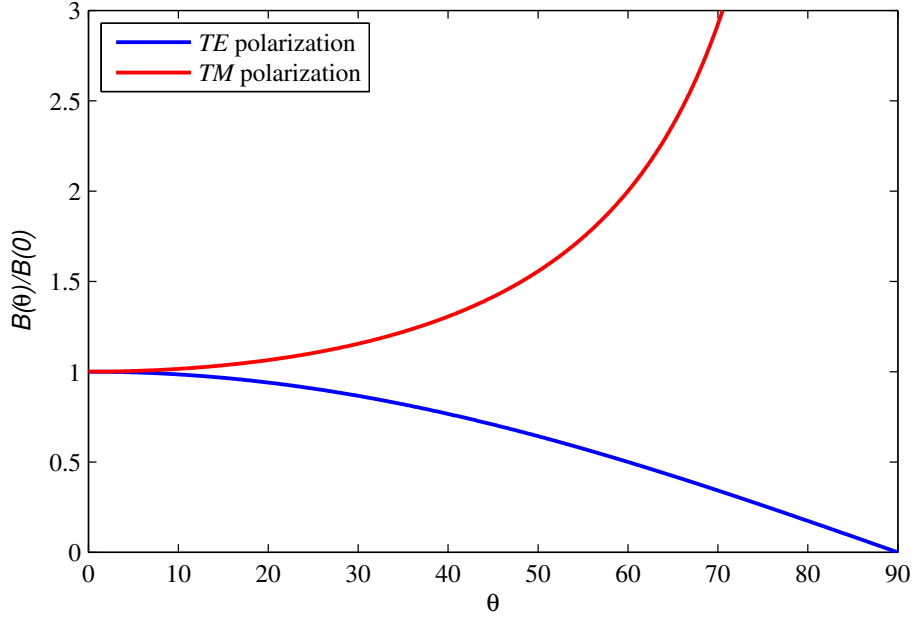
Figure 3.5: Bandwidth limit for PEC-backed arrays (3.10) as a function of scan angle θ for TE (H-plane) and TM (E-plane) polarizations. Limit is normalized to unity at broadside.

The bandwidth limit of (3.10) is plotted in Fig. 3.5 as a function of scan angle, for both TE and TM polarization. For linearly polarized arrays, TE polarization corresponds to scanning in the H-plane and TM polarization corresponds to scanning in the E-plane, as shown in Fig. 3.6. Interestingly, for TE polarization (H-plane scanning), the bandwidth limit is reduced as the array is scanned further from broadside, but the bandwidth limit for TM polarization (E-plane scanning) is increased with larger scan angle. This phenomenon can be understood by considering the boundary conditions at the surface of the PEC ground plane.

As the scan angle θ is increased, the electrical thickness of the array becomes small ($k_z h \to 0$ as $\theta \to 90°$). Therefore at large scan angles, the field radiating from the
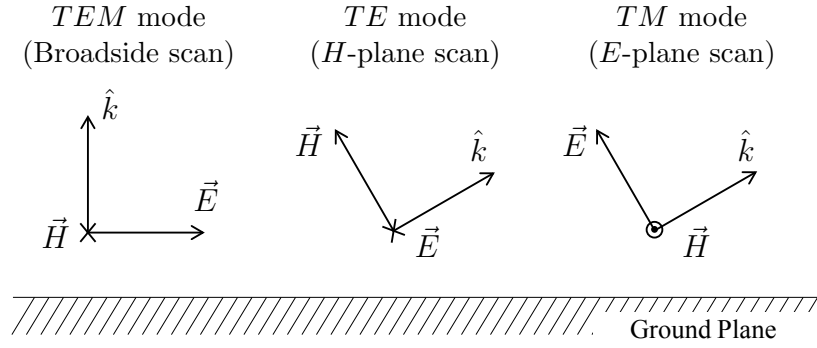
Figure 3.6: Electric and magnetic fields of fundamental plane wave mode under TE and TM polarizations. At large scan angles the E and H fields of the TE mode violate ground plane boundary conditions, whereas the TM fields do not. The bandwidth limit is therefore much more restrictive for H-plane scanning than for E-plane scanning.

array must satisfy the PEC ground plane boundary conditions, which require that both the tangential $(\hat{x}, \hat{y})$ component of the E field and the normal $(\hat{z})$ component of the H field go to zero. Examining Fig. 3.6, we see that for large scan angles, the TE polarized fields violate the boundary condition, but the TM fields do not. For this reason, the effect of the nearby ground plane becomes increasingly restrictive when scanning in the H-plane, with the effective load reactance becoming infinite and the bandwidth going to zero as $\theta \to 90°$. Conversely, when scanning to large angles in the E-plane, the radiating fields do satisfy the ground plane boundary conditions, even when the array is quite thin. This causes the ground plane reactance to vanish and the bandwidth limit to become (theoretically) unbounded.

This analysis is of course only valid in the specific case where the polarization is purely TE or TM. Because these two polarizations have rather different responses at large scan angles, it may be of interest to consider what happens when both modes

76

are excited simultaneously. This will allow us to derive a general bandwidth limit that applies to PEC-backed arrays of arbitrary polarization.

3.4   Bandwidth Limits: Arbitrary Polarization

If both TE and TM modes are excited, we cannot use the simplified two-port model from Fig. 3.4, but must consider the full three-port network of Fig. 3.3. It is obvious that the impedance bandwidth at the feed port must depend on the relative excitation of the TE and TM modes. For example, the overall array bandwidth limit must converge to (3.10) with $p = 1$ when only the TE mode is excited, and to (3.10) with $p = -1$ when only the TM mode is excited. However, when both modes are excited, it is less obvious what constraint are placed on the response at the feed.

For example, scanning a linearly polarized array in the intercardinal planes will excite both TE and TM modes. For many arrays, we find that the impedance mismatch in the intercardinal planes tends to be in-between the E- and H-plane performance. Thus, we might expect the multi-mode limits to be bounded above and below by the individual TE and TM limits from (3.10). However, in the case of electrically small antennas, it is well known that a simultaneous excitation of both TE and TM modes can result in greater bandwidth (lower Q) than either mode is capable of individually [92]. It is therefore a question of significant interest whether such multi-mode improvements may also be achieved in PEC-backed arrays.

Determining the bandwidth limits for arbitrary polarization is a multi-port matching problem. The theoretical conditions for the physical realizability of a multi-port matching network were given in [93], and a methodical process for enforcing these conditions was developed in [84, 85]. However, these existing techniques are rather

77

cumbersome and do not yield convenient closed-form limits for arbitrary excitation of the two radiating modes. The frequency response of each scattering parameter must be defined *a priori*, e.g. as a Butterworth or Chebyshev function of a given order. A unitary scattering matrix is then constructed from these specific functions, and a system of equations is solved to satisfy the constraints of [93]. However, this technique has limited practical applicability as it requires a separate explicit solution for every possible excitation function. It also requires an assumption about the optimal frequency response of the TE-TM coupling, which may not be known. Moreover, evaluation of the resulting equations becomes tedious for more complex higher-order responses. Specifically, neither a closed-form "infinite-order" bandwidth limit as in (3.10), nor the general integral formulation of the limit as in (3.9), can be constructed using existing methods.

Here, we demonstrate a new technique that does not suffer from these limitations. By expressing the scattering parameters as a low-frequency asymptotic series, we develop constraints for the lowest order terms without needing to explicitly define the higher order terms. A general limit can then be written as an integral of impedance mismatch over frequency, as in (3.9), using the dispersion relations. Unlike previous multi-port matching solutions, this result is valid for all excitation functions and does not require a priori knowledge of the TE-TM coupling. For arbitrary and frequency-independent polarization, the result is a simple closed-form expression for the maximum bandwidth of any lossless and reciprocal PEC-backed array.

3.4.1 Multi-port Matching of the PEC-backed Array

Consider the three-port network for a PEC-backed array shown in Fig. 3.3. We assume that the scattering matrix $\mathbf{S}(s)$ is lossless[10] ($\mathbf{S}(s)\mathbf{S}^T(-s) = \mathbf{I}$) and reciprocal ($S_{ij}=S_{ji}$). If the array admits an equivalent circuit constructed from lumped elements, then the scattering matrix is also rational. However, distributed elements may be considered in the limit by allowing the number of lumped elements to be arbitrarily large. Given this network, we wish to establish constraints for the impedance match at the array feed (port 1) given the reactive loads at the TE port (port 2) and the TM port (port 3), and the relative excitation of the TE and TM ports, i.e. the polarization of the array.

Series Form of the Scattering Matrix

Because we are principally concerned with the behavior of the network in the vicinity of the transmission zero at $s = 0$, we represent each scattering parameter as a Taylor series around the origin,

$$S_{11}(s) = a_{11,0} + a_{11,1}s + a_{11,2}s^2 + \mathcal{O}(s^3),$$

$$S_{22}(s) = -1 + a_{22,1}s + a_{22,2}s^2 + \mathcal{O}(s^3),$$

$$S_{33}(s) = -1 + a_{33,1}s + a_{22,2}s^2 + \mathcal{O}(s^3),$$

$$S_{12}(s) = a_{12,n}s^n + a_{12,n+1}s^{n+1} + \mathcal{O}(s^{n+2}),$$

$$S_{13}(s) = a_{13,m}s^m + a_{13,m+1}s^{m+1} + \mathcal{O}(s^{m+2}),$$

$$S_{23}(s) = a_{23,1}s + a_{23,2}s^2 + \mathcal{O}(s^3), \quad \text{as } s \to 0.$$

$$(3.13)$$

[10]The assumption of losslessness is somewhat restrictive. Although losses that are applied at the feed may still be accounted for as in (3.12), our method requires that the TE-TM coupling network be completely lossless. Unfortunately, lossy arrays must still consider the TE or TM modes individually.

We have made use of the fact that the shunt inductive loads on ports 2 and 3 forces $S_{22}(0) = S_{33}(0) = -1$. Likewise, all transmission paths have a transmission zero at the origin, and thus $S_{12}(0) = S_{13}(0) = S_{23}(0) = 0$. For $S_{12}(s)$ and $S_{13}(s)$, we define the order of the zero at the origin as $n \geq 1$ and $m \geq 1$, respectively. We furthermore remark that passivity requires that the first two non-zero terms of each series have opposite sign, and thus $a_{22,1} \geq 0$ and $a_{33,1} \geq 0$ [94].

In order to define the polarization of the array, we introduce the function $\alpha(s)$ as the ratio of the TE excitation to the TM excitation,

$$\alpha(s) = S_{12}(s)/S_{13}(s). \tag{3.14}$$

We will initially assume[11] that $n \geq m$, so that $\alpha(s)$ is finite at the origin, and define $\alpha(0) = \alpha_0$.

The Fano-Youla matching relations (2.42) establish constraints for the terms $a_{22,1}$ and $a_{33,1}$,

$$a_{22,1} \leq 2L_{TE}, \tag{3.15}$$

$$a_{33,1} \leq 2L_{TM}. \tag{3.16}$$

Note that these constraints can also be obtained directly from (3.1)-(3.2). In addition to the Fano-Youla limits at the individual ports, the physical realizability constraints for the overall network from [93] must be satisfied. In Appendix A we show that this produces a third constraint,

$$a_{23,1}^2 \leq (2L_{TE} - a_{22,1})(2L_{TM} - a_{33,1}). \tag{3.17}$$

---

[11]This does not necessarily result in a reduction of generality. The case of $n < m$ can be considered by reassigning the TE mode to port 3, and the TM mode to 2, respectively. Or (with somewhat less rigor) by allowing $|\alpha_0| \to \infty$.

The goal is to derive a corresponding constraint for the mismatch at port 1 which satisfies (3.15)-(3.17).

Determining a Matching Constraint for the Feed Port

When solving the simpler two-port matching problem, the relationship between the mismatch at the feed port and the mismatch at the load port is trivial, since $|S_{11}| = |S_{22}|$ for a lossless and reciprocal two-port. More specifically, the scattering matrix can be written in canonical form as [95]

$$\mathbf{S} = \frac{1}{g} \begin{pmatrix} h & f \\ f & \pm h_* \end{pmatrix},$$ (3.18)

where f and h are polynomials in s that define the transmission and reflection roots, and g is a polynomial in s that defines the poles, common to all parameters. Thus, S_{11} and S_{22} have the same poles, and S_{11} has the same roots as S_{22}, mirrored across the $j\omega$ axis[12].

The canonical form of a lossless reciprocal three-port is not as simple as (3.18). However, a similar condition can be established for the three-port which relates the feed port (port 1) to the load ports (ports 2 and 3) [96],

$$S_{11*} = \frac{1}{\det[\mathbf{S}]} \det \begin{bmatrix} S_{22} & S_{23} \\ S_{23} & S_{33} \end{bmatrix}.$$ (3.19)

Writing the scattering parameters as $S_{ij} = f_{ij}/g$, $S_{ii} = h_{ii}/g$, and noting that $\det[\mathbf{S}] = \pm g_*/g$ for a lossless network [97], we can write (3.19) as

$$\hat{S}_{11} = \frac{h_{11*}}{g} = \pm(S_{22}S_{33} - S_{23}^2).$$ (3.20)

where $\hat{S}_{11}$ is equal to S_{11} after all of the roots have been reflected across the $j\omega$ axis. This is equivalent to multiplying S_{11} by an all-pass function h_{11*}/h_{11}, and thus

---

[12]The paraconjugate operator h_* moves a root at s_0 to the frequency $-s_0$, but because all roots must occur in conjugate pairs, this is equivalent to mirroring across the $j\omega$ axis.

$|\hat{S}_{11}(j\omega)| = |S_{11}(j\omega)|$. Therefore, the magnitude of the reflection coefficient at the array feed port is determined completely by the reflection coefficients at the two Floquet ports, along with the TE-TM coupling coefficient.

We have now defined the necessary constraints that must be satisfied at the Floquet ports (3.15)-(3.17), and have established a relationship between the impedance match at the Floquet ports and the impedance match at the feed port (3.20). However, solving these expressions requires knowledge of S_{23}, the coupling between the TE and TM modes. This in turn depends on the relative excitation of the two Floquet modes, i.e. on the polarization of the array. To further explore this relationship, it is useful to represent the three-port scattering matrix in a canonical form.

Canonical Form for Lossless Reciprocal Three-Port Networks

A canonical form for an arbitrary three-port lossless, reciprocal matrix is given in [97], and described below. As in (3.18), the canonical form allows us to represent the matrix with polynomial functions that describe the various roots and poles of the network. From this form, it is possible to derive several basic relations for the coupling between the TE and TM ports.

We proceed to represent the scattering parameter S_{ij} in rational form with a polynomial f_{ij} which defines the roots of S_{ij}, and a polynomial g that defines the poles of the network,

$$S_{ij} = \frac{f_{ij}}{g}. \tag{3.21}$$

Following the method of [97], we factor the polynomial which describes the transmission zeros, f_{ij}, $(i \neq j)$, as

$$f_{ij} = \theta_{ij}m_{ij}. \tag{3.22}$$

We denote the set of all of the roots of polynomial f as $\overline{f}$. We define $\overline{\theta_{ij}}$ and $\overline{m_{ij}}$ as

$$\overline{\theta_{ij}} = \overline{f_{ij}} \cap \overline{f_{ij*}}, \quad i,j = 1,2,3, \quad i \neq j, \tag{3.23}$$

$$\overline{m_{ij}} = \overline{f_{ij}} - \overline{\theta_{ij}}, \quad i,j = 1,2,3, \quad i \neq j. \tag{3.24}$$

Thus, $\overline{\theta_{ij}}$ are the roots of S_{ij} that are also roots of S_{ij*}. These roots are either located on the $j\omega$ axis or are paired with another root located symmetrically across the $j\omega$ axis. The roots $\overline{m_{ij}}$ are not located on the $j\omega$ axis, and do not have a matching root mirrored across the $j\omega$ axis.

The polynomial θ_{ij} is further factored as

$$\theta_{ij} = f_0 f_i f_j, \quad i,j = 1,2,3, \quad i \neq j, \tag{3.25}$$

where

$$\overline{f_0} = \overline{\theta_{12}} \cap \overline{\theta_{13}} \cap \overline{\theta_{23}}, \tag{3.26}$$

$$\overline{f_i} = \overline{\theta_{ij}} \cap \overline{\theta_{ik}} - \overline{f_0}. \tag{3.27}$$

Therefore, we now have the factorization of the roots of S_{ij} as $f_{ij} = f_0 f_i f_j m_{ij}$. Note that S_{ij} and S_{ij*} do not share any roots that are not also shared by at least one other transmission function. Additionally, f_0 and f_i ($i = 1,2,3$) may share roots, but f_i and f_j ($i,j = 1,2,3$; $i \neq j$) may not, since such a root would be present in all paths and must thus belong to f_0. The polynomials f_i are either purely even or purely odd, as determined by $\epsilon_i = \pm 1$,

$$f_{i*} = \epsilon_i f_i, \quad i = 0,1,2,3. \tag{3.28}$$

Given this factorization of the transmission zeros, the canonical form allows us to define the rest of the scattering matrix [97],

$$S_{ij} = f_0 f_i f_j m_{ij}/g, \quad i \neq j, \quad i,j = 1,2,3, \tag{3.29}$$

83

$$S_{ii} = \epsilon_i(\epsilon_0 m_{ij}m_{ik}n_{jk*} - n_{ij}m_{ik}m_{jk*} - n_{ik}m_{ij}m_{jk*})/g, \quad i,j,k = 1,2,3, \qquad (3.30)$$

where n_{ij} and g are polynomials defined by

$$g = n_{12}m_{13}m_{23} + n_{13}m_{12}m_{23} + n_{23}m_{12}m_{13}, \qquad (3.31)$$

$$n_{ij}m_{ij*} + \epsilon_0 n_{ij*}m_{ij} = f_0 f_k f_{k*}, \qquad (3.32)$$

with g is a Hurwitz polynomial (all roots are in the open LHP). We note that this guarantees that $\mathbf{S}$ is analytic in the RHP.

An important result follows directly from this canonical representation. If a root belongs to both m_{ij} and m_{ik}, then it must also be a root of both g and S_{ii}. Such a root is also a pole, and is considered a degenerate root of S_{ij}, S_{ik}, and S_{ii} because the root and pole cancel and have no net effect on these functions.

From this canonical form, we may develop a new and useful relationship between the mismatch at the TE and TM ports, the TE-TM coupling, and the polarization of the array. This will in turn allow us to determine a matching limit for the feed port using (3.15)-(3.17) and (3.20).

A Useful Relationship for TE-TM Coupling in PEC-backed Arrays

We apply the above canonical form to the PEC-backed array system of Fig. 3.3. Expanding each canonical polynomial as a power series around the origin, we have

$$f_i(s) = f_{i,0} + f_{i,1}s + \mathcal{O}(s^2),$$

$$m_{ij}(s) = m_{ij,0} + m_{ij,1}s + \mathcal{O}(s^2),$$

$$n_{ij}(s) = n_{ij,0} + n_{ij,1}s + \mathcal{O}(s^2),$$

$$g(s) = g_0 + g_1 s + \mathcal{O}(s^2), \quad \text{as } s \to 0.$$

$$(3.33)$$

By definition, m_{ij} cannot have a zero at the origin, and thus $m_{ij,0} \neq 0$. We may normalize the polynomials such that $m_{ij,0} = 1$, moving the constant factor to the

84

polynomials f_i. For the three-port network given in Fig. 3.3, there is a transmission zero in all paths at DC. The polynomial f_0 thus has a root at $s = 0$, and $f_{0,0} = 0$.

From (3.32), we find that if $\epsilon_0 = 1$, then $n_{12,0} = n_{13,0} = n_{23,0} = 0$. From (3.31) this yields $g_0 = 0$ which would violate the condition that $g(s)$ is a Hurwitz polynomial, i.e. it cannot have a root at the origin. Thus, ϵ_0 must equal -1. Comparing (3.13) with (3.30)-(3.31), we also find that $\epsilon_2 = \epsilon_3 = 1$. A corollary is that both n and m in (3.13) must be odd, and that if $\alpha(s)$ has a zero (or pole) at the origin, then it must be a zero (or pole) of even order.

From (3.32) we compute the coefficient $n_{ij,1}$,

$$n_{ij,1} = \frac{f_{0,1}f_{k,0}^2}{2} + m_{ij,1}n_{ij,0}. \tag{3.34}$$

Using this, we can then compute the coefficients $a_{22,1}$, $a_{33,1}$, and $a_{23,1}$ from (3.30),

$$a_{22,1} = \frac{f_{0,1}f_{2,0}^2}{g_0} + 2m_{13,1}, \tag{3.35}$$

$$a_{33,1} = \frac{f_{0,1}f_{3,0}^2}{g_0} + 2m_{12,1}, \tag{3.36}$$

$$a_{23,1} = \frac{f_{0,1}f_{2,0}f_{3,0}}{g_0}. \tag{3.37}$$

The coefficient $m_{ij,1}$ can be written in terms of the roots $\overline{m_{ij}}$,

$$m_{ij,1} = -\sum_{r \in \overline{m_{ij}}} \frac{1}{r}. \tag{3.38}$$

We note that the sum in (3.38) can equivalently be extended over the complete set of non-zero roots of S_{ij}, since all other non-zero roots of S_{ij} that do not belong to $\overline{m_{ij}}$ will sum to zero, due to (3.23). Moreover, we can define these roots in terms of the polarization function $\alpha(s)$.

To do so, we partition the roots of S_{12} and S_{13} as shown in Fig. 3.7. The roots of S_{12} that are not shared by S_{13} are defined by the roots of $\alpha(s)$. Likewise, the roots
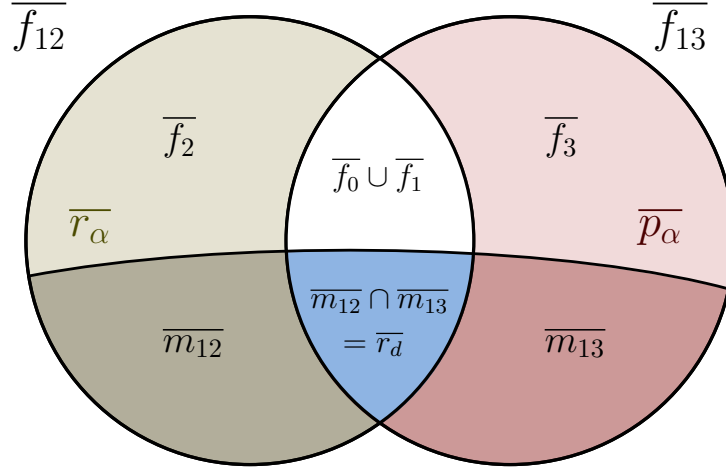
Figure 3.7: Partition of the roots of S_{12} and S_{13}. The roots that are common to $\overline{m_{12}}$ and $\overline{m_{13}}$ are defined as $\overline{r_d}$. These roots are degenerate (pole/zero pairs). The unique roots of S_{12} and S_{13} are defined by the zeros and poles of $\alpha(s)$, $\overline{r_\alpha}$ and $\overline{p_\alpha}$, respectively.

of S_{13} that are not shared by S_{12} are defined by the poles of $\alpha(s)$. We denote the

roots of $\alpha(s)$ by the set $\overline{r_\alpha}$, and the poles of $\alpha(s)$ by the set $\overline{p_\alpha}$. We then define the

quantities $\Sigma_{r\alpha}$ and $\Sigma_{p\alpha}$ as the sum of the inverse of the non-zero roots and poles of

$\alpha(s)$, respectively,

$$\Sigma_{r\alpha} = \sum_{r \in \overline{r_\alpha}, r \neq 0} \frac{1}{r}, \tag{3.39}$$

$$\Sigma_{p\alpha} = \sum_{p \in \overline{p_\alpha}, p \neq 0} \frac{1}{p}. \tag{3.40}$$

The set of roots that are common to $\overline{m_{12}}$ and $\overline{m_{13}}$ are denoted by $\overline{r_d}$. As described

above, these represent degenerate roots of S_{12}, S_{13}, and S_{11}, i.e. they are pole/zero

pairs that cancel and have no direct effect on these parameters. We define Σ_{rd} as

$$\Sigma_{rd} = \sum_{r \in \overline{r_d}} \frac{1}{r}. \tag{3.41}$$

Because all of the roots in $\overline{r_d}$ are also poles, they must be in the LHP and $\Sigma_{rd} \leq 0$. From (3.38)-(3.41) we may write $m_{12,1}$ and $m_{13,1}$ as

$$m_{12,1} = -\Sigma_{r\alpha} - \Sigma_{rd}, \tag{3.42}$$

$$m_{13,1} = -\Sigma_{p\alpha} - \Sigma_{rd}. \tag{3.43}$$

Finally, we identify the ratio $f_{2,0}/f_{3,0}$ as α_0 from (3.14). Combining (3.35)-(3.37) with (3.42)-(3.43), we obtain the following identity

$$\hat{a}_{22,1} = a_{23,1}\alpha_0 = \hat{a}_{33,1}\alpha_0^2, \tag{3.44}$$

where

$$\hat{a}_{22,1} = a_{22,1} + 2\Sigma_{p\alpha} + 2\Sigma_{rd}, \tag{3.45}$$

$$\hat{a}_{33,1} = a_{33,1} + 2\Sigma_{r\alpha} + 2\Sigma_{rd}. \tag{3.46}$$

The expressions (3.44)-(3.46) therefore directly relate the TE-TM coupling to the mismatch at each Floquet port and to the polarization function $\alpha(s)$.

Enforcing Realizability Constraints

We may now impose the realisability constraints (3.15)-(3.17) using the parameters defined in (3.44)-(3.46). From (3.15) and (3.16), we obtain

$$\hat{a}_{22,1} \leq 2L_{TE} + 2\Sigma_{p\alpha} + 2\Sigma_{rd}, \tag{3.47}$$

$$\hat{a}_{22,1} \leq (2L_{TM} + 2\Sigma_{r\alpha} + 2\Sigma_{rd})\alpha_0^2. \tag{3.48}$$

If $\alpha_0 = 0$ (corresponding to $n > m$), then $a_{23,1} = 0$ from (3.44). In this case, (3.17) is automatically satisfied. Otherwise, if α_0 is finite and non-zero, we obtain

$$\hat{a}_{22,1}^2 \leq (2L_{TE} + 2\Sigma_{p\alpha} + 2\Sigma_{rd} - \hat{a}_{22,1})\left(\alpha_0^2(2L_{TM} + 2\Sigma_{r\alpha} + 2\Sigma_{rd}) - \hat{a}_{22,1}\right). \tag{3.49}$$

We find that in order for (3.47)-(3.49) to be simultaneously satisfied, the following condition must hold,

$$2L_{TE} + 2\Sigma_{p\alpha} + 2\Sigma_{rd} + \alpha_0^2(2L_{TM} + 2\Sigma_{r\alpha} + 2\Sigma_{rd}) > 0. \tag{3.50}$$

Under this condition, we solve (3.49) for $\hat{a}_{22,1}$,

$$\hat{a}_{22,1} \leq 2\frac{(L_{TE} + \Sigma_{p\alpha} + \Sigma_{rd})(L_{TM} + \Sigma_{r\alpha} + \Sigma_{rd})}{(L_{TE} + \Sigma_{p\alpha} + \Sigma_{rd}) + (L_{TM} + \Sigma_{r\alpha} + \Sigma_{rd})\alpha_0^2}. \tag{3.51}$$

Together, (3.50)-(3.51) are sufficient to satisfy (3.47)-(3.49), and thus all of the physical realizability constraints for the matching network in Appendix A are satisfied.

These expressions provide an upper bound for $\hat{a}_{22,1}$, and from (3.44)-(3.46), an upper bound is determined for $a_{22,1}$ and $a_{33,1}$. It remains to apply (3.20) to obtain a corresponding limit at port 1. We may write the series expansion of $\hat{S}_{11}(s)$ as

$$\epsilon_1 \hat{S}_{11}(s) = -1 + \hat{a}_{11,1}s + \mathcal{O}(s^2). \tag{3.52}$$

From (3.20) and (3.13), we find

$$\hat{a}_{11,1} = a_{22,1} + a_{33,1}. \tag{3.53}$$

From (3.44)-(3.46) and (3.51), we then find

$$\hat{a}_{11,1} \leq -2\left(\Sigma_{r\alpha} + \Sigma_{p\alpha} + 2\Sigma_{rd}\right) + 2\frac{(L_{TE} + \Sigma_{p\alpha} + \Sigma_{rd})(L_{TM} + \Sigma_{r\alpha} + \Sigma_{rd})(1 + \alpha_0^2)}{(L_{TE} + \Sigma_{p\alpha} + \Sigma_{rd}) + (L_{TM} + \Sigma_{r\alpha} + \Sigma_{rd})\alpha_0^2}. \tag{3.54}$$

This now allows us to establish a bound on the impedance bandwidth at port 1. Using the fact that $\hat{S_{11}}$ must be analytic in the RHP, we apply a dispersion relation such as (2.52) which yields an integrated bandwidth limit for $|S_{11}| = |\hat{S}_{11}|$, viz.

$$\hat{a}_{11,1} = \eta + \frac{2}{\pi} \int_0^\infty \omega^{-2} \log|1/S_{11}(j\omega)|d\omega \tag{3.55}$$

where η is a term that depends on the open RHP zeros of $\hat{S}_{11}$,

$$\eta = \sum_{r \in \text{RHP zeros of } \hat{S}_{11}} \frac{2}{r} \geq 0. \tag{3.56}$$

Thus the bandwidth is maximized if $\hat{S}_{11}$ has no open RHP zeros, i.e. if it is minimum phase.

Roots of S_{11} that belong to the set $\overline{r_d}$ are in the LHP, and therefore represent RHP roots of $\hat{S}_{11}$. Therefore η is bounded by

$$\eta \geq -2\Sigma_{rd}, \tag{3.57}$$

which becomes an equality if $\overline{r_d}$ are the only RHP zeros of $\hat{S}_{11}$. However, because $\overline{r_d}$ are degenerate pole/zero pairs for S_{11}, S_{21}, and S_{31}, these roots may be chosen independently of the specified gain, polarization, and feed reflection coefficient functions. Thus, we are free to choose $\overline{r_d}$ as needed to maximize bandwidth and performance. This is accomplished by setting $\Sigma_{rd} = 0$.

The limits (3.50) and (3.54) then become

$$\Sigma_{p\alpha} + \alpha_0^2 \Sigma_{r\alpha} > -L_{TE} - \alpha_0^2 L_{TM}, \tag{3.58}$$

$$I_{max} = -\pi \left(\Sigma_{r\alpha} + \Sigma_{p\alpha}\right) + \pi \frac{(L_{TE} + \Sigma_{p\alpha})(L_{TM} + \Sigma_{r\alpha})(1 + \alpha_0^2)}{(L_{TE} + \Sigma_{p\alpha}) + (L_{TM} + \Sigma_{r\alpha})\alpha_0^2}, \tag{3.59}$$

where I_{max} is an upper bound for the integral,

$$\int_0^\infty \omega^{-2} \log|1/S_{11}(j\omega)| d\omega \leq I_{max}. \tag{3.60}$$

We initially assumed that the zero at the origin of the TE mode was equal to or greater than the zero at the origin of the TM mode, i.e. $n \geq m$ and α_0 is bounded. As noted above, the case of $m > n$ can be handled by swapping the assignment of the TE and TM modes to ports 3 and 2, respectively. However, the result is equivalent

89

to allowing $|\alpha_0| \to \infty$ and evaluating (3.58)-(3.59) in the limit. In this sense, the above result can be interpreted as general.

Therefore, the relations (3.58)-(3.60) establish fundamental constraints for the bandwidth of $S_{11}(s)$, under arbitrary polarization. Given a rational function $\alpha(s)$ that describes the behavior of polarization over frequency, the values α_0, $\Sigma_{r\alpha}$, and $\Sigma_{p\alpha}$ are computed. The inductances L_{TE} and L_{TM} are determined by the array geometry, from (3.5)-(3.6). Provided that (3.58) is satisfied by the polarization function, the impedance bandwidth limit for $S_{11}(s)$ is given by (3.59)-(3.60).

We will next consider several basic polarization functions and observe their effect on impedance bandwidth.

3.5   Bandwidth Limits: Constant Linear Polarization

The simplest and most useful choice of polarization is one that does not vary over the band of operation. If the polarization is frequency independent, then $\alpha(s) = \alpha_0$ and $\Sigma_{r\alpha} = \Sigma_{p\alpha} = 0$. In this case, the constraints (3.58)-(3.59) simplify to

$$I_{max} = \frac{\pi L_{TE} L_{TM}(1 + \alpha_0^2)}{L_{TE} + L_{TM}\alpha_0^2}. \tag{3.61}$$

Further, α_0 must be real and thus if the polarization is constant over frequency, it must be linear. Using Ludwig's third definition of polarization [98], we define $\alpha_0 = \tan\phi$, where ϕ is the azimuthal scan angle, with $\phi = 0°$ in the E-plane (pure TM polarization), and $\phi = 90°$ in the H-plane, (pure TE polarization). Substituting this into (3.61), along with (3.5)-(3.6), we have

$$I_{max} = \frac{\pi \mu_r h}{c} \frac{1}{\cos\theta \cos^2\phi + \sec\theta \sin^2\phi}. \tag{3.62}$$

As expected, this reduces to (3.9) for $\phi = 0°$ (with $p = -1$) and $\phi = 90°$ (with $p = +1$). However, the explicit consideration of both TE and TM modes has allowed us to extend the bandwidth limits for linearly polarized arrays from the principal planes to the entire hemispherical scan volume. As in (3.10), we can compute the maximum bandwidth limit for a lossless linearly polarized array using an ideal rectangular response as

$$B_\infty(\theta, \phi) \le \frac{\pi \mu_r k_0 h}{(\cos\theta \cos^2\phi + \sec\theta \sin^2\phi) \log 1/|\Gamma_{max}|}, \tag{3.63}$$

$$BR_\infty(\theta, \phi) \le \left(1 - \frac{\pi \mu_r k_{low} h}{(\cos\theta \cos^2\phi + \sec\theta \sin^2\phi) \log 1/|\Gamma_{max}|}\right)^{-1}. \tag{3.64}$$

The bandwidth $B_\infty(\theta, \phi)$ is plotted in Figs. 3.8-3.10.

The resulting limits are as we might intuitively expect. The bandwidth varies smoothly from the H-plane where the ground plane reactance is most significant and the bandwidth is minimum, to the E-plane where the ground plane currents do not destructively interfere and the bandwidth is improved. We also note that the lowest bandwidth occurs when the TE mode is excited alone (H-plane), which can therefore be used as the limiting case for a given conical scanning volume.
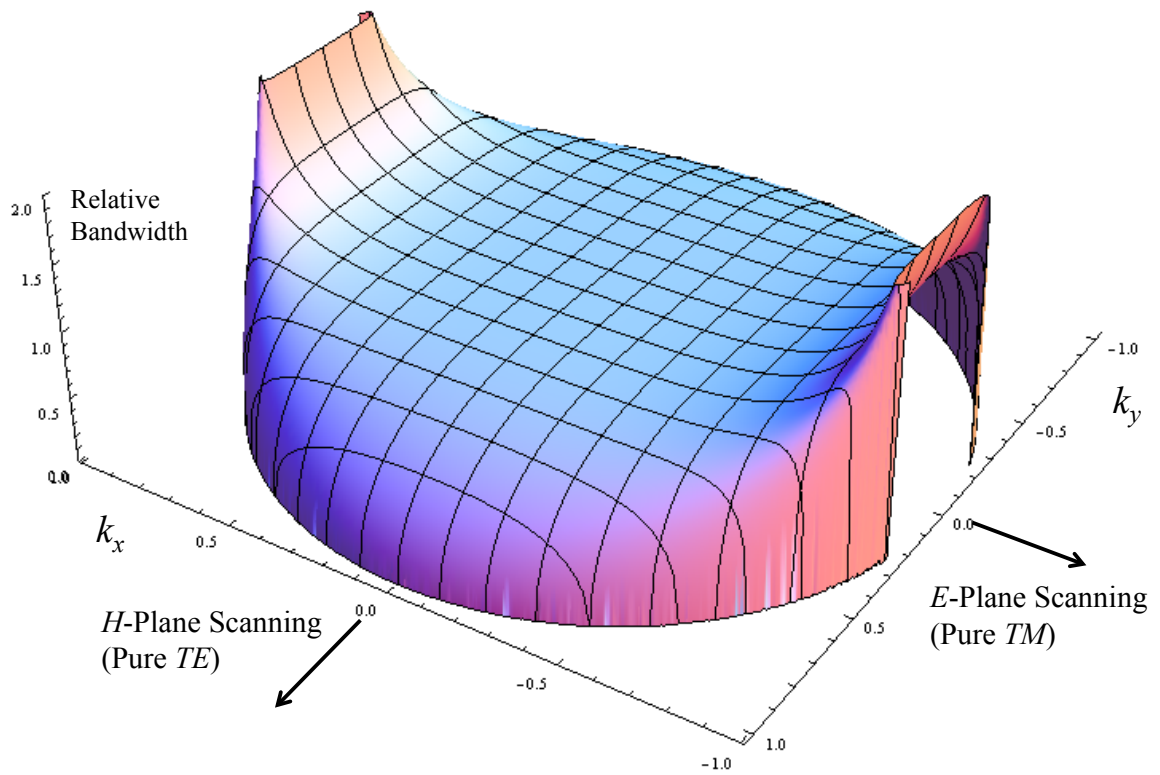
Figure 3.8: Relative bandwidth limits for a hemispherical scan volume of a lossless array with frequency independent linear polarization. Scan angle given in terms $k_x = \sin\theta\cos\phi$ and $k_y = \sin\theta\sin\phi$. Array is polarized in x-direction. Bandwidth is normalized with $B = 1$ at broadside.
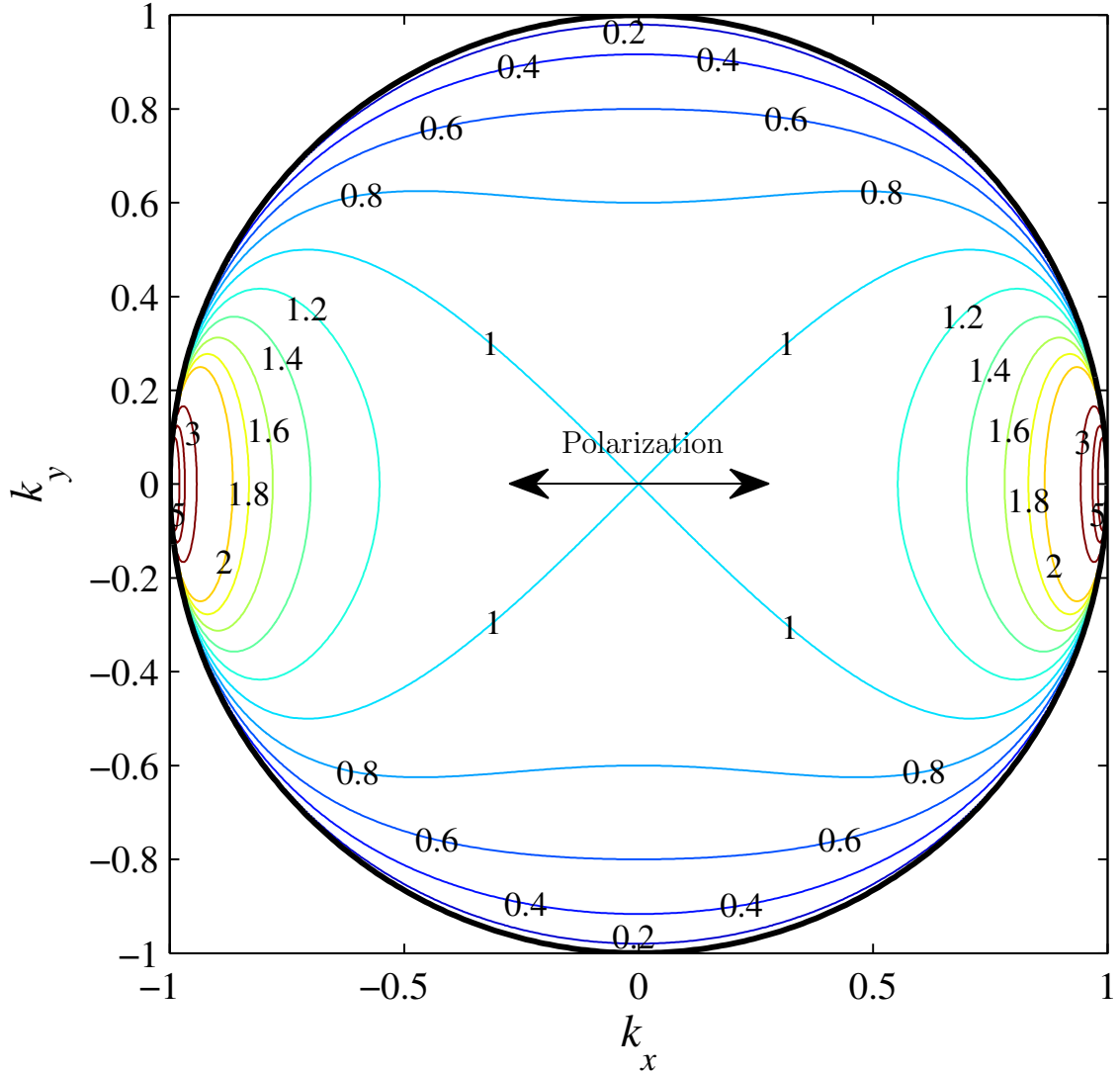
Figure 3.9: Relative bandwidth limits for a hemispherical scan volume of a lossless, reciprocal PEC-backed array with frequency independent linear polarization, plotted as contour map. Scan angle given in terms $k_x = \sin\theta\cos\phi$ and $k_y = \sin\theta\sin\phi$. Array is polarized in x-direction. Bandwidth is normalized with $B = 1$ at broadside.
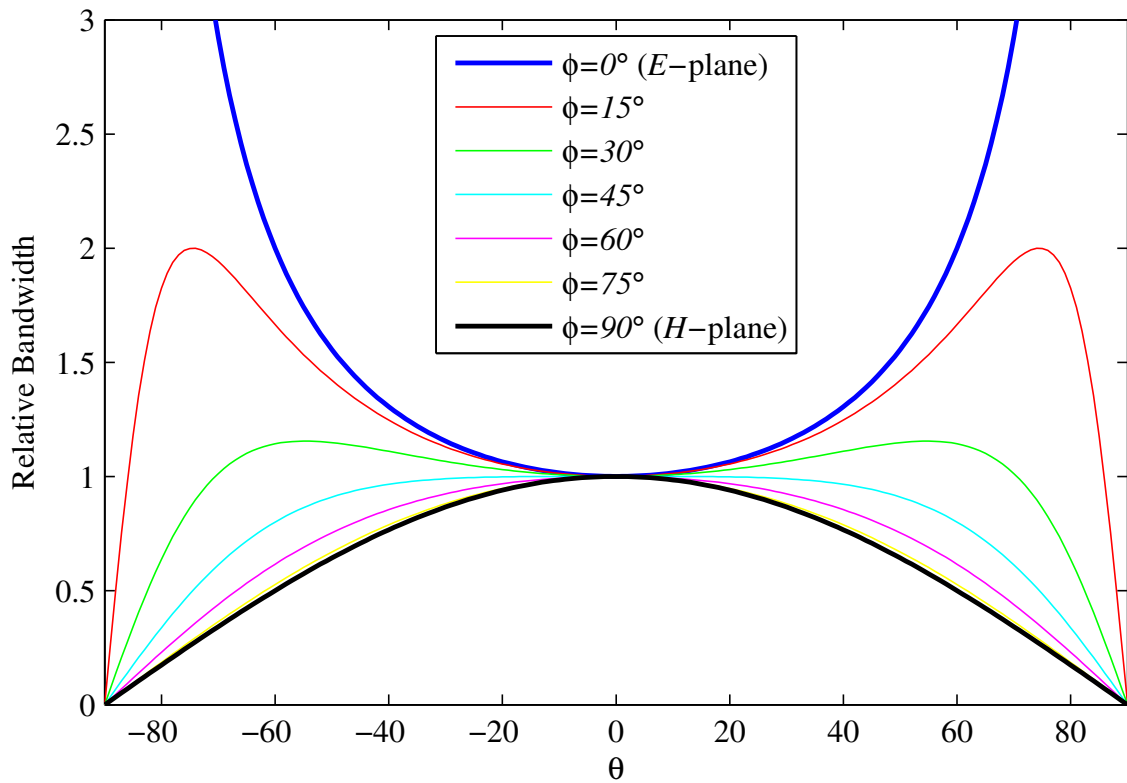
Figure 3.10: Relative bandwidth limits for a lossless array with frequency independent linear polarization, plotted in several scan planes. Scan planes are plotted in 15° increments, with $\phi = 0°$ representing the E-plane and $\phi = 90°$ the H-plane. Bandwidth is normalized with $B = 1$ at broadside.

3.6 Bandwidth Limits: Circular Polarization

As we demonstrated in the above section, if the polarization of the array is not linear, it cannot be constant over frequency. This of course complicates the discussion of bandwidth for circularly polarized arrays. If the polarization is not perfect in the band of operation, then the level of acceptable cross-polarization must be specified in order to obtain a meaningful bandwidth metric. To further complicate matters, the limit for arbitrarily polarized arrays (3.60) was derived under the assumption that the array and feed network is perfectly lossless. However, circular polarization is often implemented using two orthogonally polarized arrays combined using a 4-port quadrature hybrid. Because the 4th port is terminated in a resistive load, the above multi-mode limits do not apply. For such arrays, a more relevant performance bound is found by considering the bandwidth limits of the individual linear polarizations from (3.63). In this case, the bandwidth limit of circularly polarized arrays is comparable to that of linearly polarized arrays.

Nevertheless, some circularly polarized arrays, such as those with spiral elements, do not use dual linear apertures with hybrids, and may be analyzed as a lossless three-port system. In this case, we must define an appropriate polarization function $\alpha(s)$ in order to compute the corresponding bandwidth limit. A simple example is given by

$$\alpha(s) = \frac{s - \sigma_0}{s + \sigma_0}, \tag{3.65}$$

with σ_0 real. In this case, $\alpha(s)$ is an all-pass function, with its magnitude and phase on the real frequency axis plotted in Fig. 3.11. It can be seen that $\alpha(j\omega)$ produces good

(a) $|\alpha(j\omega)|$

(b) $\arg \alpha(j\omega)$

(c) TE/TM Polarization

(d) Circular Polarization
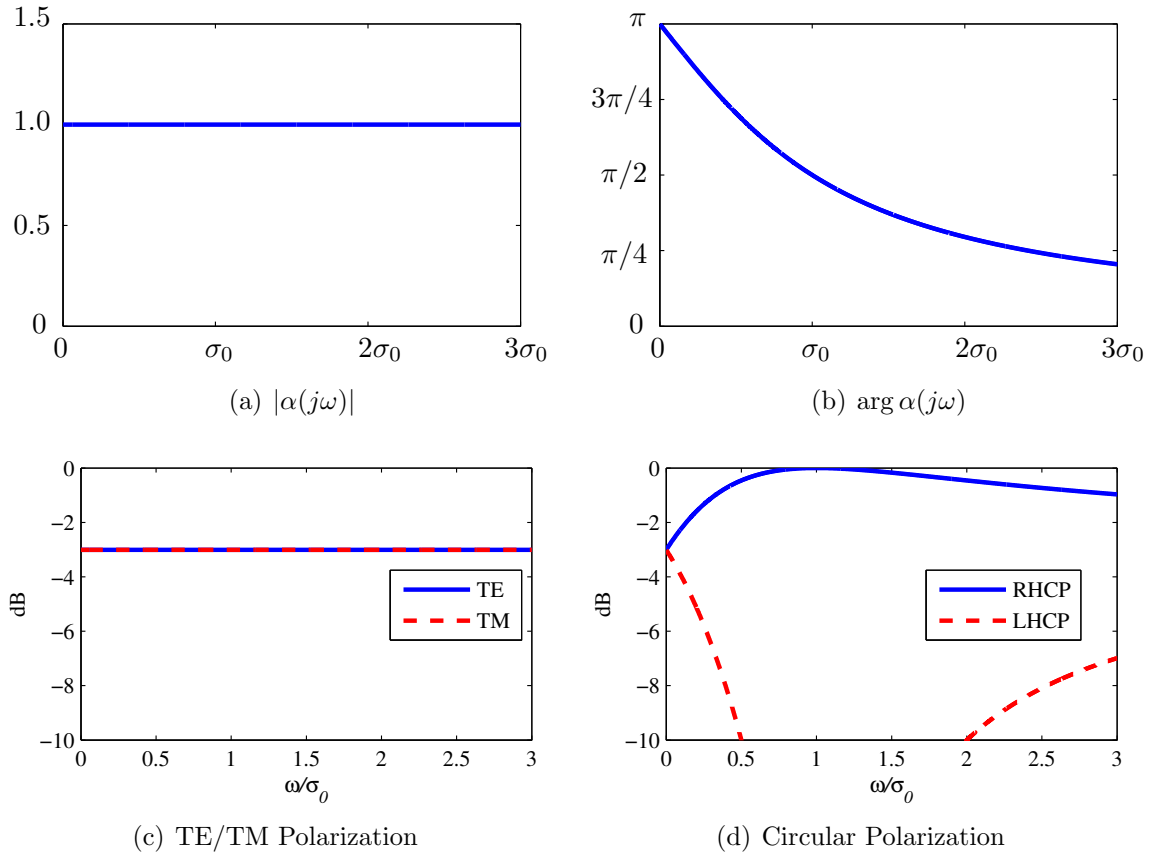
Figure 3.11: $\alpha(s)$ a simple first-order all-pass, as defined by (3.65). (a) Magnitude of $\alpha(j\omega)$ is unity for all ω. (b) Phase of $\alpha(j\omega)$ varies from π (slant linear) at DC, to $\pi/2$ at $\omega = \sigma_0$ (RHCP), to 0 (slant linear in orthogonal direction) as $\omega \to \infty$. (c) TE and TM modes are equally excited at all frequencies. (d) $\alpha(s)$ is circularly polarized near $\omega = \sigma_0$.

96

circular polarization near $\omega = \sigma_0$. However, the polarization purity deteriorates away from this center frequency, and becomes slant linear at higher and lower frequencies.

For any $\alpha(s)$ constructed from an all-pass function, we find $\alpha_0 = \pm 1$ and $\Sigma_{r\alpha} = -\Sigma_{p\alpha}$. We can then compute the limit (3.59) as

$$I_{max} = \pi L - \frac{\pi \Sigma_{r\alpha}^2}{L}, \tag{3.66}$$

where we have assumed the broadside case, with $L_{TE} = L_{TM} = L$ for simplicity. For the first-order all pass function (3.65), this limit becomes

$$I_{max} = \pi L - \frac{\pi}{L\sigma_0^2}. \tag{3.67}$$

It is clear that any such all-pass polarization function will reduce the impedance bandwidth of the array compared to the limit for constant polarization at broadside, which we find from (3.61) to be $I_{max} = \pi L$. Moreover, the simple first-order all pass function from (3.65) has a limited circular polarization bandwidth as seen in Fig. 3.11d. Improving the polarization bandwidth can be accomplished by using higher-order quadrature approximation functions [99], but this requires adding more pole/zero pairs to $\alpha(s)$, and the magnitude of $\Sigma_{r\alpha}$ quickly exceeds L, sending the impedance bandwidth to zero. Our conclusion is that lossless, reciprocal low-profile PEC-backed arrays (which excludes dual-linear arrays with matched hybrids) cannot simultaneously achieve a wide impedance bandwidth and a wide circular polarization bandwidth with high polarization purity.

We may, however, improve the impedance bandwidth by modifying our polarization function to be

$$\alpha(s) = -\frac{s^2(s - \sigma_0)}{\sigma_0^2(s + \sigma_0)}. \tag{3.68}$$

(a) $|\alpha(j\omega)|$

(b) $\arg \alpha(j\omega)$

(c) TE/TM Polarization

(d) Circular Polarization
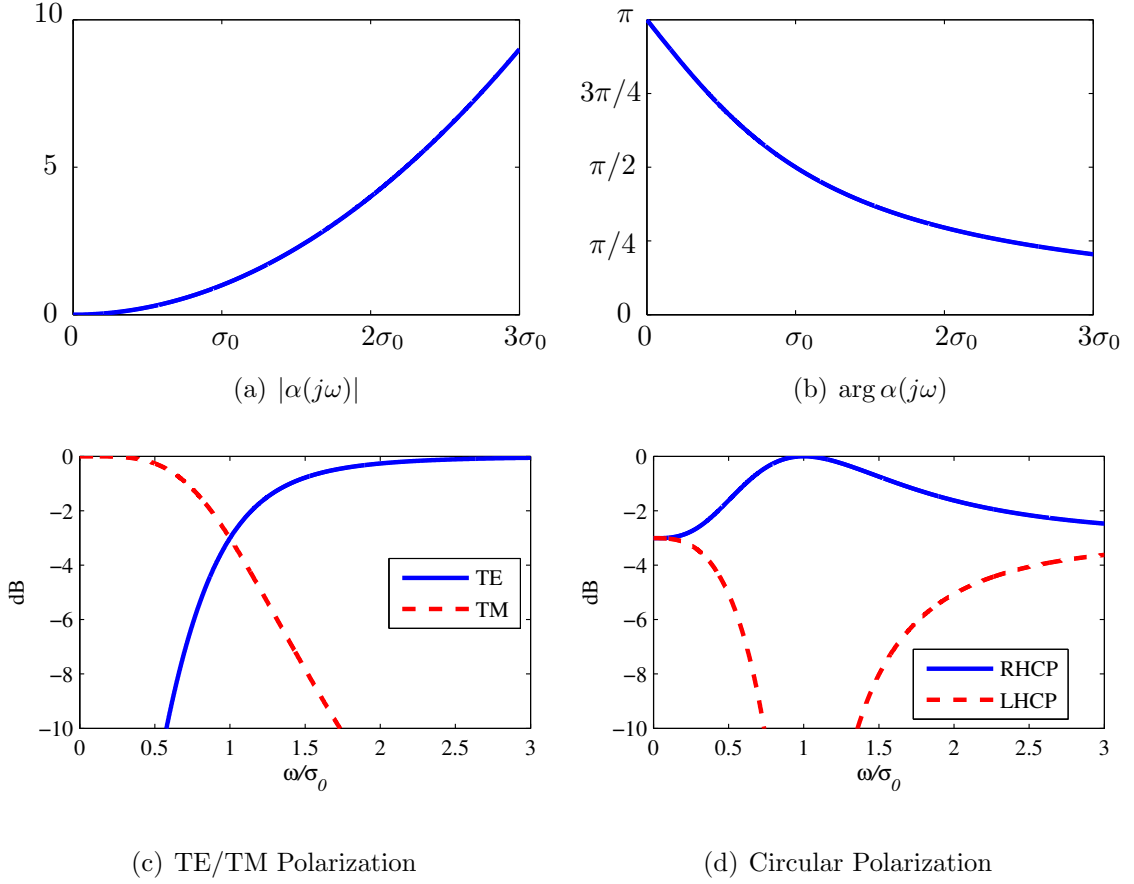
Figure 3.12: $\alpha(s)$ includes a double zero at the origin, as defined by (3.68). (a) Magnitude of $\alpha(j\omega)$ varies from 0 (pure TM) at DC to ∞ (pure TM) as $\omega \to \infty$. (b) Phase of $\alpha(j\omega)$ varies from π at DC, to $\pi/2$ at $\omega = \sigma_0$, to 0 as $\omega \to \infty$. (c) Relative excitation of TE and TM modes over frequency, showing TE and TM modes matched over separate bands. This feature allows the impedance bandwidth to be increased from the simple all-pass case. (d) $\alpha(s)$ is circularly polarized near $\omega = \sigma_0$, though with a narrower polarization bandwidth than in Fig. 3.11.

Here, we have kept the all-pass from (3.65) but have added a double zero at DC.[13] This produces a polarization response as shown in Fig. 3.12. As with the all-pass function, the polarization is circular at $\omega = \sigma_0$, but now the array has pure TM polarization ($\alpha(s) \to 0$) at low frequencies and pure TE polarization ($\alpha(s) \to \infty$) at high frequencies, as seen in Fig. 3.12. The circular polarization bandwidth is reduced, but the impedance bandwidth limit computed from (3.59) becomes

$$I_{max} = \pi L + \pi/\sigma_0. \tag{3.69}$$

Therefore, the bandwidth in this case exceeds that of constant linear polarization. Previously, we stated that a lossless array cannot realize wideband circular polarization without significantly reducing the impedance bandwidth. However, we see here that the converse is also true – by reducing the polarization bandwidth, the impedance bandwidth may be increased above that of a linearly polarized array. This advantage is of course not unlimited, and the absolute maximum impedance bandwidth for a PEC-backed array regardless of polarization can be found from (3.53),

$$I_{max} = \pi L_{TM} + \pi L_{TE}, \tag{3.70}$$

corresponding to a polarization function with the following parameters[14],

$$\Sigma_{r\alpha} \to -L_{TM}, \tag{3.71}$$

$$\Sigma_{p\alpha} \to -L_{TE}. \tag{3.72}$$

However, the polarization of such an array would vary significantly the band. In general, we find that for lossless circularly polarized PEC-backed arrays, there is a

---

[13]Note that the order of the zero at DC must be even if the array is lossless.

[14]These must be taken in the limit, because setting $\Sigma_{r\alpha} = -L_{TM}$ and $\Sigma_{p\alpha} = -L_{TE}$ violates (3.58) and gives an indeterminant result from (3.59).

fundamental tradeoff between the impedance bandwidth and the polarization bandwidth.

An explanation for this phenomenon is that the array may match to one Floquet mode at the low end of the band and the other mode at the high end of the band, as in Fig. 3.12c. Although each individual Floquet mode is still limited by (3.10), the total impedance bandwidth can be larger. The result (3.70) is therefore rather intuitive, since the absolute maximum impedance bandwidth limit is the sum of the limit for each mode.

A practical example of an array that makes use of this phenomenon is the ISPA [32], with interwoven spiral radiating elements, pictured in Fig. 1.11b. The ISPA is less than $\lambda/2$ tall at the top of the band, and yet achieves 10:1 bandwidth at broadside with VSWR $<$2:1, see Fig. 3.13a. This impedance bandwidth exceeds the theoretical limit for PEC-backed arrays with fixed polarization (3.61) by $\sim$14%. This is only possible because the ISPA has elevated cross-polarization near the band edges as shown Fig. 3.13b.

(a) Impedance bandwidth of ISPA   (b) Polarization bandwidth of ISPA
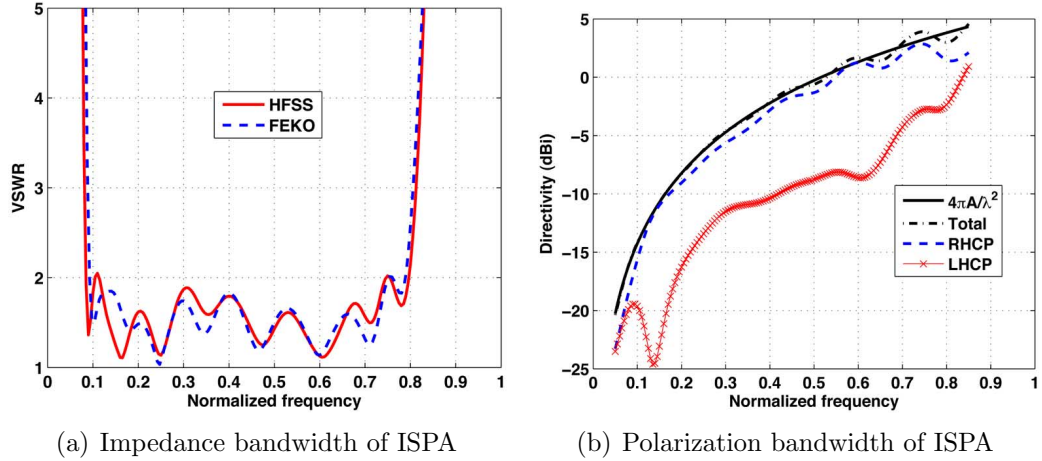
Figure 3.13: Frequency response of the ISPA, a lossless, circularly polarized PEC-backed array. (a) VSWR≤2:1 over a 10:1 bandwidth. (b) Co- and cross-polarization, showing elevated cross-polarization at edges of the band. Figures are from [32], ©2011 IEEE.

3.7 Array Complexity and Finite-Order Matching

We now concern ourselves with the optimal implementation of the array as a impedance matching network. As stated above, realization of the limits (3.10) and (3.63) require the matching network to be of infinite-order. By "order" we refer to the order of the rational polynomial representation of the elements of the scattering matrix, or equivalently the number of ladder sections required to synthesize an equivalent lumped element circuit for the array. In practice, the order of the equivalent network cannot be infinite, but is limited by the complexity of the array and feed. Unlike electrically small antennas for which first-order representations are typically appropriate, wideband arrays usually have equivalent circuits of at least second-order or higher. External matching can also be used to increase the effective order of the array.

For an array represented by an equivalent n^{th} order network, Fano [6] provides a method to compute the corresponding bandwidth limit subject to an ideal equi-ripple match, as described in Section 2.4.3. Although Fano's method requires the solution of several simultaneous transcendental equations, the limit can be approximated by substituting the quantity $(\log 1/|\Gamma_{max}|)/\pi$ with the factor K_n. For linearly polarized arrays, this yields

$$B_n(\theta, \phi) \leq \frac{\mu_r k_0 h}{K_n(\cos\theta \cos^2\phi + \sec\theta \sin^2\phi)}, \tag{3.73}$$

$$BR_n(\theta, \phi) \leq \left(1 - \frac{\mu_r k_{low} h}{K_n(\cos\theta \cos^2\phi + \sec\theta \sin^2\phi)}\right)^{-1}, \tag{3.74}$$

where n is the effective order of the array. K_n is given by [80]

$$K_n \approx b_n \sinh\left(\frac{1}{a_n} \log \frac{1}{|\Gamma_{max}|}\right) + \frac{1 - b_n}{a_n} \log \frac{1}{|\Gamma_{max}|}, \tag{3.75}$$

for lossless arrays, or

$$K_n \approx b_n \sinh\left(\frac{|\log(1 - \eta_{min})|}{2a_n}\right) + \frac{1 - b_n}{2a_n}|\log(1 - \eta_{min})|, \tag{3.76}$$

when the array contains ohmic or radiation losses. The coefficients a_n and b_n are listed in Table 2.1. Note that, as expected, (3.73) and (3.74) reduce to the infinite-order limits for $n = \infty$.

Many wideband arrays have equivalent (or approximate) circuits that can be used to determine the effective order of the array. In general, arrays containing more complex physical structures capable of multi-resonance behavior will lead to higher order equivalent networks, theoretically capable of greater bandwidth. For example, an array may contain several dielectric superstrate layers or frequency selective surfaces (FSS), with each additional layer increasing the overall order of the array.

Similarly, multi-turn spiral elements will typically be of higher-order than an array of simple dipole elements (e.g. [32] vs. [19]). Also note that, although distributed networks (such as those that include transmission lines) technically have infinite-order lumped equivalents (i.e. they are not rational), this does not imply that they are capable of reaching the infinite-order limit. In such cases, an equivalent or approximate finite-order lumped, rational representation (such as obtained by the Richards' Transformation [30]) is typically available and should be used instead.

A plot of bandwidth ratio vs. $k_{low}h$ for a non-magnetic array matched to VSWR $\leq$ 2:1 is given in Fig. 3.14 for various n. As an example, consider a lossless low profile array with $k_{low}h = 0.4$ ($h \approx \lambda_{low}/16$), matched to VSWR$\leq$ 2:1. If the array is only second-order, the bandwidth is limited to 3.2:1. However, a third-order array of the same height is capable of more than twice as much bandwidth (up to 7:1). Thus, the order (and hence the physical complexity) of the array can have a great impact on its performance.
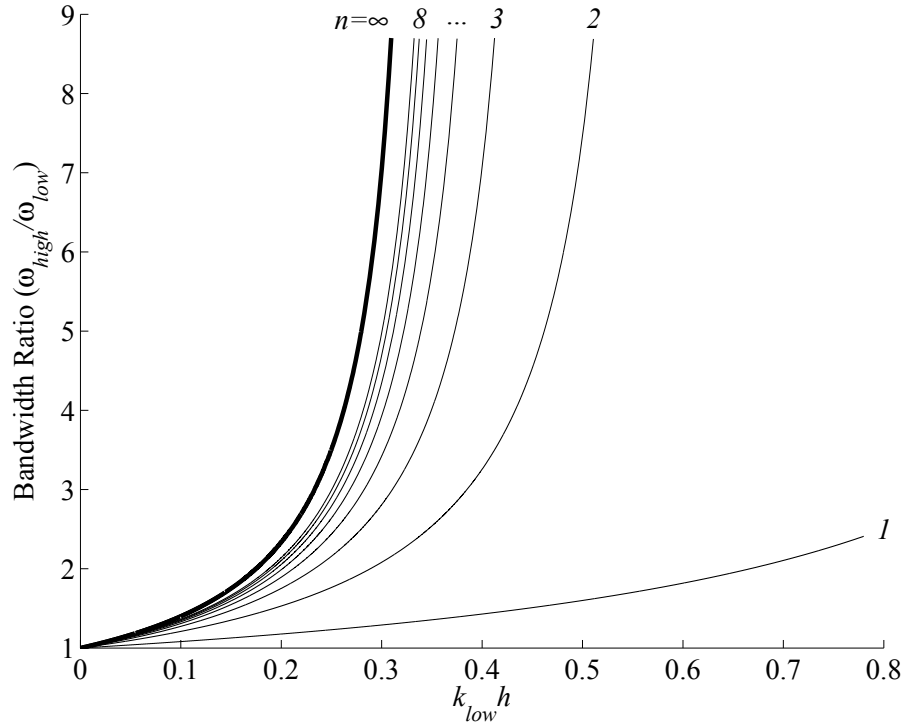
Figure 3.14: Bandwidth ratio limit $\omega_{high}/\omega_{low}$ for an arbitrary non-magnetic array of height h and order n, above a perfectly conducting ground plane with VSWR $\leq$ 2:1 and broadside scanning ($\theta = 0$).

3.8   Minimum Height for High-Pass Arrays

The bandwidth ratio limit given by (3.74) reveals the high-pass nature of a PEC-backed array. If kh is sufficiently large at the low end of the band, then ω_{high} becomes unbounded, and the array behaves as a high-pass filter. In practice, of course, the high frequency performance of the array will be limited by inter-element spacing and the onset of grating lobes. However, this can in theory be moved arbitrarily high in frequency, and is therefore not considered to be a fundamental limit for the purposes of this analysis. The minimum array thickness h_{hp} of a high-pass array scanning to

an angle θ (using TE excitation as the limiting case) can be found by solving (3.74) with $BR \to \infty$, yielding

$$h_{hp} = \frac{K_n}{2\pi\mu_r \cos\theta}\lambda_{low}. \tag{3.77}$$

From this, we find that a simple second-order, lossless, non-magnetic, high-pass array matched to VSWR $\leq$ 2:1 at broadside must be at least $\lambda_{low}/11$ tall. This is consistent with the empirical "rule of thumb" suggested in [46] of $\lambda_{low}/12$ as the minimum height for wideband arrays. However, (3.77) indicates that even thinner arrays may be possible by increasing the order of the array through increased geometrical complexity or external matching. Specifically, an infinite-order, non-magnetic, high-pass array matched to VSWR $\leq$ 2:1 at broadside has a minimum height of $\lambda_{low}/18$.

3.9   Performance of Arrays vs. Theoretical Limits

In Chapter 1, we introduced a generalized array performance metric P_A defined as

$$P_A = \frac{B \log 1/|\Gamma_{max}|}{\cos\theta_{max}}, \quad \text{for lossless arrays,} \tag{3.78}$$

$$P_A = \frac{B|\log(1-\eta_{min})|}{2\cos\theta_{max}}, \quad \text{for lossy arrays.} \tag{3.79}$$

Comparing this metric to the theoretical limits (3.10) and (3.63), we see that the maximum possible P_A for a low-profile PEC-backed array with frequency independent polarization scanning within a cone of angle θ_{max} is given by

$$P_A \leq \pi\mu_0 k_0 h, \quad \text{constant polarization.} \tag{3.80}$$

If the polarization is not constant over the band, the limit at broadside becomes

$$P_A \leq 2\pi\mu_0 k_0 h, \quad \text{arbitrary polarization, broadside.} \tag{3.81}$$
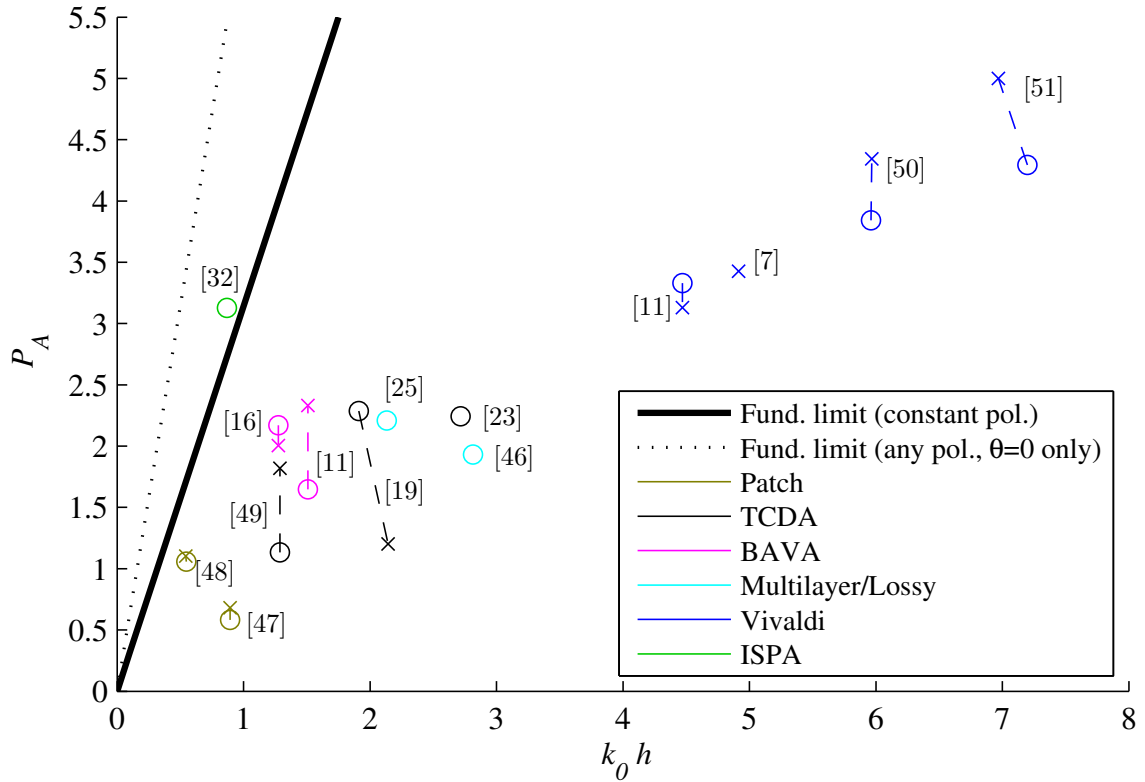
Figure 3.15: Survey of wideband array performance P_A vs. electrical thickness $k_0 h$. The fundamental limit under constant polarization is given by the heavy black line.

Fig. 3.15 revisits the survey of wideband array performance from Fig. 1.13 with the limits of (3.80)-(3.81) overlayed. With the exception of the ISPA as discussed above, we see that all of the arrays surveyed fall below the fundamental limit for arrays with constant polarization.

We notice in Fig. 3.15 that there seems to be a large design space that has not yet been utilized. The widest bandwidth arrays do not seem to follow the same slope as given by the fundamental limit, but rather diverge with a much shallower slope. We suggest that this is primarily due to the use of simple, low-order, low

Q structures in the design of wideband arrays. This is especially seen in the long tapered slot arrays, which yield significant bandwidth but are much taller than the limit suggests is optimal. It should therefore be possible to develop thinner arrays with larger bandwidths than what is achieved by current the state-of-the-art. However, accessing this design space will require new techniques such as higher-order impedance matching.

It is often assumed that wideband arrays should avoid resonant structures and minimize the amount of stored reactive energy in the array, i.e. minimize the total Q. However, as shown above in Section 3.7, this strategy cannot yield maximum bandwidth. Instead, an optimal array must act like a high-order filter or impedance matching circuit, containing many resonant stages and a large amount of total stored energy. An optimal wideband array therefore will therefore not have a small Q.

This highlights a common misunderstanding about the relationship between Q and bandwidth. The well known Q-bandwidth limit (2.61) applies *only* to simple first order loads consisting of a single resonance, such as an RLC circuit. Higher-order loads with multiple resonances have a much more complex relationship between Q and bandwidth, i.e. (2.40)-(2.44). In the case of a PEC-backed array, the bandwidth is limited by the direct interaction between the radiation resistance and the ground plane, i.e. the unloaded Q of the RL loads depicted in Fig. 3.3. It is true that the bandwidth is maximized when this Q is minimized, e.g. by increasing the thickness of the array. It is not true, however, that the bandwidth is limited by the *total Q* of the system; otherwise adding matching stages would be counter productive, and an infinite-order system would have zero bandwidth. It is for this reason that we have avoided framing the array bandwidth limits in terms of Q.

Therefore, this analysis suggests that development of thinner PEC-backed arrays with more bandwidth should be possible, and that this requires the use of higher-order matching features, rather than minimizing the total Q of the array. These additional matching features may be integrated within the array itself, or they may be included in the feed network.

Chapter 4: Bandwidth Limits for PEC-Backed Planar Arrays

In the previous chapter, general bandwidth limits were derived for arbitrary arrays backed by a PEC ground plane. However, many common types of wideband PEC-backed arrays, such as arrays of dipoles, slots, spirals, and fragmented apertures, have radiating currents that are confined to a thin planar surface as shown in Fig. 4.1. The volume between the planar radiating surface and the ground plane may be filled by air or by some lossless substrate material with relative material properties ϵ_{sub} and μ_{sub}. A lossless superstrate material layer may also be added on top of the radiating surface, with relative material properties ϵ_{sup} and μ_{sup}.

The bandwidth of such arrays is more limited than that of a completely arbitrary array whose radiating currents are allowed to fill the entire volume of the array. This is because the ground plane will short circuit the radiating surface the array not only at DC, but also whenever the height of the array is a multiple of a half-wavelength ($h = n\lambda/2$). Given this observation, it would be useful to develop a tighter bound for the bandwidth of this common family of arrays. First, we must develop a valid equivalent circuit for an arbitrary planar array.
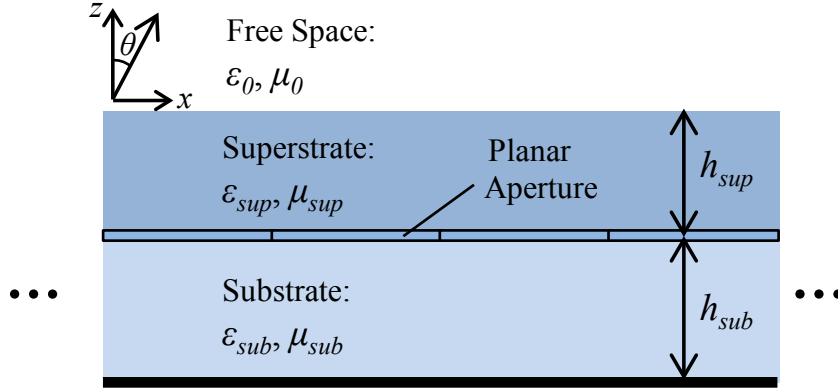
Figure 4.1: Cross section of a planar array above a conducting ground plane

4.1 An Equivalent Circuit for Planar Arrays

The fields within any two-dimensionally periodic structure may be decomposed into a set of orthogonal eigenmodes, known as *Floquet* modes (also referred to as *Bloch* modes). Any interaction that the periodic surface has with the surrounding fields may be treated by considering the coupling to these Floquet modes. We may therefore represent the planar radiating surface as a multi-port network as seen in Fig. 4.2, with a single port for the array feed, and a separate port representing the interaction of the array with each Floquet mode. We furthermore remark that, apart from the radiating surface itself, the structure as depicted in Fig. 4.1 is homogeneous in the transverse dimension. Therefore the Floquet modes will remain uncoupled outside of the multi-port network.

If the periodicity of the array is less than the grating lobe spacing, then only the two fundamental modes may propagate in free space[15]. The remaining higher-order

[15]Even if there are grating lobes present, these may be treated as losses within the network. By extension, we may even relax the requirement that the array be periodic, and the resulting limit

110
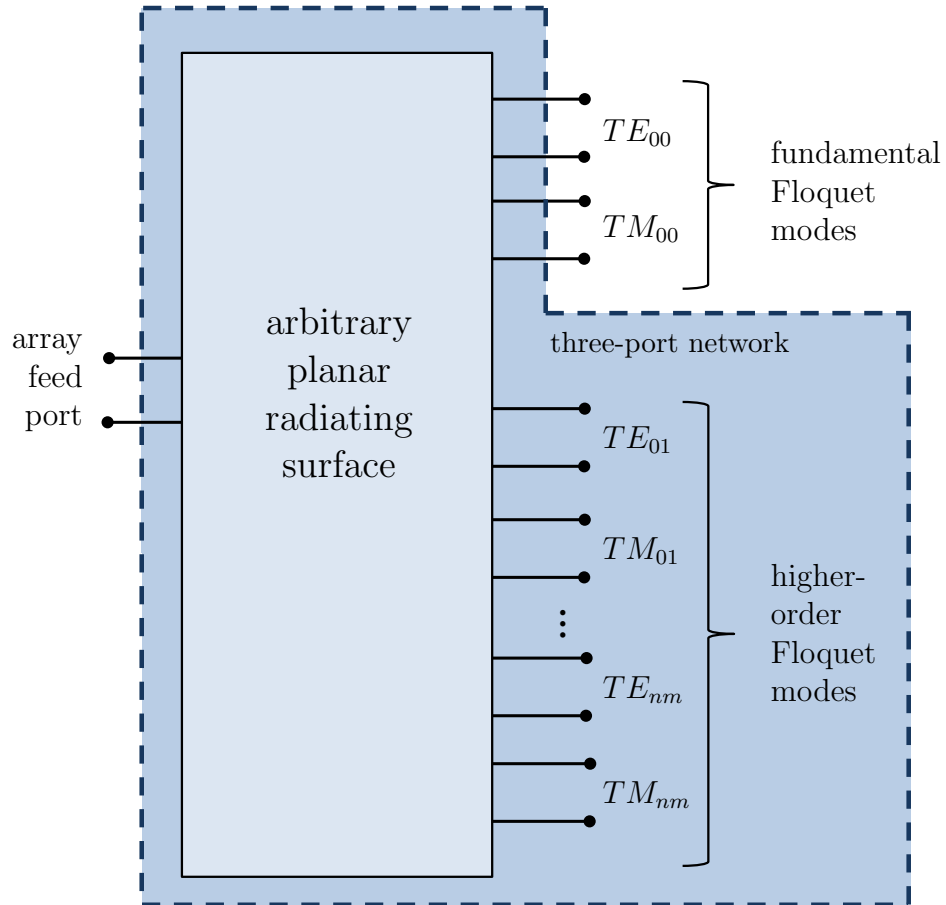
Figure 4.2: A planar radiating surface will excite a set of Floquet modes. If grating lobes are not present, all higher-order modes are evanescent and simply contribute to the reactance of the shaded network.

Floquet modes are evanescent, and if the substrate and superstrate materials are lossless, these modes cannot dissipate any real power. We may therefore collect all higher order modes and include them within the reactive network. This is depicted in Fig. 4.2 with the shaded area defining a 3-port matching network with a feed port, a fundamental TE mode port, and a fundamental TM mode port.

The characteristic impedance of the fundamental TE and TM Floquet modes is given in [100] as

$$Z_r^{TE} = \frac{\omega\mu_0\mu_r}{k_r^z}, \tag{4.1}$$

$$Z_r^{TM} = \frac{k_r^z}{\omega\epsilon_0\epsilon_r}. \tag{4.2}$$

For both modes, the propagation constant in the $\hat{z}$ direction is

$$k_r^z = k_0\sqrt{\mu_r\epsilon_r}\cos\theta_r, \tag{4.3}$$

where k_0 is the free space wavenumber, ϵ_r and μ_r are the relative material properties of each layer (i.e. substrate, superstrate, free space). The scan angle θ is measured from broadside as illustrated in Fig. 4.1, and the corresponding angle of refraction within each layer is given by $\theta_r = \sin^{-1}(\sin\theta/\sqrt{\mu_r\epsilon_r})$.

As shown by Wheeler [21], we may represent the fundamental Floquet modes with equivalent transmission lines, with impedances proportional to (4.1)-(4.2). We denote the propagation constant of each transmission line as β_r, which is equivalent to k_r^z from (4.3). Discontinuities in the $\hat{z}$ direction, such as at the ground plane, and at the superstrate-free space interface, are automatically accounted for by the transmission line properties. The resulting equivalent circuit is shown in Fig. 4.3. This equivalent

then establishes not an impedance bandwidth limit, but a gain-bandwidth limit for any PEC-backed array scanned to a particular angle.

112
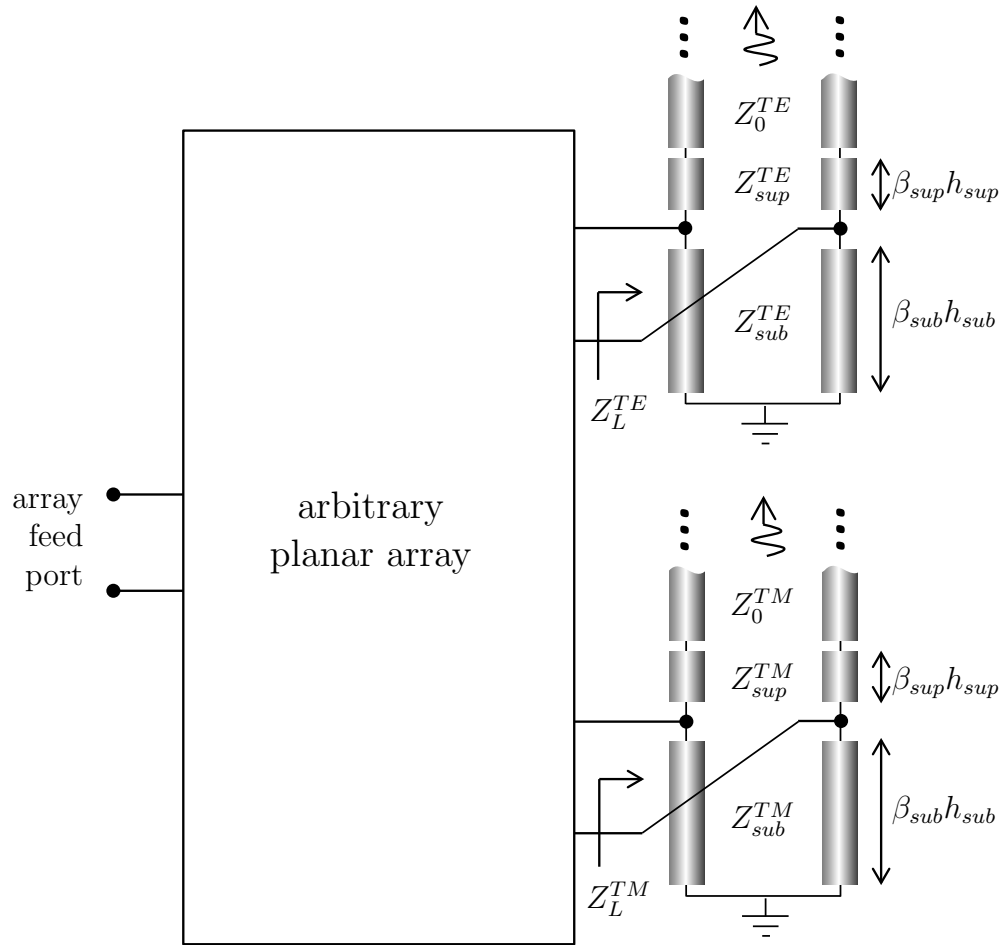
Figure 4.3: In a planar array, the TE and TM fundamental Floquet modes may be represented with transmission line circuits. The substrate, superstrate, and free space sections are represented by variations in the impedance and propagation constant of each transmission line section. The ground plane creates a short-circuit at the bottom of the substrate transmission line.

circuit is similar to those developed in [19, 101], with the exception that our model makes no assumptions about the nature of the radiating surface itself.

These transmission line circuits represent irreducible and fixed loads that describe the natural reactance of the TE and TM modes of any planar PEC-backed array with lossless materials. This equivalent network is similar to that of Fig. 3.3, but here the loads are not simple inductances, but represent the particular geometry of the planar array. As in the previous chapter, we may consider the planar radiating surface as an arbitrary matching network, with a fundamental bandwidth limit determined by the TE and TM load impedances.

4.2 Bandwidth Limits for Planar Arrays with Substrate Material Loading

We will begin by assuming the array contains some substrate material (possibly vacuum or air), and neglect the presence of a superstrate. Furthermore, we will assume the array is co-polarized with either the TE or TM Floquet mode, although the result can easily be extended to arbitrary polarization using the method developed in the previous chapter. The array can thus be modeled as a simple two-port network as shown in Fig. 4.4. The two-port network can be viewed as an impedance matching network to a load Z_L that is fixed and independent of the specific design of the planar radiating sheet. We find the impedance of the load to be

$$Z_L(j\omega) = \frac{jZ_0 Z_{sub} \tan \beta_{sub} h_{sub}}{Z_0 + jZ_{sub} \tan \beta_{sub} h_{sub}}, \tag{4.4}$$

where Z_0, Z_{sub}, and β_{sub} are given by (4.1)-(4.3).

To compute the Fano bandwidth limit for Z_L, we must first determine its transmission zeros, which are the points in the closed right-hand complex frequency plane

114
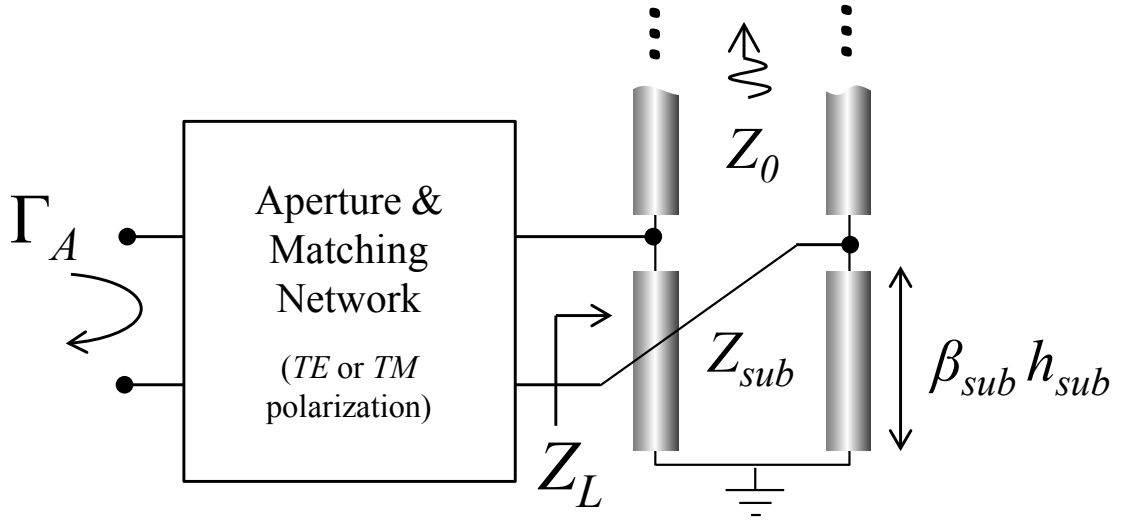
(a) Standard configuration
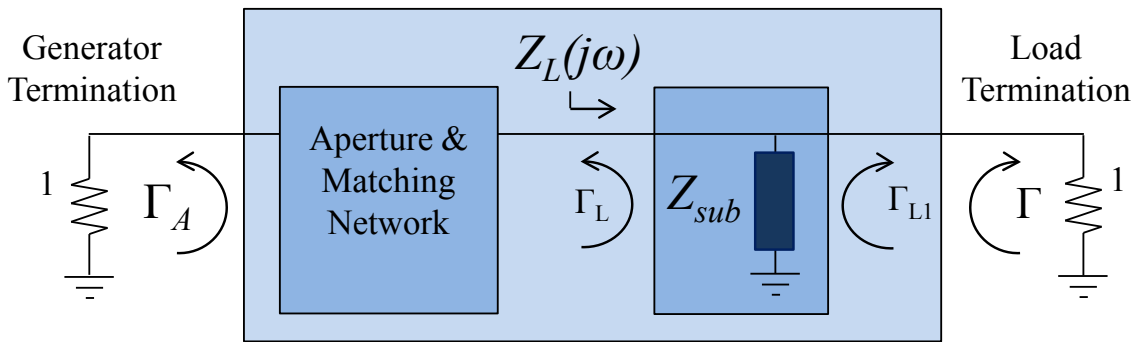
(b) Darlington configuration, with Z_0 normalized to 1Ω

Figure 4.4: Equivalent circuit for a planar array above a ground plane with no superstrate, under TE or TM excitation. Regardless of the design of the radiating surface, the load Z_L is fixed. The impedance bandwidth of the system is therefore limited by the Fano limit of Z_L.
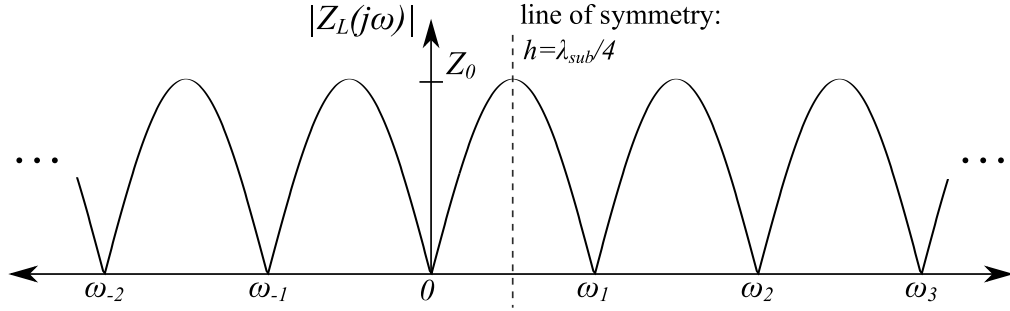
Figure 4.5: Magnitude of the impedance $Z_L(j\omega)$ seen by a planar aperture above a ground plane. $Z_L(j\omega)$ has periodic transmission zeros at multiples of half-wavelength spacing between the aperture and ground plane. Due to the symmetry of the distribution of matching constraints, the bandwidth will be maximized when the matched band is centered around $\omega_1/2$. This establishes the optimum array height to be $\lambda_{sub}^{mid}/4$.

at which no power can be delivered to the load. Whereas the general volumetric array in the previous chapter had only one known transmission zero at the origin, the planar array has one whenever $\beta_{sub}h_{sub} = m\pi$, corresponding to the periodic frequencies

$$\omega_m = \frac{m\pi c}{h\sqrt{\epsilon_{sub}\mu_{sub}}\cos\theta_{sub}}, \qquad (4.5)$$

for all integers m (see Fig. 4.5). As depicted, the principle band of interest lays between DC and the first half-wavelength resonance ω_1. We can then extend (4.4) into the full complex s-plane as,

$$Z_L(s) = \frac{Z_0 Z_{sub}\tanh(\pi s/\omega_1)}{Z_0 + Z_{sub}\tanh(\pi s/\omega_1)}. \qquad (4.6)$$

Unfortunately, because the Fano method introduces at least one non-linear equation for each additional transmission zero, calculation of the limit becomes intractable

for loads with a large number of transmission zeros[16]. However, an equivalent first-order rational impedance with only a single transmission zero can be obtained by applying a transformation from $s = \sigma + j\omega$ to a new complex frequency variable $p = \Sigma + j\Omega$,

$$\tanh(\pi s/\omega_1) \leftrightarrow p. \tag{4.7}$$

This is a type of Richards' Transformation [30], and its application to the band of interest is depicted in Fig. 4.6. The transformation $s \to p$ maps the distributed load $Z_L(s)$ in the s-domain to a first-order network $\widetilde{Z}_L(p)$ in the p-domain. The resulting impedance is rational and has only a single transmission zero at $p = 0$,

$$\widetilde{Z}_L(p) = \frac{Z_0 Z_{sub} p}{Z_0 + Z_{sub} p}. \tag{4.8}$$

The transformation (4.7) is conformal from the right hand s-plane to the right hand p-plane. Thus the analytic properties of the load on the real frequency axis are invariant under the transformation. As such, the frequency responses of $Z_L(j\omega)$ and $\widetilde{Z}_L(j\Omega)$ are identical with respect to the corresponding frequency variables, and the Fano limits may be computed in either the s- or p-domain.

However, the transformation $s \leftrightarrow p$ is not one-to-one. The lower half $[0, \omega_1/2)$ and upper half $(\omega_1/2, \omega_1]$ of the band in the s-domain are both mapped to the entire positive Ω-axis in the p-domain. Thus, the transformation is band-pass to high-pass, and valid only for the special symmetric case when the center frequency $\omega_{mid} = (\omega_{high} + \omega_{low})/2$ equals $\omega_1/2$. Nevertheless, since the distribution of the transmission zeros ω_m is also symmetric around $\omega_1/2$ (see Fig. 4.5), this special case maximizes the bandwidth of the array. For a planar array scanned to broadside ($\theta = 0$), this

---

[16]Another way of saying this is that the Fano/Youla method cannot handle distributed loads, which do not have rational impedances.

symmetry condition establishes an optimum height of $h = \lambda_{sub}^{mid}/4$, where λ_{sub}^{mid} refers to the wavelength in the substrate material at the mid-band frequency $\omega_{mid} = \omega_1/2$.

By inspecting (4.8), we see $\widetilde{Z_L}(p)$ represents a resistance Z_0 in parallel with an inductance Z_{sub}. A high-pass match to a parallel R-L load, with a maximum mismatch Γ_{max}, has a minimum cutoff frequency given by (2.59),

$$\Omega_{min} = \frac{R}{\pi L} \log \frac{1}{|\Gamma_{max}|}. \tag{4.9}$$

Assuming normal incidence ($\theta = \theta_{sub} = 0$), we obtain

$$\Omega_{min} = \frac{Z_0}{\pi Z_{sub}} \log \frac{1}{|\Gamma_{max}|} = \frac{\sqrt{\epsilon_{sub}/\mu_{sub}}}{\pi} \log \frac{1}{|\Gamma_{max}|}. \tag{4.10}$$

From (3.75) or (3.76) we may obtain the corresponding cutoff frequency for finite-order or lossy matching,

$$\Omega_{min} = K_n \sqrt{\epsilon_{sub}/\mu_{sub}}. \tag{4.11}$$

The corresponding frequency ω_{low} is determined by transforming Ω_{min} back to the s-domain from (4.7), giving

$$\omega_{low} = \arctan(\Omega_{min})\omega_1/\pi. \tag{4.12}$$

Also, via symmetry

$$\omega_{high} = \omega_1 - \omega_{low}. \tag{4.13}$$

Thus, the maximum bandwidth of an nth order planar array above a ground plane at broadside is given by

$$B_n^{planar} \leq \frac{-2 + \frac{\pi}{\arctan(K_n\sqrt{\epsilon_{sub}/\mu_{sub}})}}{\sqrt{-1 + \frac{\pi}{\arctan(K_n\sqrt{\epsilon_{sub}/\mu_{sub}})}}}. \tag{4.14}$$

The corresponding expression for the bandwidth ratio is somewhat simpler,

$$BR_n^{planar} \leq -1 + \frac{\pi}{\arctan(K_n\sqrt{\epsilon_{sub}/\mu_{sub}})}. \tag{4.15}$$

(a) Complex s-plane

(b) Complex p-plane

(c)

(d)
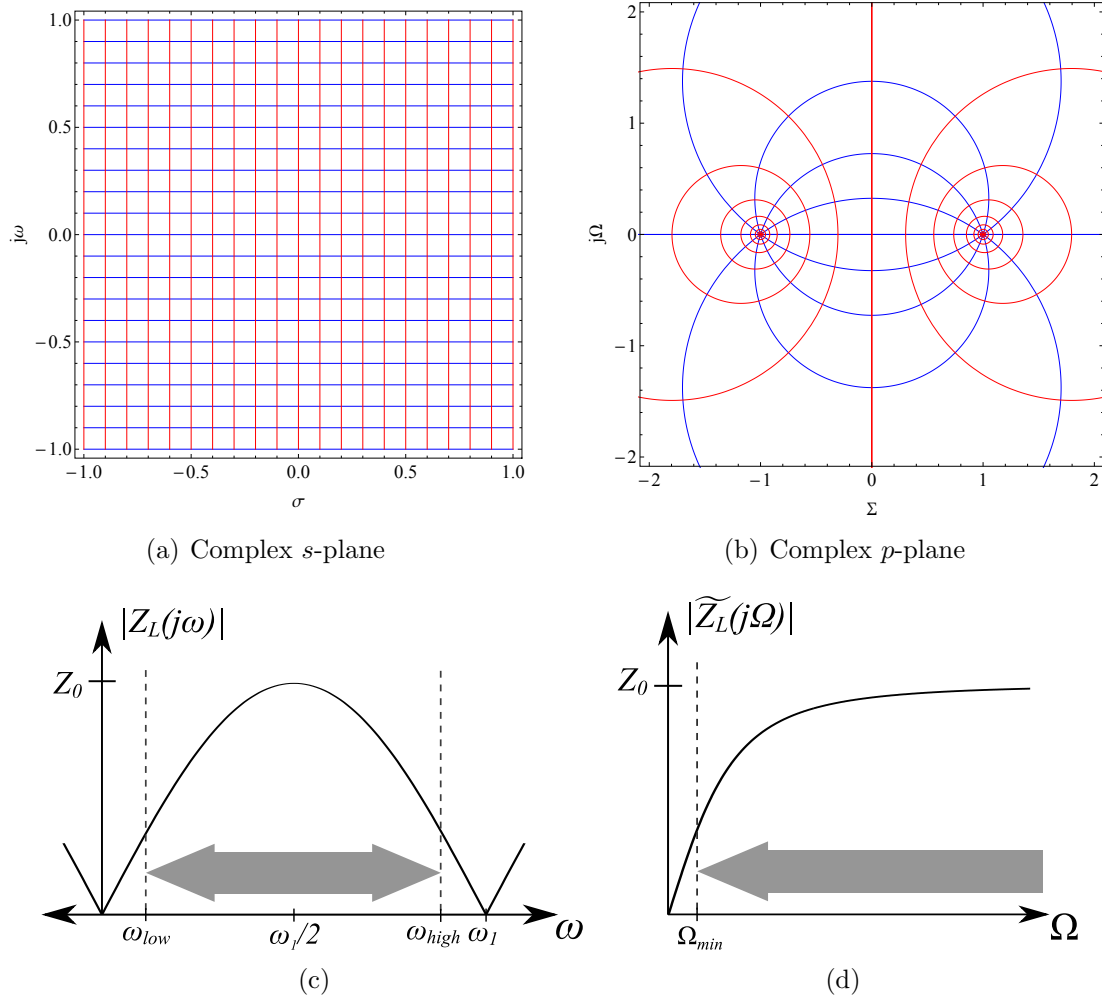
Figure 4.6: Illustration of the conformal mapping used to analyze the planar array. (a) Map of the complex s-plane, with grid showing of constant σ and ω. (b) Grid from (a) mapped to the complex p-plane. (using $\omega_1 = 1$) (c) Magnitude of load impedance in s-domain with band-pass edges ω_{low} and ω_{high} located symmetrically around $\omega_1/2$. (d) Magnitude of load impedance in p-domain, with low-pass cutoff frequency Ω_{min}. The transformation maps both ω_{low} and ω_{high} to Ω_{min}, and $\omega_1/2$ to $\Omega = \infty$.
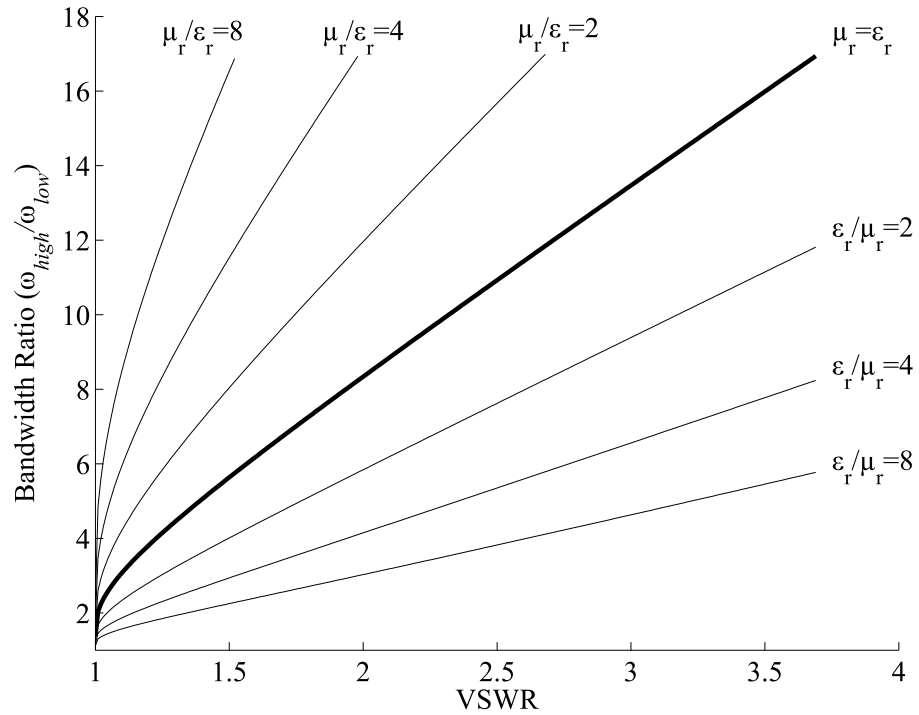
Figure 4.7: Maximum realizable bandwidth for an infinite-order planar array above a PEC-ground with lossless substrate material, scanned to broadside with constant polarization. This limit can be attained only if the radiating surface is placed a quarter-wavelength from the ground plane at mid-band.
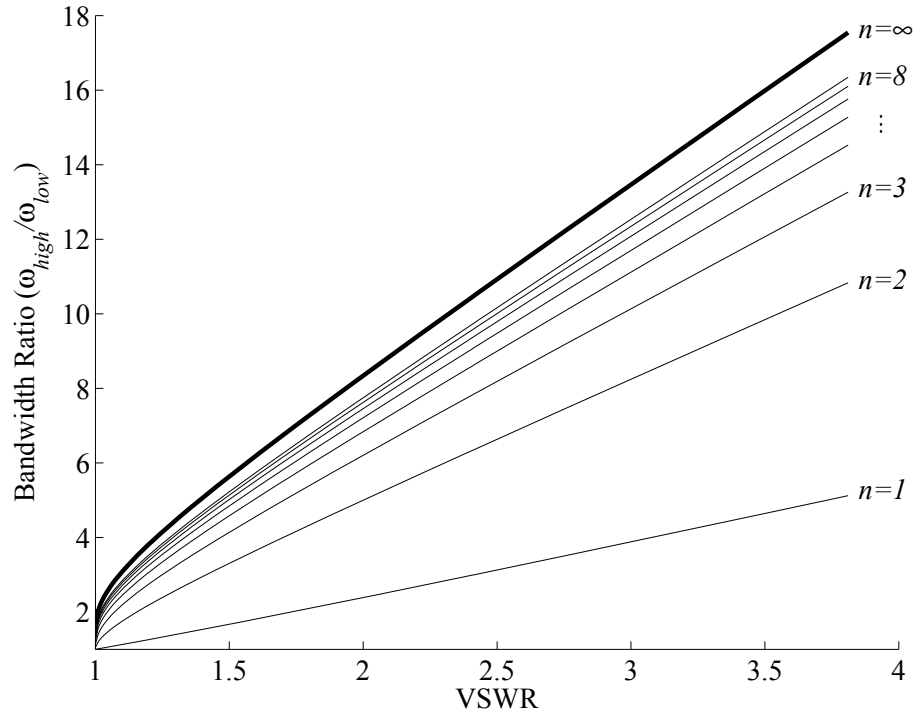
Figure 4.8: Maximum bandwidth for an nth order lossless planar array above a PEC-ground with air substrate ($\epsilon_{sub} = \mu_{sub} = 1$), scanned to broadside with constant polarization. The overall order of the array is one more than the order of the radiating surface itself.

From the above, an infinite-order planar array with air substrate $(\epsilon_{sub} = \mu_{sub} = 1)$ has a maximum bandwidth of $\sim$8.3:1 (VSWR $\leq$ 2:1). This limit can be reached only if $k_{mid}h = \pi/2$. The corresponding bandwidth limit for a volumetric array of the same height can be found from (3.74) and is $\sim$9.1:1 (using $hk_{low} = hk_{mid}2/(BR+1) = \pi/(BR+1)$). Therefore, despite its simple form, a planar array of optimal height is capable of nearly as much bandwidth as a general volumetric or multi-layer array of the same total height. However, for taller arrays, the bandwidth of an arbitrary PEC-backed array may continue to increase, while the bandwidth of the planar array will be reduced (as ω_{high} nears ω_1). The 8.3:1 limit is therefore fundamental for single layer planar arrays and can only be improved using material loading or by relaxing the matching tolerance. A plot of BR_{∞}^{planar} vs. VSWR is given in Fig. 4.7 for various dielectric and magnetic substrates. This demonstrates the well known result that dielectric substrates reduce bandwidth, whereas magnetic substrates can significantly increase the bandwidth of arrays [37].

The finite-order limits are plotted in Fig. 4.8 for $\epsilon_{sub} = \mu_{sub} = 1$, i.e. no materials used. We note that for arrays of finite complexity, the total order of the array is one more than the order of the radiating surface. This is because $\widetilde{Z_L}$ is itself a 1st order network. As an example, the Tightly Coupled Dipole Array (TCDA) has a planar radiating surface that can be approximated by a first-order L-C circuit. Thus, the total order of the TCDA is $n = 2$. Its maximum bandwidth given by (4.15) is therefore 5:1 when matched to VSWR $\leq$ 2:1. This is consistent with published results, where a bandwidth limit of 4.5:1 for TCDAs without material loading has been determined empirically [19], [38].

4.2.1 Bandwidth Limits for Low Profile and Scanning Planar Arrays

For a planar array matched to a fixed frequency band, the optimal symmetry condition of $\omega_{mid} = \omega_1/2$ cannot be maintained while scanning, because ω_1 varies with scan angle. Likewise, this symmetry is broken for arrays with $h \neq \lambda_{sub}^{mid}/4$. Therefore, electrically thin and/or scanning planar arrays will have reduced bandwidth and (4.14) will no longer provide a tight limit (although if substrate loading is used, the bandwidth may increase when scanning in the TM direction). For such arrays, numerical techniques can be used to compute the actual bandwidth limit [102].

However, under certain conditions, an improved closed-form limit may be computed by disregarding matching constraints that do not contribute significantly to the result. In general, the constraint imposed by a transmission zero is reduced as the frequency band moves further from the location of the zero. Specifically, if the scan angle is large or the array is thin, such that

$$\beta_{sub}^z h_{sub} \ll \pi, \tag{4.16}$$

then ω_1 is far from the band of interest, and its effects (as well as those of the higher transmission zeros) on the bandwidth limit are minimal. Under these conditions, the bandwidth limit is dominated by the transmission zero at DC, and the reflection coefficient Γ_W is given by (3.1) or (3.2). In this case, both μ_r and ϵ_r are known and represent the actual substrate material properties. Following the same process as in Chapter 3, the TE and TM limits for low profile scanning planar arrays are given by

$$B_n^{planar,TE}(\theta, h) \leq \frac{k_0 h \mu_r \cos\theta}{K_n}, \tag{4.17}$$

$$B_n^{planar,TM}(\theta, h) \leq \frac{k_0 h(\mu_r - \epsilon_r^{-1}\sin^2\theta)}{K_n \cos\theta}. \tag{4.18}$$

Because (4.17) and (4.18) were obtained by removing matching constraints, they overestimate the realizable bandwidth. As upper bounds, they are therefore valid for all h and θ, but only become tight limits under the condition of (4.16). If the array is required to scan to an angle of θ from normal in all directions, the overall bandwidth limit is given by the minimum of (4.14) and (4.17). For an infinite-order array with air substrate matched to VSWR $\leq$ 2:1, (4.17) will provide a tighter bound than (4.14) whenever $h \cos\theta \leq 0.229\lambda_{mid}$.

Note that if the substrate material is air ($\epsilon_r = \mu_r = 1$), then (4.17) and (4.18) are equivalent and the limit does not depend on polarization. This differs from the limits for arbitrary volumetric arrays, in that TM polarization does not yield wide bandwidths at large scan angles. This is because wide angle TM scanning requires vertical currents (see Fig. 3.6), which are not present in planar arrays.

4.3 Bandwidth Limits for Planar Arrays with Superstrate Material Loading

We now consider the effects of adding a superstrate material layer on top of the radiating planar surface. Whereas dielectric substrates reduce bandwidth, it is known that dielectric superstrates can improve bandwidth [19]. The superstrate adds a length of transmission line in series between the array and the free space termination, and can be viewed as a quarter wave transformer. The corresponding equivalent circuit is shown in Figure 4.9.

The load impedance for the circuit in Fig. 4.9 is given by

$$Z_{L,SS}(j\omega) = \frac{1}{\frac{1}{jZ_{sub}\tan(\beta_{sub}h_{sub})} + \frac{1}{Z_{sup}\frac{Z_0+jZ_{sup}\tan(\beta_{sup}h_{sup})}{Z_{sup}+jZ_0\tan(\beta_{sup}h_{sup})}}}. \tag{4.19}$$
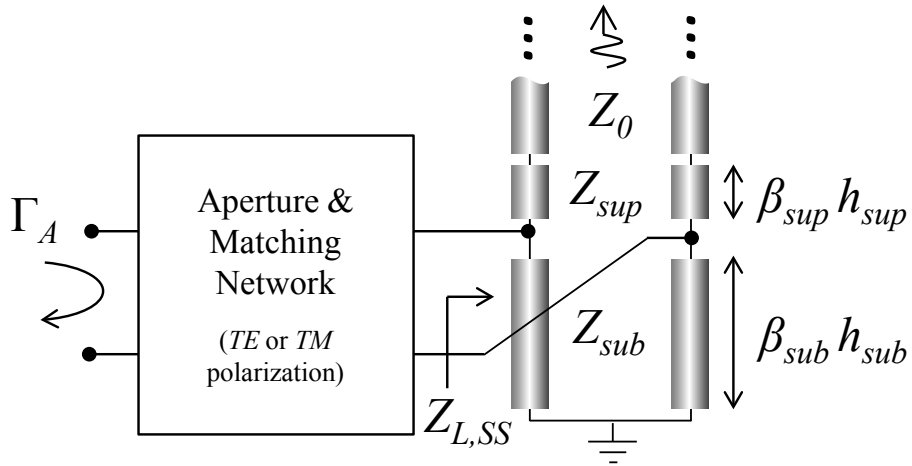
(a) Standard configuration
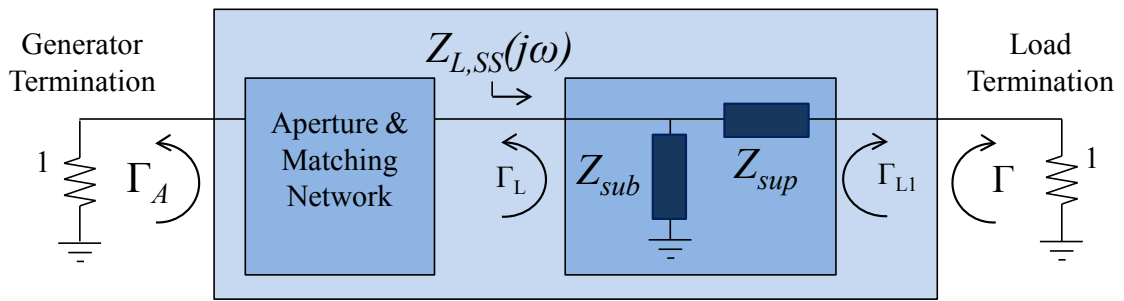
(b) Darlington representation, with Z_0 normalized to 1Ω

Figure 4.9: Equivalent circuit for a planar array above a ground plane with a lossless superstrate material slab. The load to be matched, $Z_{L,SS}$, now contains a series section of transmission line representing the superstrate.
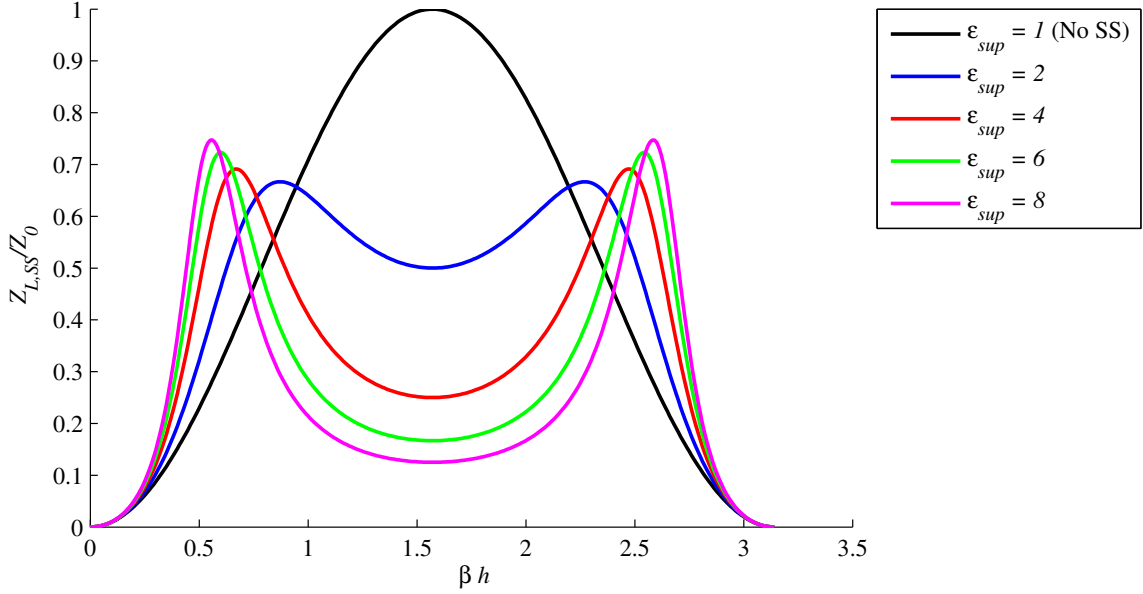
Figure 4.10: Magnitude of load impedance $|Z_{L,SS}|$ for superstrates of various dielectric constants. $Z_{sub} = Z_0$ and $\beta_{sub}h_{sub} = \beta_{sup}h_{sup}$.

An example plot of $|Z_{L,SS}(j\omega)|$ is provided in Fig. 4.10. The superstrate acts as a quarter-wave matching section, lowering the effective radiation resistance, and increasing the natural bandwidth of the load. Because the bandwidth is maximized when this quarter-wave match is centered at mid-band $(\omega_1/2)$, the optimal superstrate height is given by

$$\beta_{sup}h_{sup} = \beta_{sub}h_{sub} = \pi\omega/\omega_1. \tag{4.20}$$

Under this condition, both transmission line sections have equal electrical length, and we may apply the conformal map (4.7). After normalizing to $Z_0 = 1$ and simplifying, we obtain

$$\widetilde{Z_{L,SS}}(p) = \frac{Z_{sub}Z_{sup}^2 p^2 + Z_{sub}Z_{sup}p}{Z_{sub}p^2 + (Z_{sup}^2 + Z_{sub})p + Z_{sup}}. \tag{4.21}$$

126

The impedance is now represented as a rational polynomial, and we determine the bandwidth limits from the Fano/Youla method. In order to determine the transmission zeros of the load, we compute the functions $r(p)$ and $F(p)$ from (2.67) and (2.70),

$$r(p) = \frac{p^2 Z_{sub}^2 Z_{sup}(p^2 Z_{sup} - 1)}{\left(p^2 Z_{sub} + Z_{sup} - p(Z_{sub} + Z_{sup}^2)\right)\left(p^2 Z_{sub} + Z_{sup} + p(Z_{sub} + Z_{sup}^2)\right)}, \qquad (4.22)$$

$$F(p) = \frac{4p^2(p^2 - 1)Z_{sub}^2 Z_{sup}^2}{p^2 Z_{sub}(1 + Z_{sup}^2))^2 + p Z_{sup}(2Z_{sub} + Z_{sup}) + Z_{sup}}. \qquad (4.23)$$

The transmission zeros are then given by the RHP zeros of $F(p)$. As before, there is a transmission zero at the origin corresponding the the short circuit from the ground plane[17]. However, the introduction of the superstrate creates another transmission zero at $p = 1$. This zero is not due to the load impedance becoming either a short-circuit or open-circuit, but is mapped from the complex infinity point in the s-plane under (4.7), as seen in Fig. 4.6b. Therefore, this transmission zero corresponds to infinite electrical length (and infinite attenuation) in the superstrate. Therefore at $p = 1$ ($s \to \infty$), the radiation resistance is completely decoupled from the matching network, and referring to Fig. 4.9, the reflection coefficient Γ must equal Γ_{L1}.

Because $\widetilde{Z_{L,SS}}(p)$ has two transmission zeros, calculation of the Fano/Youla limit from (2.49) will involve multiple constraints that must be satisfied simultaneously. Following the process defined in Section 2.4, we first determine the reflection coefficient $\Gamma_{L1}(p)$ seen from the unit resistance of the load when the matching network is replaced by a unit resistance (*c.f.* Fig. 4.9b),

$$\Gamma_{L1}(p) = \frac{(Z_{sub}Z_{sup}^2 - Z_{sub})p^2 + Z_{sup}^2 p - Z_{sup}}{(Z_{sub}Z_{sup}^2 + Z_{sub})p^2 + (Z_{sup}^2 + 2Z_{sub}Z_{sup})p + Z_{sup}}. \qquad (4.24)$$

[17]Note that double zeros of $F(p)$ on the $j\Omega$ axis are treated as single transmission zeros [64].

For the simple transmission zero at $p = 0$, we must compute the the first two terms of the Taylor series of the functions $\log 1/\Gamma_{L1}(p)$, $\log 1/\eta(p)$, $\Psi(p, \xi)$ around the point $p = 0$. Since bandwidth is maximized for an all pass $\eta(p)$ with the fewest zeros that still satisfies the Fano constraints, we may assume that $\eta(p)$ has at most a single real zero at $p = \Sigma_0 > 0$. Since $\eta(p)$ must also satisfy (2.41) at the origin, we also set $\eta(0) = -1$. We therefore obtain

$$\log 1/\Gamma_{L1}(p) = j\pi + 2(Z_{sub} + Z_{sup})p + \mathcal{O}(p^2), \tag{4.25}$$

$$\log 1/\eta(p) = j\pi + \frac{2}{\Sigma_0}p + \mathcal{O}(p^2), \tag{4.26}$$

$$\Psi(p, \xi) = 0 + \frac{2}{\pi\xi^2}p + \mathcal{O}(p^2), \quad \text{as } p \to 0. \tag{4.27}$$

Plugging the above into (2.42) and (2.49) yields the first fundamental constraint for the system

$$\frac{2}{\pi} \int_0^\infty \frac{\log 1/|\Gamma(j\xi)|}{\xi^2} d\xi \leq 2(Z_{sub} + Z_{sup}) - \frac{2}{\Sigma_0}. \tag{4.28}$$

For the transmission zero at $p = 1$, we only require the first (constant) term of the Taylor series,

$$\log 1/\Gamma_{L1}(p = 1) = \log \frac{Z_{sup} + 1}{Z_{sup} - 1}, \tag{4.29}$$

$$\log 1/\eta(p = 1) = \log \frac{1 + \Sigma_0}{1 - \Sigma_0}, \tag{4.30}$$

$$\Psi(p = 1, \xi) = \frac{2}{\pi(1 + \xi^2)}. \tag{4.31}$$

Substituting this into (2.40) and (2.49) yields the second fundamental constraint for the system,

$$\frac{2}{\pi} \int_0^\infty \frac{\log 1/|\Gamma(j\xi)|}{1 + \xi^2} d\xi = \log \frac{Z_{sup} + 1}{Z_{sup} - 1} - \log \frac{1 + \Sigma_0}{1 - \Sigma_0}. \tag{4.32}$$

Equations (4.28) and (4.32) are fundamental limits for the impedance match (in the p-domain) of any physically realizable planar array with a superstrate. The constant Σ_0 may be any non-negative number which satisfies both equations. However,

128

in their present form, these limits are not particularly convenient. We may simplify things somewhat by assuming that the array has an ideal bandpass rectangular (infinite order) match on the $j\omega$-axis, with maximum mismatch of Γ_{max}. In the p-domain, this maps to a high-pass response with a low end cutoff frequency of Ω_{min}. The integrals in (4.28) and (4.32) can then be evaluated, resulting in

$$\frac{\log 1/|\Gamma_{max}|}{\pi \Omega_{min}} \leq (Z_{sub} + Z_{sup}) - \frac{1}{\Sigma_0}, \tag{4.33}$$

$$\frac{2}{\pi} \log 1/|\Gamma_{max}| \arctan \frac{1}{\Omega_{min}} = \log \frac{Z_{sup} + 1}{Z_{sup} - 1} - \log \frac{1 + \Sigma_0}{1 - \Sigma_0}. \tag{4.34}$$

We may make several observations regarding the above results. Since the left side of (4.34) is real, the arguments of the log functions on the right hand side must either both be positive or both negative. Thus, $Z_{sup} < 1$ implies $\Sigma_0 > 1$, and $Z_{sup} > 1$ implies $\Sigma_0 < 1$ ($Z_{sup} = 1$ is the degenerate case without any superstrate, which was addressed previously). From (4.33), we see that Ω_{min} is generally reduced as Σ_0 is increased, which corresponds to increased bandwidth. Therefore, dielectric superstrates therefore will generally have superior bandwidth to magnetic superstrates (the opposite result as found from substrate loading), and we will primarily concern ourselves with the former.

To avoid carrying around the resulting $j\pi$ terms, we may negate the arguments of both of the log functions. Also, for convenience we refer to (3.75) and denote $(\log 1/|\Gamma_{max}|)/\pi$ as K_∞[18]. Solving for Ω_{min}, we obtain

$$\Omega_{min} \geq \frac{K_\infty}{(Z_{sub} + Z_{sup} - 1/\Sigma_0)}, \tag{4.35}$$

$$\Omega_{min} = 1/\tan\left[\frac{1}{2K_\infty}\left(\log \frac{1 + Z_{sup}}{1 - Z_{sup}} - \log \frac{\Sigma_0 + 1}{\Sigma_0 - 1}\right)\right]. \tag{4.36}$$

[18]Note that we may not apply the finite matching values for K_n, since the limit no longer depends only on a single transmission zero, and the solution from [80] does not apply.
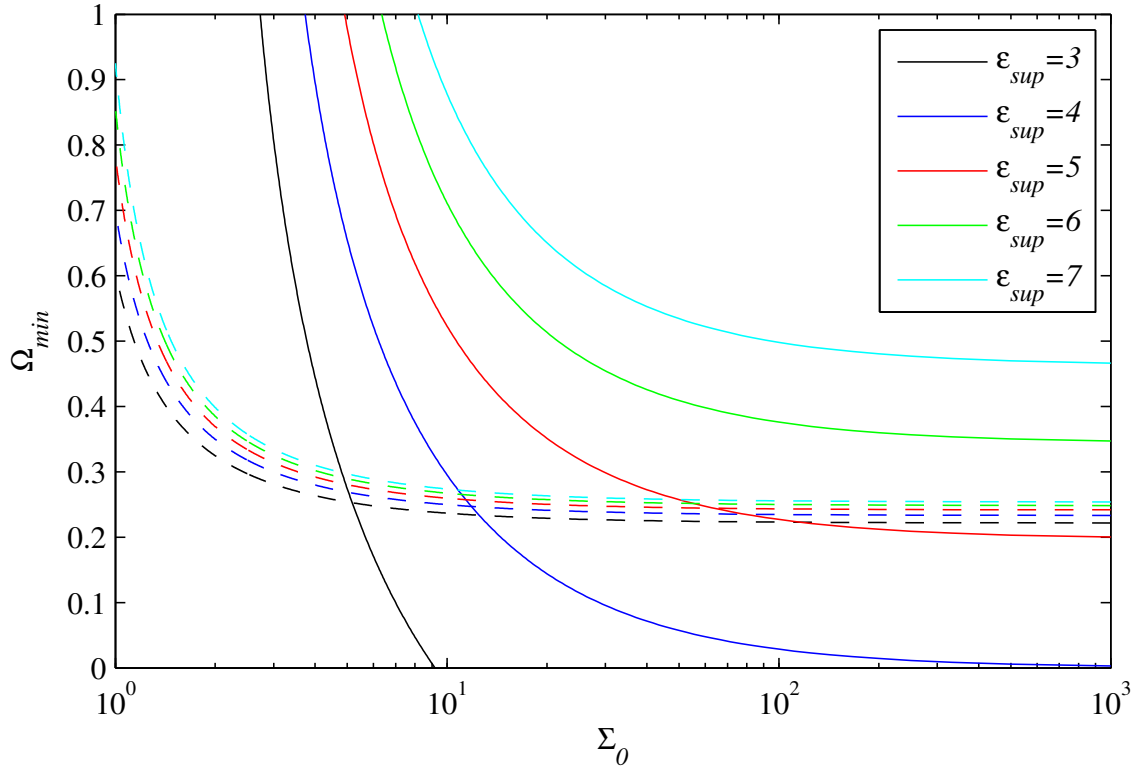
Figure 4.11: Matching constraints for various superstrate dielectric constants vs. Σ_0. Dotted lines depicts lower bound of (4.35), and solid lines depict (4.36). A valid match for a given superstrate must lie on the solid line and above the dashed line. Plot is for air substrate and VSWR=2 ($|\Gamma_{max}| = 1/3$).

The behavior of these constraints can be seen in Fig. 4.11, where each color represents a choice of superstrate dielectric. The lower bound on Ω_{min} from (4.35) is given by the dashed line, and the equation (4.36) is given by the solid line. Both curves asymptotically approach a constant as $\Sigma_0 \to \infty$, which is the minimum phase solution. For superstrates with larger dielectric constants, the curves never intersect, and the bandwidth will be set by the minimum phase solution of (4.36). For superstrates with lower dielectric constants, the curves do intersect, and the maximum bandwidth (smallest Ω_{min}) requires solving for Σ_0 at the point of intersection.

The maximum possible bandwidth for any choice of superstrate occurs when both curves share the same asymptote and intersect in the limit as $\Sigma_0 \to \infty$. From (4.35), the lowest possible Ω_{min} for an optimal choice of superstrate is therefore given by

$$\Omega_{min,opt} = \frac{K_\infty}{Z_{sub} + Z_{sup}}. \tag{4.37}$$

From (4.12)-(4.13), we then can compute the corresponding maximum bandwidth in the s-domain for a superstrate loaded planar array with optimal choice of superstrate dielectric is

$$BR_\infty^{SS,opt} = -1 + \pi \left[\arctan \frac{K_\infty}{Z_{sub} + Z_{sup}} \right]^{-1}. \tag{4.38}$$

Examining Fig. 4.11, the superstrate for which this bandwidth is possible occurs for a dielectric constant just above 5 (with an air substrate and mismatch of VSWR=2). The exact optimal dielectric constant may be expressed analytically by equating (4.35) and (4.36), with $\Sigma_0 \to \infty$. The result is a single transcendental equation which can be solved (numerically) for the optimal superstrate ϵ_{opt},

$$\arctan \left[\frac{1}{K_\infty} \left(\sqrt{\frac{\mu_{sub}}{\epsilon_{sub}}} + \sqrt{\frac{1}{\epsilon_{opt}}} \right) \right] = \frac{1}{2K_\infty} \log \frac{\sqrt{\epsilon_{opt}} + 1}{\sqrt{\epsilon_{opt}} - 1}. \tag{4.39}$$

For air substrate and mismatch of VSWR=2, the optimal superstrate ϵ_{opt} is 5.29, and the corresponding maximum bandwidth from (4.38) is 12.14:1.
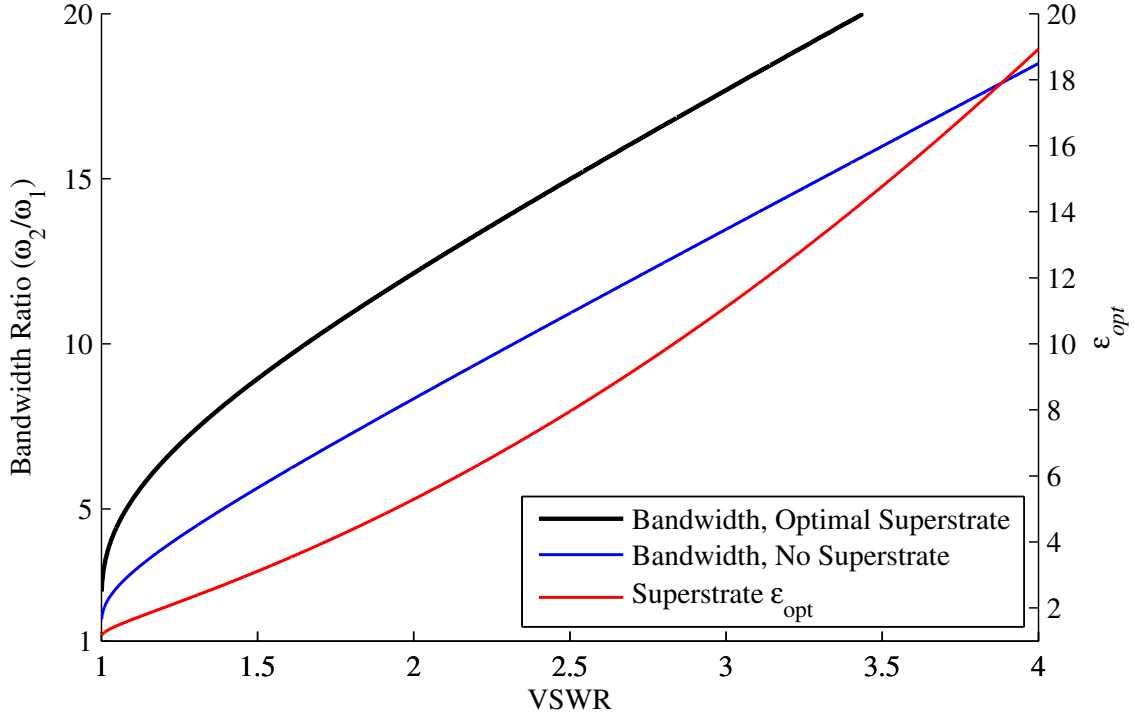
Figure 4.12: Bandwidth limits for a planar array with and without superstrate material loading. The superstrate bandwidth assumes the superstrate dielectric constant is optimal, computed from (4.39).

.

Technically, (4.38) is valid so long as $\epsilon_{sup} \geq \epsilon_{opt}$, however we will show that increasing the dielectric constant above ϵ_{opt} results in a dramatic reduction in bandwidth. For a superstrate with $\epsilon_{sup} < \epsilon_{opt}$, a closed form solution of (4.35)-(4.36) is not available. However, they may be solved numerically, with the resulting bandwidth shown in Fig. 4.13 as a function of VSWR, and in Fig. 4.14 as a function of superstrate dielectric constant.
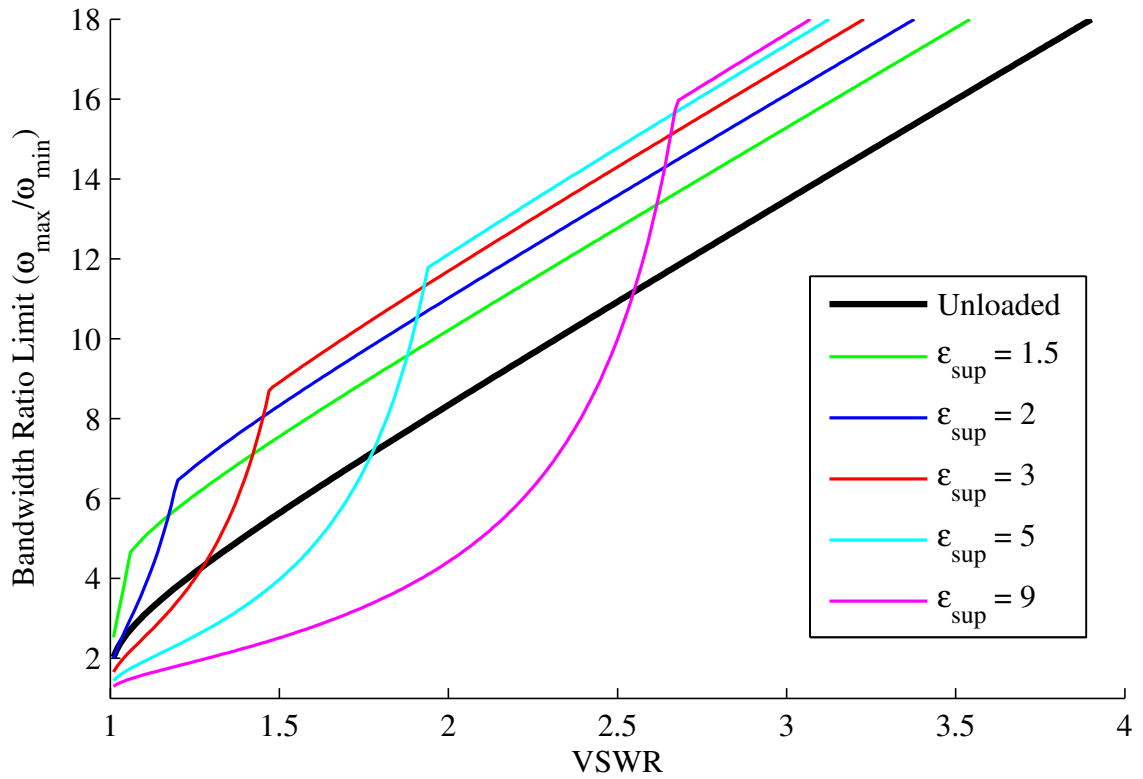
Figure 4.13: Bandwidth limits for a planar array with superstrate material loading, plotted as a function of VSWR. The upper bound traced out by this family of curves corresponds to the optimal superstrate bandwidth limit shown in Fig. 4.12. Substrate material is assumed to be air. Limits are for broadside scanning and for superstrate and substrate each quarter-wavelength at mid-band.
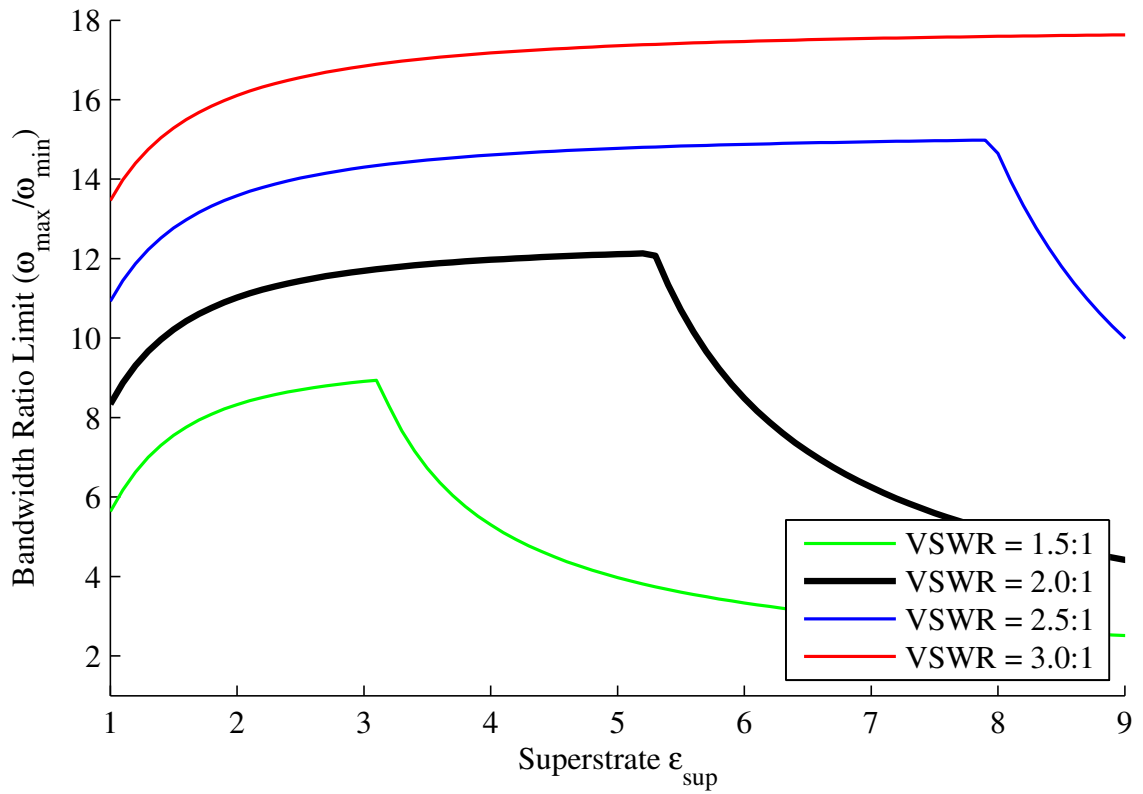
Figure 4.14: Bandwidth limits for a planar array with superstrate material loading, plotted as a function of superstrate dielectric constant. Substrate material is assumed to be air. Limits are for broadside scanning and for superstrate and substrate each quarter-wavelength at mid-band.

4.3.1 Finite Order Matching for Superstrate-Loaded Planar Arrays

In order to determine the matching limits for a finite-order superstrate-loaded planar array, we must consider the response not of a perfectly rectangular frequency response, but of a fixed-order Chebyshev rational polynomial. Previously, for the arbitrary array and planar array with substrate loading, this was straightforward and simply required substitution of the quantity K_n, given by (3.75)-(3.76). This result is from [80] and represents an approximate solution of Fano's transcendental equations from [6]. Until now, we have been able to apply this method because we were working with loads with only a single transmission zero on the $j\omega$-axis. However, because the superstrate-loaded array has two transmission zeros in the p-domain, Fano's solution for finite-order matching does not apply.

However, we may compute the finite-order limits for loads with multiple transmission-zeros using a similar method. For the finite-order limits, the matching coefficients used in the constraints (2.40)-(2.44) do not arise from a dispersion relation integral, but are rather taken directly from the Chebyshev rational polynomial. We define the reflection coefficient for an nth order high-pass network with cutoff frequency Ω_{min} as $\Gamma_n(p, \Omega_{min})$. The poles and zeros of this function are given by [6],

$$p_m = \begin{cases} \Omega_{min}/\sinh\left(-a \pm j\frac{\pi(m+1/2)}{n}\right), & n \text{ even}, \\ \Omega_{min}/\sinh\left(-a \pm j\frac{\pi m}{n}\right), & n \text{ odd}, \end{cases} \tag{4.40}$$

$$r_m = \begin{cases} \Omega_{min}/\sinh\left(-b \pm j\frac{\pi(m+1/2)}{n}\right), & n \text{ even}, \\ \Omega_{min}/\sinh\left(-b \pm j\frac{\pi m}{n}\right), & n \text{ odd}. \end{cases} \tag{4.41}$$

For a minimum phase response, $a > b > 0$ and m is an integer with $-\lfloor n/2 \rfloor \le m \le \lceil n/2 \rceil - 1$. The maximum reflection coefficient Γ_{max} within the band is given by

$$\Gamma_{max} = \frac{\cosh nb}{\cosh na}. \tag{4.42}$$

135

Fano also provided a condition that specifies the optimal ripple such that Γ_{max} is minimized within the band [6],

$$\frac{\tanh na}{\cosh na} = \frac{\tanh nb}{\cosh nb}. \tag{4.43}$$

In the case of a single transmission zero at the origin, the quantity A_1^0 is computed as

$$A_1^0 = \sum_m \frac{1}{p_m} - \sum_m \frac{1}{r_m} = \frac{1}{\Omega_{min}} \frac{\sinh a - \sinh b}{\sin \pi/2n}. \tag{4.44}$$

The bandwidth limits are then computed from (2.42) while also satisfying (4.42)-(4.43). This is difficult to do in closed form as it requires the solution of several simultaneous transcendental equations. It can either be solved numerically, or good closed form approximate solutions such as in [80] may be used.

For the superstrate-loaded array, the additional transmission zero imposes a restriction not only at the origin, but also at $p = 1$. We must therefore also compute the coefficient A_0^1, i.e.,

$$A_0^1 = \log \Gamma_n(1, \Omega_{min}). \tag{4.45}$$

Therefore, from (2.40) and (2.42), the finite-order matching constraints for the superstrate-loaded array are

$$\frac{1}{\Omega_{min}} \frac{\sinh a - \sinh b}{\sin \pi/2n} \leq 2(Z_{sub} + Z_{sup}) - \frac{2}{\sigma_0}, \tag{4.46}$$

$$\log \Gamma_n(1, \Omega_{min}) = \log \frac{Z_{sup} + 1}{Z_{sup} - 1} - \log \frac{1 + \sigma_0}{1 - \sigma_0}. \tag{4.47}$$

These equations must be solved along with the constraints (4.42)-(4.43) which define the mismatch and optimal ripple. Although a closed-form solution is not apparent, a numerical solution is not difficult. The result for air substrate and VSWR$\leq$2:1 ($\Gamma_{max} = 1/3$) is plotted in Fig. 4.15. Note that the optimal dielectric constant ϵ_{opt}
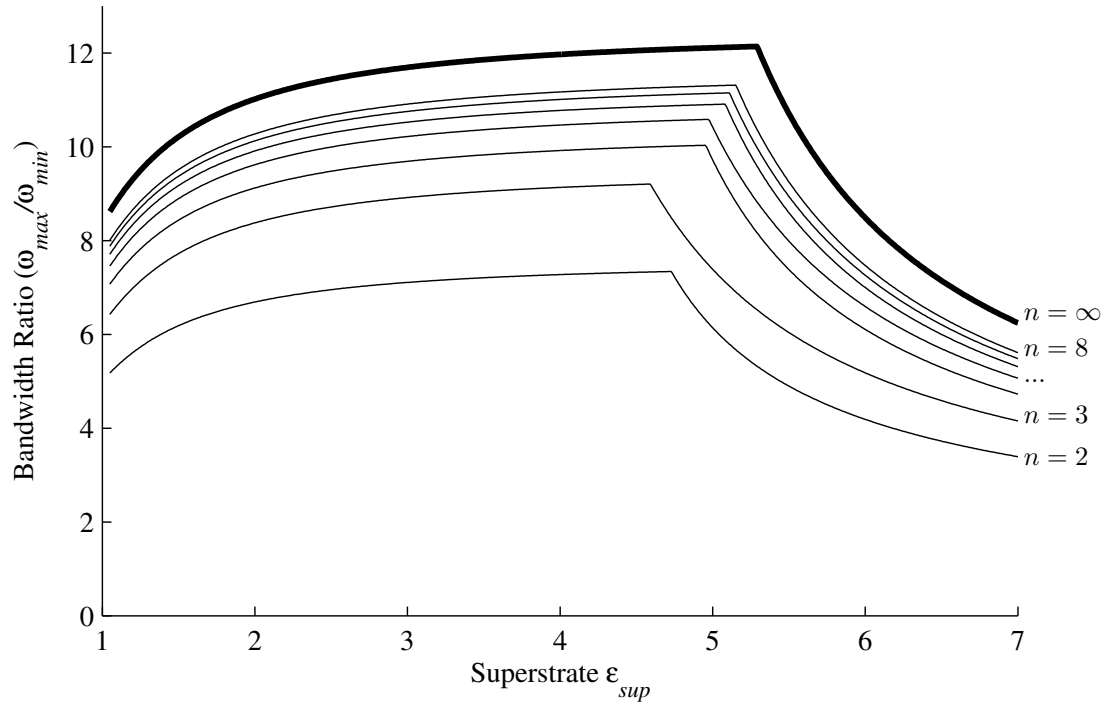
Figure 4.15: Bandwidth limits for a finite-order planar array with superstrate material loading, plotted as a function of superstrate dielectric constant. Substrate material is assumed to be air, and VSWR≤2:1. Limits are for broadside scanning and for superstrate and substrate each quarter-wavelength at mid-band. The effective order of the array is noted for each curve.

depends on the overall order of the array, and that ϵ_{opt} is slightly lower when the order is odd, and slightly higher with the order is even.

4.3.2   Empirical Verification of Bandwidth Limits

The development of bandwidth limits for planar arrays has required several rather abstract mathematical techniques. It may therefore be useful to check the accuracy of the result through empirical means. We may do this simply by designing an optimal matching network of a given order for the equivalent load, and measuring the resulting bandwidth. Such a network is shown in Fig. 4.16, which represents a superstrate-loaded planar array with a 3rd order matching network constructed from open-circuited and short-circuited quarter-wave stubs. Because the substrate and superstrate themselves comprise two additional stages, the total order of the array is $n = 5$. For a range of superstrate dielectric constants, the matching circuit was optimized for maximum bandwidth in *AWR Microwave Office* using a genetic algorithm. The results are depicted in Fig. 4.17, along with the 5th order and infinite order limits. Our empirical results appear to be consistent with the theoretical limits, lending confidence to the preceding analytical analysis.

TLOC2
ID=TL4
Z0=Zm3 Ohm
EL=90 Deg
F0=2500 MHz

TLOC2
ID=TL5
Z0=Zm1 Ohm
EL=90 Deg
F0=2500 MHz

PORT
P=2
Z=Z0 Ohm

TLIN
ID=TL1
Z0=Zss Ohm
EL=90 Deg
F0=2500 MHz

PORT
P=1
Z=Zport Ohm

TLIN
ID=TL3
Z0=Zm2 Ohm
EL=90 Deg
F0=2500 MHz

TLIN
ID=TL2
Z0=Z0 Ohm
EL=90 Deg
F0=2500 MHz

3rd order matching network

Floquet mode equivalent circuit
(substrate and superstrate)
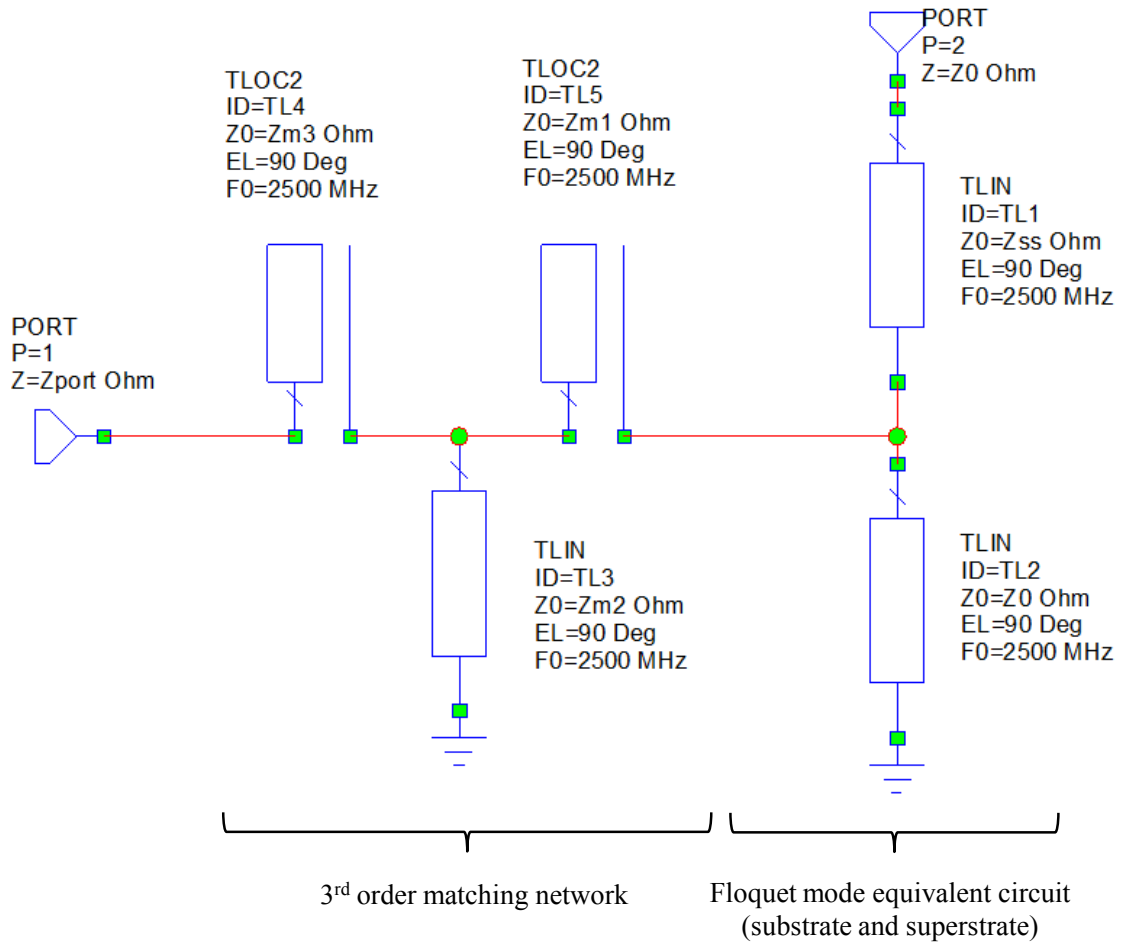
Figure 4.16: Example 5th order equivalent circuit for a superstrate-loaded array, as modeled in *AWR Microwave Office*. The array itself is 2nd order, as the substrate and superstrate comprise two reactive stages, and also contains an arbitrary 3rd order network representing the aperture and feed. For simplicity, the aperture and feed are also implemented using shunt open-circuit and short-circuit stubs, and thus the Richards' Transform maps the entire circuit to a 5th order lumped *LC* network.
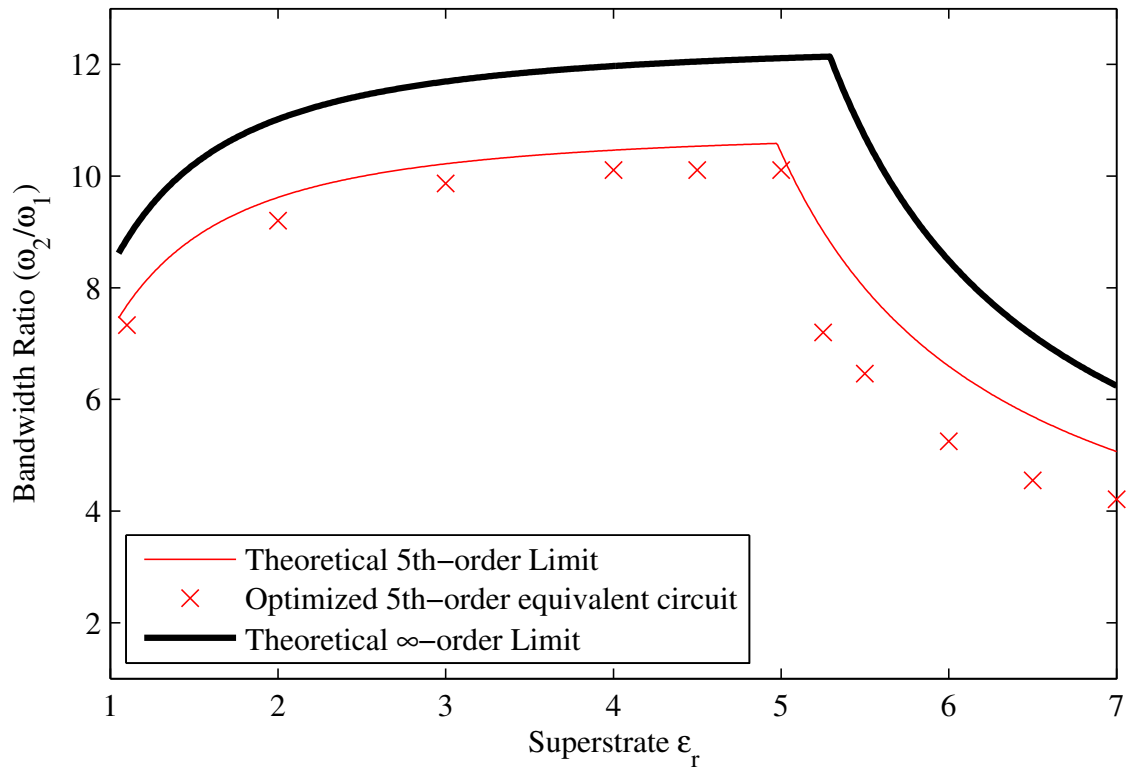
Figure 4.17: The 5th order equivalent circuit of Fig. 4.16, optimized in *ADS*, along with the theoretical 5th order limit. Also plotted is the theoretical (infinite order limit) derived above.

4.4 Wideband Backplanes, High Impedance Surfaces, and Metamaterials

The bandwidth of planar arrays is fundamentally limited by the reflections from the ground plane. As such, a designer may attempt to mitigate these reflections by introducing some type of additional matching structure between the array and ground plane. Such a structure may absorb the ground plane reflections, alter the phase of the reflection, or adjust the effective impedance of the ground plane seen at the array. Collectively, such structures are referred to as wideband backplanes, since they represent an attempt to restore the bandwidth lost from ground plane reflections.

The most straightforward wideband backplane simply uses magnetic materials. As demonstrated in this and the previous chapter, magnetic substrates can have a dramatic effect on improving bandwidth. Note that for planar arrays, the critical parameter in the bandwidth limit (4.14) is not simply the permeability μ_{sub}, but the ratio of permeability to permittivity, μ_{sub}/ϵ_{sub}, and therefore the dielectric constant must be kept small while the permeability is increased. In practice, magnetic substrates are also somewhat lossy, which furthermore improves the impedance bandwidth of the array, at the expense of efficiency.

But what about artificial magnetic materials? Could metamaterials constructed from non-magnetic components (e.g. split-ring resonators) be used effectively to increase the permeability of the array? Unfortunately, the critical value of permittivity that determines the bandwidth limit is that at DC. Although artificial magnetic materials may be synthesized over some frequency range, it is not possible using non-magnetic materials to increase the static permeability of a structure. Therefore, any

attempt to use artificial magnetic materials will still be constrained by causality and therefore by the bandwidth limits imposed by the dispersion relations based on the low-frequency response of the material.
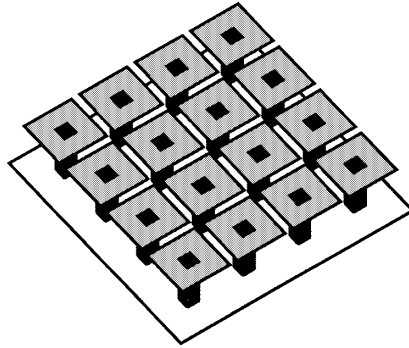
Figure 4.18: Artificial high-impedance surface, from [103], ©1999 IEEE.

Another strategy that is occasionally proposed is the use of artificial high-impedance surfaces above the PEC ground plane. An example are "thumb-tack" or "mushroom" shaped conducting structures that synthesize a high-impedance surface over some frequency band [103], see Fig. 4.18. The idea is that unlike a PEC ground plane, a engineered surface could perhaps produce reflections that are in-phase and thus avoid destructive interference, even when the array is electrically thin. Although this approach may have some practical uses, it unfortunately cannot provide any improvement beyond the impedance bandwidth limits for planar arrays presented in this chapter, if only lossless non-magnetic materials are used.

The reason for this was demonstrated by Munk [19]. Foster's Reaction Theorem states that a lossless impedance must have reactance that increases monotonically with frequency. Consider a planar array with a homogeneous substrate that is $\lambda/2$
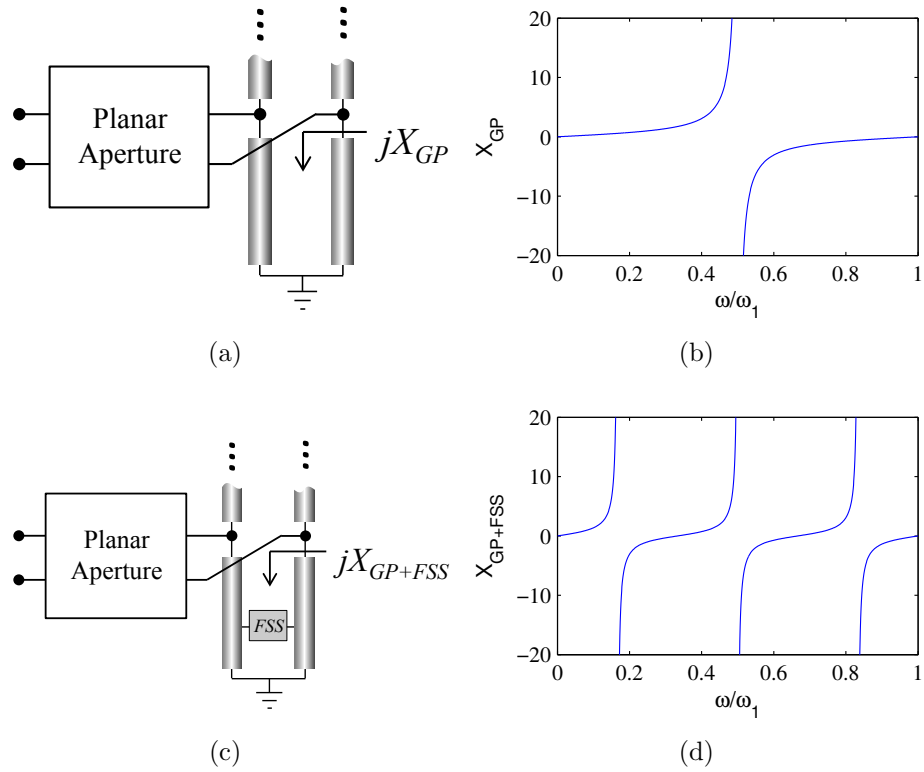
Figure 4.19: (a-b) Standard lossless, homogeneous substrate and ground plane creates a short circuit at DC and at the half-wavelength resonance. (c-d) If an artificial high-impedance surface is introduced to create a high-impedance at multiple frequencies within the band, Foster's Reaction Theorem states that this must introduce another short-circuit at some intermediate frequency. This is of course counterproductive for improving the bandwidth.

thick at the frequency ω_1, as shown in Fig. 4.19a. The impedance of the ground plane seen at the reference plane of the array begins at DC as a short-circuit, becomes an open-circuit at $\omega_1/2$, and returns back to a short circuit at ω_1, see Fig. 4.19b. Suppose we wished now to include a backplane or frequency selective surface (FSS) as in Fig. 4.19c such that the ground plane impedance is open-circuited at additional frequencies within the band. Foster's reactance theorem states that if the impedance is an open circuit at two distinct frequencies, then it must also have a short-circuit at some intermediate frequency, as seen in Fig. 4.19d. Therefore, by attempting to synthesize a wideband back-plane, we have actually made the bandwidth worse by introducing additional short circuits within the band. Munk referred to this phenomenon as the "moving ground plane that moved too fast".

We can also frame Munk's argument in terms of our bandwidth limits. If the high-impedance surface is constructed from lossless and non-magnetic materials, then whatever impedance we include in the additional block in Fig. 4.19c will increase the reactance of the load. However, the bandwidth is maximized when the reactance of the load is minimal, corresponding to a homogeneous substrate without any reactive components. Such high-impedance backplanes may be effectively used to reduce the height of a planar array, but can do so only at the expense of bandwidth. However, the low-profile planar limits (4.17)-(4.18) suggest that the same effect can be obtained simply by redesigning the planar radiating surface itself, and thus the use of additional high-impedance surfaces is not strictly required. One way to express this conclusion is that rather than designing an intermediate surface which acts as high-impedance ground plane, it is often simpler and more effective to simply excite the metamaterial surface directly, and use it as the primary radiating aperture.

144

One area that metamaterials or frequency selective surfaces may be more effectively used is not as artificial substrates, but as artificial superstrates. The bandwidth improvements that were obtained by adding a superstrate layer may also be obtained by including additional planar matching layers above the primary radiating surface. Such an approach has the advantage of avoiding bulk superstrate materials that add weight to the array and may support undesired higher-order modes or surface waves.

We can generalize these findings by stating that if multiple layers are used in a lossless planar array, it is typically best to directly excite the layer nearest to the ground plane. If additional layers are used, they should be placed above the driven layer and parasitically excited. The space between the driven layer and the ground free then should be from dielectrics or reactive components, other than necessary feed lines.

Part II: Practical Implementations of Wideband Low-Profile Antenna Arrays

Chapter 5: Wideband Feeds for Tightly Coupled Arrays

We now move from the theoretical question of the fundamental limits for low-profile PEC-backed arrays, to the practical question of how best to implement such arrays with maximum performance and minimum size, weight, and cost. We begin by considering how such arrays may be optimally excited. One of the most challenging design problems for wideband arrays is the design of a practical feed that does not deteriorate the natural wideband response of the array. Most wideband arrays have radiating elements that use *balanced* feeds, meaning that the feed point consists of two symmetrical nodes that are fed with a differential signal. This is in contrast to an *unbalanced* feed, where one node is connected to the signal line, and the other node is grounded. A simple example is a dipole, which has a balanced feed, versus a monopole which has an unbalanced feed, see Fig. 5.1.

Balanced feeds are common in wideband arrays because, as discussed in the previous chapters, the radiating elements must be removed from the ground plane in order to obtain wideband performance. Therefore, there is no good ground reference available to feed an unbalanced element. However, the problem with balanced feeds is that the electronics which drive the array, as well as the transmission lines in the feed network typically employ unbalanced feed lines, e.g. microstrip, stripline, or coaxial
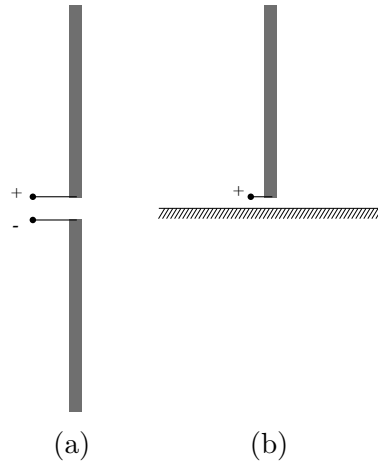
Figure 5.1: (a) A dipole is an example of a radiator with a balanced input, with positive and negative terminals. Neither terminal is grounded. A balun is required to feed a dipole from an unbalanced transmission line. (b) A monopole is an example of a radiator with an unbalanced input, with a single terminal referenced to ground. No balun is needed.
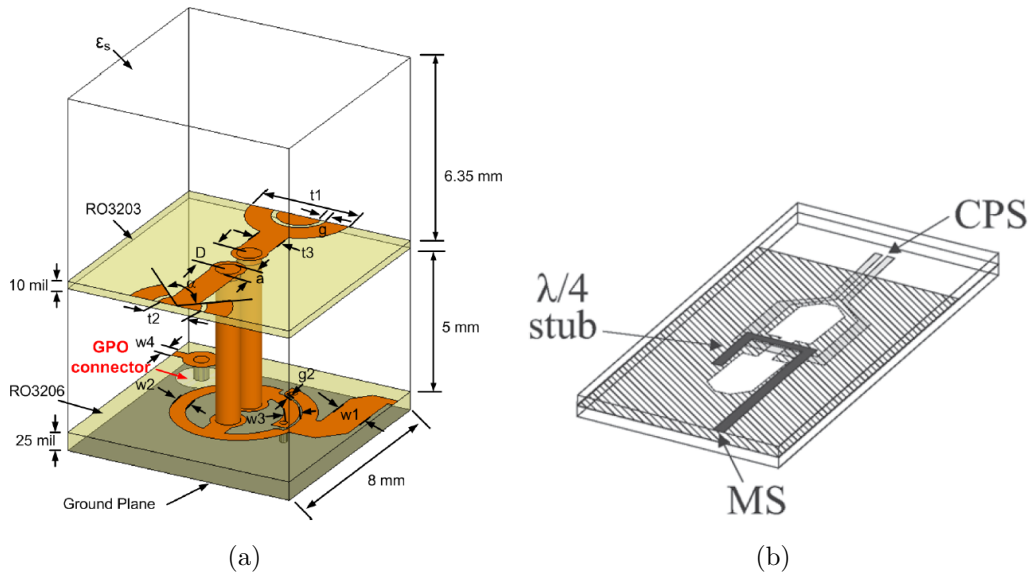
Figure 5.2: Various baluns have been proposed for coupled and connected dipole arrays. (a) TCDA with a compact balun implemented just above the ground plane, yielding 1.5:1 bandwidth, from [104], ©2010 IEEE. (b) Microstrip to co-planar stripline transition, operating as a balun for a connected dipole array, over a 1.5:1 bandwidth, from [105], ©2010 IEEE.
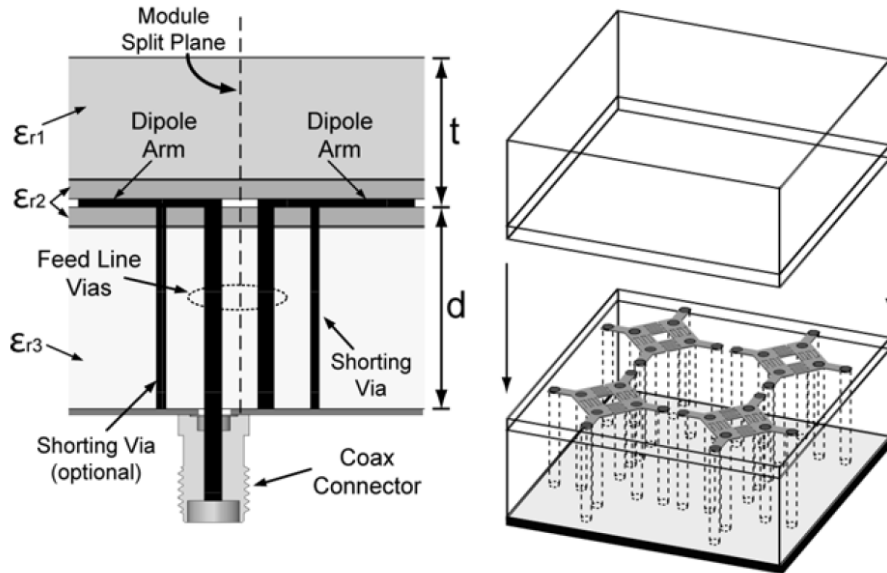
Figure 5.3: The Planar Ultrawideband Modular Array (PUMA) uses shorting posts rather than a traditional balun to avoid common-mode resonances over a 5:1 bandwidth, from [49], ©2012 IEEE.

cables. Therefore, a circuit must be employed to convert between the balanced and unbalanced parts of the network. Such a device is called a *balun*.

Ideally, a small balun could be integrated within each unit cell above the ground plane for a lightweight, low profile implementation. However the available volume is quite limited, particularly for arrays operating above 500 MHz. For example, a TCDA operating over a 6:1 bandwidth of 750-4500 MHz may have a 30 mm element-element spacing ($< \lambda/13$ at 750 MHz), with the ground plane spaced a similar distance below the dipoles. Commercially available passive baluns at microwave frequencies are generally either narrow-band or are large, heavy and expensive, and active balun circuits are limited to receive-only applications. Integration of wideband baluns within the available volume is therefore quite difficult, and previous attempts have yielded
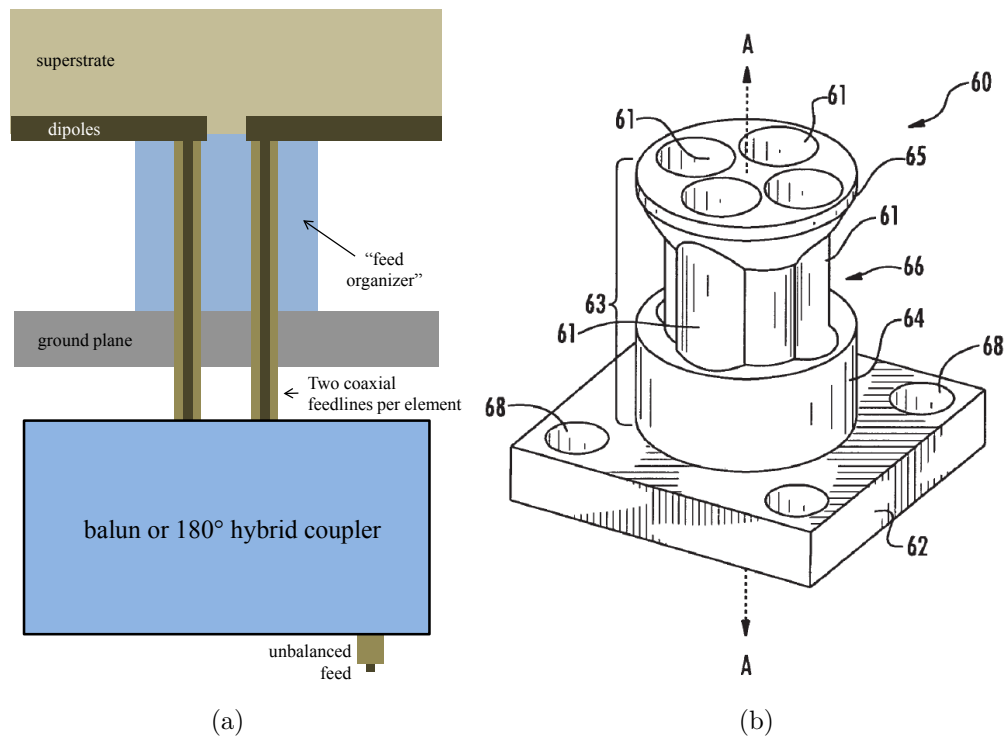
Figure 5.4: (a) Configuration of a CSA with an external balun and feed organizer.
(b) Feed organizer detail, from [106].

modest bandwidths of less than 2:1 [104, 105, 107]. Figure 5.2 illustrates several such designs. Another technique is to avoid baluns altogether and use shorting posts to mitigate common mode resonances, resulting in 5:1 bandwidth after external impedance matching, as shown in Fig. 5.3 [49].

For maximum bandwidth and performance, TCDAs currently must use bulky external baluns or 180° hybrids located below the ground plane, as shown in Fig. 5.4. In addition to the additional size, weight and cost of the balun itself, which can be significant, care must be taken not to excite so-called *common modes* on the feed lines. These can arise when balanced feed lines are left unshielded, and produce significant impedance mismatches and high cross-polarization [18]. To avoid such resonances, a structure known as a *feed organizer* is used to shield the balanced line and reduce the electrical distance between neighboring feed lines [18, 106]. The combination of external balun and feed organizer significantly increases the total size, weight, and cost of the array. However, this is currently the only way to realize the full bandwidth and performance of tightly coupled arrays.

In this chapter, we will introduce a novel technique for integrating an electrically small balun within the existing volume of a TCDA. Not only does our method preserve the naturally wide bandwidth of the TCDA, but it actually improves the array's impedance bandwidth by canceling the reactance of the array with the reactance of the balun. By including the balun as part of the matching network for the array, we obtain a higher-order impedance match, which leads to higher bandwidth from (3.73).

5.1   Equivalent Circuits for Scanning Tightly Coupled Dipole Arrays
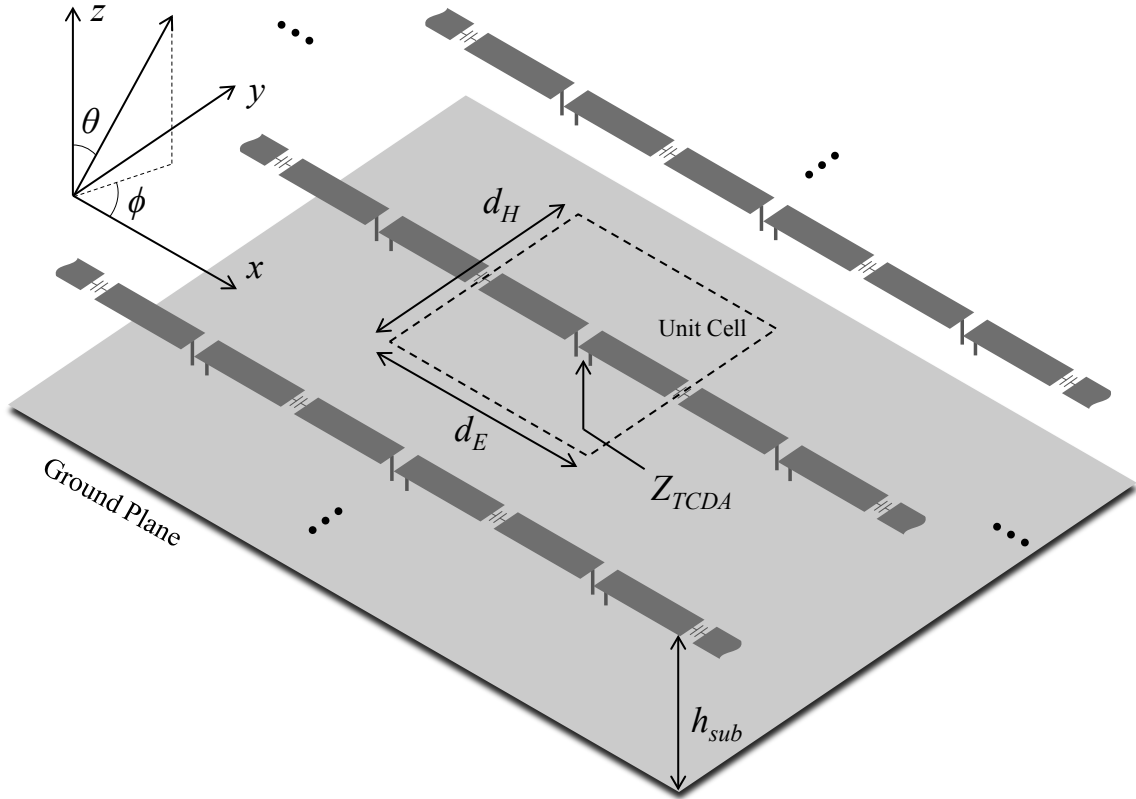
Figure 5.5: A Tightly Coupled Dipole Array (TCDA) consisting of capacitively coupled dipole elements, placed above a conducting ground plane. The dipoles are aligned with the x-axis and the ground plane is normal to the z-axis. Substrate and super-strate materials (not shown) may also be included.

A Tightly Coupled Dipole Array (TCDA) uses horizontal dipoles placed above a conducting ground plane, as shown in Fig. 5.5. By capacitively coupling neighboring dipoles, the array supports currents at wavelengths which greatly exceed the dimension of a single element. Moreover, the dipole inductance and inter-element
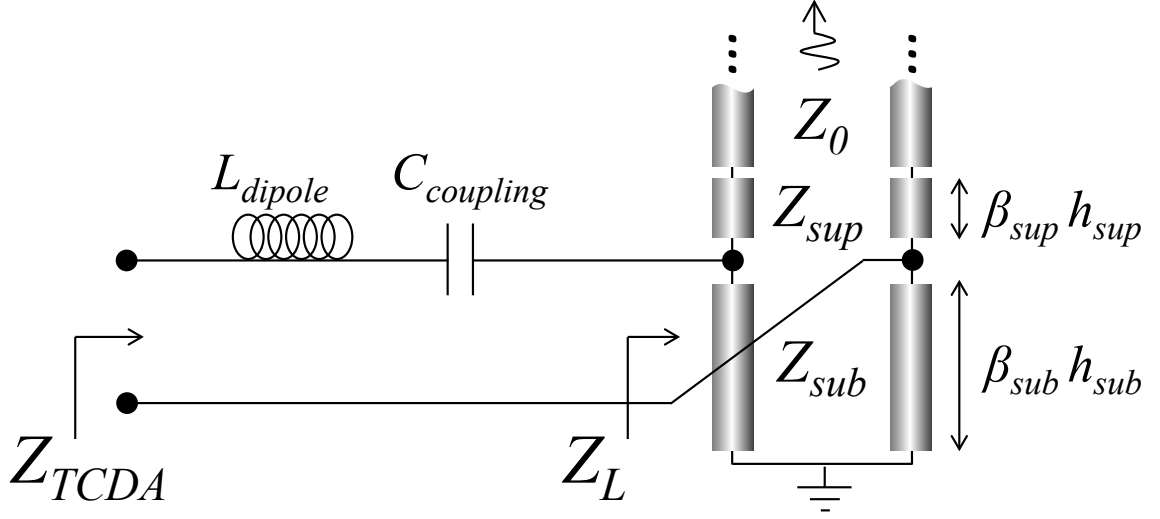
Figure 5.6: Equivalent circuit for the TCDA proposed in [19].

capacitance serve to cancel the reactance of the nearby ground plane over a wide bandwidth.

An approximate equivalent circuit for the TCDA was proposed in [19], and is shown in Fig. 5.6. In this circuit, the dipole inductance is represented by L_{dipole}, and the inter-element capacitance is denoted as $C_{coupling}$. The substrate, superstrate, and free space layers are represented by transmission line sections with properties determined by the propagating Floquet mode within each corresponding layer, $c.f.$ (4.1)-(4.3).

In general, the array may excite both the fundamental TE and the TM Floquet modes. For linearly polarized arrays, the TE mode is excited when scanning in the H-plane ($\phi = 90°$) and the TM mode is excited when scanning in the E-plane ($\phi = 0°$). The scan angle θ is illustrated in Fig. 5.5, and the corresponding angle of refraction within each layer is given by $\theta_r = \sin^{-1}(\sin\theta/\sqrt{\mu_r \epsilon_r})$. The impedance of
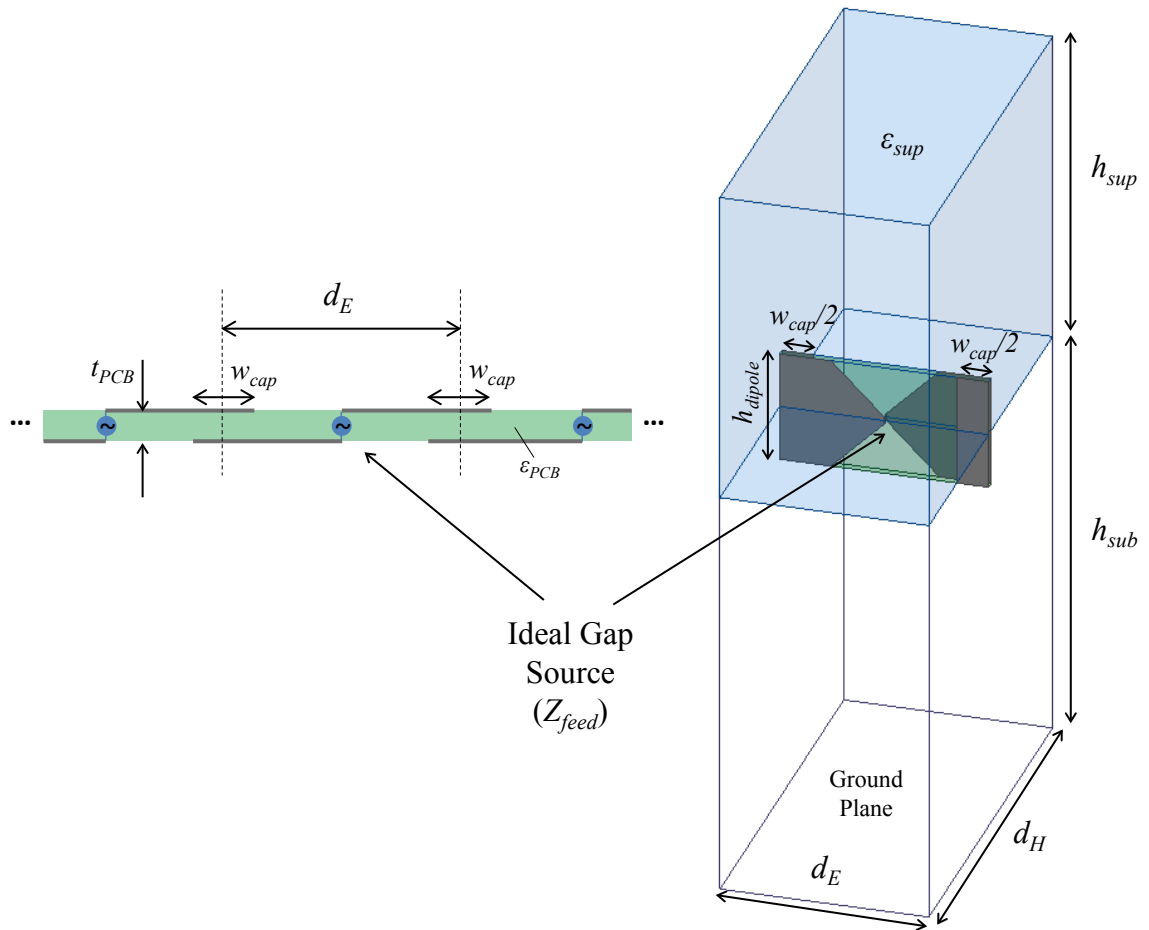
Figure 5.7: Implementation of a TCDA unit cell, using vertical printed dipoles with arms on opposite sides of a thin PCB. The model does not include a realistic feed, rather the dipole is fed with an ideal gap source. On the left is a cross section of the PCB, showing the layout of the dipoles with overlapping arms.

each transmission line section in Fig. 5.6 when scanning in the E- and H-planes is given by [21]

$$Z_r^E = \frac{d_E}{d_H} Z_{00}^{TM} = \eta \sqrt{\frac{\mu_r}{\epsilon_r}} \frac{d_E}{d_H} \cos \theta_r, \tag{5.1}$$

$$Z_r^H = \frac{d_E}{d_H} Z_{00}^{TE} = \eta \sqrt{\frac{\mu_r}{\epsilon_r}} \frac{d_E}{d_H} \frac{1}{\cos \theta_r}. \tag{5.2}$$

The propagation constant for each line is given by

$$\beta_r = k_r^z = k_0 \sqrt{\mu_r \epsilon_r} \cos \theta_r. \tag{5.3}$$

Here, $\eta \approx 377 \ \Omega$ is the characteristic impedance of free space, d_E is the E-plane (x-dimension) element spacing, and d_H is the H-plane (y-dimension) element spacing. Note that scanning in the intercardinal planes will excite both TE and TM modes simultaneously, which requires a more general model, such as given in Fig. 4.3. However, the performance of TCDAs at a given scan angle in the intercardinal planes typically varies between the E- and H-plane responses, and thus can usually be neglected when performing initial design optimizations.

5.1.1 Validation of the Circuit Model

To evaluate the accuracy of the equivalent circuit, we considered a TCDA array implementation as shown in Fig. 5.7, with dipoles that are printed on a vertically oriented printed circuit board of thickness $t_{PCB} = 0.5$ mm and dielectric constant $\epsilon_{PCB} = 3.66$. The dipole's inductance is controlled by the height h_{dipole}, and the inter-element capacitance is created by the overlap w_{cap} of the dipole arms that are printed on opposite sides of the PCB. The spacing between the the dipoles and the ground plane is h_{sub}, and the thickness of the dielectric superstrate is h_{sup}.

Prior to performing a full-wave simulation, the array is modeled in *AWR Microwave Office* with an equivalent circuit. Three copies of the circuit are created,

(a) Broadside

(b) 45° H-Plane Scan
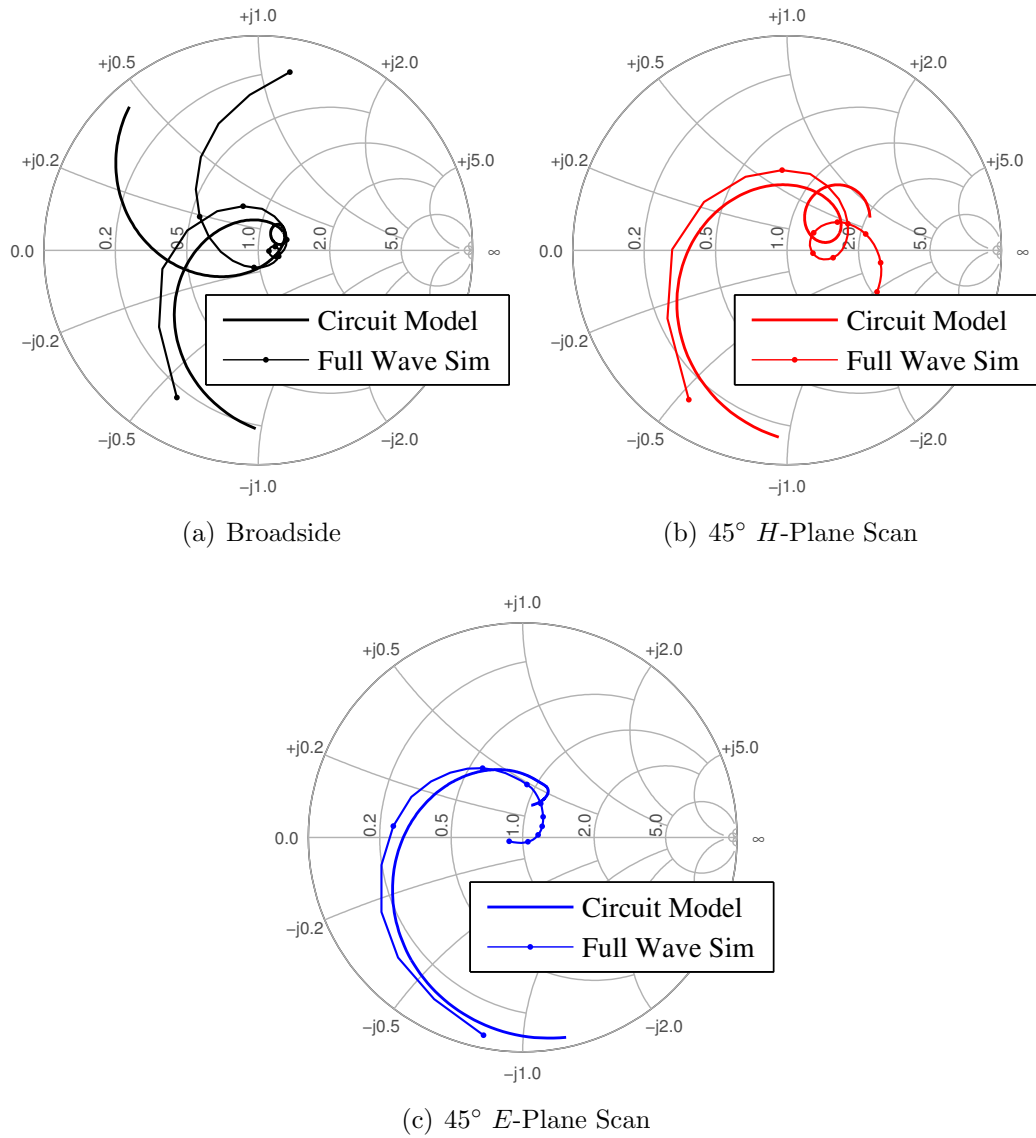
(c) 45° E-Plane Scan

Figure 5.8: Reflection coefficient of TCDA without feed, using the equivalent circuit model (Fig. 5.6) and the full wave simulation (Fig. 5.7) with parameters given by Table 5.1. (a) Broadside scan. (b) 45° $E-$plane scan. (c) 45° $H-$plane scan. Other than h_{dipole}, all array dimensions are directly computed from the corresponding circuit values and have not been fine-tuned, except for h_{dipole}.

Table 5.1: Optimized Circuit Values and Dimensions of TCDA without Feed

Equivalent Circuit (Fig. 5.6)		Physical Dimensions (Fig. 5.7)	
Z_0, Z_{sub}	188 Ω	d_E	14 mm
Z_{sup}	144 Ω	d_H	28 mm
Z_{feed}	100 Ω	Z_{feed}	100 Ω
$\beta_{sub} h_{sub}$	84° at 2.5 GHz	h_{sub}	28.3 mm
$\beta_{sup} h_{sup}$	64° at 2.5 GHz	h_{sup}	21.7 mm
$C_{coupling}$	2.0 pF	w_{cap}	4.2 mm
L_{dipole}	3.0 nH	h_{dipole}	7.6 mm
		ϵ_{sup}	1.7
		t_{PCB}	.5 mm
		ϵ_{PCB}	3.66
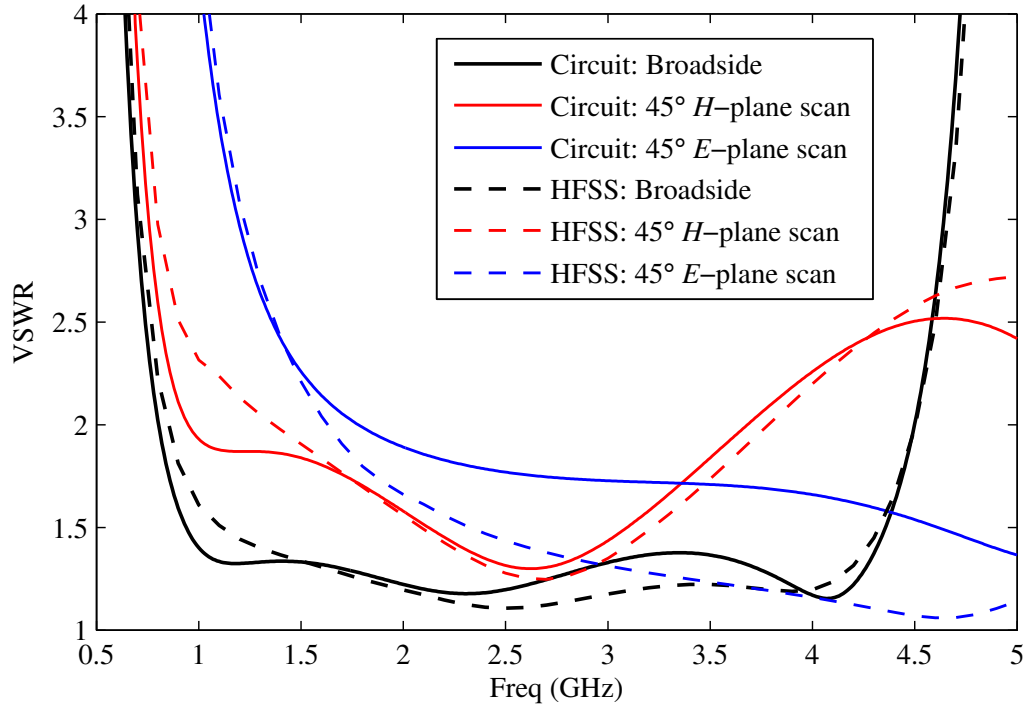
Figure 5.9: VSWR of TCDA without feed, using the equivalent circuit model (Fig. 5.6) and the full wave simulation (Fig. 5.7) with parameters given by Table 5.1. All array dimensions are directly computed from the corresponding circuit values and have not been fine-tuned, except for h_{dipole}.

157

corresponding to broadside, 45° E-plane, and 45° H-plane scanning. These scan conditions are modeled by adjusting the impedance and length of the transmission line sections, per (5.1)-(5.3). For reasons discussed in the following sections, we fix $Z_0 = 188$ Ω and $Z_{sup} = 144$ Ω, which corresponds to a rectangular unit cell $(d_E/d_H = 1/2)$ and a superstrate dielectric constant of $\epsilon_{sup} = 1.7$. The dipole was fed by a 100 Ω lumped gap source. Under these conditions, the remaining circuit components were optimized for maximum bandwidth at broadside, using using a genetic algorithm. Due to the simplicity of the circuit, optimization is relatively fast with convergence in less than one minute. The resulting values are given in Table 5.1, and the response of the circuit model is shown in Figs. 5.8-5.9.

With the exception of the dipole inductance, each physical dimension of the array can be directly computed from the corresponding circuit value, and the unit cell then simulated using *Ansys HFSS v.14*. The physical thicknesses of the substrate and superstrate are determined from the electrical length of the corresponding transmission lines, and w_{cap} is computed from $C_{coupling}$ using a parallel plate capacitor model. The dipole inductance was then tuned by adjusting h_{dipole} until the simulation was roughly in agreement with the circuit model. The resulting dimensions are also given in Table 5.1, and the response of full-wave simulation is compared to the circuit model in Figs. 5.8-5.9 at broadside, and when scanning to 45° in the principle planes. Although further fine-tuning of the physical model could then have been performed, we have not done so in order that the quality of the initial design computed directly from the circuit components may be evaluated.

It is clear that despite its simplicity, the circuit of Fig. 5.6 provides a reasonable representation of the scanning TCDA that can be efficiently analyzed and optimized

using standard circuit modeling tools. As such, it is a convenient and valuable tool, both for developing a rough initial design, as well as for providing critical guidance when fine-tuning the array. However, both the above circuit and physical model are incomplete because neither accounts for the presence of a feed. This is critical because in addition to the impedance of the feed circuit itself, any conducting structure placed between the ground plane and dipoles will also disrupt the fields within the substrate. Because these effects are not accounted for in the above circuit model, it is less accurate for modeling TCDAs with practical feeds. Nevertheless, we will show that this limitation can be mitigated by making a minor adjustment to the equivalent circuit.

5.2 An Improved Equivalent Circuit for a Tightly Coupled Dipole Arrays with a Feed

In a practical implementation, a TCDA must be excited by feed lines running from the ground plane to the dipoles, thus the above representation of the substrate as a homogeneous slab is insufficient. At broadside and when scanning in the H-plane, the feed lines do not have much effect, since the substrate mode is TE and the electric field polarization is normal to the vertical feed. However, when scanning in the E-plane, the presence of a feed has a significant impact.

The effect of the feed can be seen in Fig. 5.10, where the electric and magnetic fields are plotted for two TCDAs, each scanned to 45° in the E-plane. Although the radiating dipoles of both arrays are identical, the first TCDA is fed by an ideal gap source, whereas the second TCDA contains a realistic feed structure. For the TCDA without feed lines, the substrate fields are accurately represented by the fundamental TM Floquet mode. However, when the feed structure is introduced, the electric
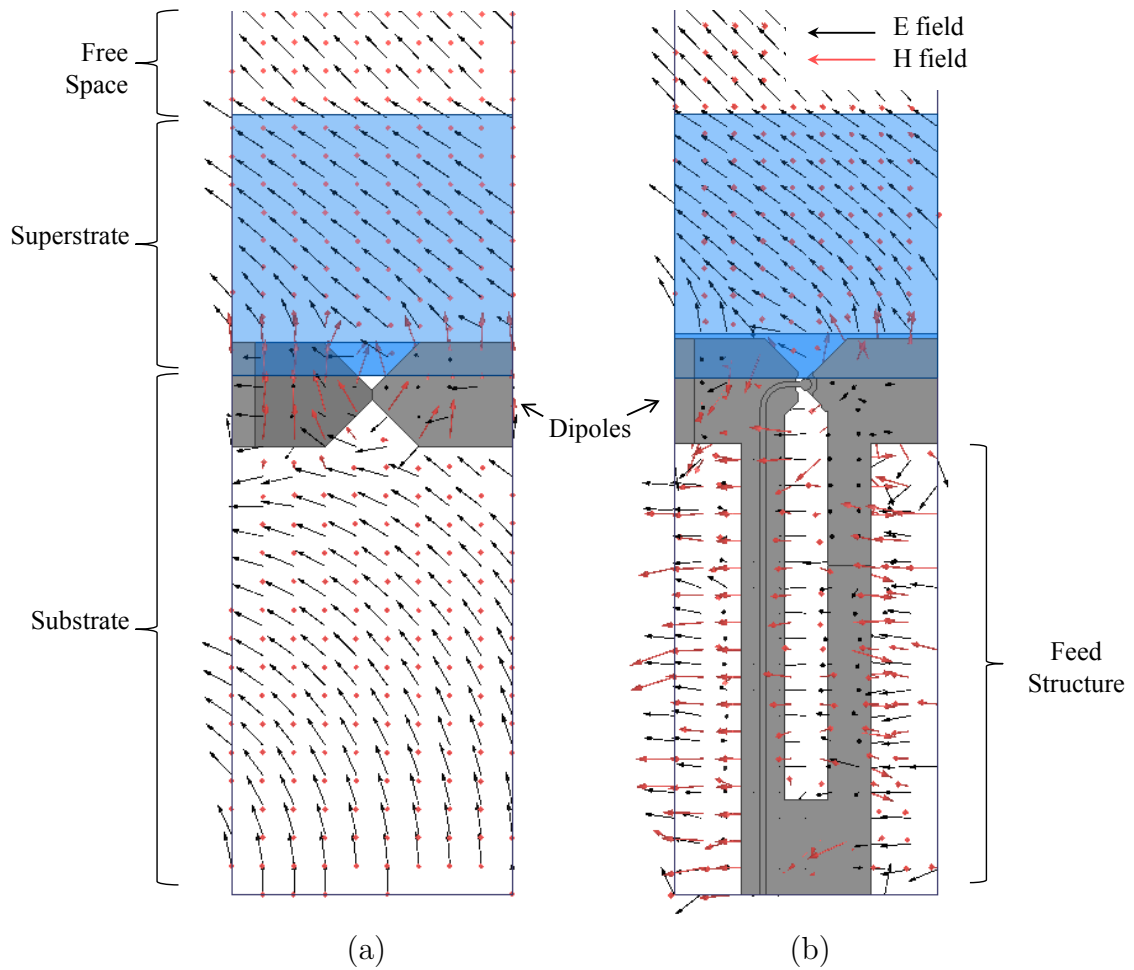
Figure 5.10: Electric and Magnetic fields in the unit cell of the TCDA, when scanning to 45° in the E-plane. (a) A TCDA unit cell with ideal gap source and no feed structure. In this case, the magnetic fields in the substrate, superstrate, and above the array are all transverse to $\hat{\mathbf{z}}$, i.e. the TM mode. (b) A TCDA unit cell with vertical conducting feed lines. The fields in the substrate are strongly influenced by the feed. Both electric and magnetic fields are transverse to $\hat{\mathbf{z}}$, and form a quasi-TEM mode.

(a) Broadside

(b) 45° H-Plane Scan

(c) 45° E-Plane Scan
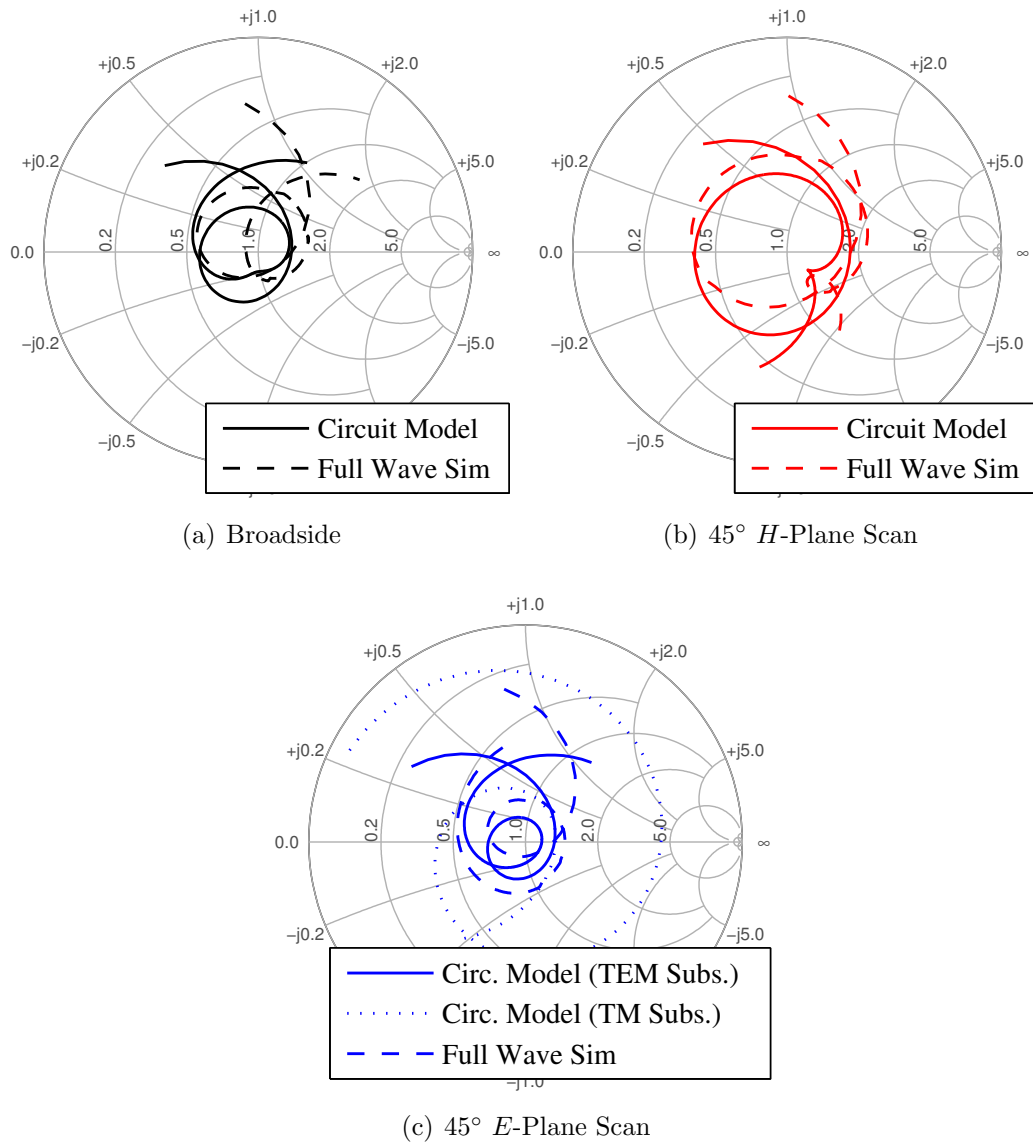
Figure 5.11: Reflection coefficient of TCDA with feed circuit, using the equivalent circuit model (Fig. 5.14) with values given in Table 5.2, and the full wave model of a "half" unit cell (Fig. 5.10b) with dimensions given in Table 6.1. (a) Broadside scan. (b) 45° $H-$plane scan (c) 45° $E-$plane scan, showing circuit response using both TM substrate mode via (5.1)-(5.3), and TEM substrate mode via (5.4)-(5.5)
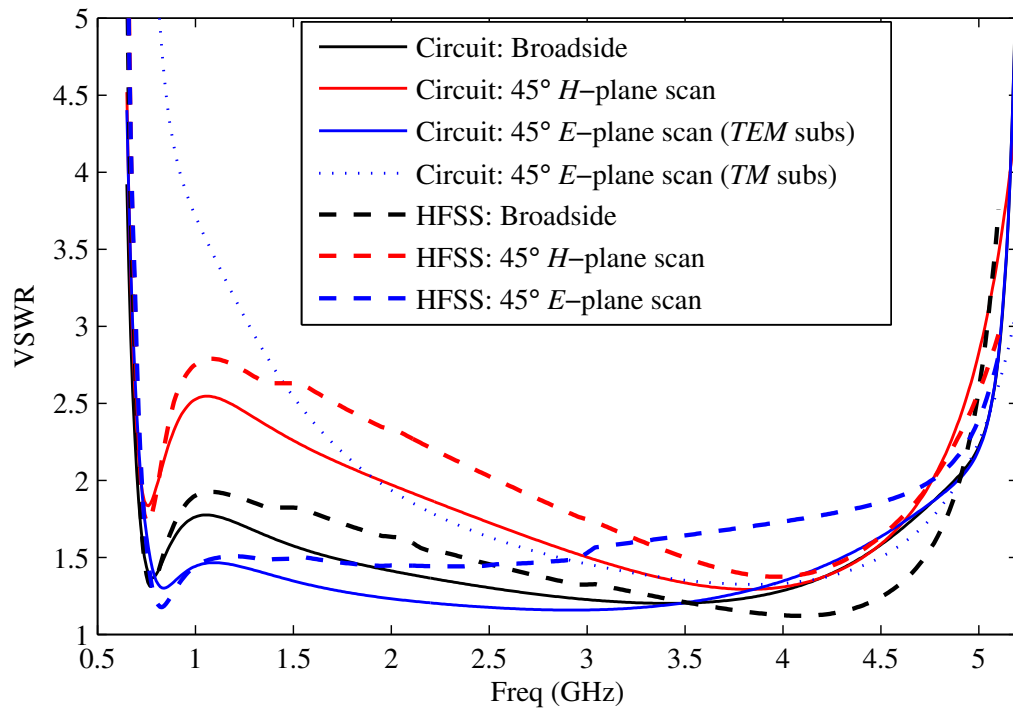
Figure 5.12: VSWR of TCDA with feed circuit, using the equivalent circuit model (Fig. 5.14) with values given in Table 5.2, and the full wave model of a "half" unit cell (Fig. 5.10b) with dimensions given in Table 6.1.

field in the substrate couples strongly to the feed lines, forming a guided quasi-TEM mode. Unlike the TM Floquet mode described by (5.1) and (5.3), the impedance and propagation constant of the TEM mode in the substrate do not significantly vary when scanning in the E-plane. Therefore, when vertical feed lines are present, a more accurate representation for the substrate for E-plane scanning is given by

$$Z_{sub}^E = \eta \sqrt{\frac{\mu_r}{\epsilon_r}} \frac{d_E}{d_H}, \tag{5.4}$$

$$\beta_{sub}^E = k_0 \sqrt{\mu_r \epsilon_r}. \tag{5.5}$$

For H-plane scanning, (5.2) and (5.3) remain accurate. The circuit model can now be optimized over all three scan positions (Broadside, 45° E-plane, and 45° H-plane). The improvement provided by (5.4)-(5.5) is illustrated in Figs. 5.11-5.12, which compare a full wave simulation of a TCDA with an integrated feed to its equivalent circuit using both the standard Floquet mode substrate model and the proposed TEM substrate model. As seen, the TEM substrate circuit model for E-plane scanning is significantly more accurate vs. the standard TM Floquet mode substrate model, especially at lower frequencies. The details of the actual feed design used in this analysis is discussed in the following section.

5.3   Wideband Baluns for Tightly Coupled Dipole Arrays

Although the above section presents a useful equivalent circuit model for a TCDA radiating element, much of the challenge in designing a practical TCDA lies in the particular details of the feed circuit. The dipoles must be fed differentially, whereas practical feed networks and electronics employ unbalanced circuits, and thus a balun is needed for each element. Unfortunately, low-loss passive baluns with sufficient

163

bandwidth are often large, heavy, and expensive. Moreover, the optimal input impedance of a TCDA with a square unit cell is typically ∼200 Ω. Thus, a wideband 50 Ω to 200 Ω transformer is also required, further increasing the size and weight of the feed.

To eliminate the need for the impedance transformer, we may reduce the E-plane dimension d_E of the unit cell by a factor of 2, which correspondingly reduces Z_{TCDA} to ∼100 Ω. Each square unit cell then contains two "half" elements, each containing a dipole and a balun (see Fig. 5.13). However, rather than feeding each half-element individually (which would double the number of phase shifters and T/R modules), the pair can be combined in parallel to provide a single 50 Ω feed. The effective element count and unit cell size therefore remains the same, and no impedance transformers are required. This "double element" technique has also been shown to significantly reduce cross-polarization by eliminating a common mode resonance which can occur when the combined length of the dipole and feed lines becomes electrically long [105, 108]

Unfortunately, this approach also reduces the volume available for a balun since two baluns are required for each element, and an extremely compact design is required. A Marchand balun, constructed from coupled quarter-wave transmission line stubs (see Fig. 5.14), is both compact and is theoretically capable of operating over a wide bandwidth (>10:1). However, a single stage Marchand balun requires transmission lines with extreme impedance ratios $Z_{OC} \ll Z_{Bal} \ll Z_{SC}$ for wideband operation [109]. With limited available space, implementation of such impedances is challenging. Thus, a standard Marchand balun design integrated within a TCDA unit cell will have increased reactance, deteriorating the match and reducing impedance bandwidth.

(a) Square 377 Ω unit cell

(b) Two 188 Ω "half" unit cells
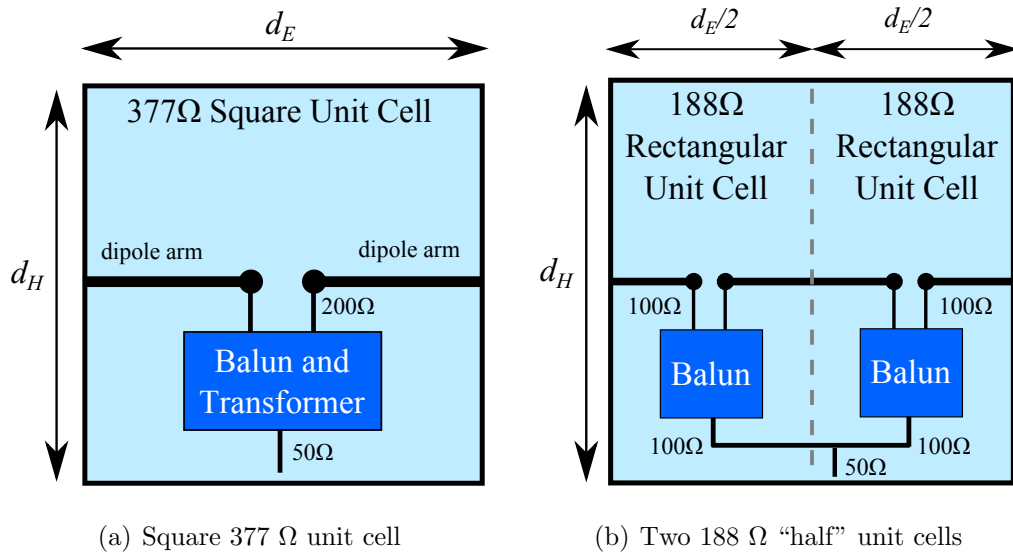
Figure 5.13: Top down representation of the unit cell. The impedance of the unit cell is proportional to the aspect ratio d_E/d_H. By splitting the cell into two halves, the impedance of each is correspondingly reduced by a factor of two. Recombining these halves in parallel again reduces the impedance at the common port by another factor of two.
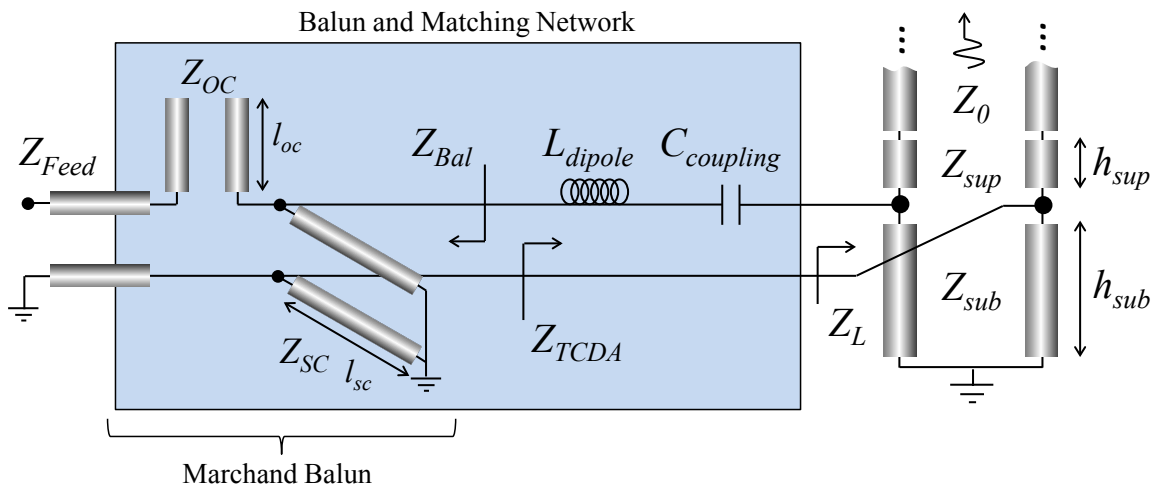
Figure 5.14: TCDA-IB equivalent circuit with a Marchand balun feed. The addition of the balun's two transmission line stubs increases the overall order of the matching network, leading to increased impedance bandwidth.

This limitation may be mitigated by tuning the reactance of the balun to cancel that of the array, as is often done in Vivaldi arrays [110]. That is, the balun may be viewed as part of the impedance matching network for the array. Here, we employ a similar reactive cancelation technique for TCDAs, and we and demonstrate that the inclusion of a reactive balun can actually improve the overall bandwidth, as compared to a TCDA that is fed with no balun.

Referring to the equivalent circuit in Fig. 5.14, the impedance Z_L, consisting of the substrate, superstrate and radiating transmission lines, is independent of the radiating aperture design and may be thought of as a fixed load for the system. As discussed in Chapter 4, the bandwidth of the TCDA (and all planar arrays) is fundamentally limited by the Fano limit of Z_L. The standard TCDA of Fig. 5.6, with series L-C components representing the coupled dipoles, operates as a single stage impedance matching network to Z_L. As shown in Fig. 5.9, optimization of the circuit model with no feed circuit yielded $\sim$5.5:1 bandwidth with VSWR$\leq$2:1 at broadside and VSWR$\leq$2.5:1 when scanning to 45° in the H-plane. This bandwidth is limited by the simplicity of the single stage impedance match provided by the standard TCDA design. However, if a multi-stage matching network is employed (such as provided by the reactive Marchand balun), this bandwidth can be further increased.

In the circuit of Fig. 5.14, the stubs Z_{OC} and Z_{SC} along with L_{dipole} and $C_{coupling}$ form a three stage match to Z_L. Through simple circuit optimization, a maximum bandwidth of 8.9:1 (VSWR$\leq$2) was achieved when only broadside scanning was considered. Referring to Fig. 4.15, we see that this is consistent with the maximum limit for a 5th order array (the substrate and superstrate sections along with the 3rd order matching network) with a superstrate of $\epsilon_{sup} = 1.7$. When optimizing over scan

Table 5.2: Optimized Circuit Values of TCDA with Integrated Balun

Z_0, Z_{sub}	188 Ω
Z_{sup}	144 Ω
h_{sub}	82° at 2.5 GHz
h_{sup}	59° at 2.5 GHz
L_{dipole}	3.5 nH
$C_{coupling}$	1.25 pF
Z_{OC}	20 Ω
Z_{SC}	169 Ω
l_{oc}	52° at 2.5 GHz
l_{sc}	77° at 2.5 GHz

volume using (5.1)-(5.5), a 7.3:1 bandwidth was achieved with VSWR≤2 at broadside and VSWR≤2.5 for 45° scanning in all planes, a 33% increase in bandwidth from the standard TCDA of Fig. 5.6.

There is of course a fundamental tradeoff between bandwidth and maximum scan angle. Our design reflects a rather conservative matching tolerance of VSWR≤2.5:1, and greater bandwidth and/or scanning could be achieved by using a more relaxed matching requirement. Optimized circuit values are given in Table 5.2, and the performance is plotted above in Fig. 5.12.

Therefore, by incorporating the balun within the matching network, the bandwidth of the overall array is significantly increased, while the total size, weight and cost of the array is reduced by eliminating the need for bulky external wideband baluns. We refer to this design approach as the Tightly Coupled Dipole Array with

Integrated Balun (TCDA-IB). In the following chapter, we discuss the physical implementation and design of the TCDA-IB, including measured results from an 8×8 prototype array.

Chapter 6: The Tightly Coupled Dipole Array with Integrated Balun (TCDA-IB)

As described in the previous chapter, a pair of compact Marchand baluns constructed from quarter-wave transmission line stubs may be used to efficiently excite a TCDA element. In this chapter, we detail the implementation of this approach in an actual array design, which we refer to as the *Tightly Coupled Dipole Array with Integrated Balun* (TCDA-IB).

6.1 Physical Implementation of the Marchand Balun

We begin with the physical implementation of the Marchand balun design from the previous chapter, with equivalent circuit shown in Fig. 5.14. A sketch of the balun is shown in Fig. 6.1a. The unbalanced input is a simple microstrip or stripline trace with impedance Z_{feed}. This is fed at the bottom of the balun and runs to the top, where the ground plane is split into two thin traces. This represents the short-circuited stub with impedance Z_{SC}. The feed line crosses the top of the split in the ground plane, and travels back down the other side, ending in an open circuited stub. This section represents the stub Z_{OC}. The balanced output is located at the top of the balun, where the feed line crosses the split in the ground plane.

balanced output (twin-lead)

$+$ $-$

Z_{Feed}

Z_{OC}

Z_{SC}

unbalanced
input
(microstrip)

ground

(a)

balanced output

$+$ $-$

primary
loop

secondary
loop

Capacitance to ground
tuned by length and
impedance of Z_{OC}

unbalanced
input

(b)
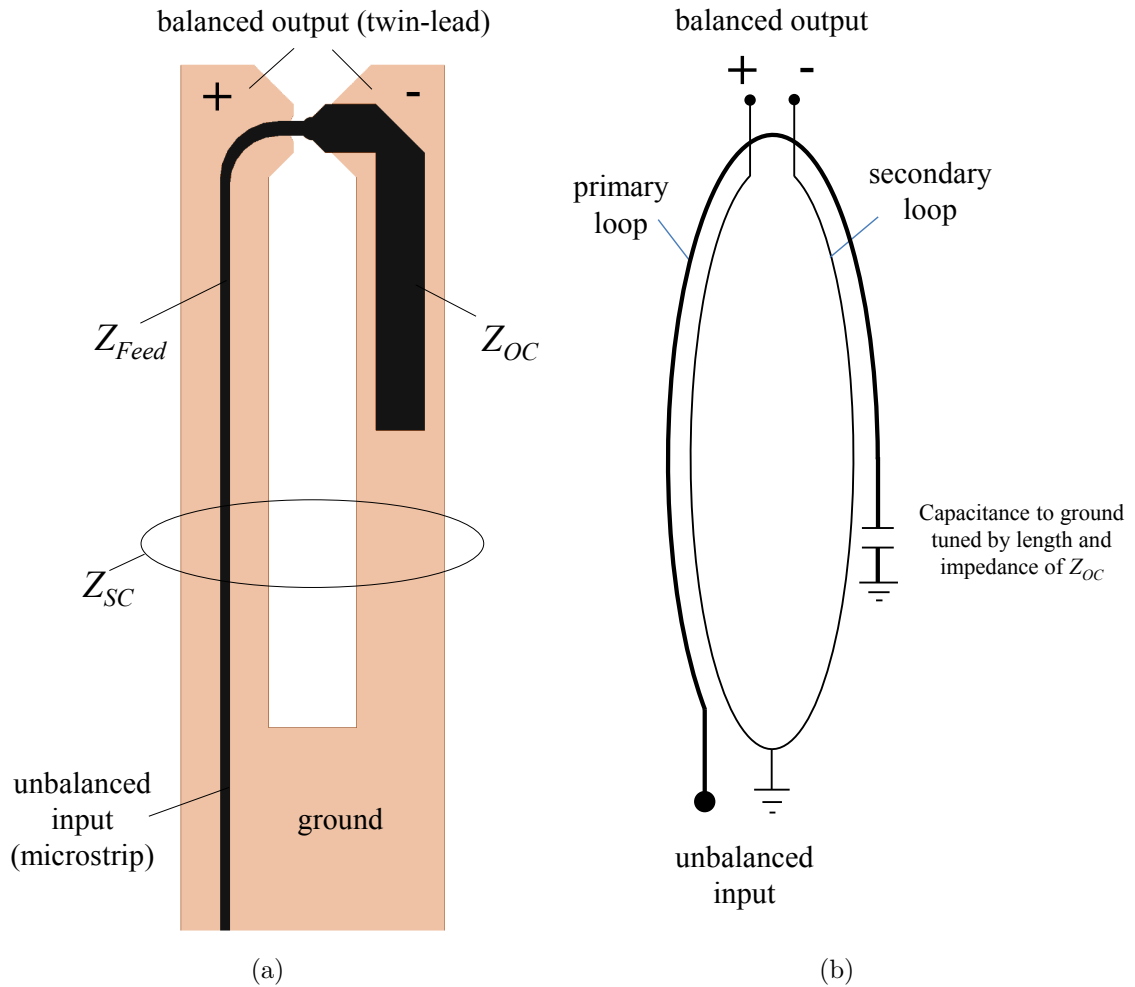
Figure 6.1: (a) Physical representation of the Marchand balun. (b) Conceptual representation of the Marchand balun, showing it to be a simple transformer. The unbalanced line feeds the primary loop, and the secondary loop excites the balanced output. The secondary loop is grounded in the center at the bottom, which balances the output voltage with respect to the ground of the unbalanced input. The frequency response and impedance match of the balun is determined by the impedances and lengths of the transmission line sections.

The RF frequency response and impedance match of the balun can best be understood by examining the equivalent circuit in Fig. 5.14. However, this does not necessarily indicate how the balun works or how the unbalanced input is converted to a balanced output. This can be best understood by considering the simplified sketch shown in Fig. 6.1b. The Marchand balun clearly forms two coupled loops. The primary loop is formed by the transmission lines Z_{feed} and Z_{OC}, and the secondary loop is formed by Z_{SC}. The primary loop is excited at the bottom of the balun with a transmission line that is referenced to ground, i.e. it has an unbalanced input. This loop then couples to the secondary loop, which is tied to ground at its midpoint. The voltage at the output terminals of the secondary loop is therefore centered around the ground voltage, and forming a balanced differential output.

This balun is compact and sufficiently small to fit within the unit cell of the array. The dipoles are connected to the balanced output at the top of the balun, and the balun's ground plane can be connected to the array ground plane.

6.2   Physical Implementation of the TCDA-IB

The full TCDA-IB unit cell design is depicted in Fig 6.2. The balun and dipole elements are printed together on a single 3-layer printed circuit board. The PCB is fabricated from two *Rogers 4350B* ($\epsilon_r = 3.66$) boards laminated together using a prepreg layer of *Rogers 4450B* ($\epsilon_r = 3.3$). L_{dipole} is controlled by the width of the dipole arms, which are printed on opposite sides of the board, and $C_{coupling}$ is controlled by the amount of overlap between the arms. We note that Z_{feed} is a 100 Ω microstrip line, and Z_{OC} is implemented as a stripline. Z_{SC} is formed by twin vertical metal strips, which also serve as ground planes for Z_{feed} and Z_{OC}. Vias were
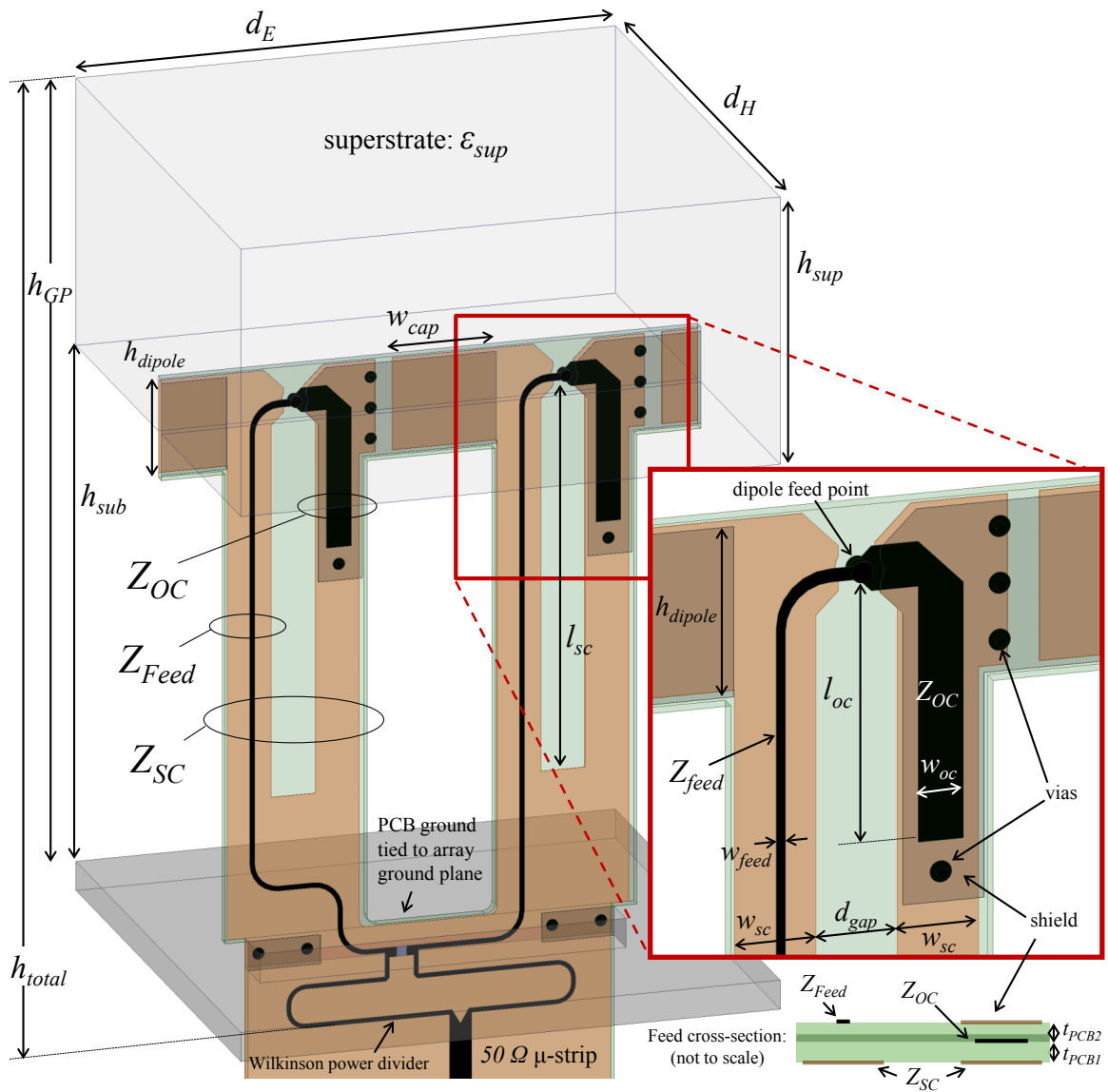
Figure 6.2: Implementation of a unit cell of the TCDA-IB. Each unit cell contains two 100Ω baluns, fed by a single 50Ω microstrip trace. Dimensions are provided in Table 6.1.

Table 6.1: Optimized Dimensions of TCDA with Integrated Balun

d_E	28 mm
d_H	28 mm
h_{sub}	27 mm
h_{sup}	14 mm
h_{GP}	41 mm
h_{total}	45.8 mm
h_{dipole}	4.8 mm
w_{cap}	5.25 mm (dual pol: 4.8 mm)
w_{feed}	0.13 mm
l_{sc}	20.8 mm
l_{oc}	7.9 mm
w_{sc}	2.3 mm
w_{oc}	1.3 mm
d_{gap}	2.3 mm
t_{PCB1}	10 mil 4350B
t_{PCB2}	6.6 mil 4350B + 3.6 mil 4450B
ϵ_{sup}	1.7
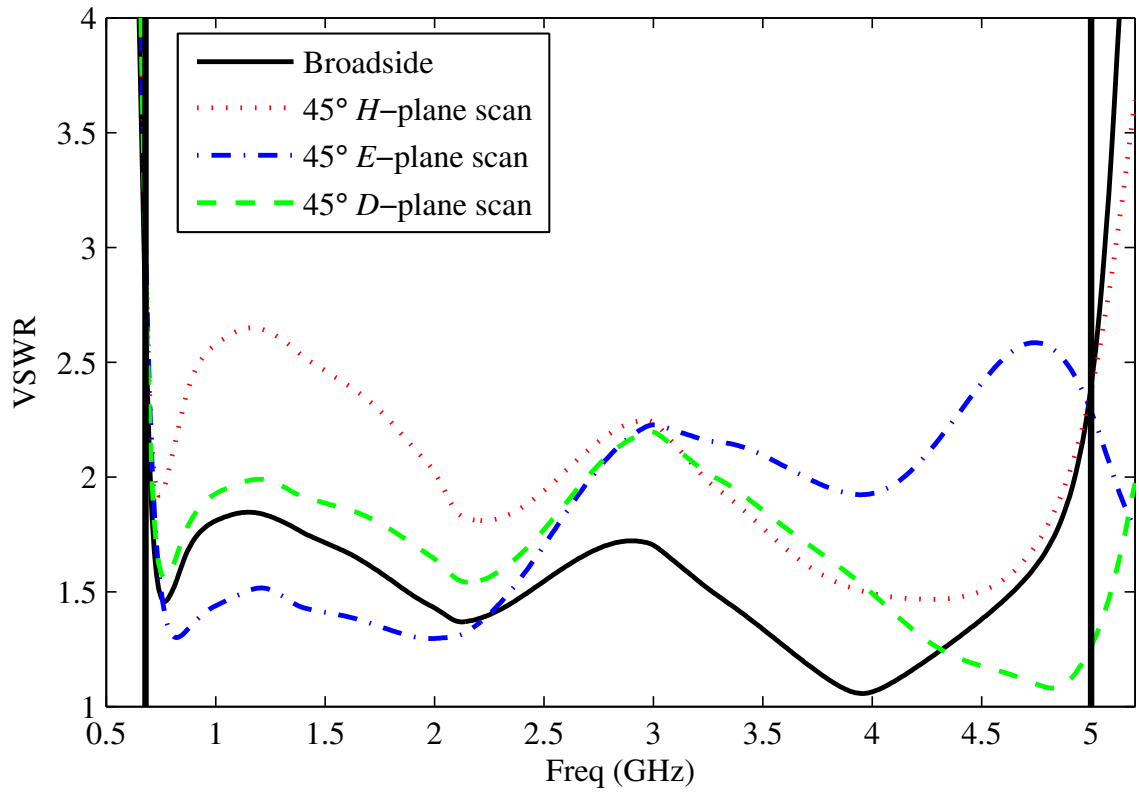
Figure 6.3: Simulated VSWR of TCDA-IB, matched from 0.68-5.0GHz (7.35:1 BW). This simulation differs from that of Fig. 5.12 only in that the entire "double" unit cell is modeled with both baluns and the Wilkinson combiner.
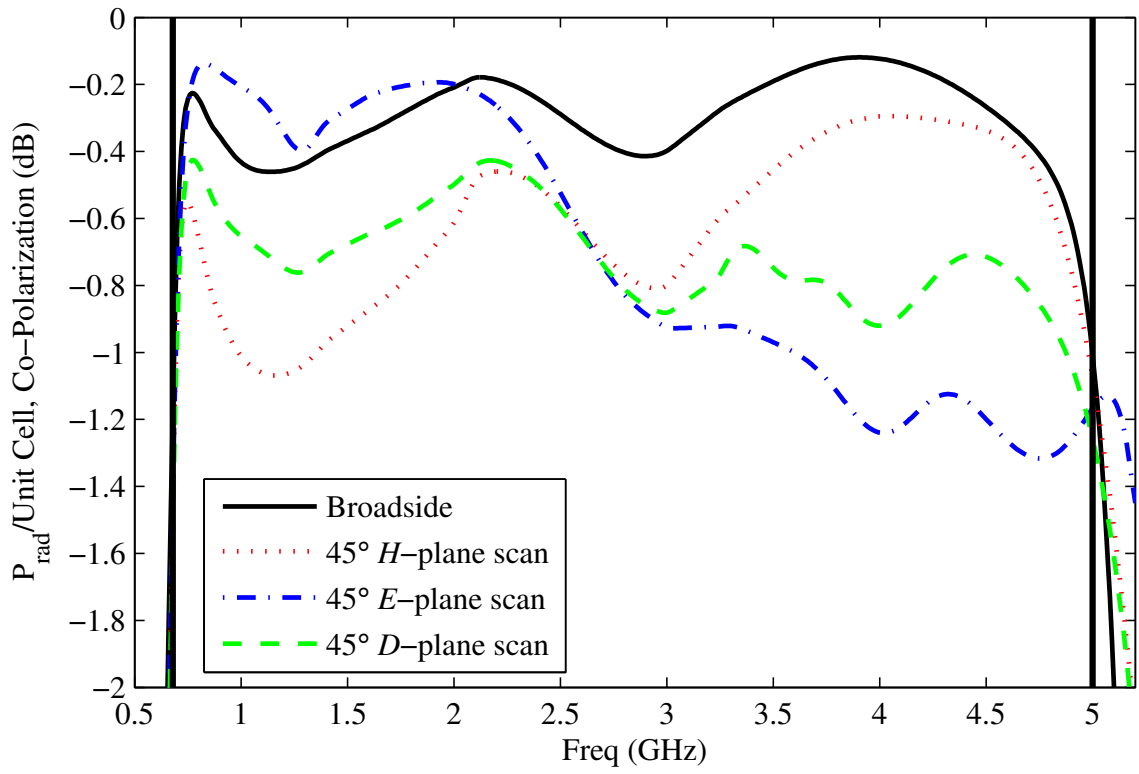
Figure 6.4: Simulated co-polarized gain per unit cell of TCDA-IB.
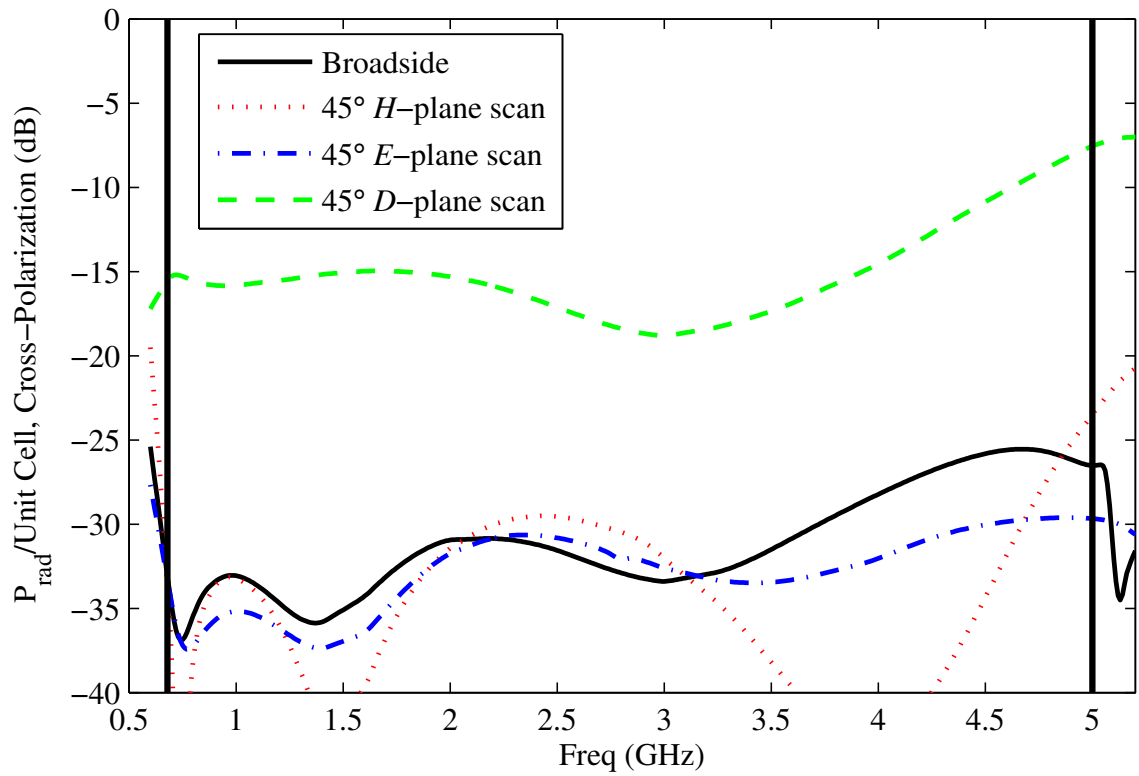
Figure 6.5: Simulated cross-polarized gain per unit cell of TCDA-IB using Ludwig's third definition, illustrating excellent cross-polarization in the principal planes and better than -15 dB over most of the band in the D-plane.

introduced to connect the upper and lower Z_{OC} grounds and tie the Z_{feed} trace to the Z_{OC} trace at the dipole feed point.

Before attempting to optimize the full unit cell shown in Fig 6.2, a rectangular "half" element (*c.f.* Fig. 5.10b) was designed, based on the optimized equivalent circuit. Simple models for the transmission line structures Z_{OC} and Z_{SC} were used to estimate initial dimensions of the balun, as determined by the corresponding circuit values. The design was then simulated using *Ansys HFSS* v.14, and the response was compared to that of the equivalent circuit. Because the effects of adjusting a given parameter could be quickly analyzed with the circuit model prior to running computationally expensive simulations, the array could be fine-tuned quickly and efficiently by iterating between *HFSS* and the equivalent model. The final optimized dimensions are given in Table 6.1, and the comparison of the equivalent circuit to the full-wave simulation (of the "half" unit cell) is shown Figs. 5.11-5.12. Although the agreement between the full wave simulated response and the equivalent circuit is not perfect, it is sufficient to enable efficient fine-tuning of the array.

Two such "half" elements were then combined to form a full square unit cell (as shown in Fig. 6.2). The two 100 Ω feeds are combined by a Wilkinson divider below the ground plane to form a single 50 Ω microstrip trace. The simulated VSWR for the complete "double" unit cell, measured at the common 50 Ω input is given in Fig. 6.3. The array achieves 7.35:1 impedance bandwidth (0.68-5.0 GHz) with VSWR≤2 at broadside, and VSWR≤2.65 when scanning to 45° in all planes. The realized gain and radiation efficiency of the array as seen in Fig. 6.4a is high, with total ohmic and mismatch losses <0.5 dB at broadside and <1.3 dB over scan volume. The cross-polarization is shown in Fig. 6.5 is also low (using Ludwig's third definition [98]),

except in the D-plane at the top of the band, where it exceeds -10 dB. However, the cross polarization is reduced when a second orthogonal polarization is added, as we show below in Section 6.3.

The width of all printed lines and spaces is $\geq$0.13 mm (10 mil) and the entire structure can be easily manufactured using low-cost printed circuit board technology. Standard PCB fabrication allows for 5 mil lines and spaces, the therefore scaling the design to operate at frequencies up to $\sim$10GHz is straightforward. However, when scaling to frequencies above X-band, reoptimization to accommodate manufacturing tolerances may result in reduced bandwidth. Nevertheless, the smallest features (e.g. width of the feed trace, PCB thickness, via size, etc.) are not resonant dimensions and would not necessarily need to be directly scaled.

If desired, T/R modules or phase shifters can be integrated directly on the circuit board below the ground plane, after the Wilkinson divider, resulting in a low cost compact electronically scanning array. This level of integration is not possible with a standard TCDA, because of the need for external baluns located between the array and electronics.

6.2.1 Practical Considerations and Design Rules for the TCDA-IB

There are several practical issues that must also be considered when designing the TCDA-IB to avoid undesired modes and detrimental resonances. The problem of common mode currents is well known for tightly coupled and connected arrays. These common modes were described in [49] and [111], and correspond to a resonance between adjacent vertical feeds. For the TCDA-IB, this mode forms when d_H (the distance between the feed boards) reaches a half-wavelength. However, excessive

reduction of d_H results in oversampling and increased T/R module costs. For our design, the element spacing in both dimensions is set at 28 mm, which is 93% of the $\lambda/2$ grating lobe spacing at 5 GHz.

Another undesired resonance can occur within the balun due to parasitic coupling between the open circuited stub Z_{OC} and the trace Z_{feed}. We avoid this resonance by extending one of the dipole arms as a shield for the Z_{OC} stub, which converts it from microstrip to stripline (see Fig. 6.2). This also helps to lower the impedance Z_{OC}, further improving the balun's bandwidth.

Surface waves present another possible source of resonances in scanning arrays. Although high contrast superstrate dielectrics can improve the impedance bandwidth at broadside (c.f. Fig. 4.15), they may also support surface waves that can cause scan blindness. Therefore the selection of the superstrate material requires careful consideration between the required bandwidth and scanning performance. Here, we avoid surface waves by using a superstrate with a relatively low dielectric constant of $\epsilon_{sup} = 1.7$, and an air substrate. However, if the array did not need to scan, a superstrate dielectric constant of $\epsilon_{sup} \approx 5$ would result in greater bandwidth and a thinner array.

When connecting the two baluns together to form a single feed for the double element, it might be assumed that a reactive split would be desirable so as to minimize resistive losses. However, this allows a loop resonance to form between the two elements when the array is scanned. This resonance is prevented by using a matched Wilkinson divider, which introduces isolation between the two balun circuits. Unlike the standard Wilkinson design with three 50 Ω ports, this design has a 50 Ω input and two 100 Ω outputs, resulting in a frequency independent impedance match. The

isolation between the output ports does depend on the electrical length of the divider and is therefore band limited. However, it is not necessary to maintain perfect isolation in order to suppress the loop resonance, and a single stage divider is sufficient. We note that unlike what was claimed in [27], we did not observe unacceptable losses when scanning our double element design in the E-plane. As seen in Fig. 6.4, the worst-case loss is 1.3 dB at the top of the band, which represents ∼0.5 dB reactive loss due to impedance mismatch and ∼0.8 dB ohmic losses. To minimize the space required below the ground plane, the Wilkinson is meandered as shown in Fig. 6.2.

The vertical PCB is installed in the ground plane through a slot which is sufficiently wide to allow the microstrip feed and Wilkinson to pass through. However if the slot is too long, it may resonate due to the dielectric loading from the PCB. Therefore vias are introduced at the edges of the PCB card in the slot to reduce its electrical width to less than $\lambda/2$ in the dielectric, as shown in Fig. 6.2. Electrical connection between the PCB ground and the array ground plane is maintained along the back of the slot with conducting gasket or fingerstock. Additional construction details, as well as measured results from an earlier TCDA-IB design are provided below in Section 6.4.

6.3   A Dual-Polarized TCDA-IB

Many wideband array applications require dual-linear or dual-circular polarizations. Therefore, it may be desired to add a second orthogonal set of elements to the TCDA-IB array. For arrays printed on vertical printed circuit boards, a common manner of constructing a dual-polarized array is to use an "egg-crate" construction, in which partial slots are cut to allow crossing boards to fit together as shown in Fig.
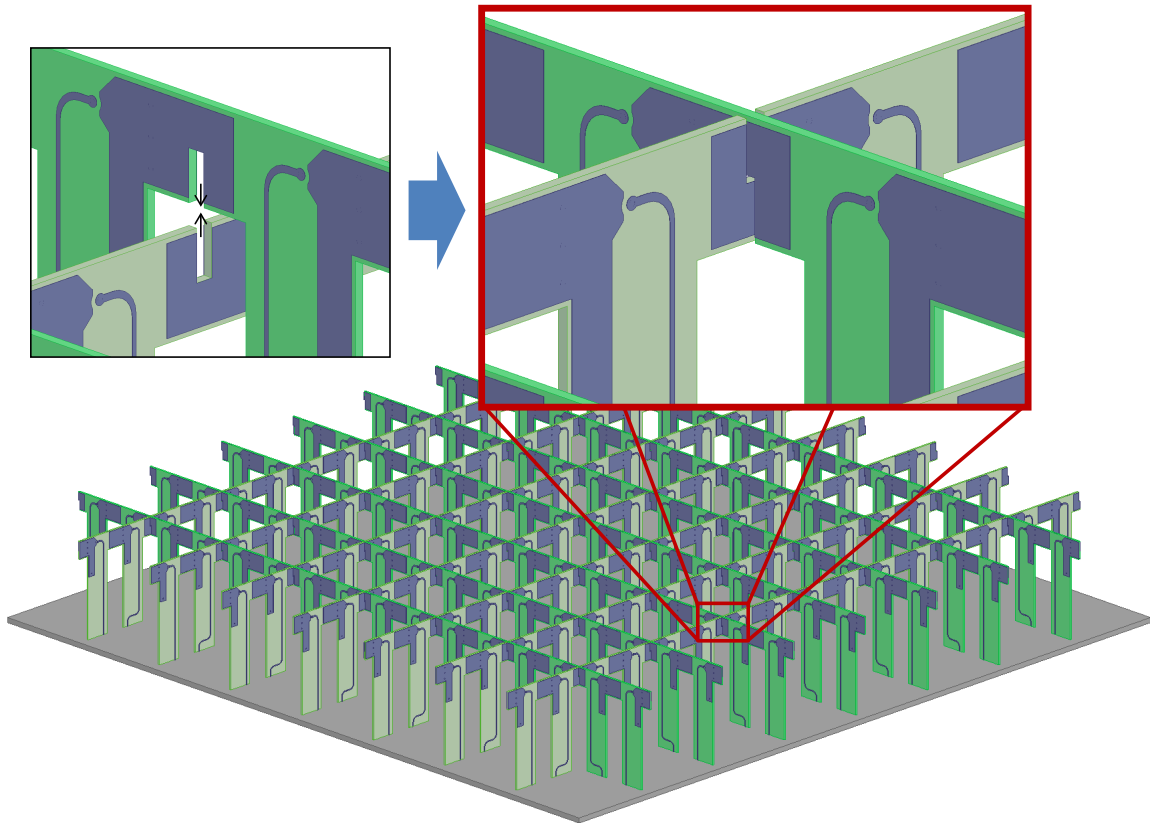
Figure 6.6: "Egg-crate" implementation of dual-polarized TCDA-IB. Orthogonal elements intersect at the coupling capacitance via a partial slot cut in both boards. The elements are otherwise unchanged from the single-polarized design of Fig. 6.2. A small gap is preserved between the orthogonal elements and no soldering is required at the joint.

Dual-Polarized TCDA-IB, VSWR
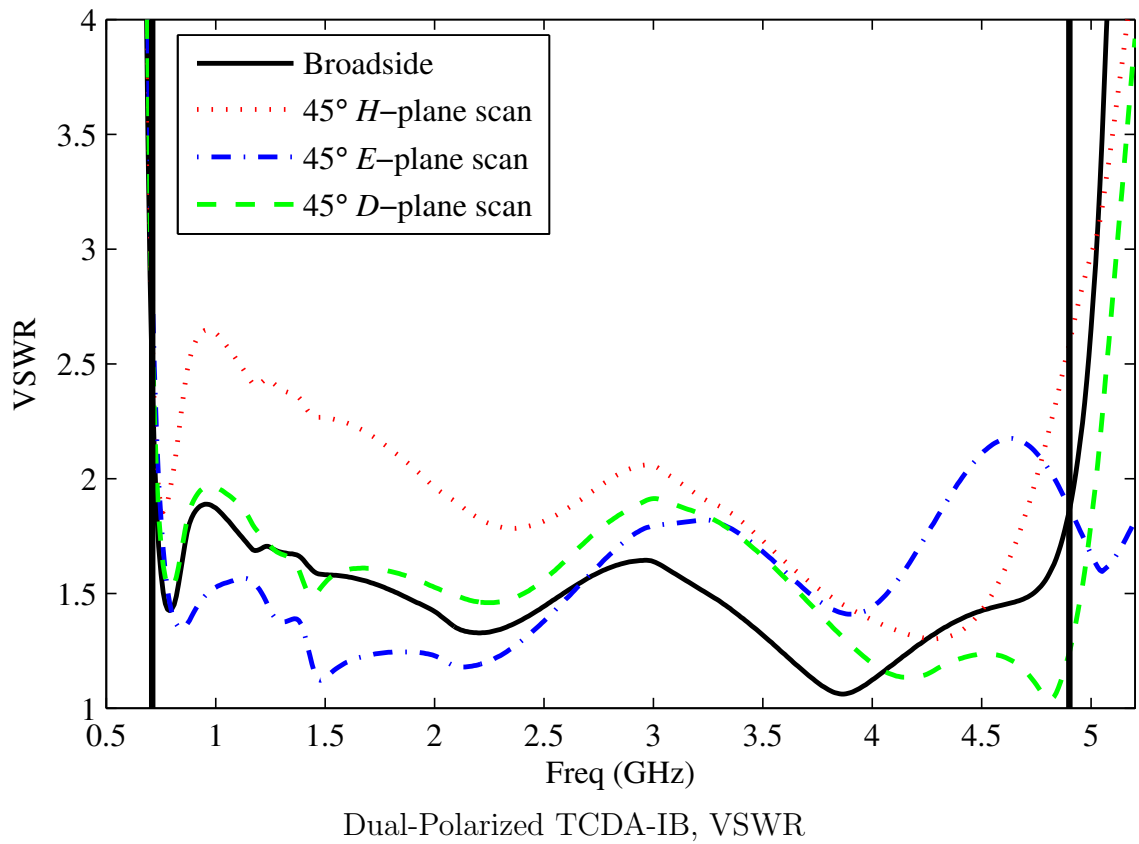
Figure 6.7: Simulated VSWR of the dual-polarized TCDA-IB unit cell, with one polarization excited and the other terminated. Array is matched to <2.65:1 in all scan planes from 0.71-4.9GHz
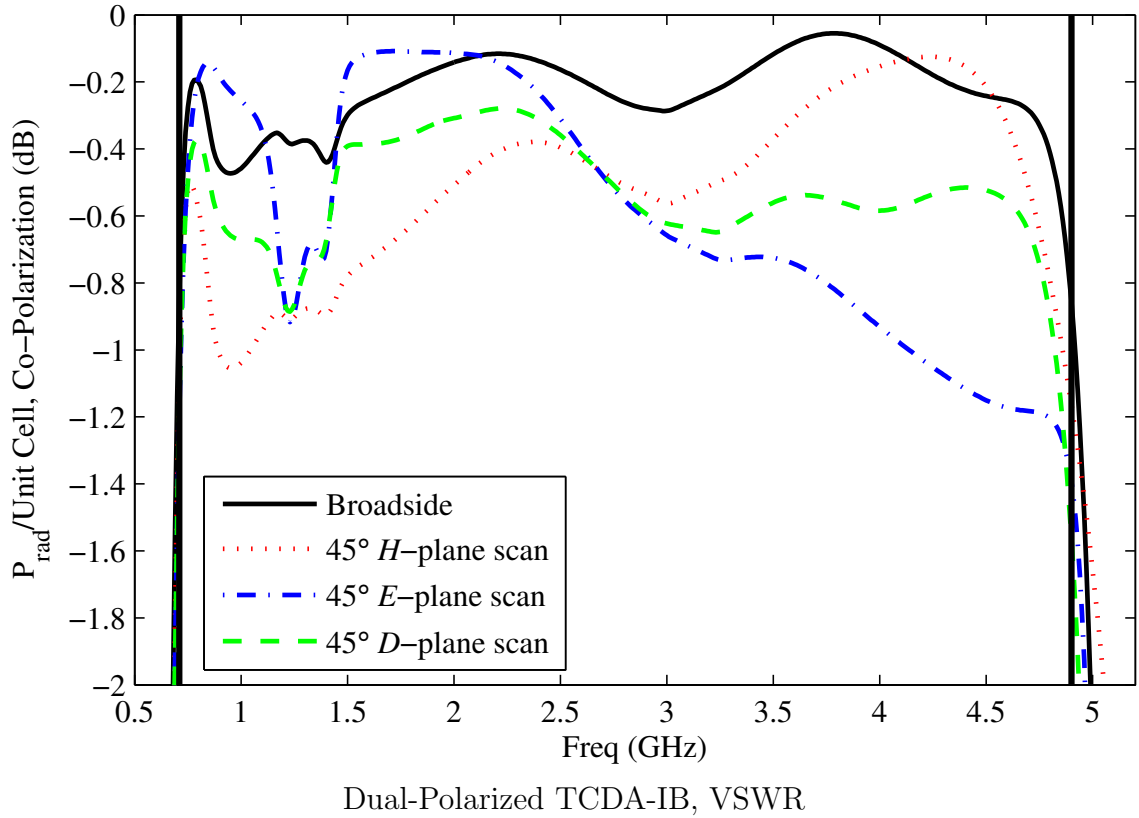
Figure 6.8: Simulated co-polarized gain of the dual-polarized TCDA-IB unit cell, with one polarization excited and the other terminated.
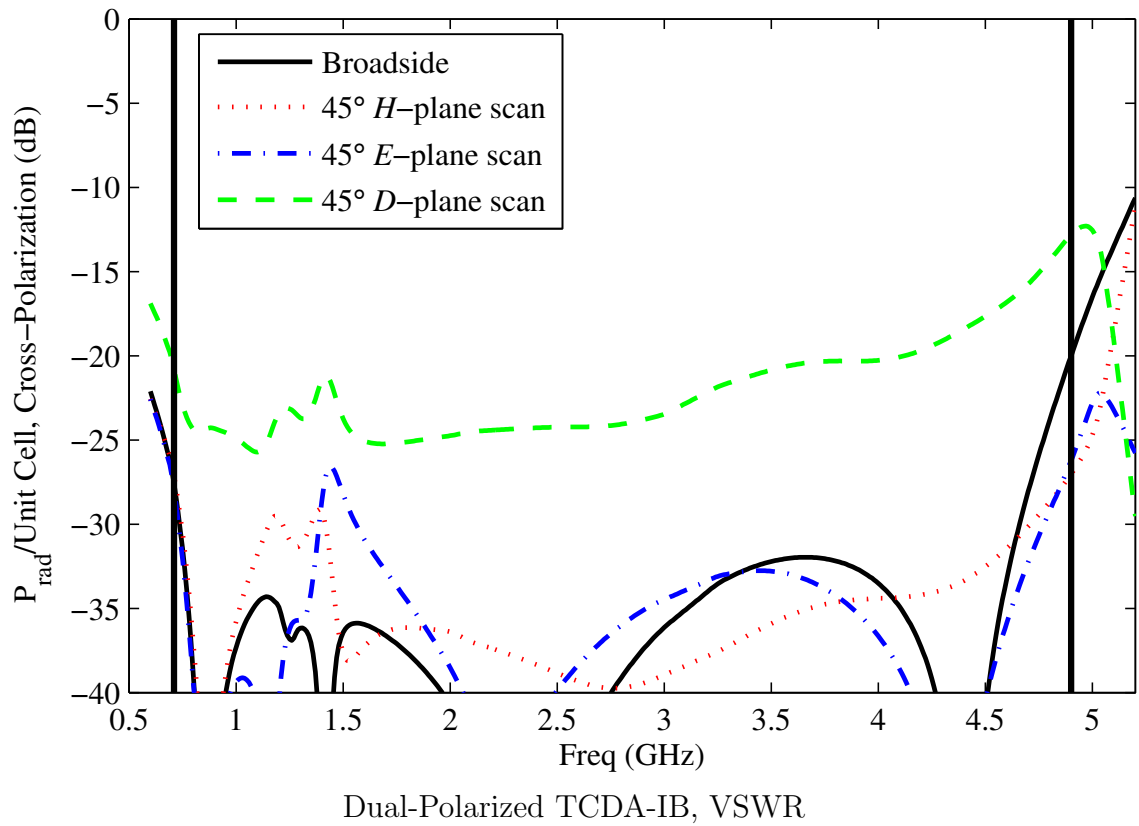
Figure 6.9: Simulated cross-polarized gain of the dual-polarized TCDA-IB unit cell, with one polarization excited and the other terminated.
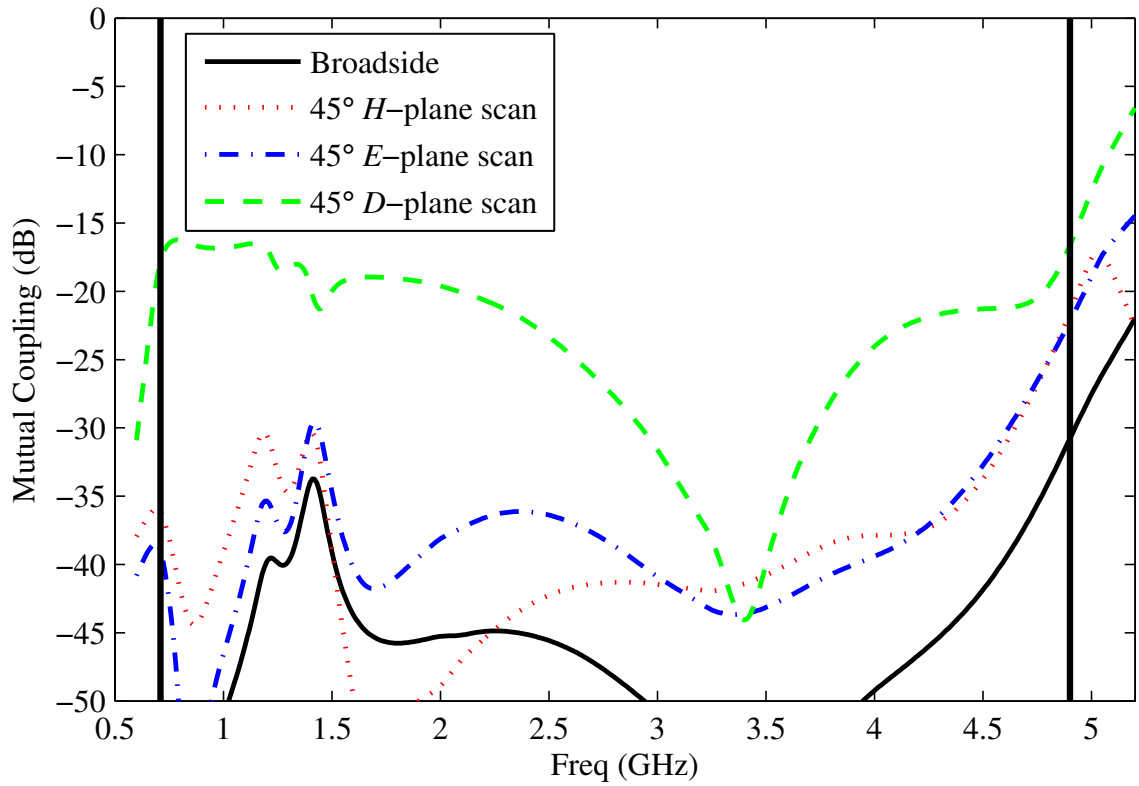
Figure 6.10: Simulated coupling between the neighboring orthogonal elements within the dual-polarized TCDA-IB array of Fig. 6.6.

6.6. To minimize interference between baluns, the boards do not cross at the feed centers, but rather cross at the overlapping capacitive sections yielding elements with offset phase centers, similar to [49].

By leaving a small $0.010''$ gap between the metallization of the orthogonal elements, no electrical connection or soldering is required at the joints, allowing for simple assembly and maintenance of the dual-polarized array. Parametric analysis indicates that the gap may be varied from $0.005\text{-}0.015''$ without significant impact on the performance of the array. The gap size may be controlled with a dielectric shim or tape, or by adding unmetallized outer layers to the PCB stackup. Other than the addition of the slot and an adjustment of w_{cap} to 4.8 mm, the dual-polarized element has not been re-tuned and all dimensions are unchanged from Table 6.1.

The simulated VSWR, co-polarized gain, and cross-polarized gain of the dual polarized TCDA-IB unit cell are shown in Figs. 6.7-6.9. Other than a slight reduction in impedance bandwidth to 6.9:1 (which may be improved by additional fine tuning of the dual-polarized design), the VSWR and co-polarized gain are similar to the single polarized TCDA-IB design (*c.f.* Figs. 6.3-6.5). However, the addition of the second polarization has reduced the cross-polarization by $\sim$5 dB from the single polarized design (*c.f.* Fig. 6.5). Specifically, the cross polarization is $<$ -20 dB over most of the band, with a worst case of -13 dB in the 45° D-Plane at the top of the band. The port-to-port coupling between the orthogonal elements is shown in Fig. 6.10 and is $<$-30 dB at broadside and $<$-15 dB when scanning in the D-plane.
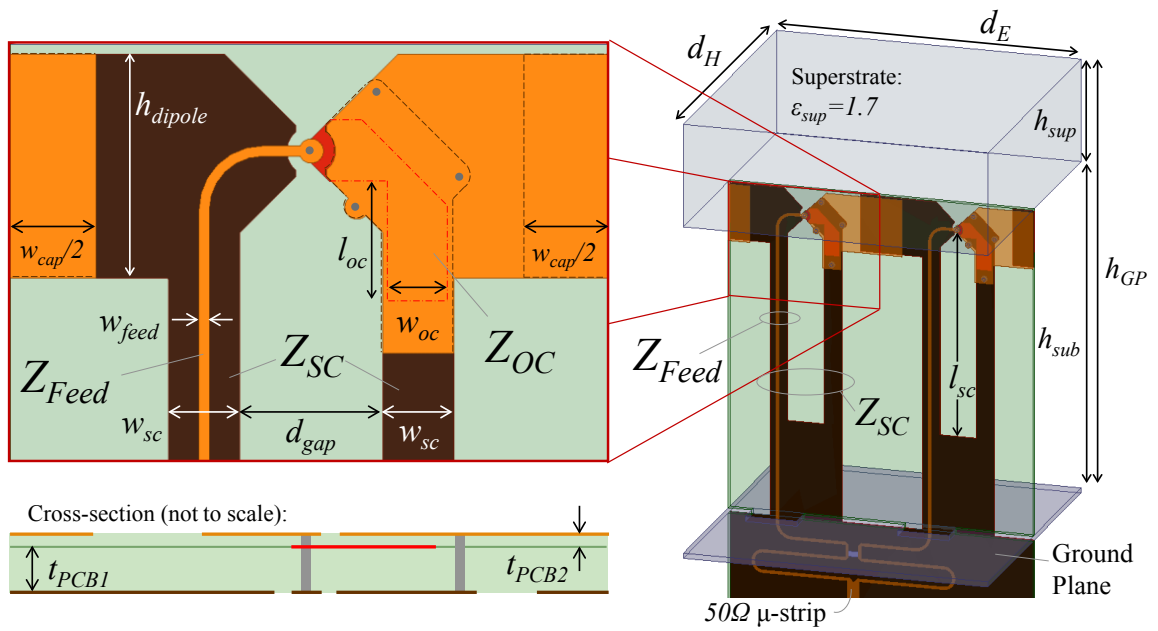
Figure 6.11: Sketch of the TCDA-IB design used for the 8×8 prototype array. Dimensions are listed in Table 6.2. This represents an earlier design with slightly reduced bandwidth than the final TCDA-IB of Fig. 6.2.

Table 6.2: Dimensions of TCDA-IB Prototype

d_E	30 mm
d_H	30 mm
h_{sub}	32.3 mm
h_{sup}	12.7 mm
h_{GP}	45 mm
h_{total}	63.5 mm
h_{dipole}	5.6 mm
w_{cap}	4.3 mm
w_{feed}	0.13 mm
l_{sc}	20.6 mm
l_{oc}	3 mm
w_{sc}	1.8 mm
w_{oc}	1.5 mm
d_{gap}	3.6 mm
t_{PCB1}	16 mil 4003C
t_{PCB2}	4 mil 4450B
ϵ_{sup}	1.7
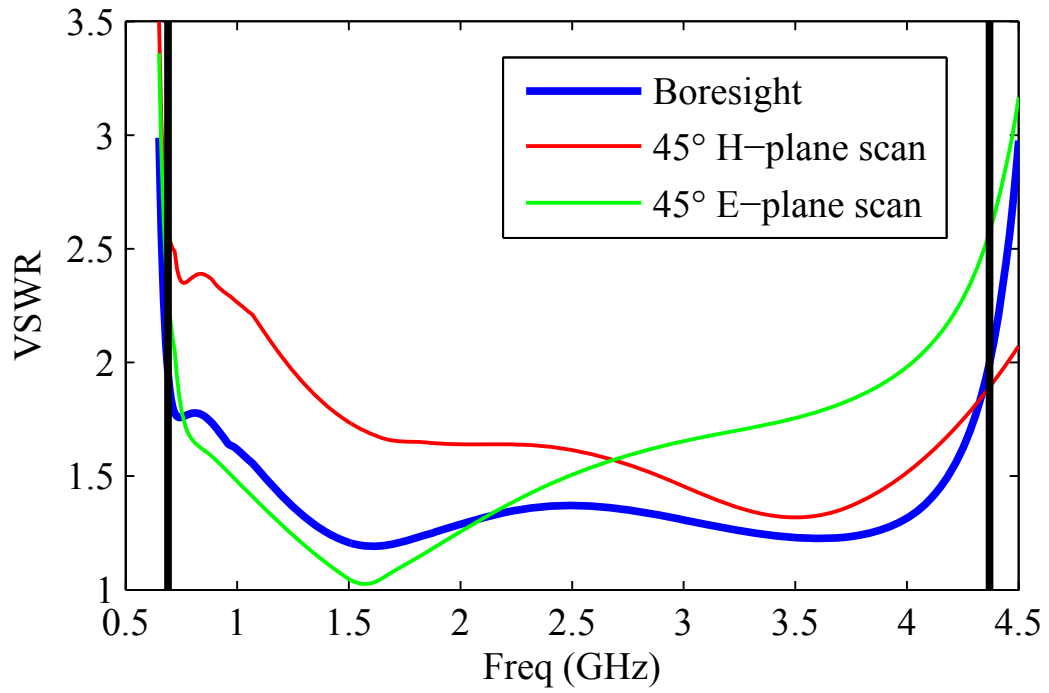
Figure 6.12: Simulated VSWR of the priliminary TCDA-IB design from Fig. 6.11. The array is matched from 0.69-4.37GHz with VSWR<2.5 over a ±45° scan volume
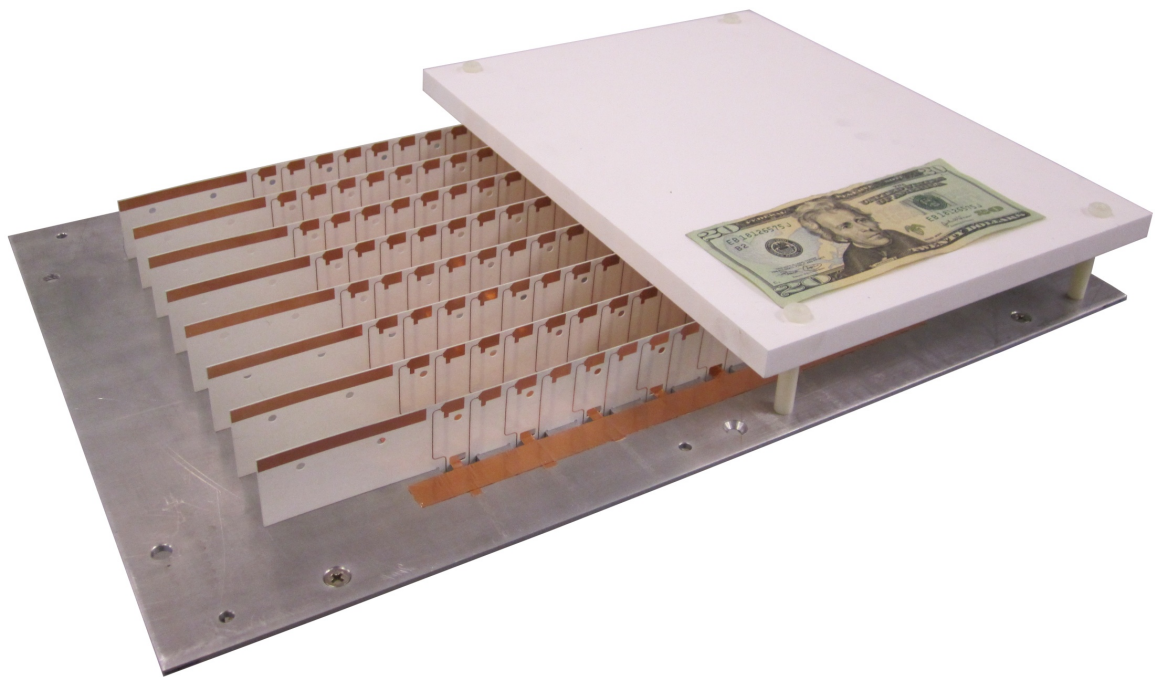
Figure 6.13: Photograph of the fabricated 8×8 TCDA-IB prototype with half of the superstrate removed to show the array details. Note the extended dipole arms of the edge elements.
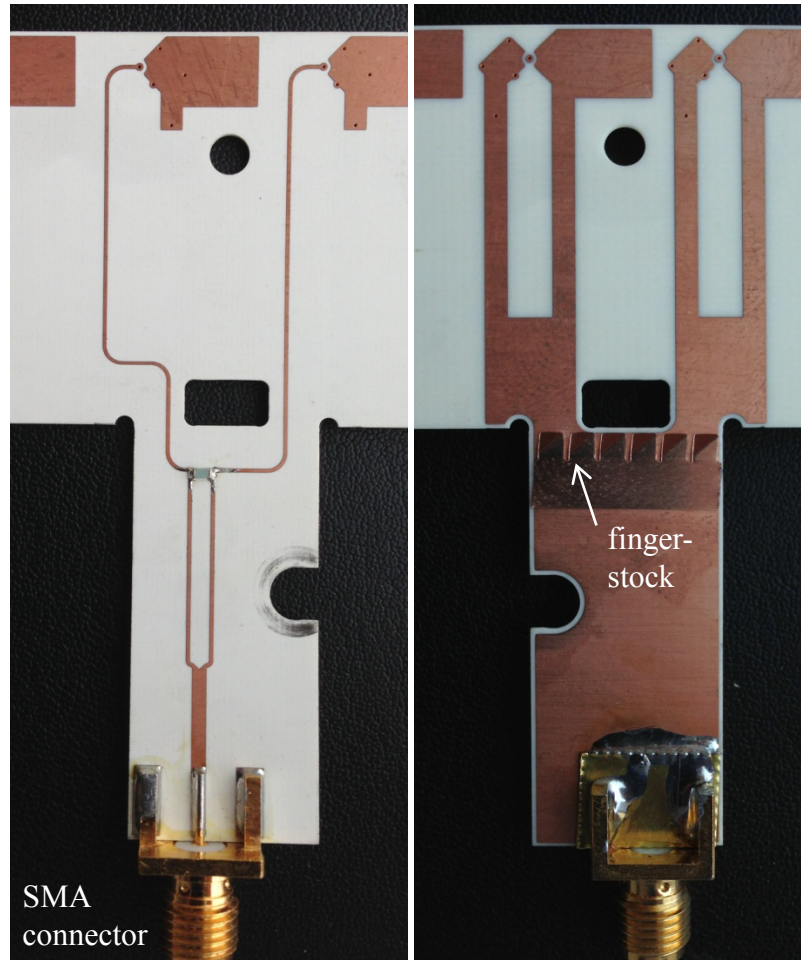
Figure 6.14: Closeup of single element of TCDA-IB prototype element, showing both front and back metallization.

Figure 6.15: Closeup of TCDA-IB prototype aperture showing element details.
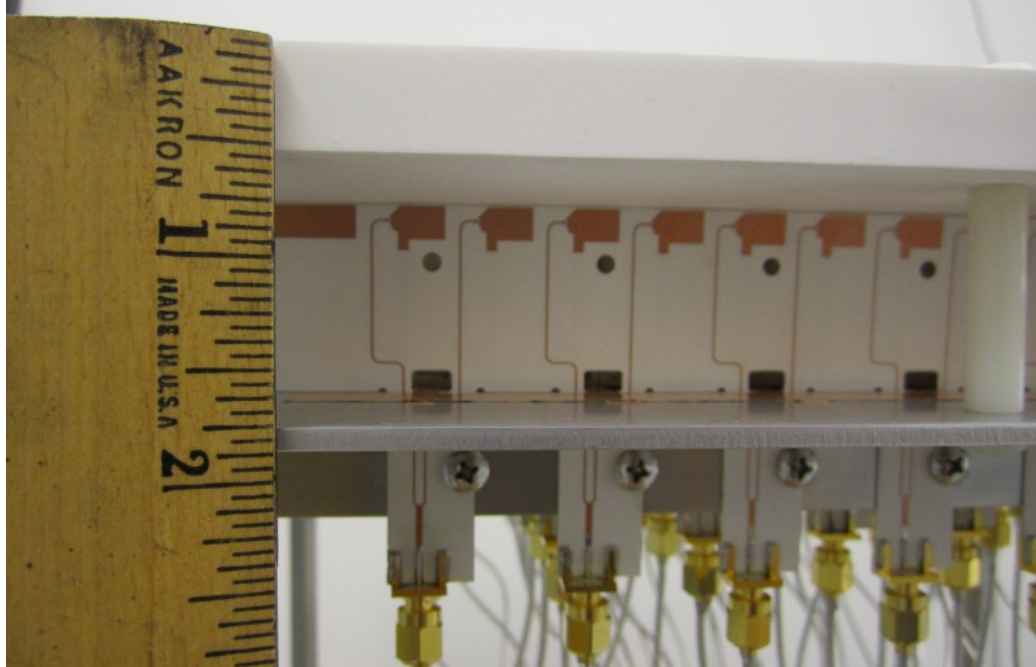
Figure 6.16: Profile of TCDA-IB prototype, showing total height above ground plane of 1.75″.

6.4 Design and Construction of an 8×8 Prototype TCDA-IB Array

In order to verify the performance of the TCDA-IB concept, an 8×8 prototype TCDA-IB was constructed. The design is shown in Fig. 6.11, and is similar to that described in Section 6.2. However, the prototype design was optimized before the development of the improved scanning circuit model described in Section 5.2. As a result it has a somewhat reduced operational bandwidth of 6.3:1 (0.69-4.37 GHz). The simulated VSWR for the prototype design is shown in Fig. 6.12, and the dimensions are provided in Table 6.2.

An 8×8 array was constructed from this design, as pictured in Figs. 6.13-6.18. To terminate the edges of the array, the dipole arms were extended by an additional 60

Figure 6.17: Detail of TCDA-IB prototype underside showing element mounting and coaxial connectors.

Figure 6.18: Entire TCDA-IB prototype array showing 64:1 power divider network.

mm, effectively adding 2 rows of short-circuited elements. Terminating the array in this manner was suggested in [112] as a method to improve gain bandwidth without reducing efficiency, which can suffer when using resistively terminated edge elements.

The array was constructed on a $12''\times18''$ aluminum plate and was covered by a 12.7 mm ($0.5''$) thick superstrate ($\epsilon_{sup} = 1.7$) of the same size, held in place by small nylon rods around the perimeter of the array. The height of the array is 45 mm ($1.77''$) from the top of the superstrate to the ground plane, and 63.5 mm ($2.5''$) to bottom of the Wilkinson. The active area of the 64 elements is 576 cm^2 (89 in^2). When the extended dipole arms are included, the total area of the array is 864 cm^2 (134 in^2). Rectangular holes were cut in the ground plane allowing the vertical cards to be installed, which were held in place by right angle brackets below the ground plane. A small piece of copper fingerstock was used to maintain electrical contact between the array ground and the vertical PCB ground layer, as shown in Fig. 6.13b. A 50 Ω SMA connector was installed on each element, which is in turn fed by a matched 64:1 divider located below the ground plane. The array was scanned by adjusting the lengths of the feed cables.

To allow room for the SMA connector, the opening in the ground plane was large enough to introduce a resonance, so conductive tape was used to reduce the hole size after the boards were installed, as seen in Fig. 6.13b. Note that this is unnecessary in the updated design of in Fig. 6.2, due to the introduction of grounding vias in the PCB.
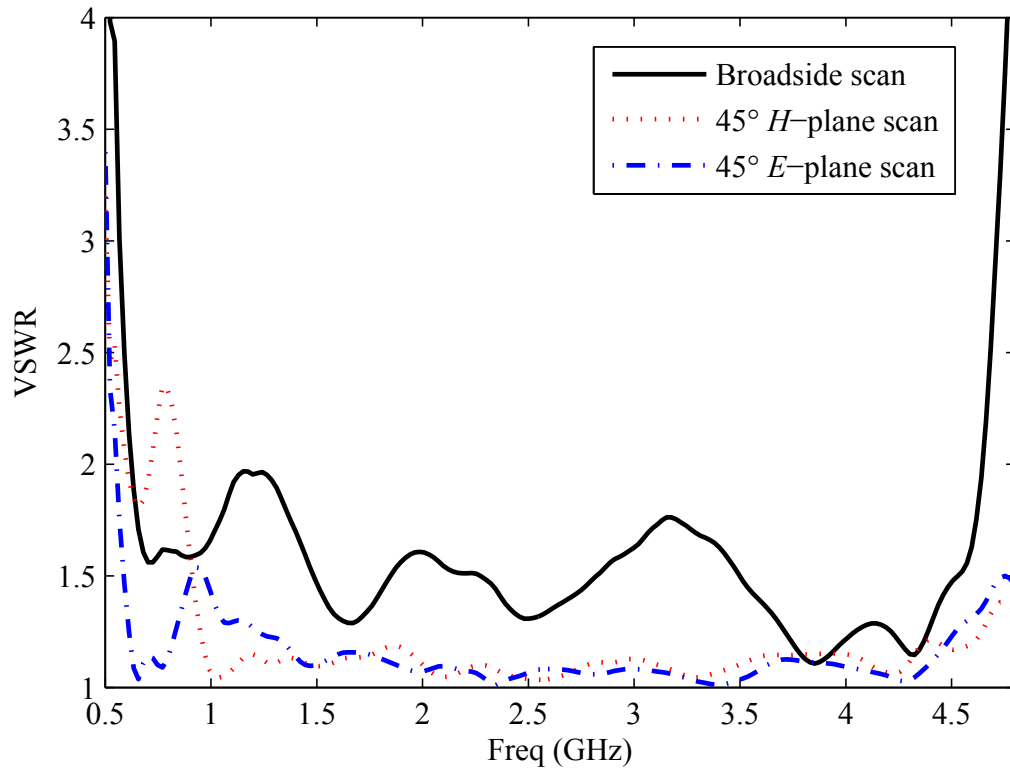
Figure 6.19: Measured VSWR of the TCDA-IB prototype, measured through a 64:1 matched power divider. The return loss was compensated for the round trip insertion loss of the power divider and cables. Scanning VSWR is artificially low due to out-of-phase reflections absorbed within the power divider.
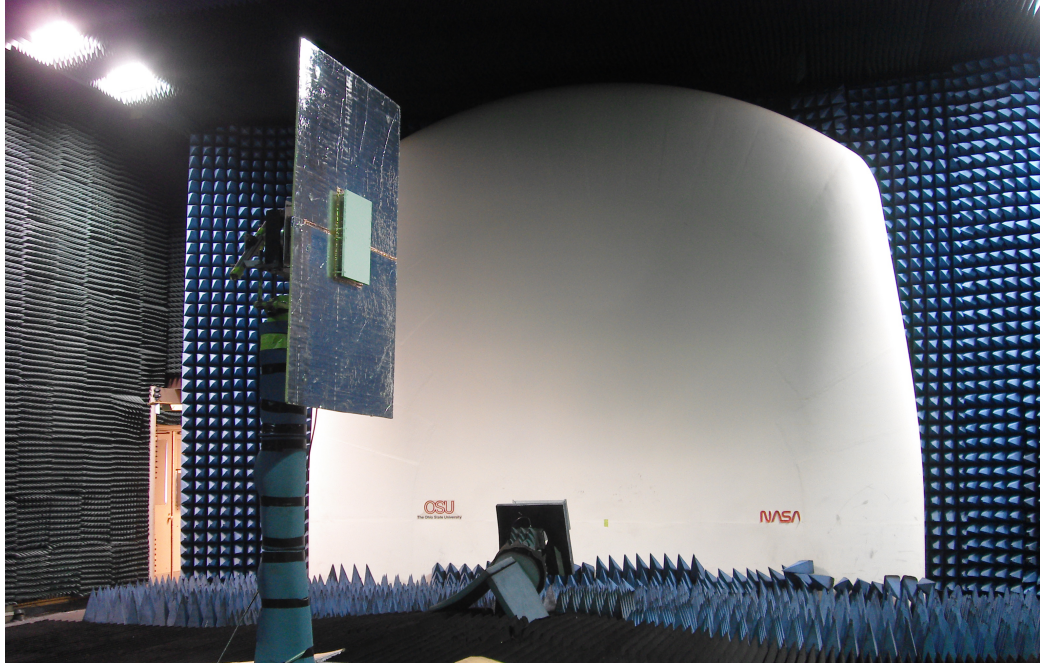
Figure 6.20: The prototype TCDA-IB was mounted on a $4' \times 6'$ ground plane and measured in the anechoic compact range at The Ohio State University.

6.5 Measured TCDA-IB Results

The measured VSWR of the array is shown in Fig. 6.19 and is less than 2:1 at broadside and under 2.5:1 while scanning to $\pm 45°$ in both planes over the entire operational band (0.67-4.37 GHz). The measurement was taken at the common port of the 64:1 divider, and the VSWR data has been compensated by the round trip insertion loss of the divider and cables. Note that when scanning, the reflections from the elements are not in-phase and thus the reflected power is mostly absorbed within the power divider, resulting in artificially low measured VSWR at the common port.
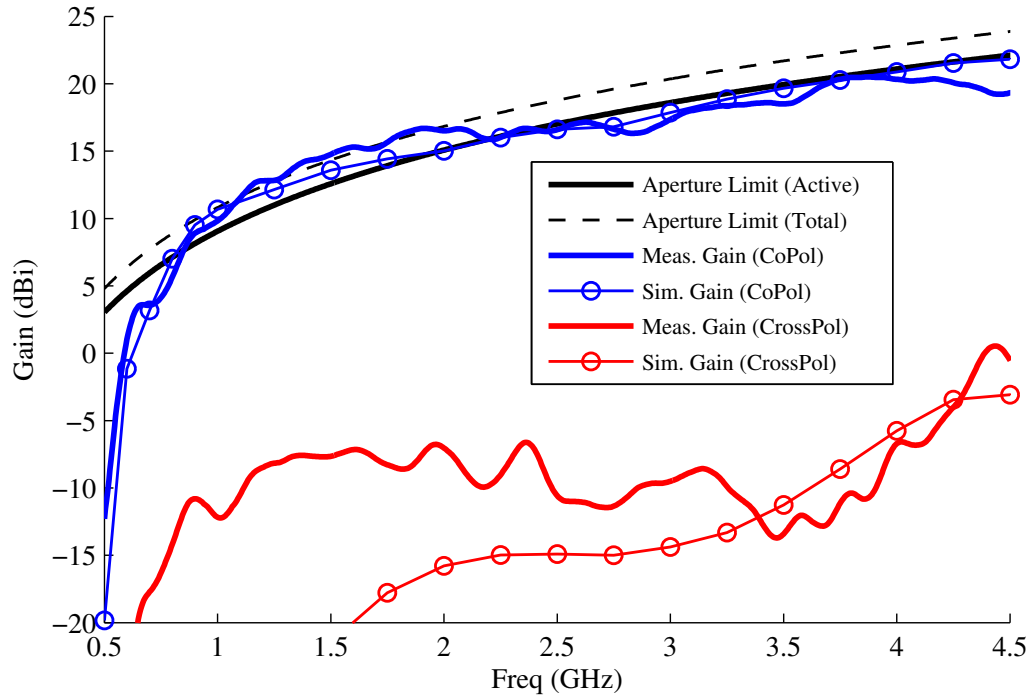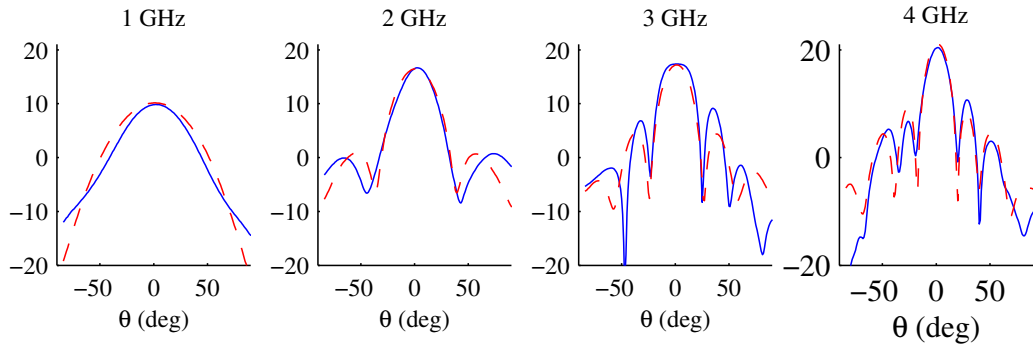
Figure 6.21: Measured co- and cross-polarized gain of the 8×8 TCDA-IB prototype at broadside. (a) Gain at broadside vs. frequency. Also plotted is the theoretical aperture limit for the array, calculated using the area of the active elements, as well as the total area including the extended dipole arms. (b) Measured patterns in E-plane (blue solid) and H-plane (red dotted) at several frequencies
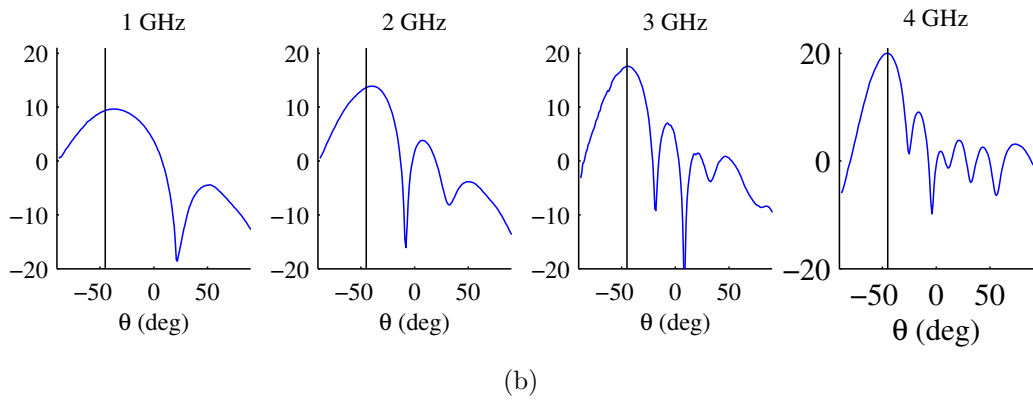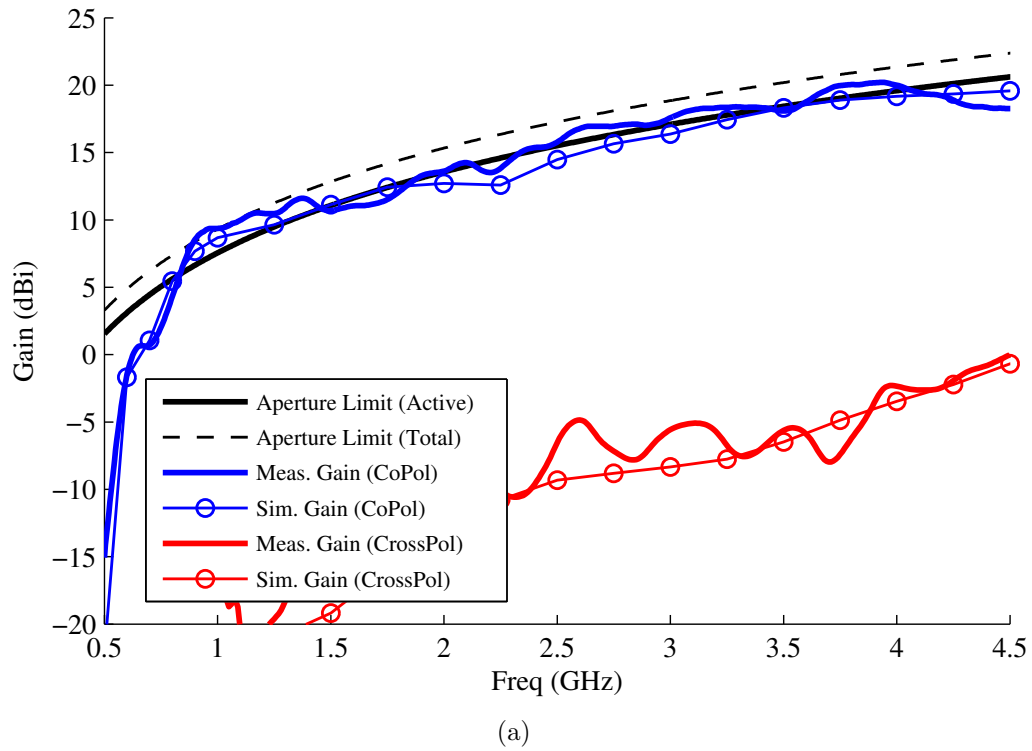
Figure 6.22: Measured gain of the TCDA-IB prototype, scanning to 45° in the H-plane. (a) Gain vs. frequency at nominal beam center. (b) Gain pattern in H-plane at several frequencies. The nominal beam center at 45° is noted by a vertical line.

(a)

(b)
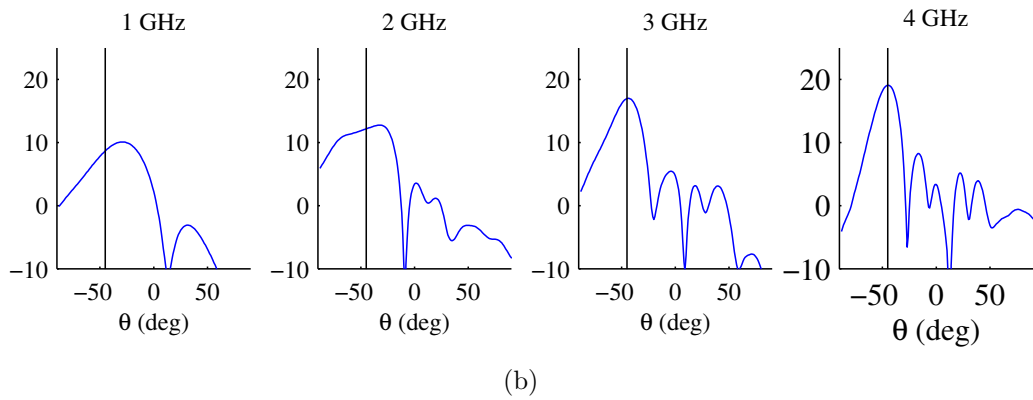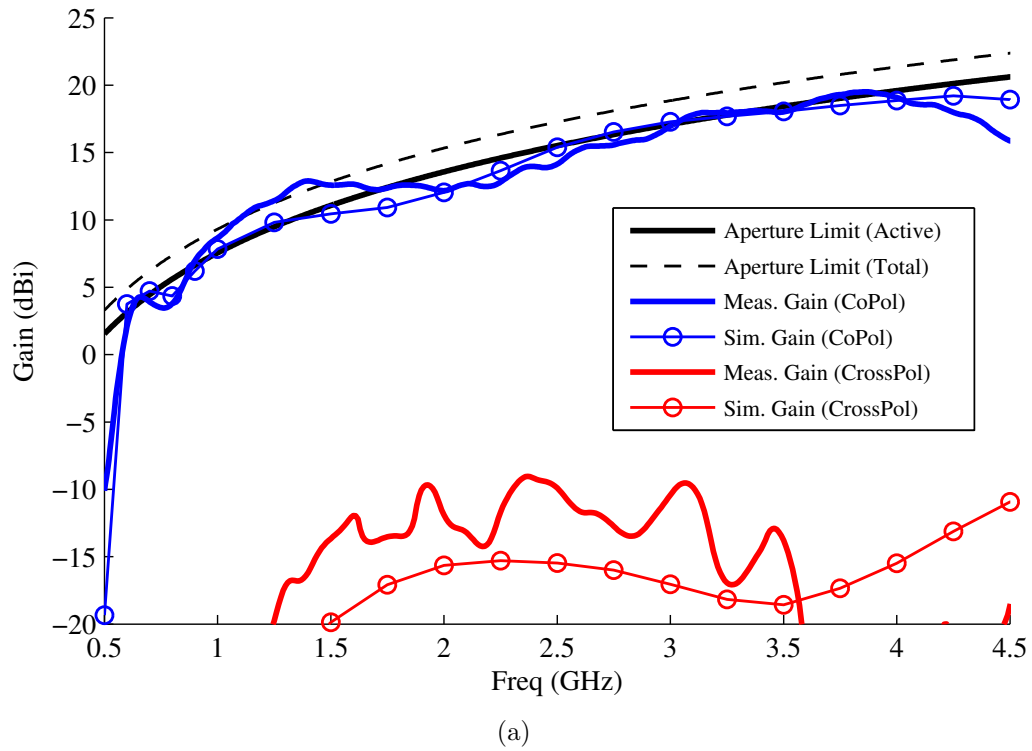
Figure 6.23: Measured gain of the TCDA-IB prototype, scanning to 45° in the *E*-plane. (a) Gain vs. frequency at nominal beam center. (b) Gain pattern in *E*-plane at several frequencies. The nominal beam center at 45° is noted by a vertical line.
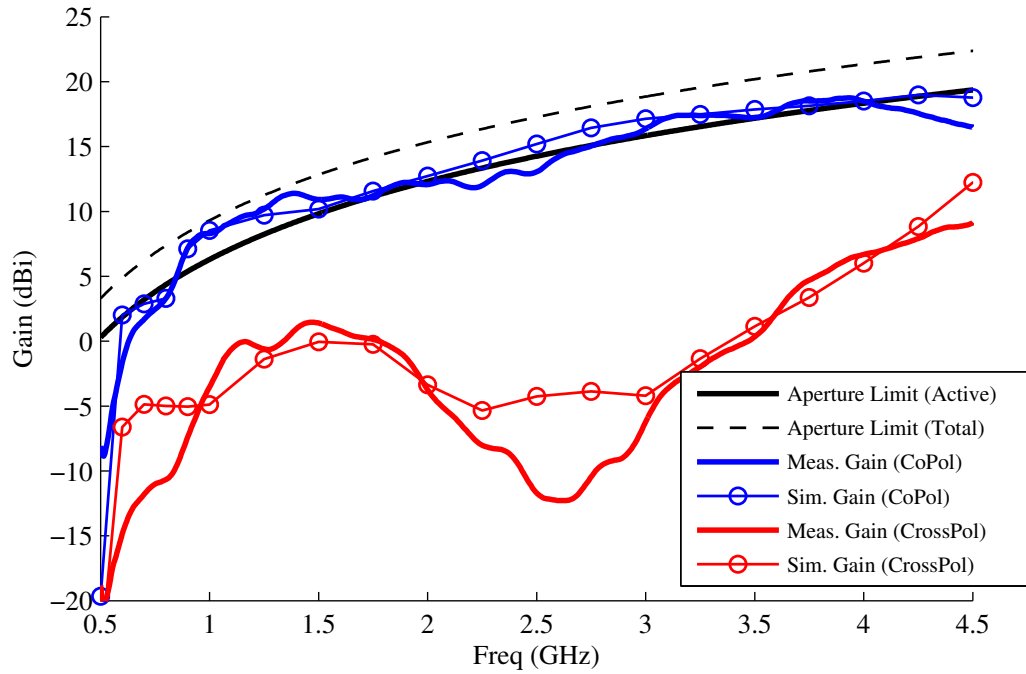
(a)
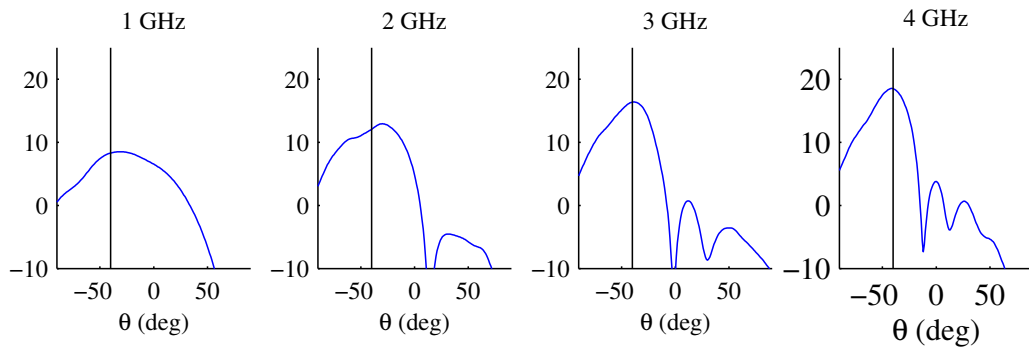
(b)

Figure 6.24: Measured gain of the TCDA-IB prototype, scanning to 45° in the *D*-plane. (a) Gain vs. frequency at nominal beam center. (b) Gain pattern in *D*-plane at several frequencies. The nominal beam center at 45° is noted by a vertical line.
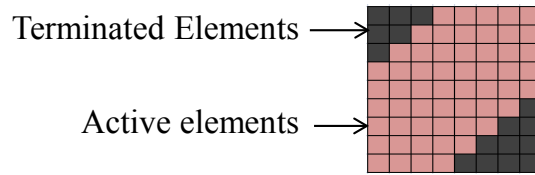
Figure 6.25: The *D*-plane feed excited only 48 of 64 elements, with the center 8 diagonals in progressive phase, and the remaining elements in two corners terminated in matched loads. The maximum gain is reduced by ∼1.25dB, and the $\hat{\theta}$ and $\hat{\phi}$ beamwidths are unequal.
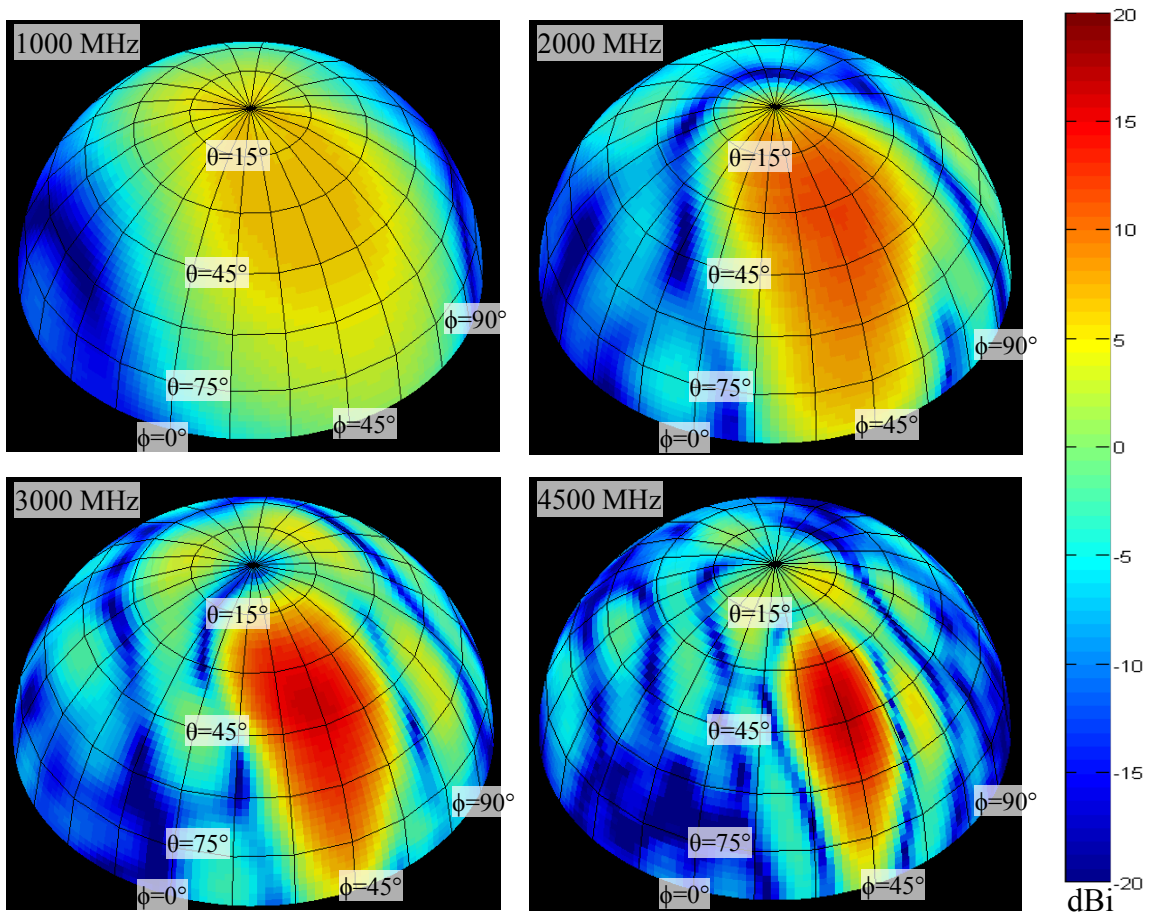
Figure 6.26: Full patterns of the TCDA-IB prototype array scanning in the *D*-plane. Nominal beam center is at $\theta = 45°$, $\phi = 45°$.

The array was then mounted to a larger $4' \times 6'$ ground plane and measured in ElectroScience Laboratory Compact Range, see Fig. 6.20. The measured gain and patterns of the array is shown in Figs. 6.21-6.26 at broadside and when scanning to $45°$ in the E-, H-, and D-planes. For the D-plane patterns, full three-dimensional patterns are depicted in Fig. 6.26.

The gain of these measurements has been offset by the measured insertion loss of the power divider and cables. The simulated gain of the finite array is also plotted, along with the theoretical gain limit for the aperture area. This limit is computed using both the area of only the actively fed elements, as well as the total area including the extended dipoles. Because the extended dipoles increase the effective aperture size in the E-plane dimension, the H-plane beam is slightly broader than the E-plane beam, especially at lower frequencies, as seen in Fig. 6.21b. Some beam broadening and beam squint is also apparent between 2-3GHz, which is thought to be due to edge-launched waves that occur in finite tightly coupled and connected arrays [113, 114]. Because such waves propagate along the dipoles, the effects are seen more strongly in the E-plane than in the H-plane. However, the gain is within 3dB of the theoretical limit in all scan-planes over a 6.6:1 bandwidth (0.67-4.37 GHz), and the measured performance matches the simulations very well. Furthermore, the cross-polarized gain (using Ludwig's third definition [98]) of the array is more than 15 dB below that of the co-polarized gain over the majority of the band, though it exceeds -10 dB in the D-plane at the top end of the band. As noted above, the cross-polarization can be significantly mitigated in a dual-polarized implementation.

Chapter 7: Wide-Angle Scanning of Tightly Coupled Arrays

In addition to wide bandwidth performance, wide-angle scanning is a critical feature of high performance antenna arrays. However, the problem of implementing a single array that simultaneously has a wide bandwidth and a large scan volume is doubly challenging, because the impedance of the radiating plane wave varies with scan angle. Wide-scan arrays therefore must not only implement a wide-band impedance match, but the load impedance is a moving target. Although this variation is relatively small and manageable for modest scan angles (e.g. 45° or less), it can become quite large and difficult to compensate for as the array scans to wide angles. Therefore increasing the scan angle typically results in more limited bandwidth.

In the previous chapter, we demonstrated an array with an integrated matching balun than scans to 45° in all scan planes over a 7.35:1 bandwidth. This involved tuning the array at a point that was a compromise between various scan conditions. However, some applications require scanning to even wider angles, e.g. $\geq 60°$, and a similar compromised tuning approach would significantly reduce the bandwidth. We would like to find an alternate solution for scanning to large angles without compromising the TCDA-IB's wide bandwidth.

Table 7.1: Optimized Bandwidth of TCDA-IB Circuit, VSWR ≤ 2.5

θ_{max}	Broadside only	H-plane only	E-plane only	Entire Scan Volume
0°	10:1	10:1	10:1	10:1
45°	N/A	11.7	11.1	7.7:1
60°	N/A	9:1	14.3:1	5.5:1
70°	N/A	7.7:1	16.7:1	3.3:1
80°	N/A	1.9:1	2.3:1	1.5:1

7.1 Optimizing for Wide-Angle Scanning

Using the equivalent circuit of Fig. 5.14, we can attempt to optimize the array for wide scan angles in the straightforward manner. Using a genetic algorithm included in the software *AWR Microware Office*, we optimized the circuit for maximum bandwidth, with VSWR$\leq$2.5:1. This was done at broadside, and for scanning to an angle θ_{max} in the E- and H-planes. We also optimized the design using all three scan positions as simultaneous constraints, providing us with an optimal "compromise" for simultaneously matching the array over the entire scan volume. In all cases, the component values are restricted to realistic values that may be realized in the TCDA-IB implementation. The superstrate dielectric constant ϵ_{sup} is fixed at 1.7 to avoid surface waves and scan blindness. The results are given in Table 7.1.

It is clear that an array optimized at a specific scan angle is capable of significantly more bandwidth than an array which operate over a large scan volume. Note that this practical issue is not accounted for in the theoretical limits from Chapters 3-4. In practice, a scanning array cannot easily be optimized for a single scan position without de-tuning the performance at other scan positions. This is another reason why practical arrays generally under-perform relative to the theoretical limits.

However, this problem could be mitigated if the array was reconfigurable so that it could be continuously re-tuned as it scanned. Rather than forcing a static array to implement a "compromised" match that is constant for every scan position, a reconfigurable array could theoretically provide an optimal match over the entire scan volume. We will next explore how such a reconfigurable array could be implemented in practice

7.2 Wide-Angle Scanning with Switchable Ground Plane

Perhaps the simplest reconfigurable element to include in an array is a variable capacitor, which can be implemented with a varactor diode. For example, a varactor could be inserted between the tips of neighboring dipoles, allowing $C_{coupling}$ to be tuned while scanning. However, this alone does not provide sufficient wideband compensation for the variation in scan impedance. After some experimenting with the equivalent circuit model, it was determined that the most critical parameter which affects the scanning response of a wideband planar array is the distance between the array and ground plane. Because the electrical length of the substrate varies with $\cos\theta$ (under TE polarization), the optimal ground plane distance when scanning to $60°$ is double that when scanned to broadside. Therefore, an array with a moveable ground plane could provide a much larger scan volume than a static array.

The equivalent circuit was once again optimized over the scan volume, but the ground plane distance and dipole capacitance were permitted to vary with scan, with all other features fixed. The resulting bandwidth improved from 5.5:1 to 8.3:1 when coving a $60°$ cone (VSWR $\leq$ 2.5:1), almost as much as the maximum possible $60°$
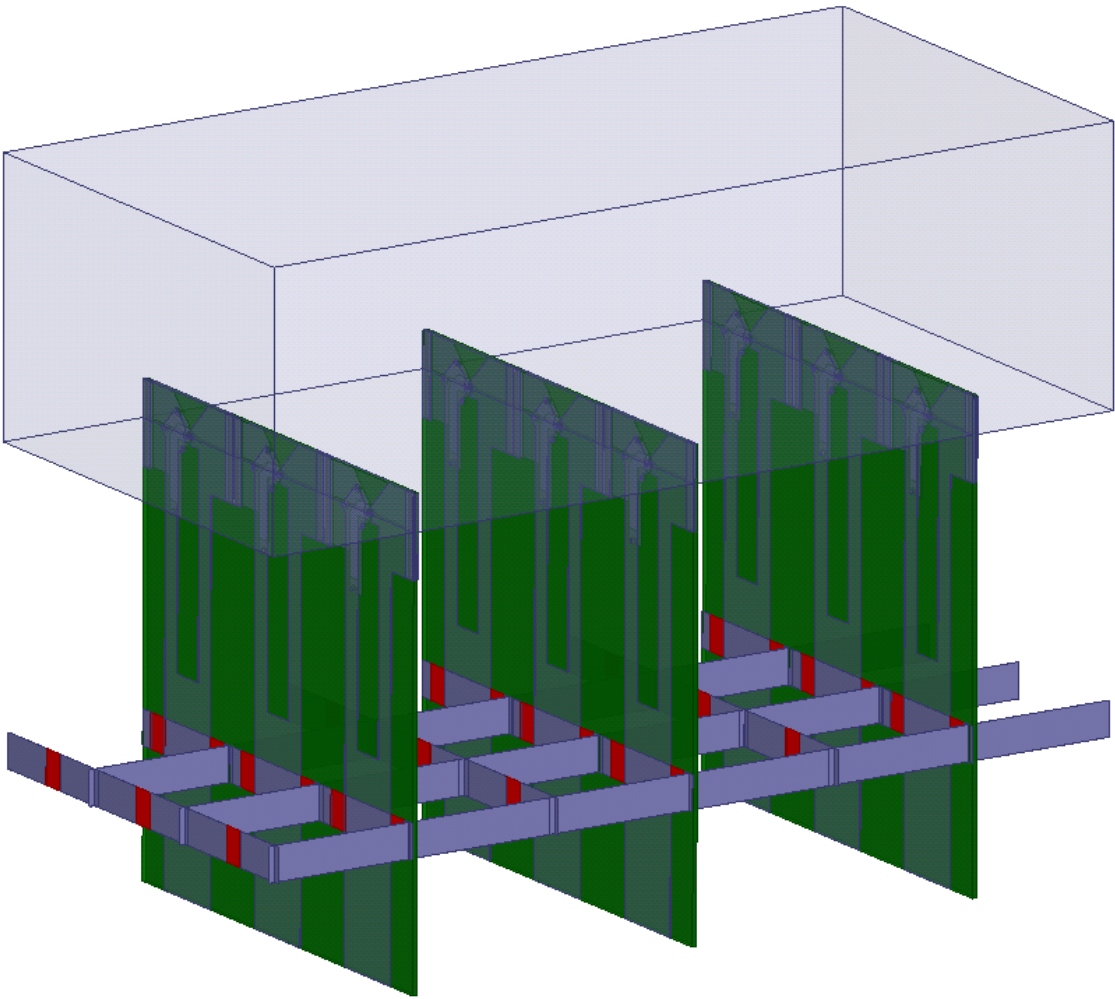
Figure 7.1: TCDA with screen forming "switchable" ground plane. The red squares indicate the location of switches. A fixed PEC ground plane (not shown) is located at the bottom of the array.

TE bandwidth from Table 7.1. Wide angle scanning would seem to be possible if a movable ground plane could somehow be implemented.
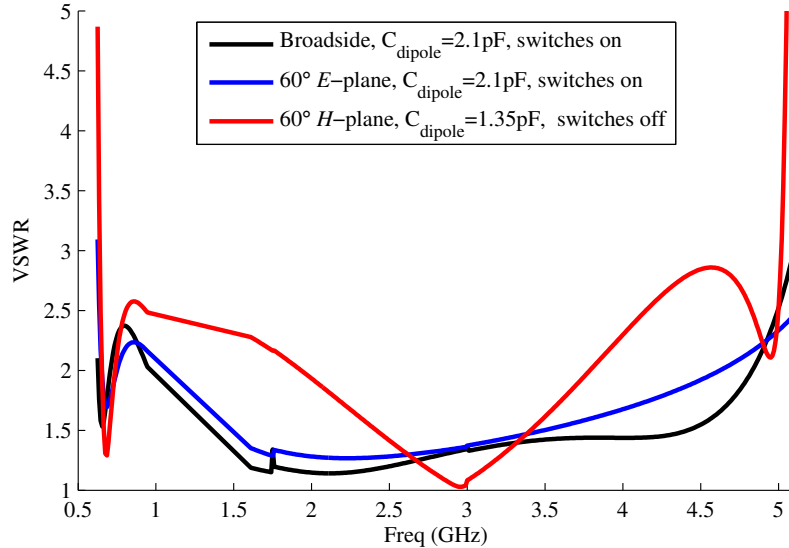
Figure 7.2: Simulated VSWR of TCDA-IB with switchable ground plane and tunable dipole capacitance, matched over 630MHz-5GHz (8:1 BW). Unfortunately, the impedance match at intermediate scan angles is significantly worse.

Of course mechanically moving the ground plane is not likely to be practical for most applications. However, we can approximate a reconfigurable ground plane by placing a conducting screen between the dipoles and fixed ground plane, as shown in Fig. 7.1. If switches are inserted within the screen, then it could be switched between reflective and transparent states. When the switches are on (conducting), the screen acts as an effective ground plane at a closer distance, for use with broadside and TM scan conditions. When the switches are off, the screen is (approximately) transparent, and the distance between the dipoles and ground plane is increased, for wide angle TE scanning. An additional tuning degree of freedom is added by

introducing varactor diodes between the dipole tips to adjust the dipole capacitance. The simulated frequency response of the system is given in Fig. 7.2 for broadside, TE and TM scanning to 60°. It is clear that the array maintains a good match over nearly 8:1 bandwidth in all three scan conditions.
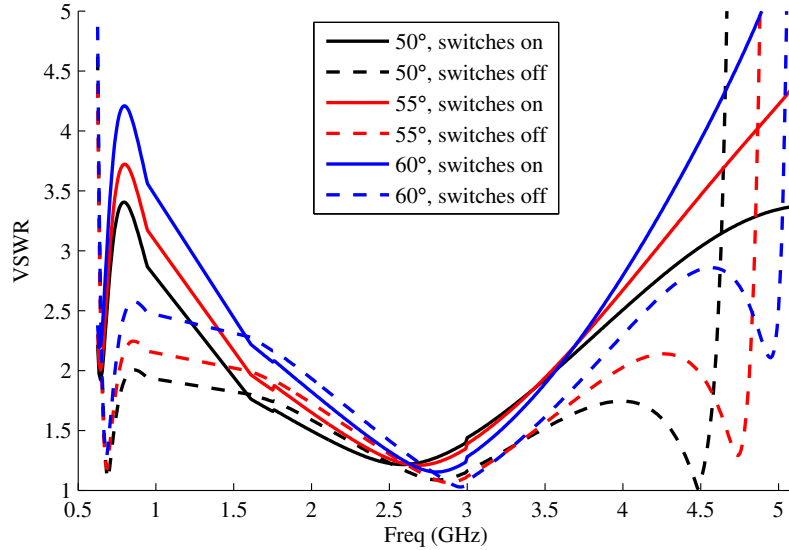
Figure 7.3: Scanning the TCDA-IB with switchable ground plane in the H-plane. Although the widest scan position at $\theta = 60°$ is well matched over the entire band when the switches are turned off, even a slight reduction in scan angle to 55° or 50° produces large mismatches whether the switches are on or off. This indicates that discrete switches are unlikely to be effective, and a continuously tunable approach is preferred for covering the entire scan volume.

Unfortunately, this approach has a fatal deficiency. Although the switchable ground plane yields a good match at the extreme scan angles for which it is optimized, the intermediate scan angles are poorly matched. This is because the switchable ground plane operates only in only two discrete states, whereas a scanning array must operate over a continuum of scan angles. As seen in Fig. 7.3, if the array is

scanned to 50°, the on-state mode results in a ground plane that is still much too close, yielding a poor match across the band, especially at low frequencies. However, in the off-state mode, the ground plane is now too far away, and half-wavelength short-circuit resonance has moved into the operational band. An attempt was made to add a second switchable layer, but even this did not provide sufficient "resolution" for wideband continuous scanning. For this approach to work over the entire scan volume, the number of switchable surfaces must be dramatically increased, which is unlikely to provide an efficient and cost-effective solution for extending the array scan volume. However, we may approximate this effect using continuously tunable elements.

7.3 Wide-Angle Scanning with a Continuously Tunable Substrate Layer

Figure 7.4: Circuit model for a wide-scan TCDA with tunable substrate layer. Note the variable capacitors C_{surf} and $C_{Coupling}$, implemented with varactor diodes.

Rather than using discrete switches, a continuously tunable method will be required in order to cover the entire scan volume. When modeling the above switchable ground plane, it was observed that the "off state" mesh was not completely transparent, but seemed to increase the effective electrical length of the substrate. The layer creates a "slow wave" structure which increases the substrate's effective wave number. The effect depends on the inductance of the wires and capacitance of the switches (L_{surf} and C_{surf}), and therefore can be varied by using a varactor diode to tune C_{surf}. By also using varactors to adjust the dipole capacitance $C_{coupling}$, the result is a continuously tunable array that can be electronically reconfigured for any scan position. An equivalent circuit model is shown in Fig. 7.4, and the physical implementation is shown in Fig. 7.5.

Optimization of the circuit in Fig. 7.4 indicates that a bandwidth of 6.6:1 can be obtained for 60° scanning (with VSWR≤2.5:1). This is less than the 8.3:1 bandwidth that is theoretically possible by physically adjusting the ground plane height, and is only slightly more than the 5.5:1 bandwidth possible with a fixed non-reconfigurable array. The reason for the reduction in performance is that the tunable surface is highly frequency dependent (it can be thought of as a Frequency Selective Surface, or FSS). The performance improvement when scanning in the H-plane are significant at the upper end of the band, but the low frequency performance is still limited by the physical thickness of the substrate h_{sub}. Although the low-end response can be compensated somewhat by adjusting $C_{coupling}$, the result is not as wideband as an actual moving ground plane. However, this limitation is less severe than it may initially seem. Because the reconfigurable layer makes the substrate seem electrically thicker, the physical array height is reduced. The array with switchable ground plane
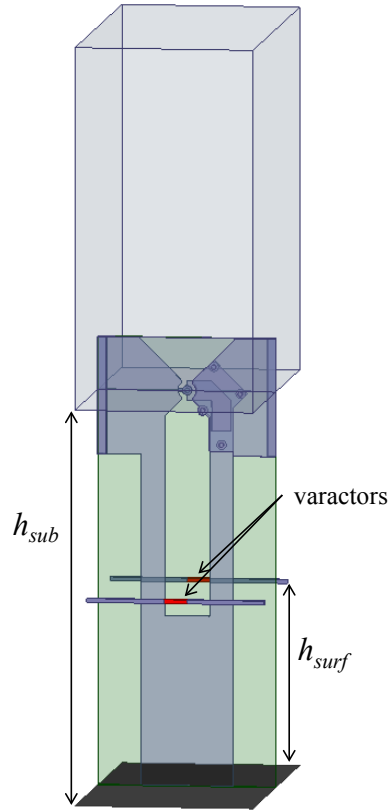
Figure 7.5: TCDA-IB unit cell with tunable substrate layer. The tunable layer consists of two thin horizontal wires per unit cell, populated with tunable varactor diodes, indicated in red. Biasing the layer is straightforward, and can be done at the array edges without disturbing the individual elements. Varactors also load the dipole tips, which can be easily biased through the balun's ground plane.

in Fig. 7.1 has a total height of 2.4″, whereas the continuously tunable array of Fig. 7.5 is only 1.86″ tall.

Therefore, the reduction in bandwidth is a natural result of the reduction in thickness. Although the tunable substrate array has 12% less bandwidth than the switched ground plane array, it is also 22.5% thinner. Its height to bandwidth ratio is actually superior to the switched ground plane approach of Fig. 7.1.

The advantages of the tunable substrate layer approach become even more apparent as the scan volume is further increased. For an array scanning to 70°, the equivalent circuit of Fig. 7.4 predicts a 5.4:1 bandwidth, which is significantly more than the 3.3:1 bandwidth possible with a non-reconfigurable TCDA. The full wave simulated frequency response for both the 60° and 70° scanning designs are shown in Fig. 7.6, and depict not only the response at the maximum scan angles, but also at angles throughout the scan volume (in 10° increments of θ and ϕ). Unlike the switchable substrate design, the continuously tunable substrate permits an efficient match over the entire scan volume.
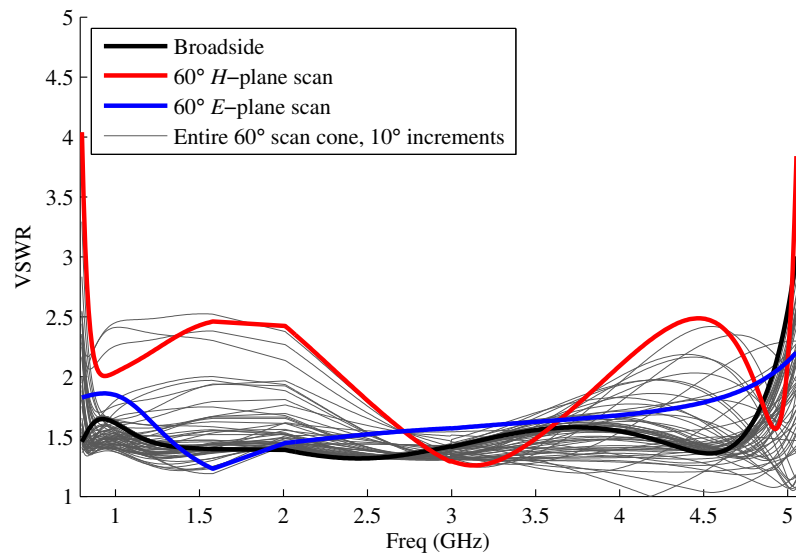
(a)
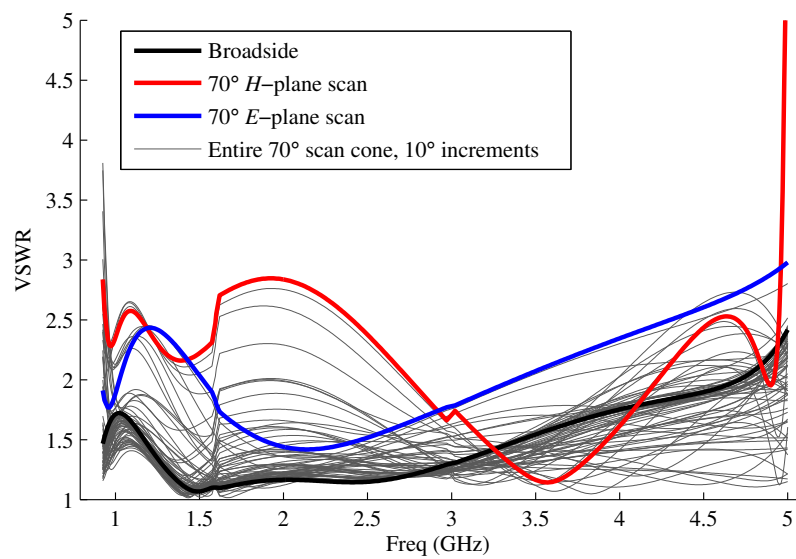
(b)

Figure 7.6: Impedance bandwidth of the reconfigurable TCDA-IB from Fig. 7.5. (a) Optimized for ±60° scan volume, with 6.6:1 bandwidth. (b) Optimized for ±70° scan volume, with 5.4:1 bandwidth.

7.4 Practical Design Considerations and Challenges

The above analysis was performed with idealized tunable capacitors rather than with realistic varactor diode models. The capacitances optimized within the tunable substrate layer used an extremely large tuning range (1-80 fF), which is unavailable in commercial varactors. When the capacitance ratio is limited to a more realistic 5:1 ratio (13-65 fF), the optimized equivalent circuit bandwidth was reduced from 6.6:1 to 5.9:1 for the 60° scanning array, and from 5.4:1 to 5:1 for the 70° scanning array. Although varactors may not be available at such low capacitance values, multiple devices can be used in series to the same effect.

Fortunately, other than limited tuning range, there are not many performance reductions expected from physical components. Although devices will contain a small series resistance, simulation suggests that this has almost no effect on the arrays bandwidth or efficiency, since it is in series with such a large reactive impedance. There are also no problems involved with biasing the devices, since they can be daisy chained together and biased at the edges of the array. This may result in large voltages if the total number of devices is large, and in such cases it may be preferable to provide several additional bias points within the array.

In addition to challenges associated with tuning, there are also several practical issues regarding the array design itself. Cross-polarization is a major challenge for any wide-scan array. The simulated cross-polarization is given in Fig. 7.7 in the *D*-plane (where the cross-polarization is highest), for scan angles up to 70°. It is clear that the cross polarization is significantly elevated at large scan angles. This is not due to any specific design changes associated with the reconfigurable ground plane; the cross-polarization while scanning to 45° is comparable to that of Fig. 6.5. This
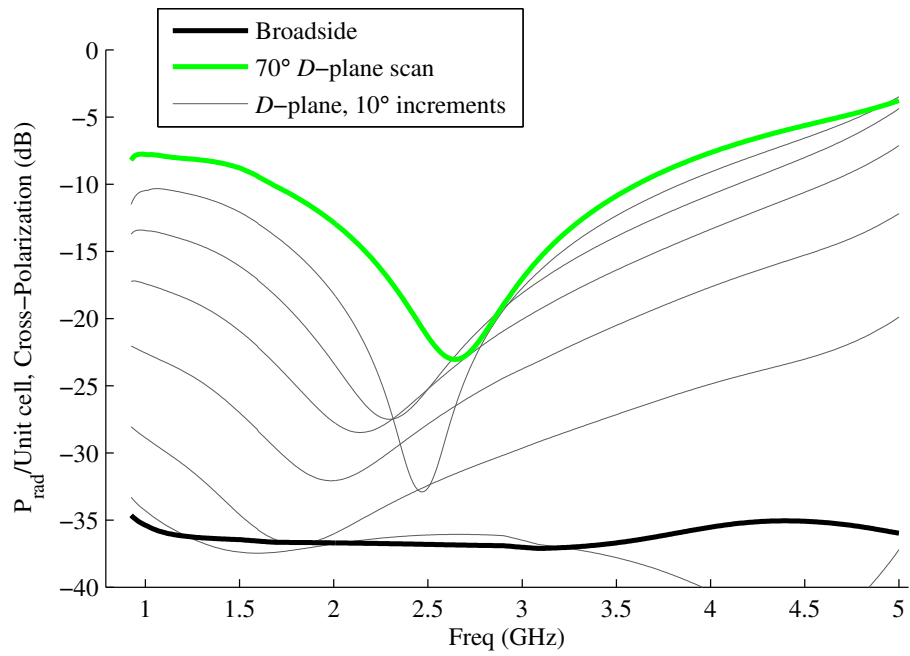
Figure 7.7: Simulated co-polarized and cross-polarized radiated power for wide-scan TCDA in the D-Plane. The polarization is defined using the Ludwig-3 definition. Curves are labeled with the scan angle measured from normal.

elevated cross-polarization is intrinsic to TCDA-type arrays, and is exacerbated here by the extremely large scan angles achieved by the proposed design. It is well known that cross polarization can be reduced if the total height of the array is reduced, at the expense of bandwidth. However, if low cross polarization at extreme scan angles is critical, then an alternate solution may be required.

Another drawback to the current design is that the element spacing is only 23 mm, whereas the 5 GHz half-wavelength spacing is 30 mm. The consequence is that the array is over populated and would need 70% more T/R modules than is theoretically required. Element size was reduced to better match the full-wave simulation with the circuit model, for a proof-of-concept design. A larger element size may be possible through further optimization, though it is not known exactly how performance might be affected. Because the circuit model does not account for the size of the element, it is not yet possible to optimize this dimension with the equivalent circuit, and therefore further optimization requires manually tuning the full wave model. The use of a more sophisticated circuit model which accounts for element spacing and the electrical length of the dipole, such as [115], could potentially improve to the design process.

Chapter 8: Conclusions and Future Work

As stated in the Introduction, the goal of this thesis has been to address two questions regarding to low-profile PEC-backed arrays. First: What are their fundamental limits of performance? And second: How might we improve the design of practical arrays, in order to approach these fundamental limits?

In the first part of this thesis we provided an answer to the first question by deriving a fundamental bound on the impedance bandwidth of any electrically large PEC-backed array constructed from passive, LTI, and reciprocal materials. For arrays of constant polarization, this limit is a simple closed-form expression which depend only on the array's matching efficiency, thickness, scan angle, permeability, as well as the order (complexity) of the array. Limits were also derived for lossless PEC-backed arrays of arbitrary polarization, and it was determined that such arrays can only obtain wide polarization bandwidth if they are linearly polarized.

We also developed limits for the special case when all of the radiating currents in the array are confined to a single plane, including substrate and/or superstrate material loading. Because of the ground plane creates periodic resonances over frequency in this case, a high-pass response is not possible for lossless planar arrays. Rather, the array has a maximum bandwidth that cannot be exceeded, regardless of array height. The bandwidth limit at broadside for such an array without material

219

loading is 8.3:1 (for VSWR $\leq$ 2:1) if the array is allowed to be infinitely complex, and 5:1 if the radiating surface has a simple 1st order equivalent impedance, such as simple coupled dipole or slot arrays. Contrasting the bandwidth limit for planar arrays to the general limit for volumetric arrays highlights the benefits of features such as superstrates, lossy backplanes, and multi-layer or volumetric radiators. If the array is sufficiently tall, these design features can yield extremely large bandwidths. However, for low profile arrays ($k_{mid}h < \pi/2$), a planar design is theoretically capable of near-optimal performance, despite its relatively simple form.

In the second part of this thesis, we applied our knowledge of the fundamental limits to address the question of how to design a practical array with performance that approaches the theoretical limit. These limits were obtained by considering the array as an impedance matching network, therefore we applied this perspective to the design problem as well. We showed that a simple Marchand balun can be used as a multi-stage impedance matching network for a Tightly Coupled Dipole Array (TCDA), while also providing a practical transition from the balanced input of the dipoles to an unbalanced feed. This design, which we refer to as the *Tightly Coupled Dipole Array with Integrated Balun* (TCDA-IB), eliminates the need for bulky external baluns, and provides a bandwidth improvement of over 30% compared to a standard TCDA. The TCDA-IB and TCDA arrays, along with an example balun and 180° hybrid are drawn to scale in Fig. 8.1. The TCDA-IB has a height of only $0.68\lambda_{high}$ above the ground plane, and achieves an impedance bandwidth of 7.35:1 with a low VSWR of <2.65:1 over the entire ±45° scan volume. The baluns are printed on the same substrate as the array itself and thus their cost and weight is minimal. T/R modules or phase shifters can be integrated directly onto the same PCB below the

220

TCDA-IB:

TCDA:

41mm

51mm

"Feed organizer"

50Ω Unbalanced Feed

Balanced Feed

External 180° Hybrid
MCLI HJ-26
5.9"x1.75"x0.2"
1-6GHz
~1.6dB Loss
$1000/ea.

External Balun
Picosecond 5310A
1.5"x1.75"x0.5"
4MHz-6.5GHz
~3dB Loss
$1500/ea.

50Ω Unbalanced Feed

7.35:1 BW
3 in³, 15g, $10
per element

5.5:1 BW
>8 in³, >100g, >$1000
per element
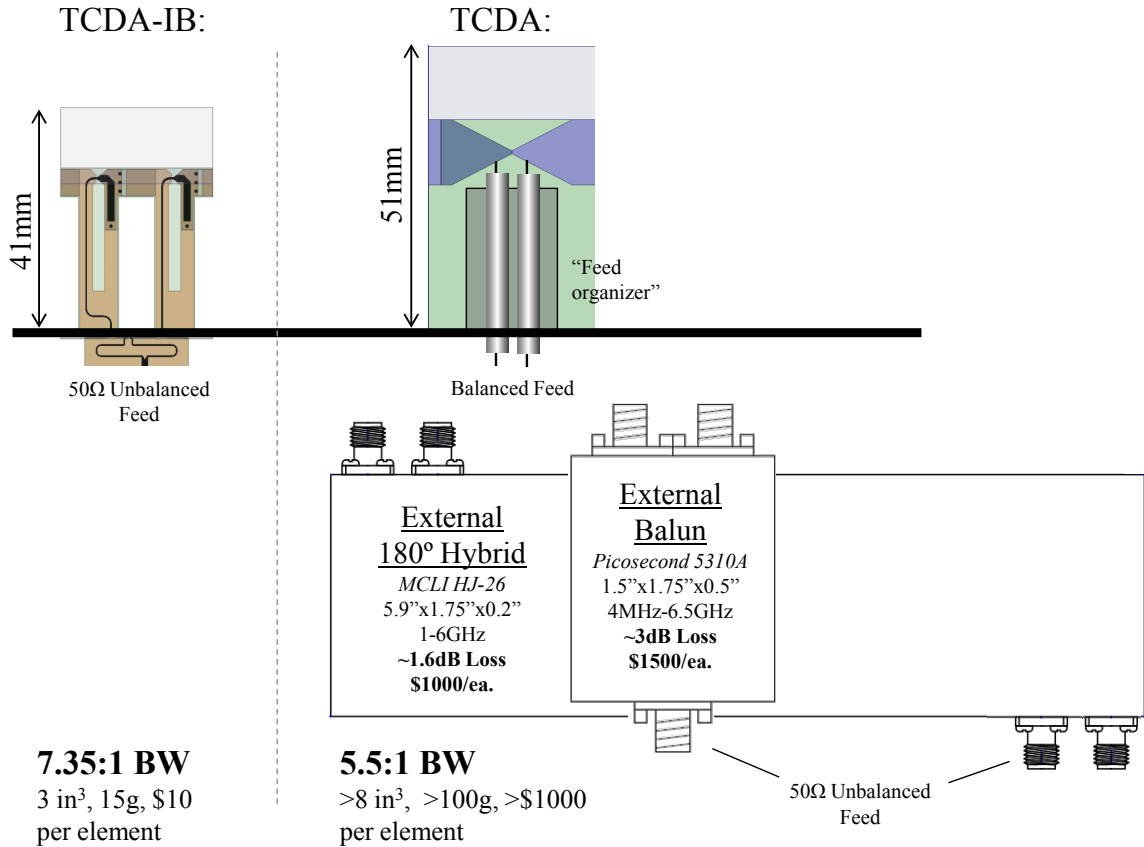
Figure 8.1: To scale comparison of the TCDA-IB unit cell with integrated balun to the standard TCDA which requires external baluns or 180° hybrids at each element to implement a wideband scanning array. It is clear that the integration of a compact balun has significant size, weight and cost advantages. Additionally the performance is significantly improved, since the bandwidth is increased from 5.5:1 to 7.35:1, and the insertion loss from the balun is significantly reduced.

ground plane, enabling an extremely compact wideband electronically scanned array. An 8×8 element prototype array was built to validate the TCDA-IB design, and compared very well relative to simulation.

8.1 Comparison of TCDA-IB Performance to Fundamental Limits

A comparison of the TCDA-IB to other PEC-backed arrays and to the fundamental limits is plotted in Fig. 8.2. The performance of each design is given in terms of the new metric P_A which was introduced in Chapter 1, and provides single number to represent the bandwidth, scan angle, and matching efficiency of the array. Also plotted are the theoretical limits for P_A, which were derived in Chapter 3.

As seen in Fig. 8.2, the TCDA-IB designs of Chapters 6-7 have the largest P_A of any of the surveyed arrays of similar height (other than the ISPA). However, like most scanning arrays, the static TCDA-IB of Chapter 6 still has limited bandwidth because of compromises that must be made when matching an array over a range of scan angles. A strategy for overcoming this limitation was proposed in Chapter 7 by integrating reconfigurable components within the TCDA-IB structure. Two reconfigurable TCDA-IB designs were proposed, one that can scan to $\pm 60°$ over a 5.9:1 bandwidth, and one that can scan to $\pm 70°$ over a 5:1 bandwidth.

Although the theoretical limits impose a fundamental performance bound for wideband low-profile arrays, we have shown that there is significant room for improvement from the current state-of-the-art. We have also proposed and demonstrated several techniques for moving closer to this bandwidth limit, such as higher-order impedance matching and the use of reconfigurable arrays. Referring to Fig. 8.2, our TCDA-IB designs achieve significantly greater bandwidth and superior scanning than any other PEC-backed array of similar thickness.
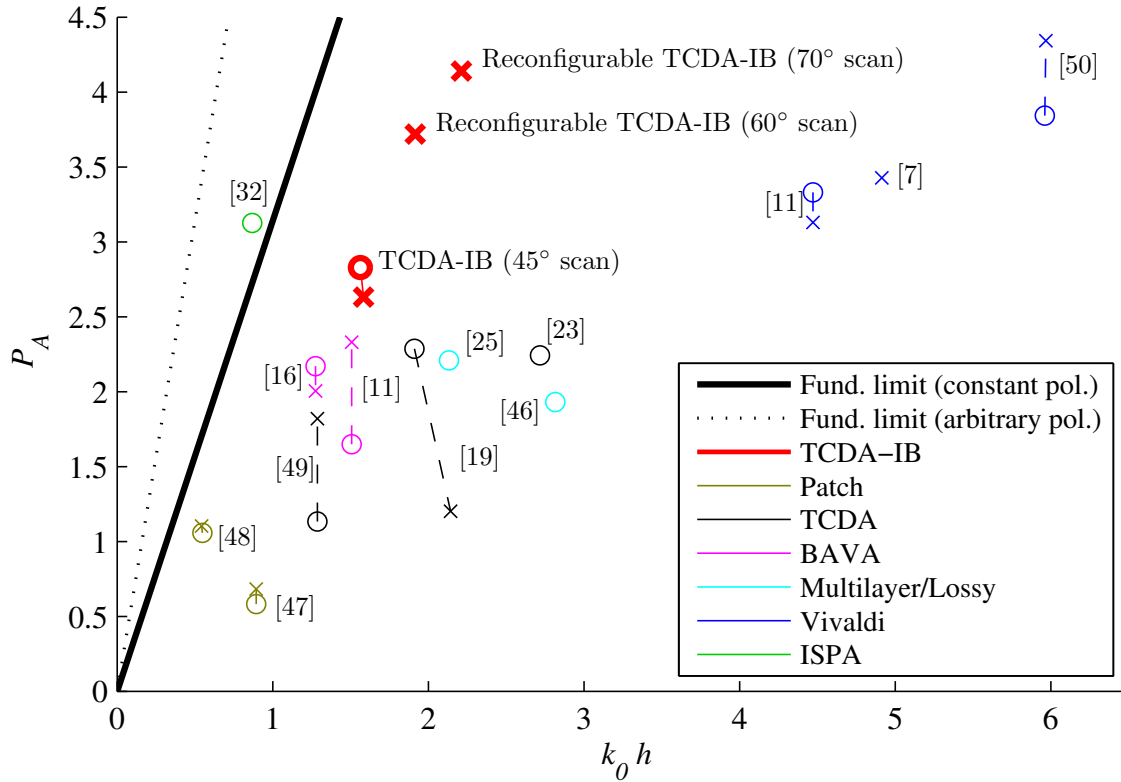
Figure 8.2: Survey of wideband array performance P_A vs. electrical thickness $k_0 h$. The fundamental limit under constant polarization is given by the heavy black line, and the limit for arbitrary polarization is given by the dotted line. The TCDA-IB designs of Chapters 6-7 are shown in red.

Our tightly coupled dipole array with a compact integrated balun (TCDA-IB) is a simple, low cost array system with extremely wide bandwidth and excellent scanning capabilities. We believe that the TCDA-IB is the first low-profile array that is capable of greater than 7:1 bandwidth while maintaining a low impedance mismatch (VSWR < 2.65:1) over a large scan volume ($\pm 45°$), and which does not require active

or external baluns, or lossy materials. The TCDA-IB is therefore an attractive technology for a variety of wideband communication and sensing applications, especially for small platforms where reducing size, weight, and cost is critical.

8.2   Opportunities for Future Work

As stated above, the area of wideband low-profile phased arrays remains a rich field of study. In particular there are several areas related to the research in this thesis that we believe present excellent opportunities for further investigation. These topics are discussed briefly here.

Bandwidth Limits for Finite PEC-backed Arrays

The bandwidth limits in this thesis are valid for infinitely periodic arrays. Of course, real world arrays are finite and suffer from truncation effects. In particular, tightly coupled arrays are especially susceptible to edge-born surface waves that can significantly affect performance [113]. In theory, finite arrays must of course satisfy the small-antenna limits. However, these limits are currently not well suited for characterizing finite PEC-backed arrays for several reasons.

The Wheeler-Chu limits [4,5] are based on individual radiating spherical modes. These modes can be distinguished between those that can propagate above a ground plane and those cannot. In this way, the ground plane reactance can be accounted for by analyzing only those modes that satisfy the PEC boundary conditions. However, even modestly sized phased arrays are not electrically small, and therefore will radiate a superposition of many spherical modes. There is not therefore a straightforward manner to determine the gain-bandwidth limits of a finite PEC-backed array using the Wheeler-Chu limits.

An alternate antenna gain-bandwidth limit was proposed by Gustafsson [62]. This limit is not based on the individual spherical modes, but rather on a dispersion rule formed from the scattering response of the antenna. The low-frequency (Rayleigh) scattering for any object is bounded by its geometry [116]. This in turn is fundamentally related to the maximum possible gain of the antenna by the *Forward Scattering Theorem* [117]. In this way, a gain-bandwidth limit can be established that does not assume a specific spherical mode, and therefore provides a fundamental limit even for large, directive arrays. However, this method cannot accurately consider the effects of the ground plane reactance. We attempted to modify the formulation using a version of the forward scattering theorem for half-space problems [118]. However, the resulting scattering function is not causal when referenced to the ground plane surface, making it difficult to apply the dispersion relations. A similar approach for a PEC-backed dipole was attempted in [119], but the limitation due to non-causality was not addressed.

High Frequency Implementation

Our TCDA-IB design is a practical and low cost design, particularly suited for arrays operating from UHF to X-band (∼300 MHz - 12 GHz). For frequencies lower than this, commercial baluns are available with sufficient bandwidth and minimal size, weight, and cost. At higher frequencies, our overall design strategy of using a compact reactive balun to improve the bandwidth of the array is still valid. However, the specific implementation shown in Fig. 6.2 may be difficult to implement because scaling the smaller features may not be possible using standard PCB fabrication. The implementation of the TCDA-IB at higher frequencies might involve the redesign

225

of the balun to eliminate the smallest features, or could use alternate fabrication methods to improve resolution.

Practical Wideband Power Distribution

Another important issue not addressed in this thesis is the problem of how to efficiently distribute the RF signal to each element. Power dividers suffer from similar size, weight, cost, and bandwidth limitations as the baluns themselves. For multi-octave wideband arrays, achieving low loss power distribution in a low-profile compact structure is a hard problem. This is not an issue specific to the TCDA-IB design, but is a problem for all low-profile wideband arrays.

Bibliography

[1] "Nielsen's law of internet bandwidth," http://www.nngroup.com/articles/nielsens-law-of-internet-bandwidth/.

[2] "Sorry, America: Your wireless airwaves are full," http://money.cnn.com/2012/02/21/technology/spectrum_crunch/index.htm.

[3] G. C. Tavik *et al.*, "The advanced multifunction RF concept," *IEEE Trans. Microw. Theory Tech.*, vol. 53, no. 3, pp. 1009–1020, Mar. 2005.

[4] H. A. Wheeler, "Fundamental limitations of small antennas," *Proc. IRE*, vol. 35, no. 12, pp. 1479–1484, Dec. 1947.

[5] L. J. Chu, "Physical limitations of omni-directional antennas," *Journal of Applied Physics*, vol. 19, no. 12, pp. 1163–1175, 1948.

[6] R. M. Fano, "Theoretical limitations on the broadband matching of arbitrary impedances," *Journal of the Franklin Institute*, vol. 249, pp. 57–83, Jan. 1950.

[7] H. Holter, T.-H. Chio, and D. H. Schaubert, "Experimental results of 144-element dual-polarized endfire tapered-slot phased arrays," *IEEE Trans. Antennas Propag.*, vol. 48, no. 11, pp. 1707–1718, Nov. 2000.

[8] A. Gunn, "Radionet: Advanced radio astronomy across europe," in *Organizations and Strategies in Astronomy*, ser. ASTROPHYSICS AND SPACE SCIENCE LIBRARY, A. Heck, Ed. Springer Netherlands, 2006, vol. 7, pp. 171–180.

[9] L. Lewis, M. Fassett, and J. Hunt, "A broadband stripline array element," in *Proc. IEEE Antennas Propag. Soc. Int. Symp. (APSURSI)*, vol. 12. IEEE, Jun. 1974, pp. 335–337.

[10] P. J. Gibson, "The vivaldi aerial," in *Microwave Conference, 1979. 9th European*. IEEE, 1979, pp. 101–105.

[11] D. H. Schaubert, S. Kasturi, A. O. Boryssenko, and W. M. Elsallal, "Vivaldi antenna arrays for wide bandwidth and electronic scanning," in *EuCAP - European Conference on Antennas & Propagation.* IET, Nov. 2007, pp. 1–6.

[12] R. Kindt and D. Taylor, "Polarization correction in dual-polarized phased arrays of flared notches," in *Proc. IEEE Antennas Propag. Soc. Int. Symp. (APSURSI).* IEEE, Jul. 2011, pp. 1961–1964.

[13] W. Elsallal *et al.*, "A sige-based ku-band digital beamforming array for high speed on-the-move comm/radar system," in *Proc. IEEE Int. Symp. on Phased Array Sys. and Tech. (ARRAY).* IEEE, Oct. 2010, pp. 868–875.

[14] J. D. S. Langley, P. S. Hall, and P. Newham, "Balanced antipodal vivaldi antenna for wide bandwidth phased arrays," *Microwaves, Antennas and Propagation, IEE Proceedings*, vol. 143, no. 2, pp. 97–102, Apr. 1996.

[15] J. J. Lee, S. Livingston, and R. Koenig, "A low-profile wide-band (5:1) dual-pol array," *IEEE Antennas Wireless Propag. Lett.*, vol. 2, no. 1, pp. 46–49, 2003.

[16] M. W. Elsallal and J. C. Mather, "An ultra-thin, decade (10:1) bandwidth, modular BAVA array with low cross-polarization," in *Proc. IEEE Antennas Propag. Soc. Int. Symp. (APSURSI).* IEEE, Jul. 2011, pp. 1980–1983.

[17] C. E. Baum, "Some characteristics of planar distributed sources for radiating transient pulses," *Sensor and Simulation Note 100*, Mar. 1970.

[18] C. A. Balanis, Ed., *Modern Antenna Handbook*, 1st ed. Wiley-Interscience, Sep. 2008.

[19] B. A. Munk, "Broadband wire arrays," in *Finite Antenna Arrays and FSS*, 1st ed. Wiley-IEEE Press, Jul. 2003, ch. 6, pp. 181–213.

[20] ——, *Frequency Selective Surfaces: Theory and Design*, 1st ed. Wiley-Interscience, Apr. 2000.

[21] H. A. Wheeler, "The radiation resistance of an antenna in an infinite array or waveguide," *Proc. IRE*, vol. 36, no. 4, pp. 478–487, Apr. 1948.

[22] H. Wheeler, "Simple relations derived fom a phased-array antenna made of an infinite current sheet," *IEEE Trans. Antennas Propag.*, vol. 13, no. 4, pp. 506–514, Jul. 1965.

[23] B. Munk *et al.*, "A low-profile broadband phased array antenna," in *Proc. IEEE Antennas Propag. Soc. Int. Symp. (APSURSI)*, vol. 2. IEEE, Jun. 2003, pp. 448–451 vol.2.

[24] M. Jones and J. Rawnick, "A new approach to broadband array design using tightly coupled elements," in *MILCOM 2007 - IEEE Military Communications Conference.* IEEE, Oct. 2007, pp. 1–7.

[25] W. F. Moulder, K. Sertel, and J. L. Volakis, "Superstrate-enhanced ultrawideband tightly coupled array with resistive FSS," *IEEE Trans. Antennas Propag.*, vol. 60, no. 9, pp. 4166–4172, 2012.

[26] R. C. Hansen, "Linear connected arrays [coupled dipole arrays]," *IEEE Antennas Wireless Propag. Lett.*, vol. 3, no. 1, pp. 154–156, Dec. 2004.

[27] D. Cavallo, "Connected array antennas: Analysis and design," Ph.D. dissertation, Technische Universiteit Eindhoven, 2011.

[28] A. Neto and J. J. Lee, "Infinite bandwidth long slot array antenna," *IEEE Antennas Wireless Propag. Lett.*, vol. 4, pp. 75–78, 2005.

[29] Y. Mushiake, "Self-complementary antennas," *IEEE Antennas Propag. Mag.*, vol. 34, no. 6, pp. 23–29, Dec. 1992.

[30] P. I. Richards, "Resistor-transmission-line circuits," *Proc. IRE*, vol. 36, no. 2, pp. 217–220, Feb. 1948.

[31] J. J. Lee, S. Livingston, and D. Nagata, "A low profile 10:1 (200-2000 MHz) wide band long slot array," in *Proc. IEEE Antennas Propag. Soc. Int. Symp. (APSURSI).* IEEE, Jul. 2008, pp. 1–4.

[32] I. Tzanidis, K. Sertel, and J. L. Volakis, "Interwoven spiral array (ISPA) with a 10:1 bandwidth on a ground plane," *IEEE Antennas Wireless Propag. Lett.*, vol. 10, pp. 115–118, 2011.

[33] B. Thors, H. Steyskal, and H. Holter, "Broad-band fragmented aperture phased array element design using genetic algorithms," *IEEE Trans. Antennas Propag.*, vol. 53, no. 10, pp. 3280–3287, Oct. 2005.

[34] A. Neto and J. J. Lee, "Ultrawide-band properties of long slot arrays," *IEEE Trans. Antennas Propag.*, vol. 54, no. 2, pp. 534–543, Feb. 2006.

[35] H. Steyskal, J. Ramprecht, and H. Holter, "Spiral element for wide-band phased arrays," in *Proc. IEEE Antennas Propag. Soc. Int. Symp. (APSURSI)*, vol. 4. IEEE, Jun. 2004, pp. 3976–3979 Vol.4.

[36] P. Friederich *et al.*, "A new class of broadband, planar apertures," in *Antennas and Applications Symposium, Allerton IL*, Sep. 2001.

[37] R. C. Hansen and M. Burke, "Antenna with magneto-dielectrics," *Microwave and Optical Technology Letters*, vol. 26, no. 2, pp. 75–78, 2000.

[38] J. A. Kasemodel, "Low-profile ferrite loaded UWB tightly coupled dipole array," in *Proc. IEEE Antennas Propag. Soc. Int. Symp. (APSURSI)*. IEEE, Jul. 2011, pp. 1973–1975.

[39] F. Erkmen, C.-C. Chen, and J. L. Volakis, "UWB magneto-dielectric ground plane for low-profile antenna applications," *IEEE Antennas Propag. Mag.*, vol. 50, no. 4, pp. 211–216, Aug. 2008.

[40] V. G. Harris *et al.*, "Recent advances in processing and applications of microwave ferrites," *Journal of Magnetism and Magnetic Materials*, vol. 321, pp. 2035–2047, Jul. 2009.

[41] L. Zhang, A. Puri, K. Sertel, J. L. Volakis, and H. Verweij, "Low loss Z-type $Ba_3Co_2Fe_{24}O_{41}$ hexaferrites for antennas and rf devices," *IEEE Trans. Magn.*, vol. 47, no. 8, pp. 2149–2152, Aug. 2011.

[42] V. G. Harris *et al.*, "Ba-hexaferrite films for next generation microwave devices (invited)," *Journal of Applied Physics*, vol. 99, no. 8, pp. 08M911+, 2006.

[43] G. M. Yang *et al.*, "Loading effects of self-biased magnetic films on patch antennas with substrate/superstrate sandwich structure," *Microwaves, Antennas & Propagation, IET*, vol. 4, no. 9, pp. 1172–1181, Sep. 2010.

[44] A. Thakur, A. Chevalier, J. L. Mattei, and P. Queffelec, "Low-loss spinel nanoferrite with matching permeability and permittivity in the ultrahigh frequency range," *Journal of Applied Physics*, vol. 108, no. 1, pp. 014 301–014 301–4, Jul. 2010.

[45] B. A. Munk, T. W. Kornbau, and R. D. Fulton, "Scan independent phased arrays," *Radio Science*, vol. 14, no. 6, pp. 1979–1990, Dec. 1979.

[46] J. G. Maloney, B. N. Baker, R. T. Lee, G. N. Kiesel, and J. J. Acree, "Wide scan, integrated printed circuit board, fragmented aperture array antennas," in *Proc. IEEE Antennas Propag. Soc. Int. Symp. (APSURSI)*. IEEE, Jul. 2011, pp. 1965–1968.

[47] M. J. Buckley, J. Wolf, B. J. Herting, J. Mather, D. Manson, and J. B. West, "Wide band and wide scan metamaterial loaded radiating elements," in *Antennas and Applications Symposium, Allerton IL*, Sep. 2010.

[48] R. Erickson *et al.*, "Wideband and wide scan phased array microstrip patch antennas for small platforms," in *EuCAP - European Conference on Antennas & Propagation*. IET, Nov. 2007, pp. 1–6.

[49] S. S. Holland and M. N. Vouvakis, "The planar ultrawideband modular antenna (PUMA) array," *IEEE Trans. Antennas Propag.*, vol. 60, no. 1, pp. 130–140, Jan. 2012.

[50] M. Stasiowski and D. Schaubert, "Broadband array antenna," in *Antennas and Applications Symposium, Allerton IL*, Sep. 2008.

[51] R. W. Kindt and W. R. Pickles, "Ultrawideband all-metal flared-notch array radiator," *IEEE Trans. Antennas Propag.*, vol. 58, no. 11, pp. 3568–3575, Nov. 2010.

[52] D. F. Sievenpiper *et al.*, "Experimental validation of performance limits and design guidelines for small antennas," *IEEE Trans. Antennas Propag.*, vol. 60, no. 1, pp. 8–19, Jan. 2012.

[53] R. D. L. Kronig, "On the theory of dispersion of X-rays," *Journal of the Optical Society of America*, vol. 12, pp. 547+, Nov. 1926.

[54] H. A. Kramers, "La diffusion de la lumiere par les atomes," *Atti Congr. Intern. Fisica*, pp. 545–557, 1927.

[55] C. C. Lee, M. Lahham, and B. G. Martin, "Experimental verification of the Kramers-Kronig relationship for acoustic waves," *IEEE Trans. Ultrason., Ferroelectr., Freq. Control*, vol. 37, no. 4, pp. 286–294, Jul. 1990.

[56] C. Sohl, M. Gustafsson, and G. Kristensson, "The integrated extinction for broadband scattering of acoustic waves," *Journal of the Acoustical Society of America*, vol. 122, no. 6, pp. 3206–3210, Dec. 2007.

[57] H. M. Nussenzveig, *Causality and dispersion relations, Volume 95 (Mathematics in Science and Engineering)*. Academic Press, Feb. 1972.

[58] C. Sohl, M. Gustafsson, and G. Kristensson, "Physical limitations on broadband scattering by heterogeneous obstacles," *Journal of Physics A: Mathematical and Theoretical*, vol. 40, no. 36, pp. 11 165+, Aug. 2007.

[59] M. C. Villalobos, H. D. Foltz, and J. S. McLean, "Broadband matching limitations for higher order spherical modes," *IEEE Trans. Antennas Propag.*, vol. 57, no. 4, pp. 1018–1026, Apr. 2009.

[60] J. R. Taylor, *Scattering Theory: The Quantum Theory of Nonrelativistic Collisions (Dover Books on Engineering)*. Dover Publications, May 2006.

[61] J. Volakis, C.-C. Chen, and K. Fujimoto, *Small Antennas:Miniaturization Techniques & Applications*, 1st ed. McGraw-Hill Professional, Jun. 2010.

[62] M. Gustafsson, C. Sohl, and G. Kristensson, "Physical limitations on antennas of arbitrary shape," *Proceedings of the Royal Society A: Mathematical, Physical and Engineering Science*, vol. 463, no. 2086, pp. 2589–2607, Oct. 2007.

[63] J. S. Toll, "Causality and the dispersion relation: Logical foundations," *Physical Review Online Archive*, vol. 104, no. 6, pp. 1760–1770, Dec. 1956.

[64] H. J. Carlin and P. P. Civalleri, *Wideband Circuit Design (Electronic Engineering Systems)*, 1st ed. CRC Press, Nov. 1997.

[65] W.-K. Chen, *Broadband Matching - Theory and Implementations*, 2nd ed. World Scientific Pub Co Inc, 1988.

[66] S. H. Hall and H. L. Heck, "Advanced signal integrity for high-speed digital designs." Wiley-IEEE Press, Mar. 2009, pp. 331–336.

[67] L. D. Paarmann, *Design and Analysis of Analog Filters*, 1st ed. Springer, Jun. 2001.

[68] K. N. Rozanov, "Ultimate thickness to bandwidth ratio of radar absorbers," *IEEE Trans. Antennas Propag.*, vol. 48, no. 8, pp. 1230–1234, Aug. 2000.

[69] M. Gustafsson and D. Sjoberg, "Physical bounds and sum rules for high-impedance surfaces," *IEEE Trans. Antennas Propag.*, vol. 59, no. 6, pp. 2196–2204, Jun. 2011.

[70] R. W. Ziolkowski and A. Erentok, "At and below the Chu limit: passive and active broad bandwidth metamaterial-based electrically small antennas," *Microwaves, Antennas & Propagation, IET*, vol. 1, no. 1, pp. 116–128, Feb. 2007.

[71] S. Deb and S. D. Gupta, "Absorption and dispersion in metamaterials: Feasibility of device applications," *Pramana*, vol. 75, pp. 837–854, Nov. 2010.

[72] B. A. Munk, *Metamaterials: Critique and Alternatives*, 1st ed. Wiley-Interscience, Feb. 2009.

[73] M. Gustafsson and D. Sjöberg, "Sum rules and physical bounds on passive metamaterials," *New Journal of Physics*, vol. 12, no. 4, pp. 1–18, Apr. 2010.

[74] C. Sohl, M. Gustafsson, and G. Kristensson, "Bounds on metamaterials in scattering and antenna problems," in *EuCAP - European Conference on Antennas & Propagation*. IET, Nov. 2007, pp. 1–4.

[75] ——, "Physical limitations on metamaterials: restrictions on scattering and absorption over a frequency interval," *Journal of Physics D: Applied Physics*, vol. 40, no. 22, pp. 7146–7151, Nov. 2007.

[76] H. W. Bode, *Network Analysis and Feedback Amplifier Design*. D. Van Nostrand Company, 1945.

[77] D. Youla, "A new theory of broad-band matching," *IEEE Trans. Circuit Theory*, vol. 11, no. 1, pp. 30–50, Mar. 1964.

[78] H. J. Carlin, "Gain-bandwidth limitations on equalizers and matching networks," *Proc. IRE*, vol. 42, no. 11, pp. 1676–1685, Nov. 1954.

[79] ——, "Darlington synthesis revisited," *IEEE Trans. Circuits Syst. I*, vol. 46, no. 1, pp. 14–21, Jan. 1999.

[80] A. R. Lopez, "Review of narrowband impedance-matching limitations," *IEEE Antennas Propag. Mag.*, vol. 46, no. 4, pp. 88–90, Aug. 2004.

[81] Y.-S. Zhu and W.-K. Chen, "On real and complex normalizations," *Circuits, Systems and Signal Processing*, vol. 12, no. 4, pp. 579–587, 1993.

[82] R. Pauli, "Darlington's theorem and complex normalization," *Int. J. Circ. Theor. Appl.*, vol. 17, no. 4, pp. 429–446, Oct. 1989.

[83] D. C. Youla, H. J. Carlin, and B. S. Yarman, "Double broadband matching and the problem of reciprocal reactance 2n-port cascade decomposition," *Int. J. Circ. Theor. Appl.*, vol. 12, no. 3, pp. 269–281, Jul. 1984.

[84] J.-L. Wan and W.-K. Chen, "Broadband matching of multi-port networks terminated in frequency-dependent loads," *Circuits, Systems, and Signal Processing*, vol. 4, no. 3, pp. 385–411, Sep. 1985.

[85] Z.-M. Wang and W.-K. Chen, "Broad-band matching of multiport networks," *IEEE Trans. Circuits Syst.*, vol. 31, no. 9, pp. 788–796, Sep. 1984.

[86] M. Gustafsson, "Broadband self-complimentary antenna arrays," in *Ultra-Wideband Short-Pulse Electromagnetics 8*, 1st ed. Springer, Sep. 2007, pp. 17–24.

[87] B. Tomasic and H. Steyskal, "Minimum Q of the element in an infinite phased array - TMz case," in *Applied Electromagnetics and Communications, 2007. ICECom 2007. 19th International Conference on*. IEEE, 2007, pp. 1–8.

[88] ——, "Minimum Q of the element in an infinite phased array," in *Proc. IEEE Antennas Propag. Soc. Int. Symp. (APSURSI)*. IEEE, Jun. 2007, pp. 145–148.

[89] L. M. Brekhovskikh, *Waves in Layered Media*, 2nd ed. Academic Press, 1960.

[90] D. Sjoberg, "Low-frequency scattering by passive periodic structures for oblique incidence: low-pass case," *Journal of Physics A: Mathematical and Theoretical*, vol. 42, no. 38, 2009.

[91] S. Darlington, "Synthesis of reactance 4-poles which produce prescribed insertion loss," *J. Math. Phys.*, vol. 18, no. 4, pp. 257–353, 1939.

[92] J. S. McLean, "A re-examination of the fundamental limits on the radiation Q of electrically small antennas," *IEEE Trans. Antennas Propag.*, vol. 44, no. 5, pp. 672+, May 1996.

[93] M. Wohlers, "Complex normalization of scattering matrices and the problem of compatible impedances," *IEEE Trans. Circuit Theory*, vol. 12, no. 4, pp. 528–535, Dec. 1965.

[94] M. Gustafsson, "Sum rules for lossless antennas," *Microwaves, Antennas & Propagation, IET*, vol. 4, no. 4, pp. 501–511, Apr. 2010.

[95] V. Belevitch, *Classical Network Theory*, 1st ed.   Holden-Day, 1968.

[96] X. Shi, C. Liang, and Y. Han, "A useful theorem for a lossless multiport network," *IEEE Trans. Microw. Theory Tech.*, vol. 43, no. 3, pp. 697–699, Mar. 1995.

[97] J. Neirynck and C. Carlin, "Synthesis of the lossless reciprocal three-port based on a canonic form of its scattering matrix," *IEEE Trans. Circuits Syst.*, vol. 28, no. 7, pp. 736–744, Jul. 1981.

[98] A. Ludwig, "The definition of cross polarization," *IEEE Trans. Antennas Propag.*, vol. 21, no. 1, pp. 116–119, Jan. 1973.

[99] S. Darlington, "Realization of a constant phase difference," Bell System Technical Journal, Tech. Rep., Jan. 1950.

[100] A. K. Bhattacharyya, "Floquet modal functions," in *Phased Array Antennas : Floquet Analysis, Synthesis, BFNs and Active Array Systems*, 1st ed. Wiley-Interscience, Mar. 2006, ch. 3.

[101] D. Cavallo, A. Neto, and G. Gerini, "Green's function based equivalent circuits for connected arrays in transmission and in reception," *IEEE Trans. Antennas Propag.*, vol. 59, no. 5, pp. 1535–1545, May 2011.

[102] J. Doane, K. Sertel, and J. Volakis, "Bandwidth limits for low profile planar arrays," in *Antennas and Applications Symposium, Allerton IL*, Sep. 2011.

[103] D. F. Sievenpiper, L. Zhang, R. F. Broas, N. G. Alexopolous, and E. Yablonovitch, "High-impedance electromagnetic surfaces with a forbidden frequency band," *IEEE Trans. Microw. Theory Tech.*, vol. 47, no. 11, pp. 2059–2074, Nov. 1999.

[104] J. A. Kasemodel, C.-C. Chen, and J. L. Volakis, "Broadband planar wide-scan array employing tightly coupled elements and integrated balun," in *Proc. IEEE Int. Symp. on Phased Array Sys. and Tech. (ARRAY)*. IEEE, Oct. 2010, pp. 467–472.

[105] D. Cavallo, A. Neto, and G. Gerini, "PCB slot based transformers to avoid common-mode resonances in connected arrays of dipoles," *IEEE Trans. Antennas Propag.*, vol. 58, no. 8, pp. 2767–2771, Aug. 2010.

[106] T. Durham, "Dual polarization antenna array with inter-element coupling and associated methods," *United States Patent*, no. US 7221322 B1, May 2007.

[107] D. Cavallo, A. Neto, and G. Gerini, "A wideband (3 to 5 GHz) wide-scan connected array of dipoles with low cross polarization," in *EuCAP - European Conference on Antennas & Propagation*. IEEE, Mar. 2012, pp. 3239–3242.

[108] A. Neto, D. Cavallo, G. Gerini, R. Grooters, and G. Toso, "Array antenna," *United States Patent*, no. US 2011/0156976 A1, Apr. 2009.

[109] D. M. L. Bartholomew, "Optimim design for a broadband microstrip balun," *Electron. Lett.*, vol. 13, no. 17, pp. 510–511, Aug. 1977.

[110] J. Shin and D. H. Schaubert, "A parameter study of stripline-fed vivaldi notch-antenna arrays," *IEEE Trans. Antennas Propag.*, vol. 47, no. 5, pp. 879–886, May 1999.

[111] S. S. Holland and M. N. Vouvakis, "The banyan tree antenna array," *IEEE Trans. Antennas Propag.*, vol. 59, no. 11, pp. 4060–4070, Nov. 2011.

[112] I. Tzanidis, K. Sertel, and J. L. Volakis, "Characteristic excitation taper for ultrawideband tightly coupled antenna arrays," *IEEE Trans. Antennas Propag.*, vol. 60, no. 4, pp. 1777–1784, Apr. 2012.

[113] A. Neto, D. Cavallo, and G. Gerini, "Edge-born waves in connected arrays: A finite infinite analytical representation," *IEEE Trans. Antennas Propag.*, vol. 59, no. 10, pp. 3646–3657, Oct. 2011.

[114] J. A. Kasemodel, C.-C. Chen, and J. L. Volakis, "Wideband planar array with integrated feed and matching network for wide-angle scanning," *IEEE Trans. Antennas Propag. (to appear)*, 2013.

[115] D. Cavallo, A. Neto, and G. Gerini, "Analytical description and design of printed dipole arrays for wideband wide-scan applications," *IEEE Trans. Antennas Propag.*, vol. 60, no. 12, p. 1, Dec. 2012.

[116] R. E. Kleinman and T. B. A. Senior, "Low and high frequency asymptotics." North Holland, Sep. 1986, vol. 2, ch. Rayleigh Scattering, pp. 1–70.

[117] H. C. van de Hulst and Physics, *Light Scattering by Small Particles.* Dover Publications, Dec. 1981.

[118] D. Torrungrueng, B. Ungan, and J. T. Johnson, "Optical theorem for electromagnetic scattering by a three-dimensional scatterer in the presence of a lossless half space," *IEEE Geosci. Remote Sens. Lett.*, vol. 1, no. 2, pp. 131–135, Apr. 2004.

[119] D.-H. Kwon, "Sum rule for conductor-backed thin-wire dipole antennas," in *Proc. IEEE Antennas Propag. Soc. Int. Symp. (APSURSI).* IEEE, Jul. 2012, pp. 1–2.

[120] A. Bernland, A. Luger, and M. Gustafsson, "Sum rules and constraints on passive systems," *Journal of Physics A: Mathematical and Theoretical*, vol. 44, no. 14, pp. 1–20, Apr. 2011.

Appendix A: Realizability Conditions for PEC-Backed Arrays

Consider the three port network representing a PEC-backed array as seen in Fig. 3.3, with scattering matrix $\mathbf{S}(s)$ described by (3.13). A theorem for the physical realizability of $\mathbf{S}(s)$ is given by Wohlers [93],

Theorem. *The necessary and sufficient conditions that an $n \times n$ matrix $\mathbf{S}(s)$ be the scattering matrix of a lumped, passive n-port normalized to n non-Foster positive real impedances $z_i(s)$ are:*

(1) $\mathbf{S}(s)$ is rational.

(2) The matrix $\mathbf{I} - \mathbf{S}^*(j\omega)\mathbf{S}(j\omega)$ be nonnegative definite for all ω where $\mathbf{S}^*(j\omega) = \mathbf{S}'(\overline{j\omega})$ and $\mathbf{I}$ is the identity matrix.

(3) The augmented admittance matrix defined as

$$\mathbf{Y_a}(s) = \frac{1}{2}\mathbf{h}^{-1}(s)\left[\mathbf{h}(s)\mathbf{h}_*^{-1}(s) - \mathbf{S}(s)\right]\mathbf{h}^{-1}(s) \tag{A.1}$$

is analytic in the open RHP, where $\mathbf{h}(s) = diag[h_1(s), h_2(s), ...h_n(s)]$, with $h_i(s)$ defined by the unique factorization,

$$h_i(s)h_{i*}(s) = r_i(s), \tag{A.2}$$

such that all of the zeros of $h_i(s)$ are in the RHP and all poles are in the LHP, and with $r_i(s)$ defined by (2.67) for the impedance which terminates the ith port.

(4a) Either $\det[1 - (\mathbf{z}(s) - 1)\mathbf{Y_a}(s)] \neq 0$ in the open RHP

   where $\mathbf{z}(s) = diag[z_1(s), z_2(s), ...z_n(s)]$, or

(4b) The matrix $[1 - (\mathbf{z}(s) - 1)\mathbf{Y_a}(s)](\mathbf{z}(s) + 1)$ has simple poles on the $j\omega$ axis, and the matrix formed by the residue of these poles be nonnegative definite.

A special case occurs when the impedances $z_i(s)$ are all analytic on the $j\omega$ axis. In this case, the fourth condition of Wohlers' theorem reduces to the requirement that $\mathbf{Y_a}(s)$ have simple poles on the $j\omega$ axis and that the residue matrix be nonnegative definite.

We will assume that the 3×3 scattering matrix $\mathbf{S}(s)$ of Fig. 3.3 is rational and unitary ($\mathbf{S}^*(j\omega)\mathbf{S}(j\omega) = 1$), thus satisfying the first two conditions. The load impedances defined by (3.7) are all analytic on the $j\omega$ axis, and thus it is sufficient to show that $\mathbf{Y_a}(s)$ is analytic in the RHP, and has simple poles on the $j\omega$ axis with a nonnegative definite residue matrix. From (A.1), we find the augmented admittance matrix $\mathbf{Y_a}(s)$ to be

$$\mathbf{Y_a}(s) =$$
$$\begin{pmatrix} \frac{1-S_{11}(s)}{2} & -\frac{(1+L_{TE}s)S_{12}(s)}{2L_{TE}s} & -\frac{(1+L_{TM}s)S_{13}(s)}{2L_{TM}s} \\ -\frac{(1+L_{TE}s)S_{12}(s)}{2L_{TE}s} & -\frac{(1+L_{TE}s)(1-S_{22}(s)+L_{TE}s(S_{22}(s)-1))}{2L_{TE}^2 s^2} & -\frac{(1+L_{TE}s)(1+L_{TM}s)S_{23}(s)}{2L_{TE}L_{TM}s^2} \\ -\frac{(1+L_{TM}s)S_{13}(s)}{2L_{TM}s} & -\frac{(1+L_{TE}s)(1+L_{TM}s)S_{23}(s)}{2L_{TE}L_{TM}s^2} & -\frac{(1+L_{TM}s)(1-S_{33}(s)+L_{TM}s(S_{33}(s)-1))}{2L_{TM}^2 s^2} \end{pmatrix}$$
$$(A.3)$$

We observe from (A.3) that $\mathbf{Y_a}(s)$ is analytic in the open RHP and the third requirement of the theorem is satisfied if and only if $\mathbf{S}(s)$ is analytic in the open RHP. We note that this corresponds to the requirement that the network be causal [6, 120].

From (A.3), all poles of $\mathbf{Y_a}(s)$ on the $j\omega$ axis are located at the origin. We can therefore write $\mathbf{Y_a}(s)$ as a Laurent series at the origin,

$$\mathbf{Y_a}(s) = \sum_{k=0}^{\infty} \mathbf{Y_{a,k}} s^k + \sum_{k=1}^{\infty} \mathbf{Y_{a,-k}} s^{-k}, \quad \text{as } s \to 0. \tag{A.4}$$

Using (3.13), we find $\mathbf{Y_{a,n}} = \mathbf{0}$ for $n \leq 2$, and thus the poles at the origin are simple. The remaining condition is that residue matrix $\mathbf{Y_{a,-1}}$ is nonnegative definite.

$$\mathbf{Y_{a,-1}} = \begin{pmatrix} 0 & 0 & 0 \\ 0 & \frac{2L_{TE}-a_{22,1}}{2L_{TE}^2} & -\frac{a_{23,1}}{2L_{TE}L_{TM}} \\ 0 & -\frac{a_{23,1}}{2L_{TE}L_{TM}} & \frac{2L_{TM}-a_{33,1}}{2L_{TM}^2} \end{pmatrix} \tag{A.5}$$

Using the fact that passivity requires $a_{22,1}$, $a_{33,1}$, L_{TE}, and L_{TM} to be non-negative, this produces the following constraints

$$a_{22,1} \leq 2L_{TE}, \tag{A.6}$$

$$a_{33,1} \leq 2L_{TM}, \tag{A.7}$$

$$a_{23,1}^2 \leq (2L_{TE} - a_{22,1})(2L_{TM} - a_{33,1}). \tag{A.8}$$

We recognize (A.6)-(A.7) as the individual Fano-Youla matching constraints for the loads at ports 2 and 3 from (2.42). However, the Fano-Youla constraints alone are not sufficient for multi-port matching problems, and Wohlers theorem imposes a third constraint (A.8). Therefore, a passive, reciprocal scattering matrix $\mathbf{S}(s)$ corresponds to a physically realizable network for the system of Fig. 3.3 if and only if it is analytic in the RHP and if the conditions (A.6)-(A.8) are satisfied.